DISS. ETH NO. 27299

Numerical Modeling and Simulation of Electric Arcs

A thesis submitted to attain the degree of

DOCTOR OF SCIENCES
(Dr. sc. ETH Zurich)

presented by

Roman Fuchs

MSc ETH Zurich

born on February 27, 1987

citizen of Unteriberg SZ

accepted on the recommendation of

Prof. Dr. Ralf Hiptmair
Prof. Dr. Siddharta Mishra
Prof. Dr. Henrik Nordborg

2021

Acknowledgment

To everyone that made this thesis possible: thank you!

I thank Henrik Nordborg for the unique opportunity writing this thesis and to let me delve into a fascinating research topic of electric arc simulations. You always had an open door for scientific questions and discussions, you had open ears in hard times, and you provided the necessary environment for pursuing this work.

I thank Ralf Hiptmair for continuous support and interest in this thesis project. I am grateful for many topical discussions. I also thank Siddhartha Mishra likewise for joining this project and many conversations. The two of you offered me a quiet desk at ETH that permitted me to focus on this work.

I thank Mario Mürmann for many invaluable discussions on electric arc simulations and other topics as well. We exchanged many tricks and hints in simulation techniques and gained insights from back-on-the-envelope calculations as well as colorfully visualized results. I enjoyed sharing a desk with you in Rapperswil.

I also thank all members at the IET Institute for Energy Technology in Rapperswil as well as the SAM Seminar for Applied Mathematics in Zurich, you all contributed in one way or another to this

Contents

Abstract

This thesis is concerned with three aspects of numerical simulations of electric arcs:

Part I extends a previous numerical scheme in 1D to 3D and non-constant timestepping for a plasma defined in an Euler-Maxwell framework. The main feature of the scheme is that it allows for the scaled Debye length as a modeling parameter to continuously blend between the full Maxwell system and the eddy current model; this feature is known as asymptotic preserving. The generalization to higher dimensions is involved because it requires a dual mesh strategy and interpolation of the electromagnetic field. The submodels of the newly designed scheme are validated with testcases; however, setting the scaled Debye length to zero unveiled that assuming a linear relation in Ohm's law prevents the new 3D scheme from being asymptotic preserving.

Part II focuses on radiation modeling. It reviews the relevant modeling assumptions that reduce the radiative transfer equation to a computationally tractable model as it is found in applied numerical simulations. However, the main issue lies in the complex structure of the absorption coefficient. We consider the Elenbaas-Heller equa-

tion as the simplest model for a wall-stabilized arc and derive the linearized equation. A sensitivity analysis permits to analyze effects of uncertainties in the spectral absorption coefficient on the arc voltage and temperature profile. We also consider the line limited Planck mean and show that an appropriately chosen renormalization length permits to retrieve the correct temperature profile at minimal computational costs.

Part III presents applied numerical simulations of electric arcs in circuit breakers. It is hard to find simulation suites that permit for a robust coupling of the numerous modeling aspects as required for applied thermal plasma simulations, which encompass gas dynamics, electromagnetism, and radiative heat transfer, rigid body motion, mesh morphing, and other modeling aspects. Our software choice enabled us to consider a low voltage circuit breaker and evaluate the contact arm motion with respect to mechanics, plasma pressure, and electromagnetic force. A second case analyzes a recent design of a high voltage direct current circuit breaker and shows results of the electric field and gas flow field complementing previous measurement. Combining a caloric estimate with the simulation results of radiative heat flux to the nozzle wall, we provide an argument for the experimental observation that wall ablation is measured only for sufficiently large currents.

Kurzfassung

Die vorliegende Dissertation befasst sich mit drei Aspekten zur numerischen Simulationen elektrischer Lichtbögen:

Teil I erweitert eine bestehende numerische Methode von 1D nach 3D und mit nicht-konstanten Zeitschritten für ein Plasma, welches durch die Euler-Maxwell-Gleichungen beschrieben ist. Der Kernaspekt des Schemas ist, dass es die skalierte Debye-Länge als Modellierungsparameter berücksichtigt um einen stetigen Übergang zwischen den vollständigen Maxwellgleichungen und dem Wirbelstrommodell zu ermöglichen. Die Verallgemeinerung in höhere Dimensionen ist anspruchsvoll, weil sie eine duale Gitterstrategie sowie eine Interpolation der elektromagnetischen Felder benötigt. Die Teilmodelle sind mit Testfällen validiert; es zeigte sich jedoch bei verschwindender Debye-Länge, dass die Annahme eines linearen Ohmschen Gesetzes es nicht erlaubt, dass das neue 3D Schema asymptotisch erhaltend ist.

Teil II beschäftigt sich mit der Strahlungsmodellierung. Es fasst die grundlegenden Modellannahmen zusammen, welche es erlauben die Strahlungstransportgleichung zu einem berechenbaren Modell für angewandte numerische Simulationen zu reduzieren. Die eigentliche

Hürde liegt in der komplexen Struktur des Absorptionskoeffizienten. Basierend auf der Elenbaas-Heller Gleichung, welche das einfachste Modell für einen wand-stabilisierten Lichtbogen ist, wird eine linearisierte Gleichung entwickelt. Eine Sensitivitätsanalyse ermöglicht das Analysieren von Unsicherheiten im spektralen Absorptionskoeffizienten in Bezug auf Lichtbogenspannung und Temperaturprofil. Im Besonderen wird die Linien-limitierte Planck-Mittelung betrachtet und es wird gezeigt, dass eine angemessene Wahl der Renormierungslänge es erlaubt, das korrekte Temperaturprofil mit wenig Rechenaufwand zu bestimmen.

Teil III zeigt angewandte numerische Simulationen zu elektrischen Lichtbögen in Leistungsschaltern. Es ist schwierig Simulationsumgebungen zu finden, die eine robuste Kopplung der Vielzahl an Modellierungsaspekten erlauben, wie sie für anwendungsnahe Plasmasimulationen benötigt werden: diese umfassen kompressible Strömungen, Elektromagnetismus, Wärmestrahlung, Festkörperbewegung, Gitterverformung, und andere. Die hier verwendete Software erlaubt es, Niederspannungsschutzschalter zu betrachten und die Bewegung der Kontaktbrücke zu bestimmen unter Berücksichtigung der Mechanik, des Plasmadrucks sowie der elektromagnetischen Kräfte. Ein zweiter Fall betrachtet ein neuartiges Design eines Gleichstromschutzschalters, und zeigt Ergebnisse zum elektrischen Feld und der Gasströmung, welche bisherige Messergebnisse ergänzen. Das Kombinieren einer kalorischen Abschätzung mit Simulationsergebnissen des Wärmestrahlungstransport zur Düsenwand erlaubt eine Erklärung von experimentellen Beobachtungen der Ablation, die nur für genügend grosse Stromstärken gemessen wurde.

1. Introduction

We are surrounded by different types of plasmas in our everyday life. We are fascinated by the diffuse and colorful northern lights, we turn the energy-saving light bulb on in the living room or the fluorescent tube in the kitchen, we observe plasma cutters when walking by the metalworking business. We also watched movies on flat screen plasma displays (before they got replaced by LCD displays) [79]. We learned about the solar corona in school, and it might be that a family member got a plasma cancer therapy (see, e.g., [88]). Our parents told us the consequences of lightning strikes in case of being outside in a thunderstorm. We are also protected by circuit breakers that are designed to withstand electric arcs while interrupting the electric current flow to our appliances in case of faults. For cost-effective designs of such technical devices we need numerical simulations as they allow for better performance predictions and optimization studies.

This brief list of examples shows that plasmas occur in many different types, and they are often grouped into natural and man-made plasmas. They are customarily classified in terms of electron temperature and electron number density, and the parameter range is huge: for instance, thermonuclear fusion plasmas exceed $10^6\,\mathrm{K}$ at

10^{20} electrons per cubic meter whereas plasmas in the ionosphere have temperatures of $10^3\,\mathrm{K}$ at 10^{12} electrons per cubic meter. [34, sec. 1.1.3]) But what is a plasma?

We start describing plasmas with an analogy to metal bodies. For instance, let us consider a copper wire. We know that they are good electrical conductors. Applying an electric potential difference between the wire endings results in an electric current, which is nothing but a directed flux of electrons. We can think of these electrons as a gas that is tied to the interior of the metal body. The electrons are free to move in this gas as they are not bound to individual atoms. These conductance electrons are accelerated by the electric field due to the applied potential, but they also collide frequently with the metal atoms which results in a finite speed while heating the solid. The ratio of electron drift velocity to electric field strength is known as electron mobility μ_e (see, e.g., [135, sec. 2.1]). This description is known as the Drude model [49, 50] which has later been supplemented by quantum theory [158], see also [9]; in fact, the electrons constitute a Fermi gas (see, e.g., [9, ch. 2]).

Experimentally, we find that the electric current $\mathbf{J}$ is proportional to the electric field $\mathbf{E}$. This is known as Ohm's law $\mathbf{J} = \sigma\mathbf{E}$ with σ termed as the electrical conductivity. In fact, the electrical conductivity is proportional to elementary charge q, electron number density n_e, and electron mobility (see, e.g., [135, eq. 2.7]): $\sigma = qn_e\mu_e$. When examining with other materials we see that good conductors are characterized by large electrical conductivities (e.g., $\sigma = 58 \times 10^6\,\mathrm{S\,m^{-1}}$ for copper) whereas insulators show values close to zero (e.g., $\sigma =$

$10^{-14}\,\mathrm{S\,m^{-1}}$ for rubber; see, e.g., [72, p. 301]). In contrast to the metal body analogy as outlined above, a plasma consists of negatively and positively charged particles, i.e., electrons and ions, respectively, as well as neutral particles; moreover, the gas is not confined inside a solid body. For a proper definition of plasmas we refer to [38, sec. 1] and [34, ch. 1].

The analogy above leads us to the categorization of ideal and resistive magnetohydrodynamics (MHD). An ideal plasma is characterized through the limiting case of infinite electrical conductivity $(\sigma \to \infty)$ which allows for significant modeling simplifications. This plasma type is of particular interest to fusion reactors (see, e.g., [59, ch. 2]). Plasmas with a finite electrical conductivity $(\sigma < \infty)$ are known as resistive plasmas. They may be described by combining the concepts of fluid dynamics and electromagnetism, and it is the electrical conductivity that acts as a coupling parameter between the two fields of physics. However, the problem occurs when we consider the limiting case $\sigma \to 0$. The system of equations (fluid dynamics and electromagnetism) becomes decoupled and other aspects become more important requiring appropriate modeling efforts.

We therefore cannot rely on a single computational method that fits all. Rather, we have to design specific algorithms that allow to treat the dominant modeling aspects appropriately. In part I, we generalize a previously published numerical scheme [45] to 3D and for arbitrary mesh topologies, including collisions among the plasma gas species. The aim is to show that the scheme is asymptotic preserving, that is, the numerical scheme works equally well if the coupling parameter

goes to zero and the system of equations becomes degenerate. We remark that our coupling parameter is not the electrical conductivity but the scaled Debye length, which allows for a continuous transition between the full set of Maxwell's equations (electromagnetic wave limit) and the quasineutral or eddy current limit.

In part II, we consider the radiative heat flux as it is the main energy transfer mode from an electric arc (a kind of thermal plasmas) to its ambient. Numerical simulations of electric arcs in circuit breakers require appropriate radiation modeling for accurately predicting the performance of a specific circuit breaker design. Let us therefore grasp the main ingredients of radiative heat transfer to start understanding the complexity.

Radiative heat transfer may be defined as the exchange of energy through photons (see, e.g., [112, p. 3]). These photons interact with the atomic structure of the participating media: their energy may be absorbed by electrons and raise their energy levels – if allowed by the quantum states – or they may gain enough energy and separate from the atomic structure leaving behind ions. Modeling and computing of the detailed effects is a separate field of research. Specialized research groups provide data for the absorption coefficient, the key parameter for modeling radiative heat transfer in electric arc simulations.

This absorption coefficient is a strong function of the radiation frequency, plasma composition, its pressure and temperature. Nevertheless, the data is still too complex for being of practical use and requires further modeling because of the limited computational power available. We worked on two aspects. Firstly, we present a sensitiv-

ity analysis of the absorption coefficient based on the Elenbaas-Heller equation [54, 55, 78], which describes the simplest setup of an electric arc (see, e.g., [67, eq. 30]) The method allows to predict the changes in arc voltage that is due to uncertainties in the absorption coefficient. Secondly, we worked on the averaging methods that are used for simplifying the spectral absorption coefficient. We have found that the line limited Planck mean allows for reducing the computational costs without trading accuracy of the results.

Part III is concerned with applied numerical simulations of electric arcs in circuit breakers. In an industrial context we need results in reasonable time. We therefore often use commercially licensed software because – among other reasons – they provide easy access with graphical user interactions to their dedicated computer programs. However, it is quite hard to find software tools that allow for a robust multiphysics coupling as required in electric arc simulations. This includes gas dynamics, electromagnetism, and radiative heat transfer as the basic components for plasma simulations and being discussed in part I and part II. But we also should permit for moving contact geometries, coupling to an external circuit model, models for electrode erosion and material ablation due to the high temperatures, and arc root models that account for effects not resolved by the actual cell size.

The simulation framework used here allowed for setting up and running the simulations in a user-friendly way with marginal efforts in case-specific additional programming. It enabled us to evaluate individual contributions to total torque in a virtual model of a low

voltage circuit breaker, as well as to study a new type of high voltage direct current (HVDC) circuit breaker design. For the latter, we provide an explanation for wall ablation as observed in their experimental work.

While elaborating this thesis, our research group at OST collaborated with international companies throughout the world. It showed us the importance of the research work and that profound knowledge on electric arc modeling is key in product development. Many discussions were driven and stimulated by scientific and application oriented questions likewise. This work is complete only in combination with the applied simulation results as presented in the last part.

Novel contributions

This thesis provides novel contributions as listed below:

Part I builds on previous work of an asymptotic preserving numerical scheme for the Euler-Maxwell system in 1D. I extend the method to 3D and for non-constant timestep size, and I have added another argument for using an implicit scheme based on stiffly accurate methods. The generalized model allows for non-uniform mesh topologies, and I provide a mesh refinement strategy that retains cell quality. The previous work is extended by including collisions among the gas species which amounts to a friction model on the continuum level description. I implemented the numerical method in C++ and performed numerical tests. However, a testcase showed that the newly

designed numerical scheme is not asymptotic preserving due to an inconsistency with Ohm's law.

Part II focuses on radiation modeling in the simplest numerical model setup of an electric arc. I present a linearized model of the Elenbaas-Heller equation at constant current that allows for a sensitivity analysis in arc voltage and temperature profile due to modeling uncertainties in the absorption coefficient. The line limited Planck averaging is reconsidered and compared to the Rosseland and Planck mean. With this averaging method for the absorption coefficients, I show that a small number of radiation bands is sufficient to retrieve the same radial temperature profile as if the full spectrum of absorption coefficients is used.

Part III considers applied numerical simulations of electric arcs in circuit breakers. I have shown that the simulation framework allows for continuous mesh morphing and automated remeshing criterion, with a self-consistent rigid body motion in a virtual model of a low voltage circuit breaker. The same simulation framework is used for numerical studies of an experimental nozzle design aimed for a high voltage direct current circuit breaker. I provide detailed results of the electric field and gas flow in the nozzle that complement recent measurement results. I also propose a caloric estimate for radiation-induced wall ablation in this circuit breaker nozzle design, and the results may explain the experimental findings that the nozzle ablation is only measureable at sufficiently large current.

Part I.

Asymptotic Preserving Plasma Model in 3D

2. Introduction

The design of numerical methods for plasma simulations is a challenging task because one has to consider many separate physical aspects and bring them together for a coupled solution of the full system. For a plasma, which is defined as a "quasineutral gas of charged and neutral particles which exhibit collective behavior" [38, p. 3], it means to combine gas dynamics with electromagnetism and include interactions of the plasma particles among themselves. This may be described by the Euler equations, Maxwell's equations, and a friction model, respectively.

These models are valid at any parameter scales compatible with a continuum description of the plasma. However, it is of practical interest to consider the limiting case known as the eddy current model which is – in mathematical terms – a singular perturbation limit. From a numerical point of view, this aspect makes the design task even more challenging as the scheme should work equally well across a large parameter range.

The main route has been laid by [45] who presented a numerical method that allows for a continuous transition from the full Euler-Maxwell system to the eddy current model. The key feature in their

numerical scheme is the property of being asymptotic preserving, i.e., the numerical discretization is compatible with the modeling parameter limiting case; here, it is given by the scaled Debye length that tends to zero. This property allows for capturing the limit model correctly. A robust coupling is a consequence from the physical fact that electrical current is identical to net mass flux of charged particles. This coupling is to be treated with an implicit timestepping method.

This work generalizes the results of [45] from 1D to 3D. We allow for arbitrary mesh topologies and augment the model by a friction model for the collision dominated plasma. The method is described in chapter 3. We start our discussion with Maxwell's equations for electromagnetism and the Euler equations for gas dynamics. We present the friction model for a minimal set of an argon plasma, and we review the asymptotic preserving property. The main work lies in the discretization that builds on the integral formulation of Maxwell's equations and relies on the Finite Integration Technique (FIT) or Cell Method (CM). A major step is taken in the reconstruction of the electric field and the implicit mass flux. The method has been implemented in a C++ computer program. Results of the numerical experiments are presented in chapter 4. The subsystems are validated and the designed numerical scheme works for the fully coupled Euler-Maxwell system for $\lambda > 0$. However, setting $\lambda = 0$ revealed an inconsistency that does not make the scheme asymptotic preserving. A summary and outlook is given in chapter 5.

3. Asymptotic-preserving multi-species Euler-Maxwell plasma model

This chapter presents the asymptotic-preserving multi-species Euler-Maxwell plasma model and its numerical discretization. In section 3.1 we revisit Maxwell's equations that describe the physical laws of electromagnetism, and we introduce the appropriate scaling to dimensionless variables. Section 3.2 presents the multi-species plasma fluid model including effects of frictional forces among the plasma species that are due to collisions at the molecular level.

The property of asymptotic-preserving is outlined in section 3.3. This concept ensures that the numerical and continuous models are consistent in the limits of vanishing temporal and spatial discretization lengths *and* small values of a physical modeling parameter. This modeling parameter is given herein by the scaled Debye length λ. The discrete model is presented in section 3.4.

3.1. Maxwell's equations

Maxwell's equations describe the dynamics of electric and magnetic fields in space. At macroscopic scales, i.e., at volume sizes that are large compared to the volume occupied by a single atom or molecule [83], they are commonly stated as a set of differential equations

$$\partial_t(\mathbf{B}) + \nabla \times \mathbf{E} = \mathbf{0}, \tag{3.1a}$$

$$\partial_t(\mathbf{D}) - \nabla \times \mathbf{H} = -\mathbf{J}, \tag{3.1b}$$

$$\nabla \cdot \mathbf{B} = 0, \tag{3.1c}$$

$$\nabla \cdot \mathbf{D} = \rho_{el}, \tag{3.1d}$$

where $\mathbf{B}, \mathbf{D}, \mathbf{E}, \mathbf{H}, \mathbf{J}$ are vector fields defined in space $\mathbb{R}^3$ and for time $t \geq 0$; the fields are known as the magnetic flux density $\mathbf{B}$ (SI unit: $\mathrm{V\,s\,m^{-2}}$), electric displacement field or electric induction $\mathbf{D}$ ($\mathrm{A\,s\,m^{-2}}$), electric field $\mathbf{E}$ ($\mathrm{V\,m^{-1}}$), magnetic field intensity $\mathbf{H}$ ($\mathrm{A\,m^{-1}}$), and electric current density $\mathbf{J}$ ($\mathrm{A\,m^{-2}}$). The volume density of free charges is denoted as ρ_{el} ($\mathrm{C\,m^{-3}}$). The equations are known as Faraday's law (3.1a), Ampere's law (3.1b), and the Gauss's laws for magnetic (3.1c) and electric field (3.1d), respectively. The fields are related by the constitutive equations or material laws

$$\mathbf{H} = \frac{1}{\mu_0}\frac{1}{\mu_r}\mathbf{B}, \tag{3.1e}$$

$$\mathbf{D} = \varepsilon_0\varepsilon_r\mathbf{E}, \tag{3.1f}$$

with ε_r and μ_r being the dimensionless, possibly spatially varying $(\varepsilon_r = \varepsilon_r(\mathbf{x}), \mu_r = \mu_r(\mathbf{x}))$ relative permittivity and permeability of isotropic material[1], respectively. The permittivity and permeability of vacuum,

$$\varepsilon_0 = 8.854\,187\,812\,8 \times 10^{-12}\,\mathrm{F\,m}^{-1}, \tag{3.2a}$$

$$\mu_0 = 1.256\,637\,062\,12 \times 10^{-6}\,\mathrm{H\,m}^{-1}, \tag{3.2b}$$

are related to the speed of light c_0 by $\varepsilon_0\mu_0 c_0^2 = 1$. In the following, we write the relative permittivity and permeability without subscript. The inverse of magnetic permeability is known as magnetic reluctivity (see, e.g., [173]), and we denote it by $\nu = \mu^{-1}$.

For a solid material being a good conductor with electrical conductivity $\sigma = \sigma(\mathbf{x})$ $(\mathrm{S\,m}^{-1})$, we also have Ohm's law

$$\mathbf{J} = \sigma\mathbf{E} \tag{3.3}$$

that relates electrical current density and electric field. Electrical current density is defined as the flow rate of charged particles across a unit surface area. In the context of plasma modeling, as we will see in section 3.3, it is crucial to perceive electrical current density as the net flux of charged particles, and therefore to identify with the net

---

[1]We consider macroscopic Maxwell's equations: the electromagnetic fields are understood as averaged fields over a volume large compared to the volume occupied by a single atom or molecule. [83, p. 13]

mass flux. Hence, we may write

$$\mathbf{J} = \sum_* \mathbf{J}_*, \quad \mathbf{J}_* := q_* n_* \mathbf{u}_*, \tag{3.4}$$

where n_* (m^{-3}) denotes the number density of species $*$, $\mathbf{u}_*$ $(\mathrm{m\,s}^{-1})$ is their velocity and q_* (C) denotes their electrical charge. The electrical charge is given as multiples of the elementary charge

$$q = 1.602\,176\,634 \times 10^{-19}\,\mathrm{C}. \tag{3.5}$$

The volume or space charge density is the net number of charged particles in an infinitesimal volume, i.e.,

$$\rho_{el} = \sum_* q_* n_*. \tag{3.6}$$

The general framework of Maxwell's equations allows to describe electromagnetic phenomena at various spatial and temporal scales. In fact, the framework describes electromagnetic waves at any frequency encompassing radio- and microwaves, visible light, and gamma rays. The equations may be simplified if the fields may be assumed to vary slowly in time and the domain is small enough, i.e., if the wavelength is much longer than the diameter of the domain. In such cases, the model equations may be reduced to the eddy current approximation or magneto-quasistatic model $(\partial_t(\mathbf{D}) \to 0)$, the electro-quasistatic model $(\partial_t(\mathbf{B}) \to 0)$, or the stationary field approximation in which both temporal derivatives are neglected. (see, e.g., [165, sec. 1.3], [5,

sec. 1.2] These approximations are used, for instance, in the analysis of transformers [e.g., 156, 155, 36], or microelectrodes or neurophysical models [e.g., 166].

Dimensional analysis allows to decide on significant terms in a specific context. Here, we consider a quasineutral plasma, i.e., a plasma in which net space charge is small for sufficiently large volumes (that is, a sphere with radius equal to Debye length λ_D, see below). [see, e.g. 34, ch. 4.5] We identify characteristic units of the underlying physical system and write $\bar{B}$, $\bar{E}$, $\bar{J}$, $\bar{\rho}_{el}$, $\bar{n}$, $\bar{x}$, $\bar{t}$, $\bar{u}$ for the scales of magnetic flux, electric field, current density, charge density, number density, space, time, and velocity. It is then natural to specify the hypotheses [45]:

(i) the space, time and velocity scales are related by $\bar{x} = \bar{u}\bar{t}$;

(ii) the charge density scale is given by $\bar{\rho}_{el} = q\bar{n}$, where q designates the value of an elementary positive charge;

(iii) the current density scale is given by $\bar{J} = q\bar{n}\bar{u}$;

(iv) the electrical energy scale is given by a thermal energy scale (which is specified later by the fluid), $q\bar{E}\bar{x} = k_B\bar{T}$, with

$$k_B = 1.380\,649 \times 10^{-23}\,\mathrm{J\,K^{-1}} \tag{3.7}$$

being Boltzmann's constant.

This leads to three free, dimensionless scaling parameters:

$$\alpha = \frac{\bar{u}}{c_0}, \tag{3.8a}$$

$$\beta = \left(\frac{\bar{u}\bar{B}}{\bar{E}}\right)^{1/2}, \tag{3.8b}$$

$$\lambda = \left(\frac{\varepsilon_0 k_B \bar{T}}{q^2 \bar{n} \bar{x}^2}\right)^{1/2} = \frac{\lambda_D}{\bar{x}}. \tag{3.8c}$$

These parameters stand for the ratio of plasma velocity to the speed of light, the ratio of induction electric field to the reference electric field, and the ratio of Debye length λ_D to the reference space scale. The Debye length λ_D, defined as

$$\lambda_D = \left(\frac{\varepsilon_0 k_B T_e}{q^2 n_e}\right)^{1/2}, \tag{3.9}$$

where T_e and n_e denote electron temperature and number density, respectively, is a characteristic length scale over which an excess or perturbation of electrical charge distribution is screened due to thermal random motion [see, e.g. 34, ch. 4.5]. With the same notation for dimensionless variables as for the physical variables, the scaled

Maxwell system then reads

$$\beta^2 \partial_t(\mathbf{B}) + \nabla \times \mathbf{E} = 0, \tag{3.10a}$$

$$\lambda^2(\alpha^2 \partial_t(\mathbf{D}) - \beta^2 \nabla \times \mathbf{H}) = -\alpha^2 \mathbf{J}, \tag{3.10b}$$

$$\nabla \cdot \mathbf{B} = 0, \tag{3.10c}$$

$$\lambda^2 \nabla \cdot \mathbf{D} = \rho_{el}, \tag{3.10d}$$

$$\mathbf{H} = \mu^{-1}\mathbf{B}, \tag{3.10e}$$

$$\mathbf{D} = \varepsilon \mathbf{E}. \tag{3.10f}$$

Let us remark on one of the limit case for small scale-free parameter values: if we chose α and β approximately equal and let them go to zero, it would lead to the electro-quasistatic model. A more general discussion of the scaling parameters and choosing them is given in [46, ch. 2.2]. However, we will focus on the $\lambda \to 0$ as outlined next.

Let us estimate the Debye length for a typical plasma at atmospheric pressure. For instance, let us consider electric arcs which are classified as partially ionized, quasineutral thermal plasma, i.e., the plasma is not dominated by Coulomb collisions, and the electron temperature is comparable to that of heavy species (atoms and ions). For the electron temperature, we find typical values $T_e = 50\,\mathrm{kK}$, estimate the number density of electrons by the ideal gas law ($p = nk_BT$), and assume an ionization degree of 1×10^{-3}. This results in a Debye length comparable to a few micrometers (µm). Since the typical length scale for electric arc simulations is on the order of millimeters and larger, we easily see that our interest lies in small parameter

values for $\lambda \approx 1 \times 10^{-5}$ to 1×10^{-3}.

We also note that the plasma velocity is on the order of $\bar{u} = 1 \times 10^4 \, \mathrm{m \, s^{-1}}$, which results in $\alpha \approx 3 \times 10^{-5}$. We therefore choose λ and α approximately equal. As the electrical conductivity of a plasma is rather high and ideal Ohm's law is valid, we find $\beta \approx 1$, see [45]. This set of equations tends to the magneto-static limit case (eddy-current model), see also [46, ch. 2.2]. Therefore, we opt for the choice

$$\alpha = \lambda, \tag{3.11a}$$

$$\beta = 1, \tag{3.11b}$$

i.e.,

$$\partial_t(\mathbf{B}) + \nabla \times \mathbf{E} = \mathbf{0}, \tag{3.12a}$$

$$\lambda^2 \partial_t(\mathbf{D}) - \nabla \times \mathbf{H} = -\mathbf{J}, \tag{3.12b}$$

$$\nabla \cdot \mathbf{B} = 0, \tag{3.12c}$$

$$\lambda^2 \nabla \cdot \mathbf{D} = \rho_{el}, \tag{3.12d}$$

$$\mathbf{H} = \mu^{-1}\mathbf{B}, \tag{3.12e}$$

$$\mathbf{D} = \varepsilon\mathbf{E}. \tag{3.12f}$$

We see that $\lambda \to 0$ leads to a quasineutral plasma ($\rho_{el} \to 0$) and the temporal derivative in Faraday's equation vanishes. That is, Maxwell's equations change their nature from a hyperbolic to a parabolic system of equations. As we will see in section 3.3, the

main issue is to find a numerical scheme that is compatible with this limiting case.

3.2. Plasma fluid modeling

3.2.1. From Boltzmann to Euler equations

Boltzmann's kinetic equation is fundamental to plasma fluid models (see, e.g., [181, ch. 1] [18, 163]). The state of a plasma can be described by the single-particle distribution functions $f_*(\mathbf{v}, \mathbf{r}, t)$ for species $*$, which is defined such that $f_*(\mathbf{v}, \mathbf{r}, t)\, \mathrm{d}\mathbf{v}\, \mathrm{d}\mathbf{r}$ is the average number of particles of species $*$ at time t in the vicinity of point $\mathbf{r}$ of the volume element $\mathrm{d}\mathbf{r}$, and with velocity near $\mathbf{v}$ in the interval $\mathrm{d}\mathbf{v}$. The conserved macroscopic quantities (mass, momentum, and energy) are found as moments of the distribution function over the velocity space. Likewise, the macroscopic conservation equations for mass, momentum, and energy are found as moments of Boltzmann's kinetic equation

$$\partial_t(f_*) + \mathbf{v} \cdot \nabla f_* + \frac{1}{m_*}\mathbf{F}_* \cdot \nabla_{\mathbf{v}} f_* = J_*, \qquad (3.13)$$

where ∇ and $\nabla_{\mathbf{v}}$ denote the divergence operators in Cartesian coordinates in space and velocity variables, respectively, and $\mathbf{F}_*$ is the external force acting on a particle of species $*$. Here, the external force is given by the electromagnetic fields $\mathbf{B}$ and $\mathbf{E}$,

$$\mathbf{F}_* = q_*(\mathbf{E} + \mathbf{v}_* \times \mathbf{B}), \qquad (3.14)$$

i.e., Lorentz force, where q_* is the electric charge of a particle of species $*$; non-electromagnetic forces are neglected.

One refers to the right hand side J_* of (3.13) as the collision integral; if it is zero, Boltzmann's equation is also known as Vlasov equation. The collision integral J_* accounts for binary collisions among the particles. It leads to source terms in the macroscopic conservation equations that may take the form, for instance, of a friction model. The following sections will use those macroscopic equations – known as Euler equations in case of vanishing viscosity – in the design of a multi-species fluid model with frictional source terms that stems from elastic and inelastic collisions.

3.2.2. Local thermodynamic equilibrium and two-temperature plasma

Thermal plasma models build largely on the assumption of local thermodynamic equilibrium (LTE), i.e., all energy modes are equilibrated and therefore described by a single equilibrium temperature. This allows to treat the gas mixture as a single fluid and to derive the required thermodynamic and transport coefficients for the mixture as a whole. Strictly speaking, gas temperature is a measure for the average kinetic energy and defined only if the species particle velocity distribution function follows a Maxwellian probability distribution (see, e.g., [113, sec. 1.4.2]).

Thermal LTE plasma models are valid for many engineering applications as an approximation for the bulk plasma. However, LTE

is violated in the outer regions in which the plasma mixes with cold gas and – in particular – in regions where the plasma interacts with solid bodies (e.g., arc roots). [19, 20] Because of their small inertia, electrons are more quickly accelerated by the electric field and gain energy on their mean free path between collisions more easily than heavy species (i.e., ions, atoms, and molecules) [164]. Moreover, collisions of electrons and heavy species is an inefficient process in equilibrating their kinetic energies because of their large mass ratio; this implies a relatively long time scale. As particles of the same species equilibrate quickly among themselves, separate temperatures are assigned for heavy species T_h and electrons T_e. However, momentum exchange is a much faster process than thermal relaxation (see, e.g., [111, eq. (II.7.6)]). The total momentum of the plasma is dominated by the heavy particles. It is therefore sufficient to describe the plasma with a single velocity field.

Plasma models that account for T_h and T_e separately are known as two-temperature or 2T models (see, e.g., [67, 68]). Significant deviation from LTE is observed, for instance, in numerical simulations of circuit breakers at and after current zero (see, e.g., [150]). Two-temperature models are often used to account more accurately for processes in the outer regions of a plasma. For instance, [16] uses a 2T model for a supersonic argon plasma jet. A 2T ionization layer model is presented in [21, 4]; cathode layer models are found in [3, 22], and the anode boundary plasma layer is reviewed in [110]. Detailed effects in the near-electrode plasma layers are accounted in [13, 14] by an advanced 2T model. Reference [160] presents a 2T model for an

inductively coupled thermal plasma. One may escalate the separation of energy modes: for instance, polyatomic species show vibrational and rotational energy modes (see, e.g., [94, 93, 92]). See also [163] for a 3T plasma model that discriminates between electron temperature, molecular vibrational temperature, and heavy-species translational-rotational temperature.

A common example for a 2T plasma is given by the fluorescent lamp (see, e.g., [56]): the low-pressure plasma inside the tube leads to visible light without the carrier gas getting very hot. It is only the electrons gas being at high temperature. The large mass ratio between electrons and heavy species leads also to other classes of plasmas. Streamers are plasma channels created due to electrical breakdown in a non-conducting medium that is suddenly exposed to a high electric field (see, e.g., [106, 53, 104]). Dielectric barrier discharges (DBD) are typically created by electrical field oscillations at high frequencies (kHz to MHz). They are used, e.g., as actuators in flow control applications [41, 131], catalysis [101], and abatement of volatile organic compounds [105]. Both plasma types are classified as non-thermal plasmas and may be described by drift-diffusion models (or density models [106]) that may be viewed as the asymptotic limit of zero-electron-mass or zero-relaxation-time of the Euler-Poisson system [86]. The species motion is dictated by the electric field and diffusion of concentration gradients. Chemical reactions and models for photo-ionization result in species creation source terms. [182, 96] A comparison of the drift-diffusion limit model and the full gas dynamic equations may be found in [131, 53].

3.2.3. Multi-species Euler equations

We consider a multi-species plasma model in the following sections. That is, each species is considered as a separate gas and described by conservation equations for mass, momentum, and energy. We retain individual velocity fields for each gas species (in contrast to 2T models), and we retain momentum inertia for all species (in contrast to drift-diffusion models) despite of the large mass ratio of electrons and heavy species.

A multi-species plasma may be considered as a gaseous collection of neutral species and charged species, i.e., electrons, ions, and neutral atoms or molecules. Each gas species is identified by an index $* = s_1, s_2, \ldots, s_N$, and we specifically refer to electrons ($* = e$), neutral species ($* = n$), and positive ions ($* = p$); neutral species and ions are also often referred to as heavy species ($* = h$). Each gas species is considered as an ideal[2] gas; thermal conductivity and viscosity are neglected to reduce model complexity. They stem from third-order moments of the particle velocity distribution function. If included, turbulence modeling raises additional questions and uncertainties to be addressed; the transport coefficients may be evaluated from collision integrals or taken from tabulated data (see, e.g., [39] for viscosity data in thermal argon plasma).

The governing equations are therefore given by the conservation laws for mass, momentum, and energy, commonly known as Euler

---

[2]More precisely: a *perfect* gas. The two terms are often mixed up. (see, e.g., [175, p. 21], [34, sec. 6.2.3])

equations (see, e.g., [99, ch. 14]) and stated as

$$\partial_t \begin{bmatrix} \rho_* \\ \rho_* \mathbf{u}_* \\ \rho_* e_{tot,*} \end{bmatrix} + \nabla \cdot \begin{bmatrix} \rho_* \mathbf{u}_* \\ \rho_* \mathbf{u}_* \otimes \mathbf{u}_* + p_* \mathbb{1} \\ \rho_* h_{tot,*} \mathbf{u}_* \end{bmatrix} = \begin{bmatrix} m_* \Gamma_* \\ m_* \mathbf{R}_* \\ m_* Q_* \end{bmatrix}, \qquad (3.15)$$

where $\rho_* = m_* n_*$ is the mass density, $\mathbf{u}_*$ denotes the gas species velocity, p_* stands for gas species pressure, $\mathbb{1}$ is the unit tensor, $e_{tot,*} = \frac{1}{2}|\mathbf{u}_*|^2 + e_*$ is the total specific energy, e_* is the internal specific energy, and $h_{tot,*} = e_{tot,*} + p_*/\rho_*$ is the total specific enthalpy. The right hand side denotes source terms for mass, momentum, and energy. The specific sources Γ_*, $\mathbf{R}_*$, and Q_*, denote the specific effective species production rate, the specific rate of change in momentum, and the specific rate of change in energy, respectively.

Our next step is to write the Euler equations in dimensionless quantities. We remark that the particle mass of electrons is much smaller than those of heavy species. We denote by $\bar{m}$ a reference mass scale, and $\bar{p}$ is pressure scale. We augment the list of scaling hypotheses (see section 3.1) by [45]:

(v) the reference particle mass $\bar{m}$ is given by that of neutral species ($\bar{m} = m_n$);

(vi) the thermal energy scale is given by the drift energy scale:

$$k_B \bar{T} = q \bar{E} \bar{x} = \bar{m} \bar{u}^2 = \bar{p} \bar{n}^{-1}. \qquad (3.16)$$

The specified energy scales (3.16) ensure that the pressure force, in-

ertia force and electric force have the same order of magnitude. [45] Moreover, we define the mass ratio

$$\varepsilon_*^2 := m_*/\bar{m} \qquad (3.17)$$

for each species; the mass ratio is approximately unity for heavy species ($\varepsilon_h^2 \approx 1$) but for electrons we have $\varepsilon_e^2 \approx 5 \times 10^{-4}$ or smaller. The dimensionless Euler equations for species $*$ are then stated as

$$\partial_t \begin{bmatrix} n_* \\ n_* \mathbf{u}_* \\ n_* e_{tot,*} \end{bmatrix} + \nabla \cdot \begin{bmatrix} n_* \mathbf{u}_* \\ n_* \mathbf{u}_* \otimes \mathbf{u}_* + \varepsilon_*^{-2} p_* \mathbb{1} \\ n_* h_{tot,*} \mathbf{u}_* \end{bmatrix} = \begin{bmatrix} \Gamma_* \\ \mathbf{R}_* \\ Q_* \end{bmatrix}. \qquad (3.18a)$$

We remark that the momentum and energy balance equations have been multiplied by the mass ratio. The system of conservation laws is concisely written in vector form as

$$\partial_t(\mathbf{U}_*) + \nabla \cdot \mathbf{F}_*(\mathbf{U}_*) = \mathbf{S}_*, \qquad (3.18b)$$

where $\mathbf{U}_*$ is the vector of conserved states, $\mathbf{F}_*$ is the vector of flux functions, and $\mathbf{S}_*$ is the vector of source terms. The scaled total specific enthalpy is given by $h_{tot,*} = e_{tot,*} + \varepsilon_*^{-2} p_*/n_*$. The scaled equation of state for ideal gases is

$$p_* = n_* T_* = (\gamma - 1)\varepsilon_*^2 n_* e_*, \qquad (3.19)$$

where γ denotes the heat capacity ratio. We note that $\gamma = \frac{5}{3}$ for

monatomic gases such as argon. The acoustic wave speed is given as

$$s_* = \left(\gamma \frac{p_*}{\varepsilon_*^2 n_*}\right)^{1/2} = (\gamma(\gamma - 1)e_*)^{1/2}. \tag{3.20}$$

The source terms are given by the cumulative effects of electromagnetism and particle collisions (see section 3.2.4 ff.),

$$\mathbf{S}_* = \begin{bmatrix} 0 \\ \mathbf{R}_*^{\text{em}} \\ Q_*^{\text{em}} \end{bmatrix} + \begin{bmatrix} \Gamma_*^{\text{coll}} \\ \mathbf{R}_*^{\text{coll}} \\ Q_*^{\text{coll}} \end{bmatrix}. \tag{3.21}$$

The electromagnetic force (3.14) acts on charged gas species and results in source terms known as Lorentz force and Ohmic heating given by,

$$\mathbf{R}_*^{\text{em}} = \varepsilon_*^{-2} q_* n_* (\mathbf{E} + \mathbf{u}_* \times \mathbf{B}), \tag{3.22a}$$

$$Q_*^{\text{em}} = \varepsilon_*^{-2} \mathbf{J}_* \cdot \mathbf{E}; \tag{3.22b}$$

Let us add two remarks: Firstly, we note that these terms are specified as volumetric source terms. If we considered an ideal plasma in eddy current approximation, they could be written in divergence form and being added to the flux term (see, e.g., [121]). Secondly, the terminology of Ohmic heat source may be misleading: the energy source term (Ohmic heating) is consistent with the momentum source term (Lorentz force) as it adds kinetic energy to the gas species. The thermal or inner energy is not affected. Conversion of kinetic energy

to inner energy occurs only by particle collision (on the microscopic level) or frictional forces (on the macroscopic level), respectively. This is also seen from a physical perspective: the electric field accelerates charged particles on their mean free path, and without collisions, this results in a directed motion. It is only due to collisions that the particles motion is randomized, i.e., kinetic energy is converted to inner energy or temperature. The collision model is presented in the next section.

A complete plasma model would also include an energy sink due to radiation (see also part II). This could be achieved by simple models such as the Stefan-Boltzmann power law or by net emission coefficients with tabulated data, e.g., from [43]. Such an energy sink term would be assigned to the electron fluid (see, e.g., [67]). Other, more sophisticated models would add significant computational costs. However, the present plasma model focuses on the design of a numerical scheme that is compatible with the limit $\lambda \to 0$ (see section 3.1 and 3.3). The radiative sink is not a model priority and therefore neglected.

3.2.4. Collision modeling

Let us consider two particles that are initially separated by a large distance and approaching one another. If the particles interact in some way resulting in principle to a measurable change, we say that a collision has occurred. Those collisions are classified into two groups (see, e.g., [111, sec. II.2], [34, sec. 3.1]): elastic and inelastic collisions.

Elastic collisions are characterized by unchanged internal energies of the collided particles. For instance, the particles may change their directions of motion but the kinetic energy of the particles is conserved. All other collisions are called inelastic. Examples of inelastic collisions are excitation, ionization, recombination, charge transfer, attachment, creation of metastable states, and dissociation processes. We remark that total mass as well as total momentum is conserved irrespective of the collision type.

The present model is made of a minimal set of species that applies to an argon plasma, i.e., electrons (e^-), neutral argon atoms (Ar), and singly charged argon ions (Ar^+). The heavy species are both in their ground states. This set of plasma species may be assumed for an argon plasma in equilibrium up to temperatures of $15\,kK$ at ambient pressure (see, e.g., [34, fig. 1.16]). More species (i.e., multiply charged argon ions) should be included for an accurate plasma model at higher temperatures. It is straight-forward to add more species to the multi-species plasma model; however, that would lead to increased computational costs to account for their conserved state variables as well as their binary collisions. We therefore limit ourselves to elastic collisions among the three gas species and inelastic collisions due to ionization and recombination, see table 3.1. Other processes (e.g. atom-atom collisions Ar + Ar) are neglected.

The following sections 3.2.5 and 3.2.6 present the elastic and inelastic collision models, respectively. They stem from the collision operator J_* (see eq. (3.13)) and its integration over velocity space in the first approximation of the Chapman-Enskog method (see, e.g.,

	Reaction	Collision type
(1)	$e^- + Ar \longrightarrow e^- + Ar$	elastic
(2)	$e^- + Ar^+ \longrightarrow e^- + Ar^+$	elastic
(3)	$Ar + Ar^+ \longrightarrow Ar + Ar^+$	elastic
(4)	$e^- + Ar \longrightarrow 2\,e^- + Ar^+$	ionization
(5)	$2\,e^- + Ar^+ \longrightarrow e^- + Ar$	recombination

Table 3.1.: Minimal set of elastic and inelastic collisions in argon plasma.

[111, sec. VIII.1], [181, p. 41]). Data of average momentum transfer cross sections are specified for collisions in an argon plasma and supplied to the source terms for the Euler equations.

3.2.5. Elastic collisions

We denote the colliding particle species by indices α and β. The fundamental data to describe collision interactions is given by the momentum transfer cross section $Q_{\alpha\beta}^{(1)}(\varepsilon)$ (SI units: m^2) tabulated with respect to the relative energy ε of the colliding particles. Cross section data for collisions in argon is given below. Then the average momentum transfer cross section $\bar{Q}_{\alpha\beta}^{(1,1)}$ is defined as

$$\bar{Q}_{\alpha\beta}^{(1,1)} = \int_0^\infty \zeta^5 \exp(-\zeta^2) Q_{\alpha\beta}^{(1)}(\varepsilon)\,\mathrm{d}\zeta, \quad \varepsilon = k_B T_{\alpha\beta}\zeta^2, \qquad (3.23\mathrm{a})$$

or, equivalently,

$$\bar{Q}_{\alpha\beta}^{(1,1)} = \frac{1}{2}\frac{1}{(k_B T_{\alpha\beta})^3} \int_0^\infty \varepsilon^2 \exp\left(-\frac{\varepsilon}{k_B T_{\alpha\beta}}\right) Q_{\alpha\beta}^{(1)}(\varepsilon)\,\mathrm{d}\varepsilon. \qquad (3.23\mathrm{b})$$

The reduced temperature $T_{\alpha\beta}$ is defined as

$$T_{\alpha\beta} = \frac{m_\alpha T_\beta + m_\beta T_\alpha}{m_\alpha + m_\beta}, \tag{3.24a}$$

and we also introduce the reduced mass $m_{\alpha\beta}$ and thermal velocity $\bar{v}_{\alpha\beta}$ defined as

$$m_{\alpha\beta} = \frac{m_\alpha m_\beta}{m_\alpha + m_\beta}, \tag{3.24b}$$

$$\bar{v}_{\alpha\beta} = \left(\frac{8k_B T_{\alpha\beta}}{\pi m_{\alpha\beta}} \right)^{1/2}. \tag{3.24c}$$

This allows to write the rates of change in momentum and energy for species α as (see, e.g., [111, eq. 6.29 ff.], [181, eq. 3.1.10 ff. and eq. 5.1.9])

$$\mathbf{R}_\alpha^{\text{coll}} = -\sum_{\beta \neq \alpha} \frac{4}{3} n_\alpha n_\beta m_{\alpha\beta} \bar{v}_{\alpha\beta}^{\text{th}} \bar{Q}_{\alpha\beta}^{(1,1)} (\mathbf{u}_\alpha - \mathbf{u}_\beta), \tag{3.25a}$$

$$Q_\alpha^{\text{coll}} = -\sum_{\beta \neq \alpha} \frac{4}{3} n_\alpha n_\beta \frac{m_{\alpha\beta}}{m_\alpha + m_\beta} \bar{v}_{\alpha\beta}^{\text{th}} \bar{Q}_{\alpha\beta}^{(1,1)}$$
$$\left(3k_B(T_\alpha - T_\beta) + (\mathbf{u}_\alpha - \mathbf{u}_\beta) \cdot (m_\alpha \mathbf{u}_\alpha + m_\beta \mathbf{u}_\beta) \right), \tag{3.25b}$$

where the summation is over all particle species.

The rate of change in energy (3.25b) accounts for differences in thermal energy and kinetic energy in the colliding species. The double-indexed quantities are symmetric in their indices, and so we

easily see that the source terms are conservative for the gas mixture as a whole.

For writing equations (3.25) in scaled quantities, we note that the scaled reduced temperature, scaled reduced mass ratio, and scaled thermal velocity, are given as

$$T_{\alpha\beta} = \frac{\varepsilon_\alpha^2 T_\beta + \varepsilon_\beta^2 T_\alpha}{\varepsilon_\alpha^2 + \varepsilon_\beta^2}, \tag{3.26a}$$

$$\varepsilon_{\alpha\beta}^2 = \frac{\varepsilon_\alpha^2 \varepsilon_\beta^2}{\varepsilon_\alpha^2 + \varepsilon_\beta^2}, \tag{3.26b}$$

$$\bar{v}_{\alpha\beta} = \left(\frac{8 T_{\alpha\beta}}{\pi \varepsilon_{\alpha\beta}^2}\right)^2. \tag{3.26c}$$

The appropriate scaling for cross sections is given by $(\bar{n}\bar{x})^{-1}$. Hence, we find

$$\mathbf{R}_\alpha^{\text{coll}} = -\sum_{\beta \neq \alpha} \frac{4}{3} n_\alpha n_\beta \varepsilon_{\alpha\beta}^2 \bar{v}_{\alpha\beta} \bar{Q}_{\alpha\beta}^{(1,1)} (\mathbf{u}_\alpha - \mathbf{u}_\beta), \tag{3.27a}$$

$$Q_\alpha^{\text{coll}} = -\sum_{\beta \neq \alpha} \frac{4}{3} n_\alpha n_\beta \frac{\varepsilon_{\alpha\beta}^2}{\varepsilon_\alpha^2 + \varepsilon_\beta^2} \bar{v}_{\alpha\beta} \bar{Q}_{\alpha\beta}^{(1,1)}$$
$$\left(3(T_\alpha - T_\beta) + (\mathbf{u}_\alpha - \mathbf{u}_\beta) \cdot (\varepsilon_\alpha^2 \mathbf{u}_\alpha + \varepsilon_\beta^2 \mathbf{u}_\beta)\right) \tag{3.27b}$$

Let us comment on the relaxation time scales for momentum and energy. One can show that the average exchange of kinetic energy in

an elastic collision is given by (see, e.g., [111, eq. 7.4])

$$\Delta E_{kin} = 2\frac{m_{\alpha\beta}}{m_\alpha + m_\beta} = 2\frac{m_\alpha m_\beta}{(m_\alpha + m_\beta)^2}. \tag{3.28}$$

This relation shows that particles with similar masses quickly equilibrate their kinetic energy or temperature, whereas energy exchange between electrons and heavy particles is inefficient. Separate temperatures are therefore assigned to the fluid species as outlined above. One can estimate the relative temperature difference for a plasma in an electric field of strength E to be proportional to (see, e.g., [34, eq. 1.12], [135, sec. 10.11])

$$\frac{T_e - T_h}{T_e} \sim \left(\frac{E}{p}\right)^2 \tag{3.29}$$

where the ratio E/p (or E/n) is known as the reduced field, a well-known parameter in gas discharge studies (e.g., Paschen's law that describes the electrical breakdown voltage [122]). In contrast to kinetic energy, the average exchange of momentum scales with $m_{\alpha\beta}$ and equilibrates much faster in collisions of large mass ratio. The relaxation time scales of energy ($\tau_{\alpha\beta}^E$) and momentum $\tau_{\alpha\beta}$ (as defined just next) are related by

$$\tau_{\alpha\beta}^E = \frac{(m_\alpha + m_\beta)^2}{2m_\alpha m_\beta}\tau_{\alpha\beta}, \tag{3.30}$$

and $\tau_{eh}^E = \frac{m_h}{m_e}\tau_{eh}$ in particular for collisions of electrons and heavy particles. [181, eq. 3.1.23]

The rates of change in momentum and energy (see eq. (3.25)) are often also written in terms of the averaged momentum transfer collision frequency (see, e.g., [181, eq. 3.1.12]),

$$\tau_{\alpha\beta}^{-1} = \frac{4}{3} n_\beta \bar{v}_{\alpha\beta} \bar{Q}_{\alpha\beta}^{(1,1)}.$$
(3.31)

Note that this quantity is not symmetric despite the notation might suggest so. It is often also expressed via the binary diffusion coefficient (see, e.g., [181, eq. 3.1.16], [3])

$$D_{\alpha\beta} = \frac{3\pi}{32} \left(\frac{8k_B T_{\alpha\beta}}{\pi m_{\alpha\beta}} \right)^{1/2} \frac{1}{n \bar{Q}_{\alpha\beta}^{(1,1)}},$$
(3.32)

with $n = \sum_* n_*$ being the total number density. Hence, one finds

$$m_{\alpha\beta} \tau_{\alpha\beta}^{-1} = \frac{n_\beta k_B T_{\alpha\beta}}{n D_{\alpha\beta}}.$$
(3.33)

We remark that binary diffusion coefficients are valid for temperatures below those for which ionization occurs (see, e.g., [115, 116, 117, 139]); the diffusion coefficients should be determined from a 2T model at temperatures larger than $5\,\text{kK}$. [139]

Elastic collisions are modeled with the following data:

- Elastic collisions of **electron-atom ($e^- + Ar$)** and **heavy particle ($Ar + Ar^+$)** interactions are modeled with cross section data retrieved in the LXCat database [107, 129]; the original data sources are found in [77] ($e^- + Ar$) and [127] ($Ar +$

Ar$^+$), respectively, and plotted in figure 3.1. A review of collision cross section data of argon is available in [136]. More recent measurements [15] show that the fitted formula in [127],

$$Q_{\mathrm{ArAr^+}}^{(1)} = 1.15 \times 10^{-18} \varepsilon^{-0.1}(1 + 0.015/\varepsilon)^{0.6}, \qquad (3.34)$$

provides a good approximation with ε in units of eV and $Q_{\mathrm{ArAr^+}}^{(1)}$ in m^2. From these data, average momentum transfer cross sections are calculated by (3.23) and shown in figure 3.2 (center and bottom).

- Elastic collisions of **electron-ion (e$^-$ + Ar$^+$)** interactions are governed by Coulomb interaction. For single-charged particles one finds (see, e.g., [181, eq. 3.1.17])

$$\bar{Q}_{ei}^{(1,1)} = \frac{(q_e q_i)^2}{32\pi\varepsilon_0^2 (k_B T_{ei})^2} \ln \Lambda_{ei}, \qquad (3.35)$$

where $\ln \Lambda_{ei}$ is known as the Coulomb logarithm defined as

$$\Lambda_{ei} = \frac{12\pi\varepsilon_0}{|q_e q_i|} k_B T_{ei} \lambda_D, \quad \lambda_D = \left(\sum_* \frac{n_* q_*^2}{\varepsilon_0 k_B T_*} \right)^{-1/2}, \qquad (3.36)$$

and λ_D denotes the Debye length. Approximate expressions for electron-ion interactions are found as (see, e.g., [3, eq. 47], [111, eq. 8.10])

$$\bar{Q}_{ei}^{(1,1)} \approx \frac{q^4}{32\pi\varepsilon_0^2 (k_B T_e)^2} \ln \Lambda_e, \qquad (3.37)$$
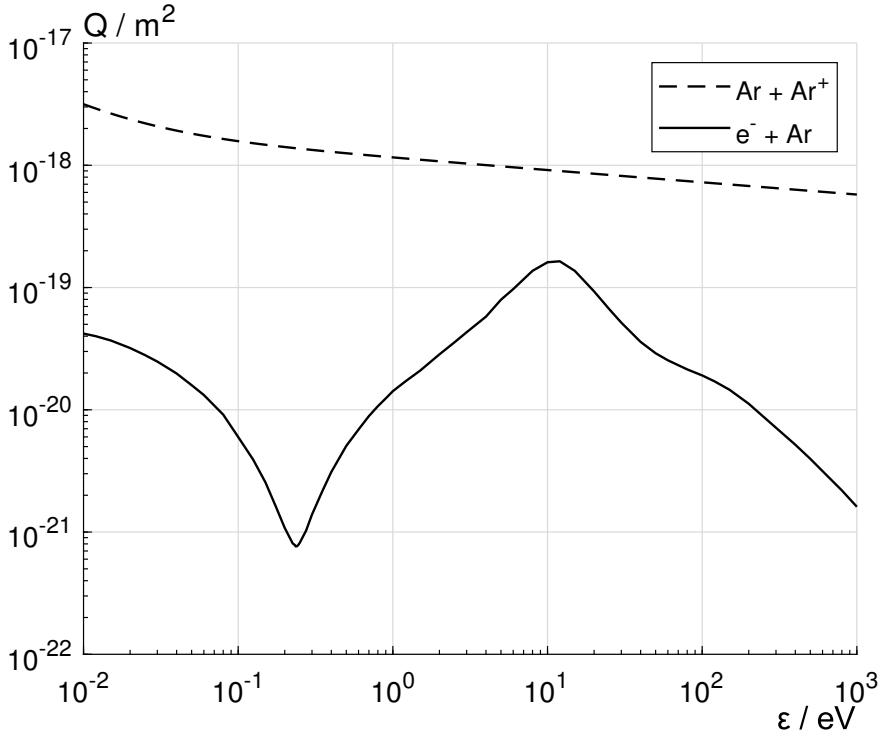
Figure 3.1.: Momentum transfer cross sections $Q^{(1)}_{\alpha\beta}$ for elastic collisions of $Ar + Ar^+$ as given by eq. (3.34) [127] (dashed line), and $e^- + Ar$ [77] (solid line).

with $\Lambda_e = 1.24 \times 10^7 T_e^{3/2} n_e^{-1/2}$ in SI units. The average momentum transfer cross sections $\bar{Q}_{ei}^{(1,1)}$ is shown in figure 3.2. Note that (3.37) depends on the electron number density n_e; substitution by the ideal gas law makes it dependent on the partial gas pressure of electrons. Negative values at low temperature are clipped to zero.

3.2.6. Inelastic collisions

We consider ionization and recombination as representative processes for inelastic collisions. Ionization refers to the process of two sufficiently energetic particles colliding such that the internal electronic structure is disrupted and results in the production of a free electron and ion. Its reverse process is known as recombination. Although both processes may be studied with any particle combinations, we focus on electron induced collisions in an argon plasma. That is, we are interested in ionization and recombination as given by the reversible reaction

$$\mathrm{e}^-(\mathbf{v}_{e,0}) + \mathrm{Ar}(\mathbf{v}_{n,0}) \rightleftarrows \mathrm{e}^-(\mathbf{v}_{e,1}) + \mathrm{e}^-(\mathbf{v}_{e,2}) + \mathrm{Ar}^+(\mathbf{v}_{i,2}), \quad (3.38)$$
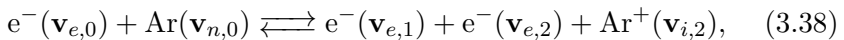
in which we denoted the particle velocities explicitly; the letter indices refer to electron (e), neutral atom (n), and ion (i), and number indices are used to distinguish individual particles. The reaction (3.38) may be viewed as a two-step process: the electron impact on the neutral atom leads to a virtual excited state $\mathrm{Ar}^*(\mathbf{v}_{\mathrm{Ar}^*,1})$ that is immediately followed by spontaneous ionization (see, e.g., [98]), and analogously
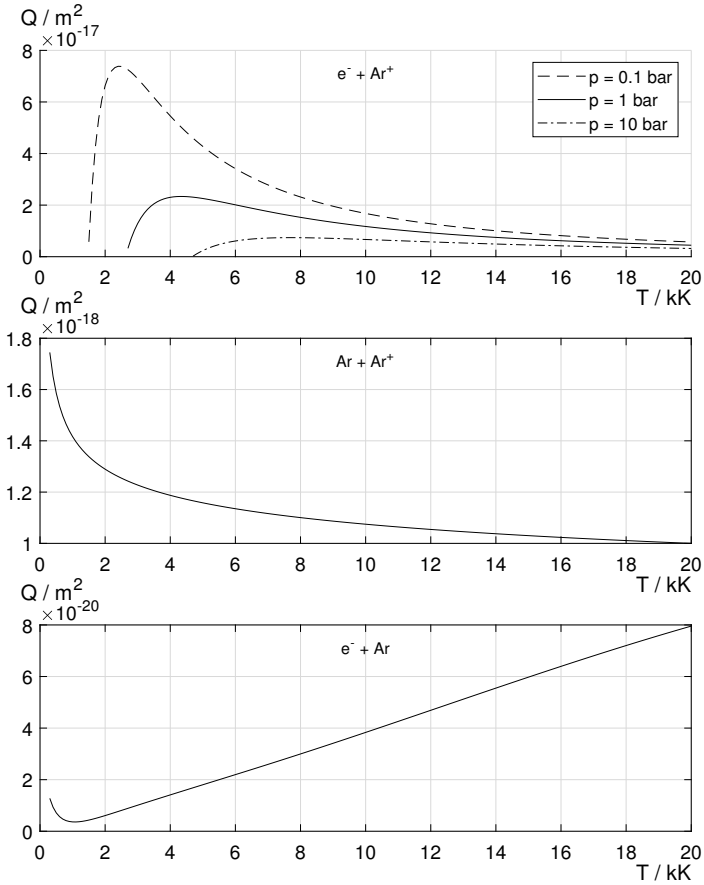
Figure 3.2.: Average momentum transfer cross sections $\bar{Q}^{(1,1)}_{\alpha\beta}$ in argon. Top: elastic Coulomb collisions as given by eq. (3.37). Center and bottom: elastic collisions of argon atoms with ions and electrons, respectively, using eq. (3.23).

for recombination.

These particle collisions are primarily due to microscopic descriptions. We summarize the model of [98] and present its structure in scale free quantities below. Its key feature is to account for the so-called multifluid effect on reaction kinetics due to relative drift velocities. The model assumes that collisions within the same fluid occur sufficiently fast to maintain a Maxwellian velocity distribution function. Similar to elastic collisions, the collision integral (see eq. (3.13)) is given in terms of collision cross sections and integrated over velocity space. This derivation is valid for a general three-body collision process but yields macroscopic model that is computationally too expensive. It is therefore key to restrict to electron-induced ionization and recombination, to employ the large mass ratio, and to assume isotropic scattering, so that one arrives at a computationally accessible collision model.

We introduce some notation for writing the collision model in concise terms. We find the center of mass velocity for ionization and recombination by momentum conservation as

$$\mathbf{U}_0 = \frac{m_e}{M}\mathbf{u}_e + \frac{m_n}{M}\mathbf{u}_n, \tag{3.39a}$$

$$\mathbf{U}_1 = 2\frac{m_e}{M}\mathbf{u}_e + \frac{m_i}{M}\mathbf{u}_i, \tag{3.39b}$$

respectively, where $M = m_e + m_n = 2m_e + m_i$ is the sum of particle

masses in the collision. In scale free terms, they are given as

$$\mathbf{U}_0 = (1 + \varepsilon_e^{-2})^{-1}\mathbf{u}_e + (1 + \varepsilon_e^2)^{-1}\mathbf{u}_n, \tag{3.40a}$$

$$\mathbf{U}_1 = 2(1 + \varepsilon_e^{-2})^{-1}\mathbf{u}_e + \varepsilon_i^2(1 + \varepsilon_e^2)^{-1}\mathbf{u}_i. \tag{3.40b}$$

The relative collision velocities are found as

$$\mathbf{w}_0 = \mathbf{u}_e - \mathbf{u}_n, \tag{3.41a}$$

$$\mathbf{w}_1 = (1 - \varepsilon_e^2)\mathbf{u}_e - \varepsilon_i^2\mathbf{u}_i = \varepsilon_i^2(\mathbf{u}_e - \mathbf{u}_i). \tag{3.41b}$$

The total energies of center of mass are denoted for ionization and recombination as

$$\mathcal{E}^{\mathrm{ion}} = \frac{1}{2}(1 + \varepsilon_e^2)|\mathbf{U}_0|^2 + \frac{3}{2}T_n, \tag{3.42a}$$

$$\mathcal{E}^{\mathrm{rec}} = \frac{1}{2}(1 + \varepsilon_e^2)|\mathbf{U}_1|^2 + \frac{3}{2}T_i, \tag{3.42b}$$

respectively. The scaled thermal electron velocity is defined as (cf. eq. (3.26c))

$$\bar{v}_e = \left(\frac{8T_e}{\pi\varepsilon_e^2}\right)^{1/2}. \tag{3.43}$$

The ionization energy for argon is $\varepsilon^* = 15.76\,\mathrm{eV}$ (see, e.g., [178]) and scaled by the energy scale $k_B\bar{T}$. Additionally, we define the ratio of ionization energy to electron temperature (both in dimensionless units)

$$x^* = \frac{\varepsilon^*}{T_e}. \tag{3.44}$$

We also introduce the thermal de Broglie wavelength of the electron gas (see, e.g., [34, sec. 6.2.2])

$$\lambda_{th} = \left(\frac{h^2}{2\pi m_e k_B T_e} \right)^{1/2}, \tag{3.45a}$$

with $h = 6.626\,070\,15 \times 10^{-34}\,\mathrm{J\,s}$ denoting the Planck constant. In scaled units it reduces to

$$\lambda_{th} = (\varepsilon_e^2 T_e)^{-1/2}. \tag{3.45b}$$

The scaling factor is given as

$$\bar{\lambda}_{th} = \left(\frac{h^2}{2\pi \bar{m} k_B \bar{T}} \right)^{1/2}, \tag{3.45c}$$

and we will use it in the model coefficients related to recombination below. If the thermal de Broglie is much smaller than the interparticle distance ($\lambda_{th} \ll n_e^{-1/3}$), the gas particles will obey Maxwell-Boltzmann statistics. This allows to write the Saha ionization equation (see, e.g., [34, sec. 1.3.1]) in scaled units as

$$\frac{n_e n_i}{n_n} = \frac{2}{\lambda_{th}^3} \frac{g_1}{g_0} \exp(-\varepsilon^*), \tag{3.46}$$

which describes the ionization degree of a plasma in thermal equilibrium. Therein, g_0 and g_1 denote the degeneracy weight of atomic states. For argon, their ratio is given as $g_1/g_0 = 6$ (see, e.g., [21]). These factors will also appear in the definition of model coefficients

related to recombination.

The particular feature of the model [98] is to account for the relative drift velocities in the collisions; therefore we also introduce the ratios of kinetic to thermal energy and denote them as

$$\lambda^{\text{ion}} = \frac{\varepsilon_e^2 |\mathbf{w}_0|^2}{2T_e}, \tag{3.47a}$$

$$\lambda^{\text{rec}} = \frac{\varepsilon_e^2 |\mathbf{w}_1|^2}{2T_e}. \tag{3.47b}$$

Then the model equations is stated with coefficients that can be stored as tables with respect to electron temperature T_e and the energy ratios λ^{ion} or λ^{rec}, respectively, as follows. One may write the rate of change in number densities with the net species production rate

$$\begin{bmatrix} \Gamma_e \\ \Gamma_i \\ \Gamma_n \end{bmatrix} = \begin{bmatrix} \Gamma^{\text{ion}} - \Gamma^{\text{rec}} \\ \Gamma^{\text{ion}} - \Gamma^{\text{rec}} \\ -(\Gamma^{\text{ion}} - \Gamma^{\text{rec}}) \end{bmatrix} = \begin{bmatrix} \Gamma^{\text{net}} \\ \Gamma^{\text{net}} \\ -\Gamma^{\text{net}} \end{bmatrix}. \tag{3.48}$$

The rates of change in momentum are given as

$$\mathbf{R}_e^{\text{coll}} = -\varepsilon_e^2 (\mathcal{R}^{\text{ion}} \mathbf{w}_0 + \mathcal{R}^{\text{rec}} \mathbf{w}_1), \tag{3.49a}$$

$$\mathbf{R}_i^{\text{coll}} = (1 + \varepsilon_e^2)(\Gamma^{\text{ion}} \mathbf{U}_0 - \Gamma^{\text{rec}} \mathbf{U}_1)$$
$$+ \varepsilon_e^2 \left(\frac{T_n - T_e}{T_e} \mathcal{K}^{\text{ion}} \mathbf{w}_0 - \frac{T_i - T_e}{T_e} \mathcal{K}^{\text{rec}} \mathbf{w}_1 + \mathcal{R}^{\text{rec}} \mathbf{w}_1 \right), \tag{3.49b}$$

$$\mathbf{R}_n^{\text{coll}} = -(1 + \varepsilon_e^2)(\Gamma^{\text{ion}}\mathbf{U}_0 - \Gamma^{\text{rec}}\mathbf{U}_1)$$

$$+ \varepsilon_e^2 \left(-\frac{T_n - T_e}{T_e}\mathcal{K}^{\text{ion}}\mathbf{w}_0 + \frac{T_i - T_e}{T_e}\mathcal{K}^{\text{rec}}\mathbf{w}_1 + \mathcal{R}^{\text{ion}}\mathbf{w}_0 \right), \quad (3.49c)$$

and the rates of change in total energy are found to be

$$Q_e^{\text{coll}} = (\Gamma^{\text{rec}} - \Gamma^{\text{ion}})\varepsilon^*$$

$$+ 2(1 + \varepsilon_e^{-2})^{-1} \left((T_n - T_e)\mathcal{J}^{\text{ion}} + (T_i - T_e)\mathcal{J}^{\text{rec}} \right)$$

$$- \varepsilon_e^2 \left(\mathcal{R}^{\text{ion}}\mathbf{w}_0 \cdot \mathbf{U}_0 + \mathcal{R}^{\text{rec}}\mathbf{w}_1 \cdot \mathbf{U}_1 \right), \quad (3.50a)$$

$$Q_i^{\text{coll}} = +\Gamma^{\text{ion}}\mathcal{E}^{\text{ion}} - \Gamma^{\text{rec}}\mathcal{E}^{\text{rec}}$$

$$+ (1 + \varepsilon_e^{-2})^{-1} \left(\frac{(T_n - T_e)^2}{T_e}\mathcal{W}^{\text{ion}} - \frac{(T_i - T_e)^2}{T_e}\mathcal{W}^{\text{rec}} \right.$$

$$\left. - 2(T_i - T_e)\mathcal{J}^{\text{rec}} \right)$$

$$+ \varepsilon_e^2 \left(-\frac{T_n - T_e}{T_e}\mathcal{K}^{\text{ion}}\mathbf{w}_0 \cdot \mathbf{U}_0 - \frac{T_i - T_e}{T_e}\mathcal{K}^{\text{rec}}\mathbf{w}_1 \cdot \mathbf{U}_1 \right.$$

$$\left. + \mathcal{R}^{\text{rec}}\mathbf{w}_1 \cdot \mathbf{U}_1 \right), \quad (3.50b)$$

$$Q_n^{\text{coll}} = -(\Gamma^{\text{ion}}\mathcal{E}^{\text{ion}} - \Gamma^{\text{rec}}\mathcal{E}^{\text{rec}})$$

$$+ (1 + \varepsilon_e^{-2})^{-1}\left(-\frac{(T_n - T_e)^2}{T_e}\mathcal{W}^{\text{ion}} + \frac{(T_i - T_e)^2}{T_e}\mathcal{W}^{\text{rec}} \right.$$

$$\left. - 2(T_n - T_e)\mathcal{J}^{\text{ion}} \right)$$

$$+ \varepsilon_e^2\left(\frac{T_n - T_e}{T_e}\mathcal{K}^{\text{ion}}\mathbf{w}_0 \cdot \mathbf{U}_0 + \frac{T_i - T_e}{T_e}\mathcal{K}^{\text{rec}}\mathbf{w}_1 \cdot \mathbf{U}_1 \right.$$

$$\left. + \mathcal{R}^{\text{ion}}\mathbf{w}_0 \cdot \mathbf{U}_0 \right). \quad (3.50c)$$

The coefficients are then given by

$$\mathcal{R}^{\text{ion}} = R_0^{\text{ion}}, \tag{3.51a}$$

$$\mathcal{K}^{\text{ion}} = \Gamma^{\text{ion}} - R_0^{\text{ion}}, \tag{3.51b}$$

$$\mathcal{W}^{\text{ion}} = J_{00}^{\text{ion}} - 2\lambda^{\text{ion}}R_0^{\text{ion}} + \lambda^{\text{ion}}\Gamma^{\text{ion}}, \tag{3.51c}$$

$$\mathcal{J}^{\text{ion}} = J_{00}^{\text{ion}} - \lambda^{\text{ion}}R_0^{\text{ion}}, \tag{3.51d}$$

$$\mathcal{R}^{\text{rec}} = R_1^{\text{rec}} + R_2^{\text{rec}}, \tag{3.51e}$$

$$\mathcal{K}^{\text{rec}} = 2\Gamma^{\text{rec}} - R_1^{\text{rec}} - R_2^{\text{rec}}, \tag{3.51f}$$

$$\begin{aligned} \mathcal{W}^{\text{rec}} = J_{11}^{\text{rec}} + J_{22}^{\text{rec}} + 2J_{12}^{\text{rec}} \\ + 4\lambda^{\text{rec}}\Gamma^{\text{rec}} - 4\lambda^{\text{rec}}R_1^{\text{rec}} - 4\lambda^{\text{rec}}R_2^{\text{rec}}, \end{aligned} \tag{3.51g}$$

$$\mathcal{J}^{\text{rec}} = J_{11}^{\text{rec}} + J_{22}^{\text{rec}} + 2J_{12}^{\text{rec}} - 2\lambda^{\text{rec}}R_1^{\text{rec}} - 2\lambda^{\text{rec}}R_2^{\text{rec}}. \tag{3.51h}$$

With definitions for auxiliary functions

$$\zeta^{(0)}(\xi) = \frac{1}{2\xi}\sinh(2\xi), \tag{3.52a}$$

$$\zeta^{(1)}(\xi) = \frac{3}{4\xi^2}\left(\cosh(2\xi) - \frac{1}{2\xi}\sinh(2\xi)\right), \tag{3.52b}$$

and auxiliary variables

$$x_1 = x_0 - \upsilon, \tag{3.52c}$$

$$x_2 = \upsilon - x^*, \tag{3.52d}$$

the transfer integrals may be written as

$$\Gamma^{\mathrm{ion}} = n_e n_n \bar{\upsilon}_e \exp(-\lambda^{\mathrm{ion}}) \\ \int_{x^*}^{\infty} x_0 \exp(-x_0)\zeta^{(0)}(\sqrt{\lambda^{\mathrm{ion}}x_0})\bar{\sigma}^{\mathrm{ion}}\,\mathrm{d}x_0, \tag{3.53a}$$

$$R_0^{\mathrm{ion}} = \frac{2}{3}n_e n_n \bar{\upsilon}_e \exp(-\lambda^{\mathrm{ion}}) \\ \int_{x^*}^{\infty} x_0^2 \exp(-x_0)\zeta^{(1)}(\sqrt{\lambda^{\mathrm{ion}}x_0})\bar{\sigma}^{\mathrm{ion}}\,\mathrm{d}x_0, \tag{3.53b}$$

$$J_{00}^{\mathrm{ion}} = n_e n_n \bar{\upsilon}_e \exp(-\lambda^{\mathrm{ion}}) \\ \int_{x^*}^{\infty} x_0^2 \exp(-x_0)\zeta^{(0)}(\sqrt{\lambda^{\mathrm{ion}}x_0})\bar{\sigma}^{\mathrm{ion}}\,\mathrm{d}x_0, \tag{3.53c}$$

$$\Gamma^{\text{rec}} = \bar{n}(\bar{\lambda}^{th})^3 \frac{g_0}{2g_1}(\varepsilon_e^2 T_e)^{-3/2} n_i n_e^2 \bar{v}_e \exp(-2\lambda^{\text{rec}}) \exp(x^*)$$

$$\int_{x^*}^{\infty} x_0 \exp(-x_0) \qquad (3.53\text{d})$$

$$\int_{x^*}^{x_0} \zeta^{(0)}(\sqrt{\lambda^{\text{rec}} x_1}) \zeta^{(0)}(\sqrt{\lambda^{\text{rec}} x_2}) \frac{\mathrm{d}\sigma^{\text{ion}}}{\mathrm{d}v} \, \mathrm{d}v \, \mathrm{d}x_0,$$

$$R_1^{\text{rec}} = \bar{n}(\bar{\lambda}^{th})^3 \frac{2}{3} \frac{g_0}{2g_1}(\varepsilon_e^2 T_e)^{-3/2} n_i n_e^2 \bar{v}_e \exp(-2\lambda^{\text{rec}}) \exp(x^*)$$

$$\int_{x^*}^{\infty} x_0 \exp(-x_0) \qquad (3.53\text{e})$$

$$\int_{x^*}^{x_0} x_1 \zeta^{(1)}(\sqrt{\lambda^{\text{rec}} x_1}) \zeta^{(0)}(\sqrt{\lambda^{\text{rec}} x_2}) \frac{\mathrm{d}\sigma^{\text{ion}}}{\mathrm{d}v} \, \mathrm{d}v \, \mathrm{d}x_0,$$

$$R_2^{\text{rec}} = \bar{n}(\bar{\lambda}^{th})^3 \frac{2}{3} \frac{g_0}{2g_1}(\varepsilon_e^2 T_e)^{-3/2} n_i n_e^2 \bar{v}_e \exp(-2\lambda^{\text{rec}}) \exp(x^*)$$

$$\int_{x^*}^{\infty} x_0 \exp(-x_0) \qquad (3.53\text{f})$$

$$\int_{x^*}^{x_0} x_2 \zeta^{(0)}(\sqrt{\lambda^{\text{rec}} x_1}) \zeta^{(1)}(\sqrt{\lambda^{\text{rec}} x_2}) \frac{\mathrm{d}\sigma^{\text{ion}}}{\mathrm{d}v} \, \mathrm{d}v \, \mathrm{d}x_0,$$

$$J_{11}^{\text{rec}} = \bar{n}(\bar{\lambda}^{th})^3 \frac{g_0}{2g_1}(\varepsilon_e^2 T_e)^{-3/2} n_i n_e^2 \bar{v}_e \exp(-2\lambda^{\text{rec}}) \exp(x^*)$$

$$\int_{x^*}^{\infty} x_0 \exp(-x_0) \qquad (3.53\text{g})$$

$$\int_{x^*}^{x_0} x_1 \zeta^{(0)}(\sqrt{\lambda^{\text{rec}} x_1}) \zeta^{(0)}(\sqrt{\lambda^{\text{rec}} x_2}) \frac{\mathrm{d}\sigma^{\text{ion}}}{\mathrm{d}v} \, \mathrm{d}v \, \mathrm{d}x_0,$$

$$J_{22}^{\text{rec}} = \bar{n}(\bar{\lambda}^{th})^3 \frac{g_0}{2g_1}(\varepsilon_e^2 T_e)^{-3/2}n_i n_e^2 \bar{v}_e \exp(-2\lambda^{\text{rec}})\exp(x^*)$$

$$\int_{x^*}^{\infty} x_0 \exp(-x_0)$$

$$\int_{x^*}^{x_0} x_2 \zeta^{(0)}(\sqrt{\lambda^{\text{rec}}x_1})\zeta^{(0)}(\sqrt{\lambda^{\text{rec}}x_2})\frac{d\sigma^{\text{ion}}}{dv}\,dv\,dx_0,$$

(3.53h)

$$J_{12}^{\text{rec}} = \frac{4}{9}\bar{n}(\bar{\lambda}^{th})^3 \frac{g_0}{2g_1}(\varepsilon_e^2 T_e)^{-3/2}n_i n_e^2 \bar{v}_e \exp(-2\lambda^{\text{rec}})\exp(x^*)$$

$$\int_{x^*}^{\infty} x_0 \exp(-x_0)$$

$$\int_{x^*}^{x_0} \lambda^{\text{rec}}x_1 x_2 \zeta^{(1)}(\sqrt{\lambda^{\text{rec}}x_1})\zeta^{(1)}(\sqrt{\lambda^{\text{rec}}x_2})\frac{d\sigma^{\text{ion}}}{dv}\,dv\,dx_0.$$

(3.53i)

The transfer integrals can be pre-computed and stored as tables with respect to T_e and λ^{ion} (or λ^{rec}, respectively). The fundamental data entering the transfer integrals is given by the ionization cross section $\bar{\sigma}^{\text{ion}}$ and its derivative with respect to the relative impact energy, $\frac{d\sigma^{\text{ion}}}{dv}$; both are functions of the collision energy $\varepsilon = x_0 T_e$. The data for ionization cross section of argon is taken from [138] and plotted in figure 3.3. As noted in the review [178], this data source is most commonly used in discharge modeling.

Figure 3.4 shows the reaction rates for ionization and recombination, defined through $\Gamma^{\text{ion}} = n_e n_n k_{\text{ion}}$ and $\Gamma^{\text{rec}} = n_e^2 n_i k_{\text{rec}}$, in the limit $\lambda^{\text{ion}}, \lambda^{\text{rec}} \to 0$. In this limit, the ratio $k_{\text{ion}}/k_{\text{rec}}$ is consistent with the Saha ionization equation. For validation, we also plot the

direct ionization rate k_{dir} as given by the approximate expression [21, eq. 58]

$$k_{\mathrm{dir}} = c_i \left(\frac{8 k_B T_e}{\pi m_e} \right)^{1/2} (\varepsilon^* + 2 k_B T_e) \exp \left(\frac{-\varepsilon^*}{k_B T_e} \right),$$

$$c_i = 18 \times 10^{-22} \, \mathrm{m^2 \, eV^{-1}}. \quad (3.54)$$

We see that the ionization reaction rates k_{ion} and k_{dir} agree rather well, and the model coincides with that of [21]. The data also compares well to [8] who provides interpolation parameters for reaction rates in the form of Arrhenius laws.

A similar model for inelastic collisions of excitation and deexcitation has been proposed in [97], but these processes are not considered in this work.
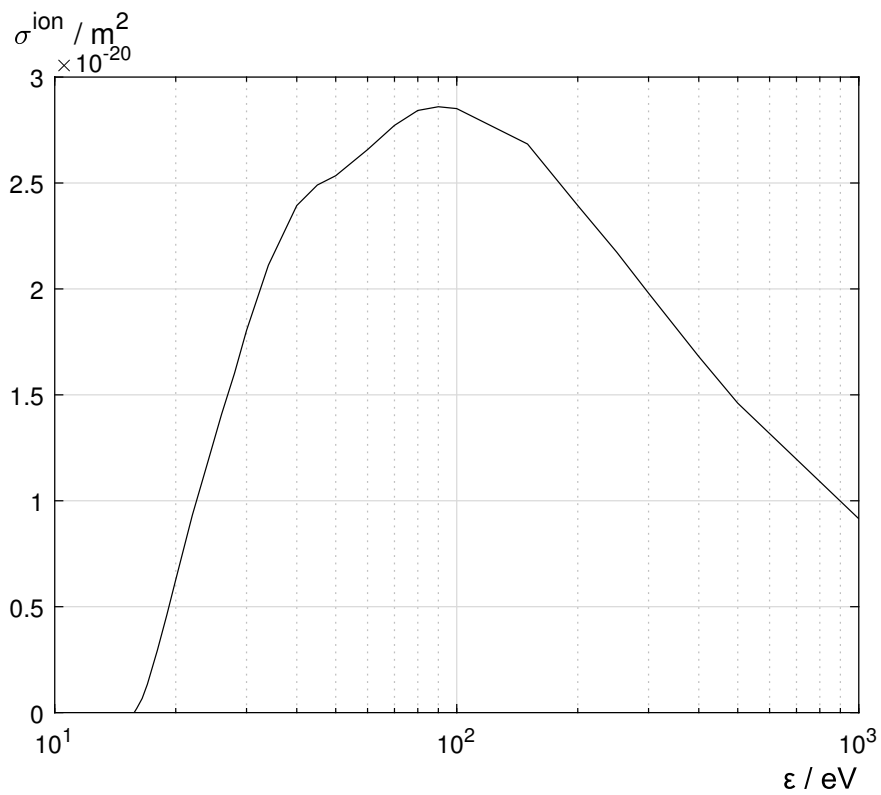
Figure 3.3.: Argon ionization cross section [138].
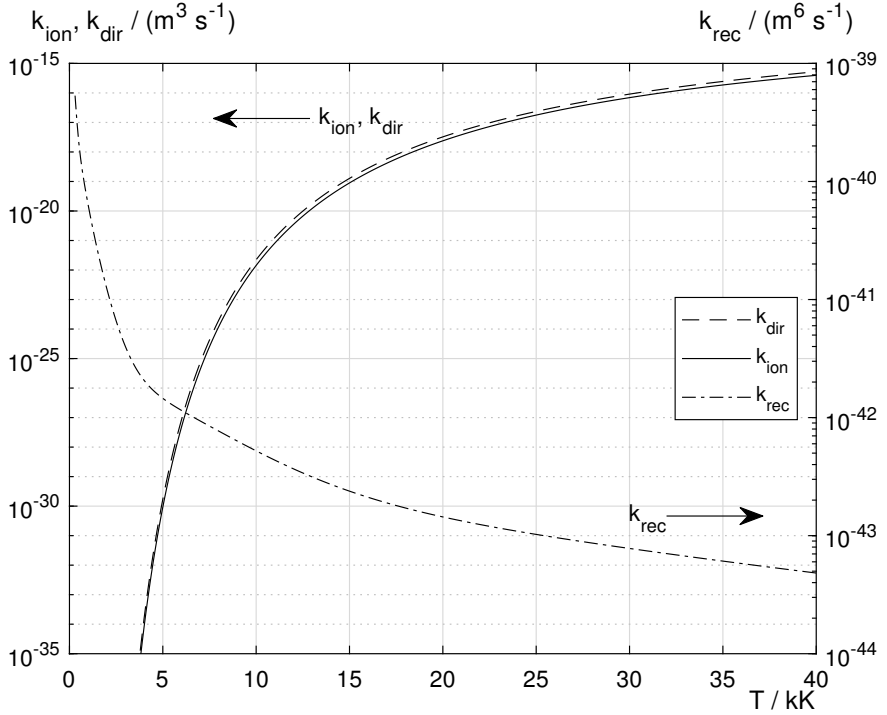
Figure 3.4.: Reaction rates for ionization k_{ion} and recombination k_{rec} in the limit $\lambda^{\text{ion}}, \lambda^{\text{rec}} \to 0$, respectively, and reaction rate for direct ionization k_{dir}, see eq. (3.54) [21, eq. (58)], as a reference.

3.3. Asymptotic preserving multi-species plasma model

3.3.1. Motivation and definition

Asymptotic preserving (AP) numerical schemes were originally introduced by Jin [84]. They are applied, for instance, to kinetic or hyperbolic equations including small scales that lead to prohibitively large computational costs when treated with classical numerical schemes. [85]

We exemplify the concept of asymptotic preserving schemes in the context of electric arcs. The bulk plasma in the arc column may adequately be considered in local thermal equilibrium (LTE) and quasineutral, and described with macroscopic length scales; however, the plasma in the fringes and arc roots (i.e., the regions of the arc column adjacent to the electrodes) are characterized by processes on microscopic length scales comparable to the mean free path of the gas particles. (see, e.g., [85, 45]) Therefore, the underlying problem involves a scaling parameter[3] λ that allows for a continuous transition between the two limiting cases of a microscopic ($\lambda \approx 1$) and a macroscopic ($\lambda \rightarrow 0$) model description.[4] In this work, the scaling parameter is found in Maxwell's equations (3.12), and given as the ratio of Debye length λ_D and the spatial scale $\bar{x}$: for $\lambda = 1$ we recover

---

[3]The scaling parameter is often also denoted by ε in the literature. See, e.g., [84].

[4]We remain in the continuum limit and use the terms *microscopic* and *macroscopic* to distinguish between the two model limiting cases; they should not be viewed as micro-/macroscopic in context of Maxwell's equations (see, e.g., [83, p. 13]).

the full Maxwell system describing electromagnetic waves, while letting $\lambda \to 0$ tends to the quasineutral or eddy current approximation model (see also [45]).

Let us turn to the definition of asymptotic preserving numerical schemes, as illustrated by the commutative diagram in figure 3.5. We denote the microscopic problem as P^λ with solutions that converge to those of the macroscopic problem P^0 as $\lambda \to 0$. We then consider a stable numerical scheme $P^\lambda_{\delta,h}$ for the microscopic problem P^λ with spatial discretization h and time step size δ. If the scheme is applied to the macroscopic problem P^0 without further precautions, the discretization (δ, h) must become small to resolve the fastest and smallest scales and induces exorbitant computational costs. It is therefore desirable that the numerical scheme works equally well in underresolved discretized domains *and* converges to the macroscopic solution independently of the scaling parameter λ and the discretization lengths (δ, h). This ensures that the same set of equations are solved in the resolved and underresolved cases.

Therefore, a numerical scheme is called asymptotic preserving if it is stable independently of the value of λ (asymptotically stable) and if the scheme $P^0_{\delta,h}$ obtained by letting $\lambda \to 0$ in $P^\lambda_{\delta,h}$ with fixed (δ, h) is consistent with P^0 (asymptotically consistent). [84, 85, 45]

The design of AP schemes requires special care for both time and spatial discretization, with time discretization often being more crucial. [85] Typically, it involves some kind of implicit formulation but the equations may still be arranged such that they can be solved explicitly. [85, 84] This is precisely the path we will follow in this

$$P^\lambda_{\delta,h} \xrightarrow{\ (\delta,h)\to 0\ } P^\lambda$$

$$\lambda\to 0 \Big\downarrow \qquad\qquad\qquad \Big\downarrow \lambda\to 0$$

$$P^0_{\delta,h} \xrightarrow{\ (\delta,h)\to 0\ } P^0$$

Figure 3.5.: Asymptotic numerical schemes commute in the limit processes of small parameter ($\lambda \to 0$) and discretizaton lengths ($(\delta, h) \to 0$). [85, 45].

work.

3.3.2. Asymptotic preserving Euler-Maxwell system

Degond et al. [45] have derived and analyzed an AP scheme for the Euler-Maxwell system; in contrast to this work, they considered a collisionless plasma in one dimension. The key concept is to consider the second-order differential equation in $\mathbf{E}$ (i.e., wave equation for $\mathbf{E}$-field)

$$\lambda^2\partial_t^2(\varepsilon\mathbf{E}) + \nabla \times \mu^{-1}\nabla \times \mathbf{E} = -\partial_t(\mathbf{J}), \qquad (3.55)$$

as obtained by substituting Faraday's law (3.1a) into Ampere's law (3.1b). Then, one notes that the electric current $\mathbf{J}$ is identical to the sum of mass fluxes (see eq. (3.4)), and its temporal derivative is

substituted by the Euler momentum equation:

$$-\partial_t(\mathbf{J}) = -\sum_* q_* \partial_t(n_* \mathbf{u}_*)$$

$$= \nabla \cdot \left(\sum_* q_*(n_* \mathbf{u}_* \otimes \mathbf{u}_* + \varepsilon_*^{-2} p_* \mathbb{1}) \right) \qquad (3.56)$$

$$- \sum_* q_*^2 \varepsilon_*^{-2}(n_* \mathbf{E} - n_* \mathbf{u}_* \times \mathbf{B}) - q_* \mathbf{R}_*^{\text{coll}}.$$

Consequently, one finds the microscopic Euler-Maxwell system (denoted as P^λ above) [cf. 45, eq. (5.29)],

$$\lambda^2 \partial_t^2(\varepsilon \mathbf{E}) + \nabla \times \mu^{-1} \nabla \times \mathbf{E} + \left(\sum_* q_*^2 \varepsilon_*^{-2} n_* \right) \mathbf{E}$$

$$= \nabla \cdot \left(\sum_* q_* \left(n_* \mathbf{u}_* \otimes \mathbf{u}_* + \varepsilon_*^{-2} p_* \mathbb{1} \right) \right)$$

$$- \sum_* q_*^2 \varepsilon_*^{-2}(n_* \mathbf{u}_* \times \mathbf{B}) + q_* \mathbf{R}_*^{\text{coll}}. \quad (3.57a)$$

The quasineutral Euler-Maxwell system (denoted as P^0 above) is then

found by the limit case $\lambda \to 0$,

$$\nabla \times \mu^{-1}\nabla \times \mathbf{E} + \left(\sum_* q_*^2 \varepsilon_*^{-2} n_* \right) \mathbf{E}$$

$$= \nabla \cdot \left(\sum_* q_*(n_*\mathbf{u}_* \otimes \mathbf{u}_* + \varepsilon_*^{-2} p_* \mathbb{1}) \right)$$

$$- \sum_* q_*^2 \varepsilon_*^{-2}(n_*\mathbf{u}_* \times \mathbf{B}) + q_*\mathbf{R}_*^{\mathrm{coll}}. \quad (3.57\mathrm{b})$$

For presenting the AP Euler-Maxwell system completely, we repeat Faraday's equation (3.1a) and Euler equations (3.18a) in scaled units:

$$\partial_t(\mathbf{B}) + \nabla \times \mathbf{E} = \mathbf{0}, \qquad (3.57\mathrm{c})$$

$$\partial_t \begin{bmatrix} n_* \\ n_*\mathbf{u}_* \\ n_*e_{tot,*} \end{bmatrix} + \nabla \cdot \begin{bmatrix} n_*\mathbf{u}_* \\ n_*\mathbf{u}_* \otimes \mathbf{u}_* + \varepsilon_*^{-2} p_* \mathbb{1} \\ n_*h_{tot,*}\mathbf{u}_* \end{bmatrix} = \begin{bmatrix} \Gamma_* \\ \mathbf{R}_* \\ Q_* \end{bmatrix}. \qquad (3.57\mathrm{d})$$

As remarked in [45], equations (3.57a) and (3.57b) for the consistent Euler-Maxwell model are not the usual Poisson equation for the electric field $\mathbf{E}$. The AP Euler-Maxwell equations (3.57) are solved implicitly for $\mathbf{E}$ while all other equations are updated explicitly. Moreover, the equation changes its nature from hyperbolic (3.57a) to elliptic (3.57b) [45] as $\lambda \to 0$, which is a signature of singularly perturbed problems (see, e.g., [167]). In fact, Faraday's and Ampere's law become a differential algebraic equation (DAE) of index 1, and special attention must be taken in the design of numerical schemes

because DAE are numerically stiff (see, e.g., [76, section VI.1]). We mention in passing that appropriate single-step schemes to DAE are known as stiffly accurate methods [134].

We note that setting $\lambda = 0$ is a good testcase (see section 4.5.3) for checking if the model is truly asymptotic preserving. This testcase made us realize that the designed 3D model is not AP; see section 4.5.3.

3.4. Discretization

This section discusses the numerical scheme in detail. We start with the geometrical setting and construct its discretization into two interlocked grids. We then present the discretized Maxwell's equations in integral formulation (Maxwell Grid Equations), and the methods for interpolating the electromagnetic fields in order to compute the Lorentz force. We also give another argument for implicit time discretization required for the AP scheme. The Euler equations are discretized with implicit mass flux which provides the consistent coupling with Maxwell's equations. Finally, we state the boundary conditions used in the two subsystems.

3.4.1. Computational domain and grid generation

We consider a cylindrical computational domain (see figure 3.6) consisting of two electrodes, a plasma domain, and an enclosing solid dielectric domain. The geometric setup is symmetric in angular and
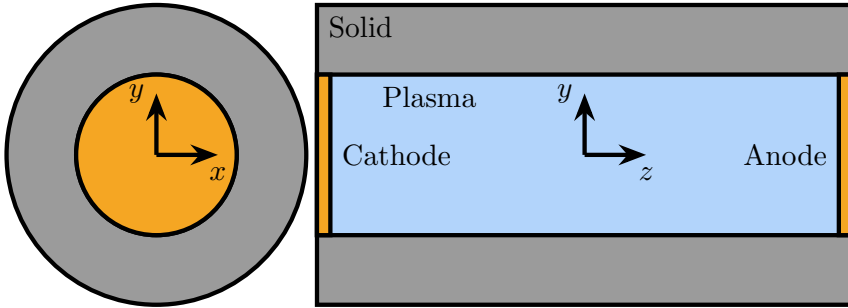
Figure 3.6.: Sketch of computational domain. The electrodes are included for reference and to define the voltage boundary conditions; the volume bodies are not modeled.

axial direction. The plasma radius and outer radius of the solid may be chosen freely. The electrodes are shown for reference but their volume bodies are not resolved in the model. One electrode is electrically grounded while the other is set to an electric potential $\varphi(t)$. We assume that the solids are thermal insulators, which implies that heat transfer is negligible across the plasma-solid interface. The lateral surface of the solid is an artificial cut-off boundary and considered as a perfect magnetic conductor. This geometric setup justifies to solve Maxwell's equations in the full domain whereas the Euler equations apply only to the plasma domain.

The spatial discretization of the computational domain and the grid generation process are described next. Although the numerical method being developed in the following sections is applicable to arbitrary grids, we focus for simplicity on a triangular mesh in cross

section that is axially extruded; i.e., a three dimensional grid given by the Cartesian product of a 2D triangular mesh in a circular domain, and a uniformly spaced discretization along the z-axis.

As we will see below, the discretization is given by two meshes that are dual and orthogonal to each other: edges of one mesh become face normals of the other, and cell centers become vertices; and vice versa. In fact, the dual mesh is found as the Voronoi decomposition of the primal mesh. We could have used a general purpose mesh generator (e.g., DISTMESH [125]); but one major issue was to control and ensure sufficiently high quality in both meshes. We therefore propose a recursive mesh refinement strategy that still allows for arbitrary fine resolutions without deteriorating mesh quality, as described next.

Let us focus on the primal mesh in circular cross section (see also figures 3.7 and 3.8). The initial mesh (level 0) is made of six equilateral triangles (see dashed lines in figure 3.7). The triangles are refined by inserting vertices at edge midpoints, splitting each triangle into four smaller ones (level 1).

We could have continued this strategy for further refinements if the underlying geometry was given by the initial hexagon. The circular shape is resolved by projecting the new boundary vertices to the cylinder radius, but this leads us to another problem: the triangles adjacent to initial boundary vertices (indicated by bullets in figure 3.7) become more right-angled at increasing refinement levels, and mesh quality gets worse – in particular for the dual mesh.

Therefore, the refinement strategy for level 2 mesh is slightly adapted as shown in figure 3.8. Triangles without boundary edges are split
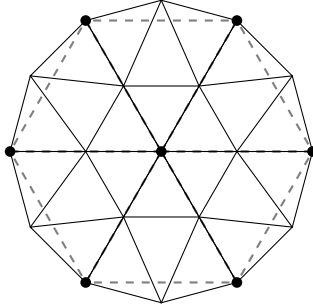
Figure 3.7.: Initial mesh (dashed lines) and first mesh refinement (solid lines). Bullets indicate vertices of the initial mesh.
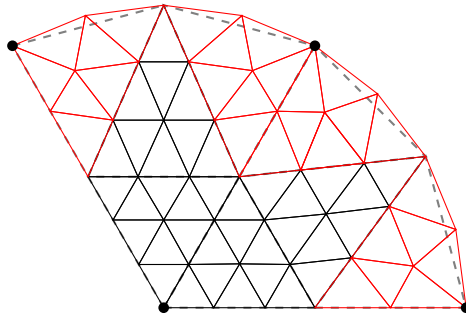
Figure 3.8.: Partial view of level 2 mesh refinement, with distinguished refinement of boundary triangles in red. Dashed lines indicate the mesh at level 1. Bullets indicate vertices of the initial mesh.
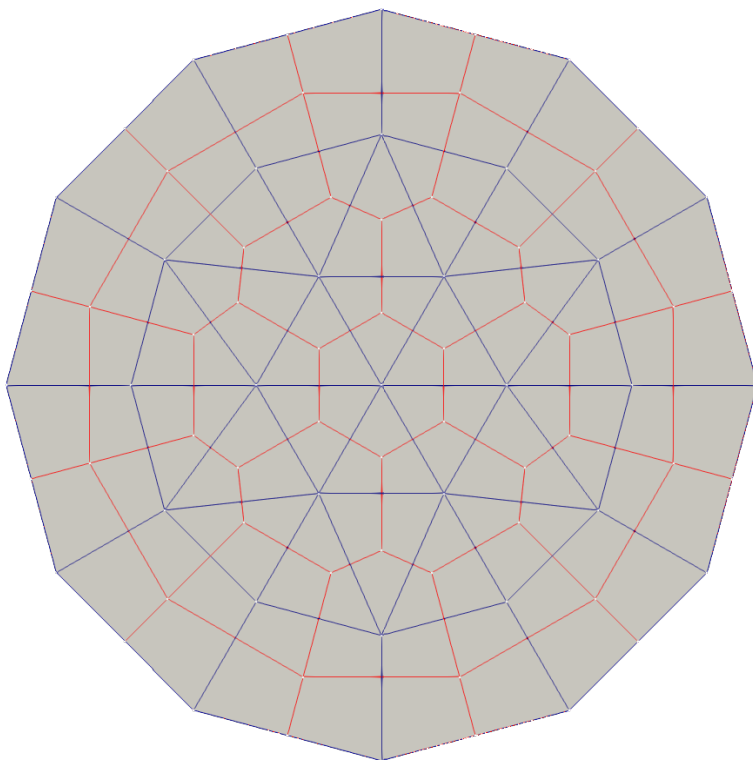
Figure 3.9.: Primal (blue) and dual (red) mesh at refinement level 1 with 1 prism layer.
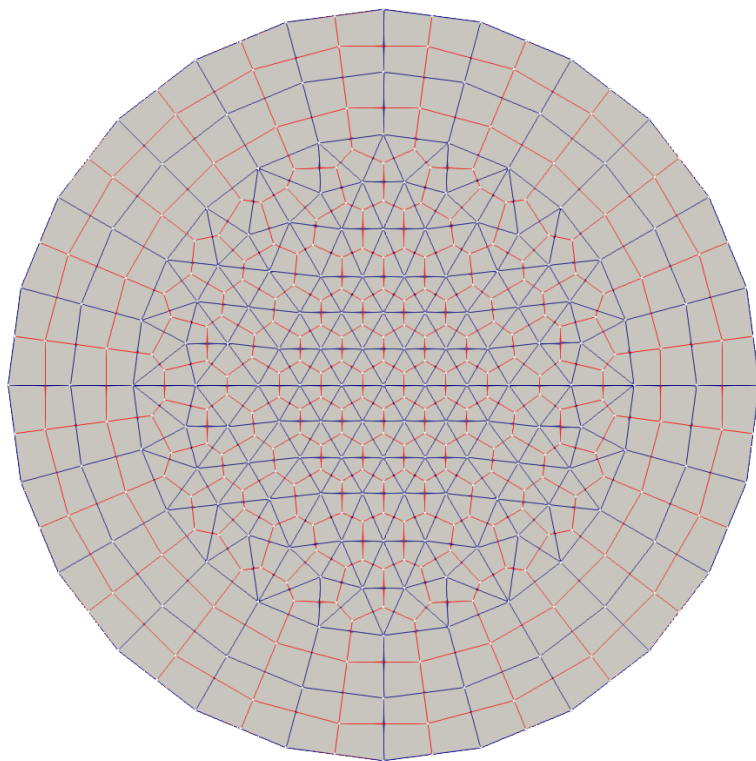
Figure 3.10.: Primal (blue) and dual (red) mesh at refinement level 2 with 2 prism layers.
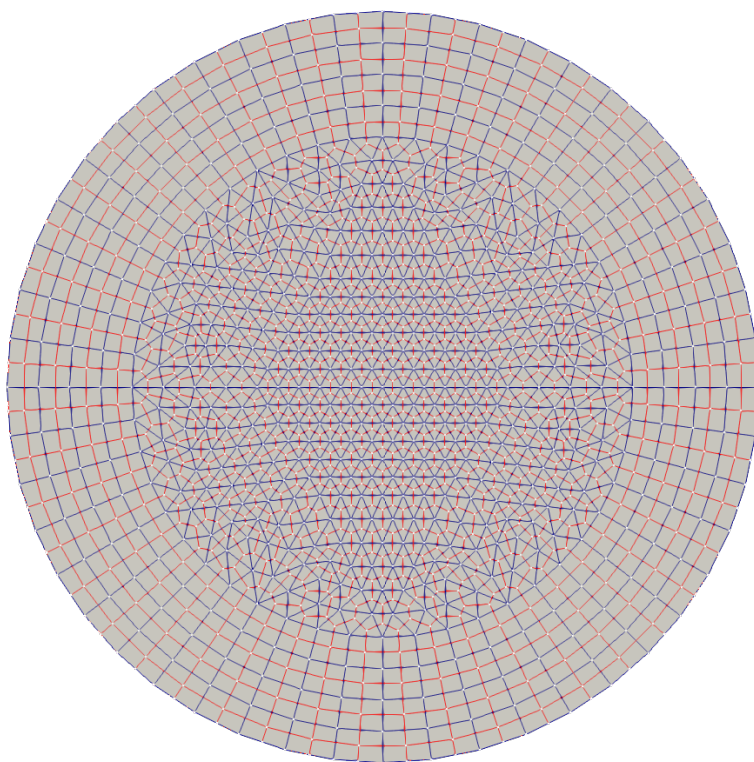
Figure 3.11.: Primal (blue) and dual (red) mesh at refinement level 3 with 4 prism layers.
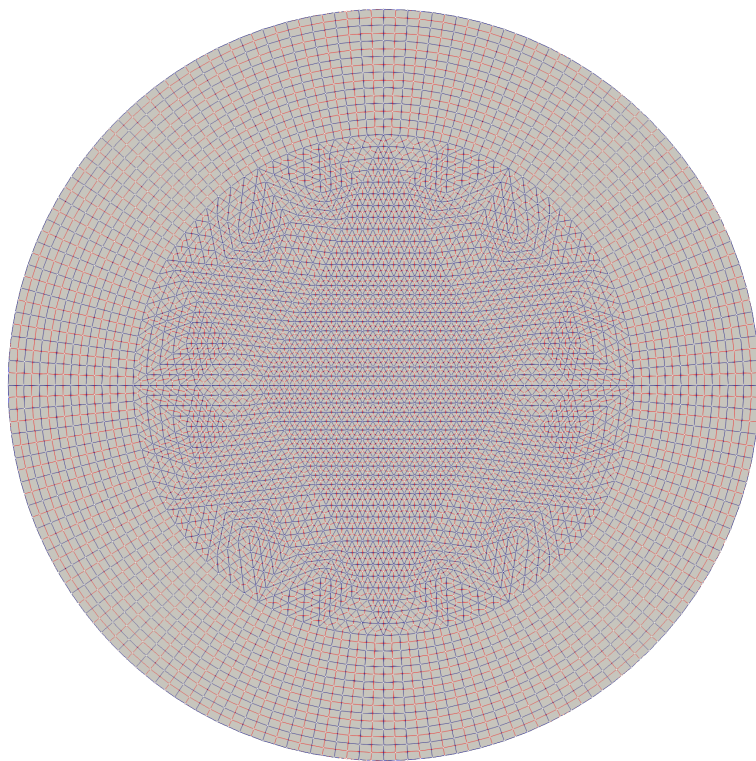
Figure 3.12.: Primal (blue) and dual (red) mesh at refinement level 4 with 8 prism layers.

into nine smaller triangles (black lines) by splitting edges into thirds. Boundary triangles are split into seven triangles (red lines) distinguished by the feature that two newly generated triangles meet at the initial boundary vertex (indicated by bullets) splitting the problematic angle. New boundary vertices are projected to the cylinder radius as explained above. In total, this modified strategy for level 2 refinement ensures that the triangles are sufficiently acute-angled which resolves the issue of degenerated dual cells. Further mesh refinements (levels 3 and higher) continue using the strategy of level 1. The mesh refinements are also seen in figures 3.9 to 3.12.

This primal mesh is used for the plasma domain. The solid domain is constructed by adding quadrilaterals in radial direction, which are often also termed as prism layers. This way, the plasma-solid interface is resolved in its circular shape. The last step in creating the primal mesh is to extrude this circular mesh along the cylinder axis in z-direction.

We may think of the primal mesh being a Delaunay decomposition of the computational domain. The primal cell centers are given by the circumcenters of the triangular faces. The dual mesh is then given by its Voronoi decomposition, that is, dual vertices are identified with primal cell centers, and dual edges are defined by the primal face normals. The dual mesh is closed by adding auxiliary edges and faces at the lateral surface of the solid domain. We remark that the plasma domains, as discretized by the primal and dual mesh are slightly different: the dual domain radius is larger by a half cell height than the primal domain. This difference becomes smaller for

finer spatial resolutions and is therefore neglected.

Figures 3.9 to 3.12 show the primal and dual mesh and their refinements in cross section. The plasma domain is given in the inner part, and resolved by the triangular primal cells, and the corresponding dual cells are hexahedrons. The outer solid domain is resolved with quadrilateral (in 3D: frustum) prism layers. The number of prism layers increases with finer meshes.

In summary, we created a pair of dual, orthogonal, regular and interlocked meshes of sufficient quality. The associated dual entities refer to the same point in space. The resulting grid topology is particularly useful for discretization of Maxwell's equations as outlined in the next section.

3.4.2. Maxwell Grid Equations

This section introduces the concept of Maxwell Grid Equations (MGE) and the Finite Integration Technique (FIT) by Weiland [174] from an applied perspective. The MGE build on the integral formulation of Maxwell's equations, which is an alternative and equivalent perspective to their formulation as partial differential equations (see, e.g., [165]). We remember that the electromagnetic fields may be discontinuous, in particular, at interfaces of different materials. However, the fluxes remain continuous, and this is a peculiar advantage of MGE and FIT. On the other hand, a rigorous convergence theory is still missing.

The method is also referred to as Cell Method (CM) [162, 6],

and can be traced back to Yee's scheme (Finite Difference in Time Domain, FDTD) [179] who realized that the electromagnetic fields should be evaluated on a staggered grid. A more abstract, mathematical framework is provided by Discrete Exterior Calculus (DEC) (see also [31, 80, 81, 73]) that provides a unified view [31] on FIT and the Finite Element Method (FEM) with Whitney forms [95] and edge elements [32]. See also [33] for a comprehensive presentation of the theory.

Let us consider a computational domain $\Omega \subset \mathbb{R}^3$ covered by a primal grid $\mathcal{G}$. For example, we may think of a tetrahedral grid, or, for simplicity, a Cartesian grid. For the sake of exposition, let us consider a polygonal face A_i with edges L_j and vertices P_l, see figure 3.13. The polygon is oriented by its unit normal vector $\mathbf{n}_i$. An edge is identified by its two connected vertices $L_j = (P_{j_0}, P_{j_1})$, and its orientation is defined by the edge vector $\mathbf{L}_j = \mathbf{x}_{j_1} - \mathbf{x}_{j_0}$ with $\mathbf{x}_l$ denoting the spatial position of vertex P_l. Then, Faraday's law (see eq. (3.12a)) integrated over face A_i may be written as

$$\partial_t \left(\underbrace{\int_{A_i} \mathbf{B} \cdot \mathrm{d}\mathbf{A}}_{=:b_i} \right) + \sum_{j=1}^{N_e} c_{ij} \underbrace{\int_{L_j} \mathbf{E} \cdot \mathrm{d}\mathbf{L}}_{=:e_j} = 0, \qquad (3.58)$$

using Stokes' theorem. The oriented incidence coefficients $c_{ij} \in \{-1, 0, 1\}$ are defined by the right hand rule of the edge vectors $\mathbf{L}_j$ with respect to the surface normal vector $\mathbf{n}_i$ (see also section 3.4.3). The integrated quantities b_i and e_j are known as magnetic flux and
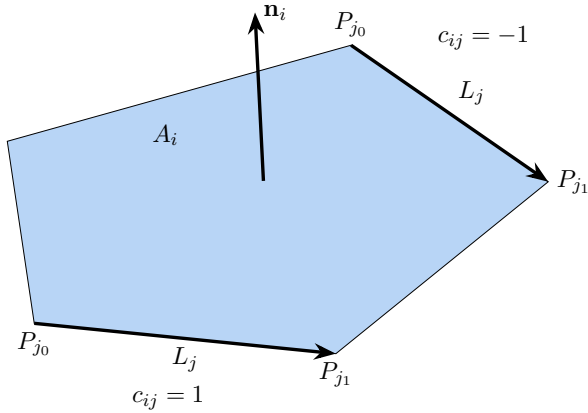
Figure 3.13.: Oriented polygon with edges, vertices, and incidence coefficients.

electric voltage, respectively. This concept is extended to a broader context as follows.

Let us consider a primal grid $\mathcal{G}$ composed of elementary volumes or cells V_k $(k = 1, \ldots, N_c)$, polygonal faces A_i $(i = 1, \ldots, N_f)$, straight lines L_j $(N_j = 1, \ldots, N_e)$, and vertices P_l $(l = 1, \ldots, N_v)$. We write the magnetic fluxes and electric voltages collectively as data vectors,

$$\mathbf{b} := (b_i)_{i=1}^{N_f}, \quad b_i := \int_{A_i} \mathbf{B} \cdot \mathrm{d}\mathbf{A}, \tag{3.59a}$$

$$\mathbf{e} := (e_j)_{j=1}^{N_e}, \quad e_j := \int_{L_j} \mathbf{E} \cdot \mathrm{d}\mathbf{L}. \tag{3.59b}$$

As outlined above, Faraday's law in integral form is then stated as

$$\partial_t(\mathbf{b}) + C\mathbf{e} = \mathbf{0}, \tag{3.60}$$

with $C = (c_{ij}) \in \{-1, 0, 1\}^{N_f \times N_e}$ being the edge-to-face incidence matrix. Matrix C is also known as the discrete curl operator. Similarly, the magnetic Gauss equation in integral form is obtained by integration over volumes and using the divergence theorem; one finds

$$S\mathbf{b} = \mathbf{0}, \tag{3.61}$$

with $S = (s_{ki}) \in \{-1, 0, 1\}^{N_c \times N_f}$ being the face-to-cell incidence matrix that is also referred to as discrete divergence operator.

The electrical potential φ is associated with vertices P_l. The data vector $\boldsymbol{\varphi}$ denotes the value of the electric potential at each primal grid vertex, i.e.,

$$\boldsymbol{\varphi} := (\varphi_l)_{l=1}^{N_v}, \quad \varphi_l := \varphi(\mathbf{x}_l), \tag{3.62}$$

and we find

$$\mathbf{e} = -G\boldsymbol{\varphi} \tag{3.63}$$

as the discrete analogue of $\mathbf{E} = -\nabla\varphi$, where

$$G = (g_{ij}) \in \{-1, 0, 1\}^{N_e \times N_v} \tag{3.64}$$

is the vertex-to-edge incidence matrix or discrete gradient operator, defined by the incidence of vertices P_j to edge L_i.

Ampere's law (3.12b) and the electric Gauss law (3.12d) show the

same structure: data vectors for magnetic voltages $\mathbf{h}$, electric flux $\mathbf{d}$, and electric currents $\mathbf{j}$ are defined in analogy to above. Additionally, we also define a data vector $\mathbf{q}$ for the space charge in cell volumes. These quantities are defined on the dual grid $\tilde{\mathcal{G}}$. That is, the data vectors are given by

$$\mathbf{h} := (h_j)_{j=1}^{N_{\tilde{e}}}, \quad h_j := \int_{\tilde{L}_j} \mathbf{H} \cdot \mathrm{d}\mathbf{L}, \tag{3.65a}$$

$$\mathbf{d} := (d_i)_{i=1}^{N_{\tilde{f}}}, \quad d_i := \int_{\tilde{A}_i} \mathbf{D} \cdot \mathrm{d}\mathbf{A}, \tag{3.65b}$$

$$\mathbf{j} := (j_i)_{i=1}^{N_{\tilde{f}}}, \quad j_i := \int_{\tilde{A}_i} \mathbf{J} \cdot \mathrm{d}\mathbf{A}, \tag{3.65c}$$

$$\mathbf{q} = (q_k)_{k=1}^{N_{\tilde{c}}}, \quad q_k := \int_{\tilde{V}_k} \rho_{el} \, \mathrm{d}V, \tag{3.65d}$$

and the two equations are stated as

$$\lambda^2 \partial_t(\mathbf{d}) - \tilde{C}\mathbf{h} = -\mathbf{j}, \tag{3.66a}$$

$$\lambda^2 \tilde{S}\mathbf{d} = \mathbf{q}, \tag{3.66b}$$

with $\tilde{C}$ and $\tilde{S}$ being the discrete curl operator and discrete divergence operator, respectively, on the dual grid. The discrete operators preserve identities from vector calculus because of the grid duality. In particular, we use the property (see also, e.g., [165, p. 64 f.])

$$\tilde{C} = C^T. \tag{3.67}$$

3.4.3. Material laws and grid entity indexing

After introducing the pair of dual grids (section 3.4.1) and the Maxwell Grid Equations (MGE, section 3.4.2) we now turn to the discrete formulations of the material laws (see eq. (3.12e) and (3.12f)). We assume for simplicity that the grids are orthogonal; non-orthogonal grids are discussed in [24], for instance. In context of discrete exterior calculus (DEC), the material laws are represented by the Hodge star operator.

Let us start by the Tonti diagram (see figure 3.14). It shows Maxwell's equations, the material laws, and the electromagnetic fields. The fields associated with the primal mesh are shown on the left, and those with the dual mesh on the right. The fields are arranged vertically by the dimension of the topological entity in increasing and decreasing order for the primal and dual mesh, respectively. The material laws relate edge values of one mesh with face values of the other mesh. A more complete diagram of the "Maxwell house" [33, sec. 12.3] and discussion may be found, e.g., in [162].

In finite formulation, we find from the flux definitions that the material laws may be stated (for uniform material properties) as

$$\mathbf{h} = M_\nu \mathbf{b}, \quad (M_\nu)_{ij} = \mu^{-1} \frac{|\tilde{L}_i|}{|A_j|}, \tag{3.68a}$$

$$\mathbf{d} = M_\varepsilon \mathbf{e}, \quad (M_\varepsilon)_{ij} = \varepsilon \frac{|\tilde{A}_i|}{|L_j|}, \tag{3.68b}$$

for dual pairs of edges and faces; spatially varying material properties

are discussed, e.g., in [31].

Let us add a few remarks on the indexing of mesh entities. Although indexing is arbitrary in general, a particular ordering may become useful when implementing the scheme in a computer program. Firstly, the sparse matrices M_ν and M_ε are diagonal if corresponding edges and faces have the same positional index in their data vectors. Secondly, it is particularly advantageous for our geometrical setup (see also sections 3.4.1 and 3.4.7) if primal vertices, edges, and faces are grouped according to their geometrical position in the domain interior Ω° or its boundary $\partial\Omega$. For such an arrangement, the data vectors of electric potentials, electric voltages, and magnetic face fluxes may be written as

$$\boldsymbol{\varphi} = \begin{bmatrix} \boldsymbol{\varphi}^\circ \\ \boldsymbol{\varphi}^\partial \end{bmatrix}, \qquad \mathbf{e} = \begin{bmatrix} \mathbf{e}^\circ \\ \mathbf{e}^\partial \end{bmatrix}, \qquad \mathbf{b} = \begin{bmatrix} \mathbf{b}^\circ \\ \mathbf{b}^\partial \end{bmatrix}, \qquad (3.69)$$

where the superscripts relate to their position in the domain.

We already touched the orientation of grid entities in the definitions of the incidence matrices (see section 3.4.2). We remark that each entity comes with an inner and outer orientation, and inner orientations of one grid induce outer orientations of the other. Orientations of edges and faces correspond to the familiar right hand rule, which is extended to vertices and volumes in a natural way; see, e.g., [6] for details. Figure 3.15 illustrates the situation for a primal edge L_i and coinciding dual face $\tilde{A}_i$. Inner orientation of L_i (edge direction) induces an outer orientation on the dual face $\tilde{A}_i$ (positive direction

primal vertices $\quad\quad\quad \varphi \quad\quad\quad\quad\quad\quad\quad\quad \rho_{el} \quad\quad$ dual volumes

$$\mathbf{E} = -\nabla\varphi \;\Big| \quad\quad\quad\quad\quad\quad\quad \Big|\; \nabla \cdot \mathbf{D} = \rho_{el}$$

$$\mathbf{D} = \varepsilon\mathbf{E}$$

primal edges $\quad\quad \mathbf{E} \;\underline{}\; \mathbf{D}, \mathbf{J} \quad$ dual faces

$$\mathbf{J} = \sigma\mathbf{E}$$

$$\partial_t\mathbf{B} + \nabla \times \mathbf{E} = 0 \;\Big| \quad\quad\quad\quad \Big|\; \partial_t\mathbf{D} - \nabla \times \mathbf{H} = -\mathbf{J}$$

$$\mathbf{H} = \mu^{-1}\mathbf{B}$$

primal faces $\quad\quad \mathbf{B} \;\underline{}\; \mathbf{H} \quad\quad$ dual edges
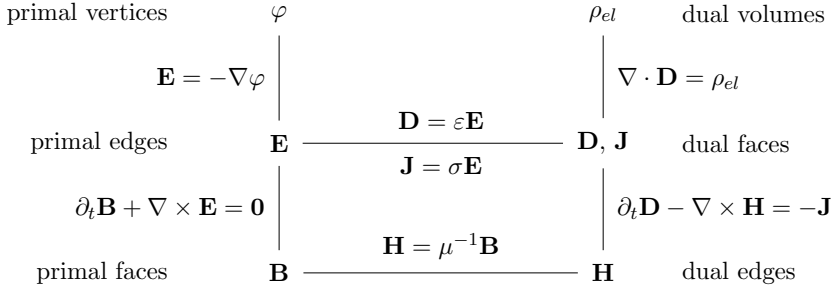
Figure 3.14.: Tonti diagram showing the differential structure of electromagnetism. See also [33, fig. 12.2], [6, figs. 1.6 and 5.5].

by the surface normal vector), and outer orientation of L_i (the right hand rule around the edge vector) induces an inner orientation on $\tilde{A}_i$ (positive orientation for its boundary edges). We also mention that primal edge midpoints are identified with dual face centers, and primal vertices are associated with dual cell centers. This provides the reason why we require acute-angled triangles in the definition of the primal grid (see section 3.4.1).

3.4.4. Interpolation of electromagnetic fields

The Euler and Maxwell's equations are coupled through Lorentz force. As we have just seen, the discretized electric field $\mathbf{E}$ and magnetic flux density $\mathbf{B}$ are defined on edge centers and face centers of the primal grid. In contrast, the plasma is defined on dual cell volumes; as we will see in section 3.4.6, the finite volume method (FVM)
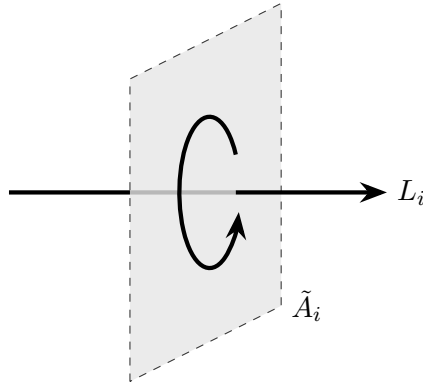
Figure 3.15.: Primal edge L_i and dual face $\tilde{A}_i$ with coherent orientations.

is applied and the cell-averaged values are taken to be representative values at the dual cell center.

Since Lorentz force is modeled as a volumetric source term (see section 3.2.3), the electromagnetic fields must be interpolated to dual cell centers (or primal vertices, equivalently) in first order accuracy. The interpolation should also yield a consistent method for Ohm's law. Interpolation of the **B**-field is rather classical, whereas interpolation of the **E**-field is more involved. The methods are discussed separately.

Magnetic flux density

The magnetic flux density **B** is interpolated on the primal grid with Raviart-Thomas elements of zeroth order [140]. These elements are

divergence-conforming, and they represent basis functions in the So-
bolev space

$$H(\mathrm{div}, \Omega) := \{v \in L^2(\Omega, \mathbb{R}^3) : \mathrm{div}\, v \in L^2(\Omega)\}, \tag{3.70}$$

where L^2 denotes the space of square Lebesque integrable functions.
For a reference triangular prism $\hat{V}$, the basis functions are given as

$$\left\{ \begin{bmatrix} \hat{x} \\ \hat{y} \\ 0 \end{bmatrix}, \begin{bmatrix} \hat{x} - 1 \\ \hat{y} \\ 0 \end{bmatrix}, \begin{bmatrix} \hat{x} \\ \hat{y} - 1 \\ 0 \end{bmatrix}, \begin{bmatrix} 0 \\ 0 \\ \hat{z} - 1 \end{bmatrix}, \begin{bmatrix} 0 \\ 0 \\ \hat{z} \end{bmatrix} \right\}, \tag{3.71}$$

associated with the prism faces. The reference prism is mapped to
an actual prism $V_k \in \mathcal{G}$ by the affine map

$$F_k : \mathbb{R}^3 \to \mathbb{R}^3, \quad \hat{\mathbf{x}} \mapsto \mathbf{x} := B_k \hat{\mathbf{x}} + b_k, \tag{3.72}$$

and the reference basis functions $\hat{f}$ of the reference prism are mapped
to V_k by the Piola transformation (see, e.g., [26, ch. 2])

$$p_k : L^2(\hat{V}) \to L^2(V_k), \quad \hat{f}(\hat{\mathbf{x}}) \mapsto f(\mathbf{x}) := \frac{1}{|\det B_k|} B_k \hat{f}(\hat{\mathbf{x}}). \tag{3.73}$$

We remark that the **B**-field is required only in the plasma domain,
and that domain coincides with the triangular prisms almost exactly
(see also section 3.4.1). It is only the primal vertices on the plasma-
solid interface that also belong to non-triangular prism cells in the
primal mesh. We neglect those contributions from the quadrilateral

cells for simplicity. This introduces a local error in the outermost dual cells of the plasma domain, which could be removed by extending the Raviart-Thomas interpolation to hexahedrons (see, e.g., [26, section 2.4]).

Electric field

Interpolation of the electric field from primal edges to dual cell centers is more involved. The problem is termed more generally as reconstruction of vector fields on unstructured, staggered grids, and it has been a recent research topic in global atmospheric modeling and ocean modeling in particular (see, e.g., [123, 172], and references therein). The problem at hand is visualized in figure 3.16: given the face centered normal components of a vector field, find an approximation of the vector field at cell center (or, more generally, at any arbitrary point inside the cell).

Perot [124] proposed a particularly general method for polyhedrons with arbitrary number of faces. The method is at least first-order accurate, and second-order for aligned polygons [123], i.e., if two opposite faces are pairwise parallel opposite. An extension with second-order corrections has been pushed forward in [170]. Other reconstruction methods are based, e.g., on Raviart-Thomas elements (designed for linear, non-divergent vector fields), Whitney elements (designed for linear, curl-conforming vector fields), least squares method [168], or radial basis functions; see [172] and [123] for a comparison. It was found that Perot's method is particularly fast and simple with com-
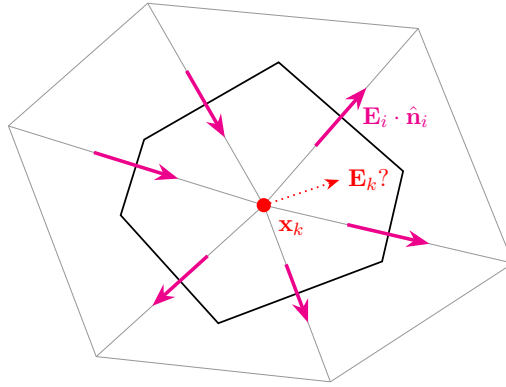
Figure 3.16.: The problem of reconstructing a vector field $\mathbf{E}$ at cell center $\mathbf{x}_k$ from values given only at face centers $\mathbf{E}_i$. Thin lines show triangular faces of the primal mesh. The thick lines indicate dual cell faces.

parable rms-errors, but relatively large errors in the maximum norm. Hybrid schemes combining Perot's and the least squares method were proposed in [123] and [170].

We choose Perot's method for reconstruction of the electric field because of its simplicity and speed. Let us consider a dual cell $\tilde{V}_k$ and denote the cell center (which coincides with its primal vertex) by $\mathbf{x}_k$, and the set of cell faces by $\mathcal{F}_k$. Then, the reconstruction $\mathbf{E}_k = \mathbf{E}(\mathbf{x}_k)$ is given by

$$\mathbf{E}_k = \frac{1}{|\tilde{V}_k|} \sum_{i \in \mathcal{F}_k} \mathbf{r}_i (\mathbf{E}_i \cdot \hat{\mathbf{n}}_i) |\tilde{A}_i|, \qquad (3.74)$$

with $\mathbf{r}_i$ denoting the local position vector from $\mathbf{x}_k$ to the center of face $\tilde{A}_i$, $\hat{\mathbf{n}}_i$ is the outward unit normal vector, and $\mathbf{E}_i$ is the vector

field at the center of face $\tilde{A}_i$.

We adapt the notation in (3.74) for our purposes in writing the equation in context of MGE (see section 3.4.2). Because of mesh construction and its orthogonality we have $\mathbf{r}_i = \frac{1}{2}\tilde{s}_{ki}|L_i|\mathbf{n}_i$, where $\mathbf{n}_i$ is the oriented dual face normal, $|\mathbf{L}_i|$ is the length of the corresponding primal edge L_i, and $\tilde{s}_{ki}$ is the face-to-cell incidence on the dual grid. We also remember that the electric voltage at edge L_i is given as $e_i = (\mathbf{E}_i \cdot \mathbf{n}_i)s_{ki}|L_i|$ (see eq. (3.59b)), and the outward unit normal vector may be substituted by $\hat{\mathbf{n}}_i = \mathbf{n}_i s_{ki}$. In total, we find

$$\mathbf{E}_k = \frac{1}{2}\frac{1}{|\tilde{V}_k|}\sum_{i\in\mathcal{F}_k}\mathbf{n}_i|\tilde{A}_i|e_i. \qquad (3.75)$$

We outline contemporaneous research results on the interpolation process as shown in [128]. Interpolation may be understood as the composition of projection and a corresponding reconstruction. It is found in [128] that the optimal point (with respect to least squares error) for reconstruction is given by the barycentric dual cell center. In fact, interpolation at this position would be exact and P_0-consistent. This result should be considered in further work. In comparison, the method given in eq. (3.75) is a compromise of implementation time and accuracy.

3.4.5. Time discretization of Maxwell Grid Equations

Degond et al. [45] proved with linear stability theory that Maxwell's equations must be solved implicitly for the scheme being asymptotic

preserving and consistent in the quasineutral limit. We provide another argument that is based on differential algebraic equations (see also section 3.3.2).

We mentioned that Faraday's and Ampere's law become a differential algebraic equation of index 1 as $\lambda \to 0$, and it is the class of stiffly accurate methods that work equally well irrespective of the actual value of the perturbation parameter λ. For Runge-Kutta methods, this class is characterized by a Butcher tableau with two properties: firstly, the last row of the coefficient matrix has identical values as in the weights vector, and secondly, the coefficient matrix is invertible. These properties ensure that the numerical scheme remains valid in the quasineutral limit, and this procedure is known as ε-embedding[5] in numerical analysis. We also note that stiffly-accurate methods are L-stable, i.e., their stability function satisfies $\lim_{z \to \infty} R(z) = 0$ (see, e.g., [76, Proposition 3.8]). Higher order methods being stiffly accurate are known as Gauss-Radau methods.

We remember that the forward and backward Euler method may be considered as special cases of the θ-method, i.e.,

$$u^{m+1} = u^m + \delta_m \left((1-\theta)F^m + \theta F^{m+1} \right), \qquad (3.76)$$

with m being the time step iteration index, $\delta_m = t^{m+1} - t^m$ timestep size, so that $\theta = 0$ is the forward Euler method, $\theta = 1$ the backward Euler method, and $\theta = 1/2$ the Crank-Nicolson method. Its stability

---

[5]Note that the perturbation parameter, here denoted by λ, is usually denoted by ε.

function

$$R(z) = \frac{1 + z(1 - \theta)}{1 - z\theta}, \quad z \in \mathbb{C},$$ (3.77)

vanishes for $z \to \infty$ if and only if $\theta = 1$, and we conclude that the backward Euler method is the only stiffly-accurate. This argument can be extended to higher order methods in time discretization.

Therefore, the evolution equations written in MGE and discretized with the implicit Euler method are given by

$$\delta_m^{-1}(\mathbf{b}^{m+1} - \mathbf{b}^m) + C\mathbf{e}^{m+1} = \mathbf{0},$$ (3.78a)

$$\lambda^2 \delta_m^{-1} M_\varepsilon(\mathbf{e}^{m+1} - \mathbf{e}^m) - \tilde{C} M_\nu \mathbf{b}^{m+1} = -\mathbf{j}^{m+1}.$$ (3.78b)

We remark that the timestep size δ_m is defined by the fluid model (see next section). Substituting Faraday's law into Ampere's law, and using Ampere's law at the previous time step with δ_{m-1} yields the evolution equation

$$(\lambda^2 M_\varepsilon + \delta_m^2 C^T M_\nu C)\mathbf{e}^{m+1}$$
$$= \lambda^2 M_\varepsilon \left(\left(1 + \frac{\delta_m}{\delta_{m-1}}\right) \mathbf{e}^m - \frac{\delta_m}{\delta_{m-1}} \mathbf{e}^{m-1} \right)$$
$$- \delta_m(\mathbf{j}^{m+1} - \mathbf{j}^m), \quad (3.79)$$

which is consistent with eq. (3.55).

3.4.6. Euler equations

As the discretization of Euler equations is rather involved, we give a short summary and an outline of this section before presenting the details.

We remember that the peculiar feature of the AP scheme is to treat the Euler mass flux implicitly (see section 3.3.2). For keeping the discrete Euler-Maxwell system consistent with the continuous model (see eq. (3.57a)) at any value of the AP parameter λ, the electric field in the Lorentz force must also be implicit. The momentum sources due to collisions (see sections 3.2.5 and 3.2.6) are explicit in the coupling to Maxwell's equations; however, we treat that term implicit in the Euler equations because of its stiff nature. This is the one and only inconsistency in the present model, but it allows to keep the electromagnetic and fluid parts separately. If the collisional sources were also implicit in Maxwell's equations, we would have to solve a large and tightly coupled system of equations.

This section has the following structure. Firstly, we review the finite volume method and the Rusanov scheme for the Euler equations. Secondly, we focus on the implicit mass flux which provides the coupling with Maxwell's equations and leads to an AP scheme. Thirdly, we present the explicit discretization of the collision sources used in Maxwell's equations. Lastly, we show the details for implicit discretization of the collision sources in solving the Euler equations.

Finite volume method

The Euler equations are defined on the dual grid $\tilde{\mathcal{G}}$. They are discretized classically with the finite volume method (FVM, see, e.g., [99]), and fluxes at grid faces are defined by the Rusanov [145] (or local Lax-Wendroff) scheme. The time semi-discrete Euler equations are given in vector format (see eq. (3.18))

$$\delta_m^{-1}(\mathbf{U}_*^{m+1} - \mathbf{U}_*^m) + \nabla \cdot \mathbf{F}_*^m = \mathbf{S}_*^m, \tag{3.80}$$

with $\mathbf{U}_*^m$ denoting the fluid species state vector at timestep m, $\mathbf{F}_*^m$ is the flux vector, and $\mathbf{S}_*^m$ is the vector of source terms. We remark that mass flux and electric field will be treated implicitly; with explicit collision sources, the terms are written in full details as

$$\mathbf{U}_*^m = \begin{bmatrix} n_*^m \\ (n_*\mathbf{u}_*)^m \\ (n_*e_{tot,*})^m \end{bmatrix}, \tag{3.81a}$$

$$\mathbf{F}_*^m = \begin{bmatrix} \mathbf{f}_{n,*}^{m+1} \\ \mathbf{f}_{m,*}^m \\ \mathbf{f}_{e,*}^m \end{bmatrix} = \begin{bmatrix} (n_*\mathbf{u}_*)^{m+1} \\ (n_*\mathbf{u}_* \otimes \mathbf{u}_* + \varepsilon_*^{-2}p_*\mathbb{1})^m \\ (n_*h_{tot,*}\mathbf{u}_*)^m \end{bmatrix}, \tag{3.81b}$$

$$\mathbf{S}_*^m = \begin{bmatrix} (\Gamma_*^{\mathrm{coll}})^m \\ \varepsilon_*^{-2}q_*(n_*^m\mathbf{E}^{m+1} + (n_*\mathbf{u}_*)^m \times \mathbf{B}^m) + (\mathbf{R}_*^{\mathrm{coll}})^m \\ \varepsilon_*^{-2}q_*(n_*\mathbf{u}_*)^m \cdot \mathbf{E}^{m+1} + (Q_*^{\mathrm{coll}})^m \end{bmatrix}. \tag{3.81c}$$

As we will see below, the implicit mass flux can be expanded and written in terms of explicit state variables (see also [45, eq. (4.32)]). Also $\mathbf{E}^{m+1}$ is computable before the fluid states are updated. This justifies to write the flux vector $\mathbf{F}_*$ with superscript m. The discrete equations for cell state $\mathbf{U}^m_{*,k}$ in the dual cell $\tilde{V}_k$ are then found as

$$\mathbf{U}^{m+1}_{*,k} = \mathbf{U}^m_{*,k} - \delta_m \frac{1}{|\tilde{V}_k|} \sum_{i \in \mathcal{F}_k} \mathbf{F}^m_{*,i}|\tilde{A}_i| + \delta_m \mathbf{S}^m_{*,k}, \qquad (3.82)$$

where $\mathbf{F}^m_{*,i} = \mathbf{F}^m_* \cdot \mathbf{n}_i$ denotes the Rusanov flux at face i, and the sum is over the set of cell faces $\mathcal{F}_k$.

The discrete fluxes at face $\tilde{A}_i$ are defined as follows. Let us consider the adjacent cells $\tilde{V}_k$ and $\tilde{V}_{k+1}$ on the left and right side as indicated by the face orientation (see figure 3.17). We also write $\tilde{A}_{k+1/2}$ for that face, and we continue our discussion with one-dimensional quantities projected in direction of the face normal $\mathbf{n}_{k+1/2}$. The Rusanov flux is defined by the adjacent fluid states,

$$\mathbf{F}^m_{*,i} = \mathbf{F}^m_{*,k+1/2} \qquad (3.83a)$$

$$= \mathbf{F}_*(\mathbf{U}^m_{*,k}, \mathbf{U}^m_{*,k+1}) \qquad (3.83b)$$

$$= \frac{1}{2}(\mathbf{U}^m_{*,k} + \mathbf{U}^m_{*,k+1}) - \frac{1}{2}s^m_{*,k+1/2}(\mathbf{F}_*(\mathbf{U}^m_{*,k+1}) - \mathbf{F}_*(\mathbf{U}^m_{*,k})), \qquad (3.83c)$$
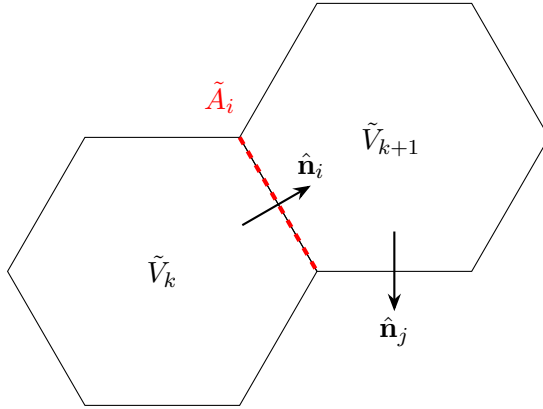
Figure 3.17.: Adjacent dual cells $\tilde{V}_k, \tilde{V}_{k+1}$ with shared face $\tilde{A}_i$ and face normal vectors $\hat{\mathbf{n}}_i, \hat{\mathbf{n}}_j$.

that is, in full details,

$$
f_{n,*,k+1/2}^{m+1} = \frac{1}{2}((nu)_{*,k}^{m+1} + (nu)_{*,k+1}^{m+1})
$$
$$
- \frac{1}{2} s_{*,k+1/2}^{m}(n_{*,k+1}^{m} - n_{*,k}^{m}), \quad \text{(3.84a)}
$$

$$
f_{m,*,k+1/2}^{m} = \frac{1}{2}((nu^2 + \varepsilon^{-2}p)_{*,k}^{m} + (nu^2 + \varepsilon^{-2}p)_{*,k+1}^{m})
$$
$$
- \frac{1}{2} s_{*,k+1/2}^{m}((nu)_{*,k+1}^{m} - (nu)_{*,k}^{m}), \quad \text{(3.84b)}
$$

$$f_{e,*,k+1/2}^m = \frac{1}{2}((nh_{tot}u)_{*,k}^m + (nh_{tot}u)_{*,k+1}^m)$$
$$- \frac{1}{2}s_{*,k+1/2}^m((ne_{tot})_{*,k+1}^m - (ne_{tot})_{*,k}^m), \quad (3.84c)$$

with $s_{*,k+1/2}^m$ denoting the local maximum wave speed for species $*$,

$$s_{*,k+1/2}^m := \max\left(s_{*,k}^m, s_{*,k+1}^m\right), \quad (3.85a)$$
$$s_{*,k}^m := \max\left(|u_{*,k}^m|, |u_{*,k}^m + c_{*,k}^m|, |u_{*,k}^m - c_{*,k}^m|\right), \quad (3.85b)$$

and the acoustic wave speed

$$c_{*,k}^m = \left(\gamma\frac{p_{*,k}^m}{\varepsilon_*^2 n_{*,k}^m}\right)^{1/2}, \quad (3.85c)$$

defined by the ideal gas law. The timestep size δ_m is given by the CFL condition (see, e.g., [99, sec. 4.4]), i.e., the maximum time span allowed such that acoustic waves do not cross cell boundaries in any dual grid cell for any fluid species.

Implicit mass flux

The numerical mass flux (see eq. (3.84a)) is implicit only in the central discretization part of the flux, while the numerical viscosity part is kept explicit; see also [45, eq. (4.32)]. Using the momentum conservation equation allows to substitute the implicit terms by explicit species states. For cell k and species $*$, the discrete momentum conservation equation projected in direction of face $i \in \mathcal{F}_k$ with normal

vector $\mathbf{n}_i$ reads

$$
\begin{aligned}
(nu)_{*,k}^{m+1} = (nu)_{*,k}^m &- \delta_m \frac{1}{|\tilde{V}_k|} \sum_{j \in \mathcal{F}_k} f_{m,*,j}^m |\tilde{A}_j| (\mathbf{n}_j \cdot \mathbf{n}_i) \\
&+ \delta_m \varepsilon_*^{-2} q_* n_{*,k}^m \mathbf{E}_k^{m+1} \cdot \mathbf{n}_i \\
&+ \delta_m \varepsilon_*^{-2} q_* ((n\mathbf{u})_{*,k}^m \times \mathbf{B}_k^m) \cdot \mathbf{n}_i + \delta_m (\mathbf{R}_{*,k}^{\text{coll}})^m \cdot \mathbf{n}_i. \quad (3.86)
\end{aligned}
$$

Therefore, substituting eq. (3.86) into eq. (3.84a) yields

$$
\begin{aligned}
f_{n,*,k+1/2}^{m+1} = \frac{1}{2}&((nu)_{*,k}^m + (nu)_{*,k+1}^m) - \frac{1}{2} s_{*,k+1/2}^m (n_{*,k+1}^m - n_{*,k}^m) \\
&- \frac{1}{2} \delta_m \sum_{k \in adj(i)} \frac{1}{|\tilde{V}_k|} \sum_{j \in \mathcal{F}_k} f_{m,*,j}^m |\tilde{A}_j| (\mathbf{n}_j \cdot \mathbf{n}_i) \\
&+ \frac{1}{2} \delta_m \varepsilon_*^{-2} q_* \sum_{k \in adj(i)} n_{*,k}^m \mathbf{E}_k^{m+1} \cdot \mathbf{n}_i \\
&+ \frac{1}{2} \delta_m \varepsilon_*^{-2} q_* \sum_{k \in adj(i)} ((n\mathbf{u})_{*,k}^m \times \mathbf{B}_k^m) \cdot \mathbf{n}_i \\
&\qquad\qquad + \frac{1}{2} \delta_m \sum_{k \in adj(i)} (\mathbf{R}_{*,k}^{\text{coll}})^m \cdot \mathbf{n}_i, \quad (3.87)
\end{aligned}
$$

where $adj(i)$ denotes the index set of adjacent cells at face i (i.e., $adj(i) = \{k, k+1\}$) introduced for shorter notation. We note that the explicit Rusanov flux is recovered in the first two terms, while the other extra terms are due to the implicit formulation. The fourth term represents the electrostatic Lorentz force with the electric field interpolated to the dual cell center. Substituting Perot's interpolation

method (see eq. (3.75)) yields

$$
\begin{aligned}
f_{n,*,k+1/2}^{m+1} = {} & \frac{1}{2}((nu)_{*,k}^m + (nu)_{*,k+1}^m) - \frac{1}{2}s_{*,k+1/2}^m(n_{*,k+1}^m - n_{*,k}^m) \\
& - \frac{1}{2}\delta_m \sum_{k \in adj(i)} \frac{1}{|\tilde{V}_k|} \sum_{j \in \mathcal{F}_k} f_{m,*,j}^m |\tilde{A}_j|(\mathbf{n}_j \cdot \mathbf{n}_i) \\
& + \frac{1}{4}\delta_m \varepsilon_*^{-2} q_* \sum_{k \in adj(i)} \frac{n_{*,k}^m}{|\tilde{V}_k|} \sum_{j \in \mathcal{F}_k} |\tilde{A}_j|(\mathbf{n}_j \cdot \mathbf{n}_i) e_j^{m+1} \\
& + \frac{1}{2}\delta_m \varepsilon_*^{-2} q_* \sum_{k \in adj(i)} ((n\mathbf{u})_{*,k}^m \times \mathbf{B}_k^m) \cdot \mathbf{n}_i \\
& + \frac{1}{2}\delta_m \sum_{k \in adj(i)} (\mathbf{R}_{*,k}^{\mathrm{coll}})^m \cdot \mathbf{n}_i. \quad (3.88)
\end{aligned}
$$

In comparison to [45, eq. (4.33)], eq. (3.88) is the equivalent expression but generalized to arbitrary grids in 3D, and for a collisional plasma. Degond et al. [45] remark that this expression is too diffusive and reduce the sum in the electrostatic Lorentz force to that of face i. However, we defer this aspect to further work and stay with (3.88).

Maxwell's and Euler equations are linked by a consistent formulation of the electrical current density and mass fluxes (see eq. (3.4)). We therefore substitute $\mathbf{j}^{m+1}$ by eq. (3.65c) and (3.88). This allows to write analogously to Ohm's law

$$
\mathbf{j}^{m+1} = \left(\sum_* q_* f_{n,*,i}^{m+1} |\tilde{A}_i| \right)_{i=1}^{N_{\tilde{f}}} = M_\sigma^m \mathbf{e}^{m+1} + \mathbf{j}_{aux}^m; \quad (3.89)
$$

the "conductivity operator" M_σ^m is proportional to the species number densities $n_{*,k}^m$, and $\mathbf{j}_{aux}^m$ summarizes all other terms not proportional to e_j^{m+1} that contribute to species mass flux. We stress that $\mathbf{j}_{aux}^m$ contains the collisional momentum source term $\mathbf{R}_*^{\text{coll}}$, which is discussed just below in more details. In summary, we may state eq. (3.79) as

$$(\lambda^2 M_\varepsilon + \delta_m^2 C^T M_\nu C + \delta_m M_\sigma^m)\mathbf{e}^{m+1}$$
$$= \lambda^2 M_\varepsilon \left(\left(1 + \frac{\delta_m}{\delta_{m-1}}\right) \mathbf{e}^m - \frac{\delta_m}{\delta_{m-1}} \mathbf{e}^{m-1} \right)$$
$$- \delta_m(\mathbf{j}_{aux}^m - \mathbf{j}^m). \quad (3.90)$$

We realized with numerical experiments that setting $\lambda = 0$ is problematic (see section 4.5.3). We should also define a small but finite conductivity (e.g., $\sigma = 10^{-6}$) in the outer solid domain for a well defined system of equations; the solver for the Maxwell system does not converge for $\lambda = 0$ if one sets $\sigma = 0$ in the dielectric domain.

Explicit collision sources in Maxwell's equations

The collision models (see sections 3.2.5 and 3.2.6) lead to source terms $\mathbf{R}_*^{\text{coll}}$ in the Euler momentum equation, and they enter into equation (3.90) via $\mathbf{j}_{aux}^m$. We discuss their discretization in this section.

The collisions lead to stiff source terms in the Euler equations and impose strong limits on the timestep size δ_m. They should be discretized implicitly as shown in the following section for the Euler equations. However, if the momentum sources $\mathbf{R}_*^{\text{coll}}$ are discretized

implicitly in the Maxwell system (see eq. (3.90)), it would lead to a big and tightly coupled system of equations. We therefore discretize $\mathbf{R}_*^{\mathrm{coll}}$ explicitly in equation (3.90) for simplicity; exploring other discretization strategies is left to future work.

The elastic collisions as well as the inelastic collisions for ionization and recombination may be written proportionally to species number densities (see eq. (3.27a) and (3.53)), i.e.,

$$n_\alpha n_\beta \psi_{\alpha\beta}, \tag{3.91a}$$

$$n_e n_n \psi^{\mathrm{ion}}, \tag{3.91b}$$

$$n_e^2 n_i \psi^{\mathrm{rec}}. \tag{3.91c}$$

The coefficients $\psi_{\alpha\beta}$, ψ^{ion}, and ψ^{rec} (below collectively referred to by ψ) mask the transfer integrals: they may be precomputed and tabulated with respect to electron temperature T_e and the dimensionless parameters λ^{ion} and λ^{rec} (see eq. (3.47)) for inelastic collisions (cf. [98]). From an implementation perspective, it is advantageous to store them as 1D or 2D table in the format $\log(\psi(T_e^{-1}, \lambda))$ and perform vectorized table lookup using (bi-)cubic spline interpolations.

Implicit collision sources in Euler equations

The collision sources (3.91) should be discretized implicitly in the Euler equations to overcome the timestep limits due to their stiff nature. We firstly outline the strategy before giving the implicit discretization details for the inelastic collision model; the implicit

elastic collision source terms are discretized in analogy.

The coefficients ψ are taken explicitly (i.e., at timestep m) because they are given as data tables. The species number densities are given in the format $f(x, y) = xy$ and $f(x, y) = x^2y$, respectively, and their Taylor expansions result in

$$x^{m+1}y^{m+1} \approx x^{m+1}y^m + x^my^{m+1} - x^my^m, \qquad (3.92a)$$

$$(x^{m+1})^2y^{m+1} \approx 2x^{m+1}x^my^m + (x^m)^2y^{m+1} - 2(x^m)^2y^m. \quad (3.92b)$$

These approximations are used for $(\Gamma^{\text{ion}})^{m+1}$ and $(\Gamma^{\text{rec}})^{m+1}$. For the other terms, we will use the approximations

$$x^{m+1}y^{m+1} \approx x^{m+1}y^m \text{ or } x^my^{m+1}, \qquad (3.93a)$$

$$(x^{m+1})^2y^{m+1} \approx (x^m)^2y^{m+1} \text{ or } x^{m+1}x^my^m, \qquad (3.93b)$$

respectively, because they lead to simpler expressions and allow to approximate the Jacobians such that the species state variables are kept in the numerators. We also substitute

$$(nT)_*^{m+1} = (\gamma - 1)\varepsilon_*^2 \left((ne_{tot})_*^{m+1} - \frac{1}{2n_*^m}(n\mathbf{u})_*^m \cdot (n\mathbf{u})_*^{m+1} \right) \quad (3.94)$$

in the following. So we can state the implicit discretization of eq. (3.53) in details and succinctly:

$$(\Gamma^{\text{ion}})^{m+1} = \psi_{\Gamma^{\text{ion}}}^m (n_e^{m+1}n_n^m + n_e^m n_n^{m+1} - n_e^m n_n^m) \qquad (3.95a)$$

$$(\Gamma^{\text{rec}})^{m+1} = \psi_{\Gamma^{\text{rec}}}^m (2n_e^{m+1}n_e^m n_i^m + (n_e^m)^2 n_i^{m+1} - 2(n_e^m)^2 n_i^m) \quad (3.95b)$$

$$(\mathcal{R}^{\text{ion}}\mathbf{w}_0)^{m+1} = \psi^m_{\mathcal{R}^{\text{ion}}}(n_n^m(n\mathbf{u})_e^{m+1} - n_e^m(n\mathbf{u})_n^{m+1}) \tag{3.95c}$$

$$(\mathcal{R}^{\text{rec}}\mathbf{w}_1)^{m+1} = \psi^m_{\mathcal{R}^{\text{rec}}}\varepsilon_i^2(n_e^m n_i^m(n\mathbf{u})_e^{m+1} - (n_e^m)^2(n\mathbf{u})_i^{m+1}) \tag{3.95d}$$

$$(\Gamma^{\text{ion}}\mathbf{U}_0)^{m+1} = \psi^m_{\Gamma^{\text{ion}}}\left(\frac{n_n^m}{1+\varepsilon_e^{-2}}(n\mathbf{u})_e^{m+1} + \frac{n_e^m}{1+\varepsilon_e^2}(n\mathbf{u})_n^{m+1}\right) \tag{3.95e}$$

$$(\Gamma^{\text{rec}}\mathbf{U}_1)^{m+1}$$
$$= \psi^m_{\Gamma^{\text{rec}}}\left(\frac{2n_e^m n_i^m}{1+\varepsilon_e^{-2}}(n\mathbf{u})_e^{m+1} + \frac{\varepsilon_i^2(n_e^m)^2}{1+\varepsilon_e^2}(n\mathbf{u})_i^{m+1}\right) \tag{3.95f}$$

$$\left(\left(\frac{T_n}{T_e}-1\right)\mathcal{K}^{\text{ion}}\mathbf{w}_0\right)^{m+1}$$
$$= \psi^m_{\mathcal{K}^{\text{ion}}}\left(\frac{T_n^m}{T_e^m}-1\right)\left(n_n^m(n\mathbf{u})_e^{m+1} - n_e^m(n\mathbf{u})_n^{m+1}\right) \tag{3.95g}$$

$$\left(\left(\frac{T_i}{T_e}-1\right)\mathcal{K}^{\text{rec}}\mathbf{w}_1\right)^{m+1}$$
$$= \psi^m_{\mathcal{K}^{\text{rec}}}\varepsilon_i^2\left(\frac{T_i^m}{T_e^m}-1\right)\left(n_e^m n_i^m(n\mathbf{u})_e^{m+1} - (n_e^m)^2(n\mathbf{u})_i^{m+1}\right) \tag{3.95h}$$

$$\left((T_n - T_e)\mathcal{J}^{\text{ion}}\right)^{m+1} = \psi^m_{\mathcal{J}^{\text{ion}}}\left(n_e^m(nT)_n^{m+1} - n_n^m(nT)_e^{m+1}\right) \tag{3.95i}$$

$$((T_i - T_e)\mathcal{J}^{\text{rec}})^{m+1}$$
$$= \psi^m_{\mathcal{J}^{\text{rec}}}\left((n_e^m)^2(nT)_i^{m+1} - n_e^m n_i^m(nT)_e^{m+1}\right) \tag{3.95j}$$

$$\left(\mathcal{R}^{\mathrm{ion}}\mathbf{w}_0 \cdot \mathbf{U}_0\right)^{m+1}$$
$$= \psi_{\mathcal{R}^{\mathrm{ion}}}^m \left(n_n^m (n\mathbf{u})_e^{m+1} - n_e^m (n\mathbf{u})_n^{m+1}\right)$$
$$\cdot \left(\frac{1}{1+\varepsilon_e^{-2}}\frac{(n\mathbf{u})_e^m}{n_e^m} + \frac{1}{1+\varepsilon_e^2}\frac{(n\mathbf{u})_n^m}{n_n^m}\right) \quad (3.95\mathrm{k})$$

$$\left(\mathcal{R}^{\mathrm{rec}}\mathbf{w}_1 \cdot \mathbf{U}_1\right)^{m+1}$$
$$= \psi_{\mathcal{R}^{\mathrm{rec}}}^m \varepsilon_i^2 \left(n_e^m n_i^m (n\mathbf{u})_e^{m+1} - (n_e^m)^2 (n\mathbf{u})_i^{m+1}\right)$$
$$\cdot \left(\frac{2}{1+\varepsilon_e^{-2}}\frac{(n\mathbf{u})_e^m}{n_e^m} + \frac{\varepsilon_i^2}{1+\varepsilon_e^2}\frac{(n\mathbf{u})_i^m}{n_i^m}\right) \quad (3.95\mathrm{l})$$

$$\left(\left(\frac{T_n}{T_e}-1\right)\mathcal{K}^{\mathrm{ion}}\mathbf{w}_0 \cdot \mathbf{U}_0\right)^{m+1}$$
$$= \left(\frac{T_n^m}{T_e^m}-1\right)\psi_{\mathcal{K}^{\mathrm{ion}}}^m \left(n_n^m (n\mathbf{u})_e^{m+1} - n_e^m (n\mathbf{u})_n^{m+1}\right)$$
$$\cdot \left(\frac{1}{1+\varepsilon_e^{-2}}\frac{(n\mathbf{u})_e^m}{n_e^m} + \frac{1}{1+\varepsilon_e^2}\frac{(n\mathbf{u})_n^m}{n_n^m}\right) \quad (3.95\mathrm{m})$$

$$\left(\left(\frac{T_i}{T_e}-1\right)\mathcal{K}^{\mathrm{rec}}\mathbf{w}_1 \cdot \mathbf{U}_1\right)^{m+1}$$
$$= \left(\frac{T_i^m}{T_e^m}-1\right)\psi_{\mathcal{K}^{\mathrm{rec}}}^m \varepsilon_i^2 \left(n_e^m n_i^m (n\mathbf{u})_e^{m+1} - (n_e^m)^2 (n\mathbf{u})_i^{m+1}\right)$$
$$\cdot \left(\frac{2}{1+\varepsilon_e^{-2}}\frac{(n\mathbf{u})_e^m}{n_e^m} + \frac{\varepsilon_i^2}{1+\varepsilon_e^2}\frac{(n\mathbf{u})_i^m}{n_i^m}\right) \quad (3.95\mathrm{n})$$

$$\left(\Gamma^{\text{ion}}\mathcal{E}^{\text{ion}}\right)^{m+1}$$

$$= \psi^m_{\Gamma^{\text{ion}}}\left(\frac{3}{2}n^m_e(nT)^{m+1}_n\right.$$

$$+\left(\frac{1+\varepsilon_e^2}{1+\varepsilon_e^{-2}}\frac{n^m_n}{2}(n\mathbf{u})^{m+1}_e + \frac{n^m_e}{2}(n\mathbf{u})^{m+1}_n\right)$$

$$\left.\cdot\left(\frac{(n\mathbf{u})^m_e}{(1+\varepsilon_e^{-2})n^m_e} + \frac{(n\mathbf{u})^m_n}{(1+\varepsilon_e^2)n^m_n}\right)\right) \quad (3.95\text{o})$$

$$\left(\Gamma^{\text{rec}}\mathcal{E}^{\text{rec}}\right)^{m+1} = \psi^m_{\Gamma^{\text{rec}}}\left(\frac{3}{2}(n^m_e)^2(nT)^{m+1}_i\right.$$

$$+\left(\frac{1+\varepsilon_e^2}{1+\varepsilon_e^{-2}}n^m_e n^m_i(n\mathbf{u})^{m+1}_e + \frac{\varepsilon_i^2(n^m_e)^2}{2}(n\mathbf{u})^{m+1}_i\right)$$

$$\left.\cdot\left(\frac{2(n\mathbf{u}_e)^m}{(1+\varepsilon_e^{-2})n^m_e} + \frac{\varepsilon_i^2(n\mathbf{u})^m_i}{(1+\varepsilon_e^2)n^m_i}\right)\right) \quad (3.95\text{p})$$

$$\left(\frac{(T_n-T_e)^2}{T_e}\mathcal{W}^{\text{ion}}\right)^{m+1}$$

$$= \psi^m_{\mathcal{W}^{\text{ion}}}\left(\frac{T^m_n}{T^m_e} - 1\right)\left(n^m_e(nT)^{m+1}_n - n^m_n(nT)^{m+1}_e\right) \quad (3.95\text{q})$$

$$\left(\frac{(T_i-T_e)^2}{T_e}\mathcal{W}^{\text{rec}}\right)^{m+1}$$

$$= \psi^m_{\mathcal{W}^{\text{rec}}}\left(\frac{T^m_i}{T^m_e} - 1\right)\left((n^m_e)^2(nT)^{m+1}_i - n^m_e n^m_i(nT)^{m+1}_e\right) \quad (3.95\text{r})$$

3.4.7. Boundary conditions

The naming of boundary faces are visualized in figure 3.18.

Let us define firstly the boundary conditions for the Maxwell system. The anode boundary Γ_a is electrically grounded and at zero potential. At cathode outer boundary Γ_c, we define the electric potential as a time-varying function $\varphi_c(t)$. The lateral cylinder surface Γ_0 takes zero flux conditions for the electric field and magnetic flux density. The plasma-solid interface Γ_{ps} does not require particular modeling because we consider materials with identical electric permittivity and magnetic permeability.

These electromagnetic boundary conditions are included into the numerical model as follows. The electric voltage at primal edges lying on the domain boundary Γ_0 are given by the gradient of the electric potential field. As a consequence, the degrees of freedom (DoF) of the Maxwell system are given by the electric voltage on primal inner edges $\mathbf{e}^\circ$ and the primal boundary vertices $\boldsymbol{\varphi}^\partial$ (see eq. (3.69)). The array of DoF is denoted as

$$\mathbf{x} := \begin{bmatrix} \mathbf{e}^\circ \\ \boldsymbol{\varphi}^\partial \end{bmatrix}. \tag{3.96}$$

We then define the "inner-identity-boundary-gradient" operator Q [82],

$$Q = \begin{bmatrix} X_{\mathbf{e}^\circ} \ \big| \ -GX_{\varphi^\partial} \end{bmatrix}, \tag{3.97}$$

with $X_{\mathbf{e}^\circ}$ being the embedding operator for inner edges and X_{φ^∂} the
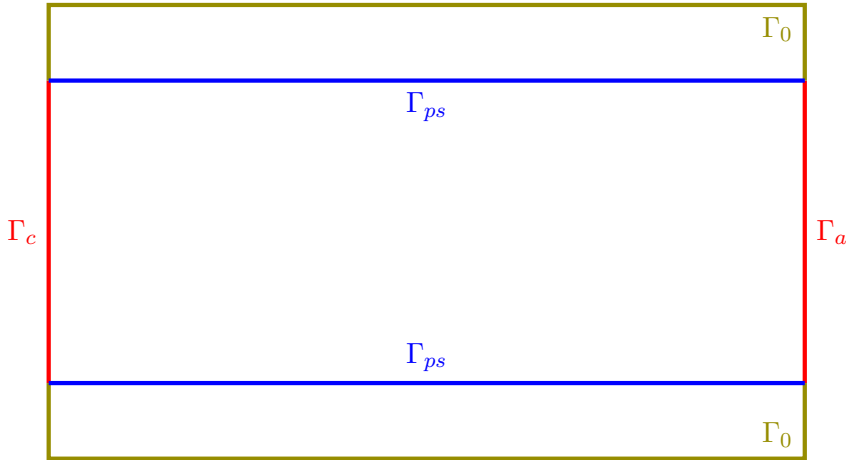
Figure 3.18.: Naming of boundary conditions in the computational model.

embedding for boundary vertices. This allows us to substitute

$$\mathbf{e} = Q\mathbf{x}. \tag{3.98}$$

Moreover, the zero-flux boundary condition implies that the discrete curl operator C should be restricted to primal edges and faces that lie in the domain interior; the discrete inner curl operator is denoted by C°. We also restrict the magnetic material law to inner faces, and denote the operator for inner primal faces as M_ν°. These substitutions are applied to the evolution equation (3.90) and we multiply from left with Q^T to symmetrize. We remark that the symmetrisation corresponds to using – in context of finite element

methods – identical test functions and basis functions. In summary, we find

$$
(\lambda^2 Q^T M_\varepsilon Q + \delta_m^2 Q^T C^{\circ T} M_\nu^\circ C^\circ Q + \delta_m Q^T M_\sigma^m Q)\mathbf{x}^{m+1}
$$
$$
= \left(1 + \frac{\delta_m}{\delta_{m-1}}\right) \lambda^2 Q^T M_\varepsilon Q \mathbf{x}^m
$$
$$
- \frac{\delta_m}{\delta_{m-1}} \lambda^2 Q^T M_\varepsilon Q \mathbf{x}^{m-1}
$$
$$
- \delta_m Q^T (\mathbf{j}_{aux}^m - \mathbf{j}^m), \quad (3.99)
$$

as the final system of equations for the Maxwell system to be solved numerically.

We now specify the boundary conditions for Euler equations that are solved in the plasma domain. The plasma-solid interface Γ_{ps} is a wall for all plasma species ($\mathbf{u}_* \cdot \mathbf{n} = 0$) with wall boundary conditions. The anode and cathode boundaries (Γ_a and Γ_c) are wall boundaries, in principle, and they would require more delicate modeling if detailed plasma physics is considered. This would include arc root effects (anode and cathode sheath potentials, see, e.g., [3, 22, 13]) as well as ablation and material deposition (see, e.g., [108] for a carbon plasma) but is left for future work. However, we restrict us for simplicity to open-wall boundary conditions, i.e., zero Neumann conditions: the gas species can leave and enter with zero-gradients.

3.5. Implementation notes

The numerical code has been written in C++. Eigen (v. 3.3.7) [74] is used for data storage and linear algebra, Alglib (v. 3.16) [25] is used for (bi-)cubic spline interpolation. Output data is written to HDF5 files (v. 1.10.4) [161], described by the XDMF (v. 3) [177] format, and visualized in Paraview (v. 5.6.0) [12]. The source code is compiled with Intel C++ Compiler (v. 2019.5.281) [1].

Equation (3.99) is solved with Eigen's BiCGStab solver for sparse systems of equations.

4. Numerical Experiments

We present numerical experiments as found by the model and method described in chapter 3. The computational domain is a cylinder (see figure 3.6) with axial length 5, plasma radius 1 and outer radius 1.5. We compare the results on three meshes. Their refinements follows the strategy of section 3.6. The refinement (see table 4.1) in axial and radial directions are consistent to keep cell aspect ratios comparable on all meshes.

We firstly perform numerical experiments to validate the submodels before solving the fully coupled Euler-Maxwell model.

Mesh name	radial refinement	axial refinement
coarse	level 2	50
medium	level 3	100
fine	level 4	200

Table 4.1.: Mesh resolutions used in the numerical experiments.

4.1. Sod's shock tube

We begin with test cases on the Euler system. Sod's shock tube [157] is a Riemann problem with zero velocity at initial time, and it is an often used test case for validating compressible flow solvers. Its main aspect lies in correct prediction of shock waves and jumps across them. The problem setup is one-dimensional and oriented with the cylinder axis in our case. The experimental setup (see also, e.g., [99, ch. 14]) is thought to consist of a diaphragm at $z = 0$ separating the domain into a high pressure (left) and low pressure (right) section.

At $t = 0$, the diaphragm is ruptured. This leads to a series of three pressure waves. The leading shock wave propagates into the low pressure region, followed by the contact discontinuity identified by a jump in number density but pressure and velocity being unaffected. A rarefaction wave moves into the high pressure region. These waves lead to five regions with fluid states that may be described exactly by the initial states, the wave speeds, and the Rankine-Hugoniot jump conditions (see, e.g., [99, ch. 11.8]) across the waves.

The numerical experiment considers a gas species with heat capacity ratio $\gamma = 5/3$ and unit mass ratio (i.e., $\varepsilon_*^2 = 1$), referring to heavy species of an argon plasma. The initial states on the left and right section are defined as

$$\begin{bmatrix} n_L \\ p_L \\ u_L \end{bmatrix} = \begin{bmatrix} 1 \\ 1 \\ 0 \end{bmatrix}, \quad \begin{bmatrix} n_R \\ p_R \\ u_R \end{bmatrix} = \begin{bmatrix} 0.125 \\ 0.1 \\ 0 \end{bmatrix}, \tag{4.1}$$

respectively. The electric and magnetic fields are set to zero, and collisional sources are neglected.

We report the fluid states at time $t = 1$. Figure 4.1 shows the fluid states for number density, pressure, and velocity for the three meshes computed by the implicit mass flux scheme (see (3.88)). We see that the numerical solutions tend towards the exact solution as the mesh is refined. The exact solution is reproduced by the numerical solutions in first order accuracy.

One distinctive feature of the numerical scheme is that mass flux is computed implicitly. Let us compare (see figure 4.2) the difference to the classical, explicit Rusanov scheme. The numerical results of the two schemes differ only slightly. The implicit scheme resolves the shock wave more accurately, whereas the resolution of the rarefaction wave is more diffusive. The results are shown only for the coarse grid for illustration; the differences in the two schemes reduce with mesh resolution and are visually almost not distinguishable.

4.2. Uniform steady electric field

This test case focuses on validating the electric field as a source term to the Euler equations. We define a uniform and steady electric field parallel to the cylinder axis and with unit field strength ($\mathbf{E} = \hat{\mathbf{z}}$), and the magnetic field is set to zero. We specify a three-species fluid of positive ions, negative ions, and neutral atoms. The ions are singly charged, and all species have unit mass ratios ($\varepsilon_*^2 = 1$). Reactions and collisions among the species are neglected. Hence, the
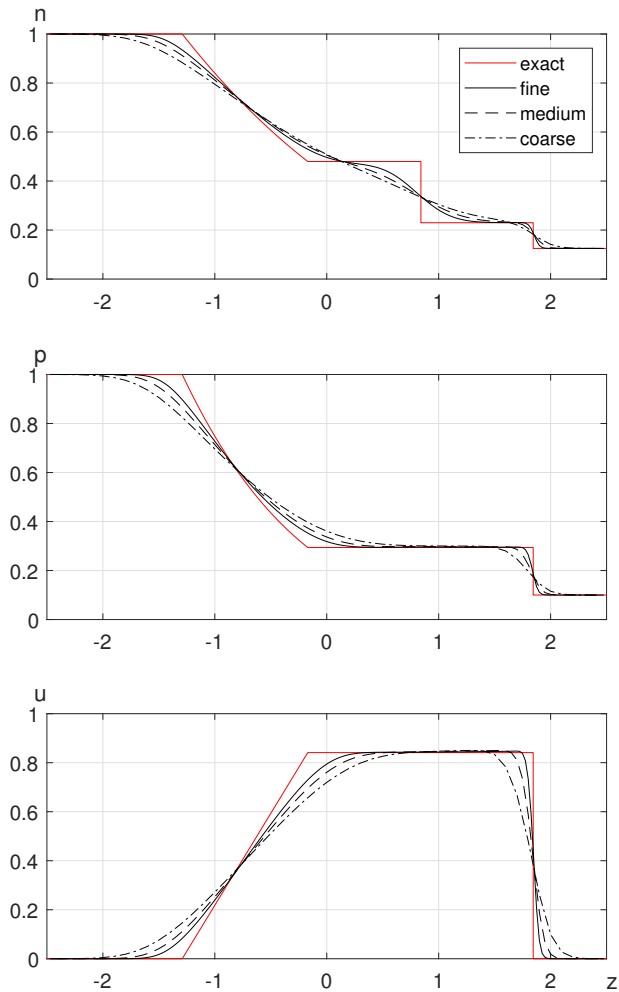
Figure 4.1.: Comparison of grid refinement for Sod's shock tube problem; data at $t = 1$ with implicit mass flux scheme.
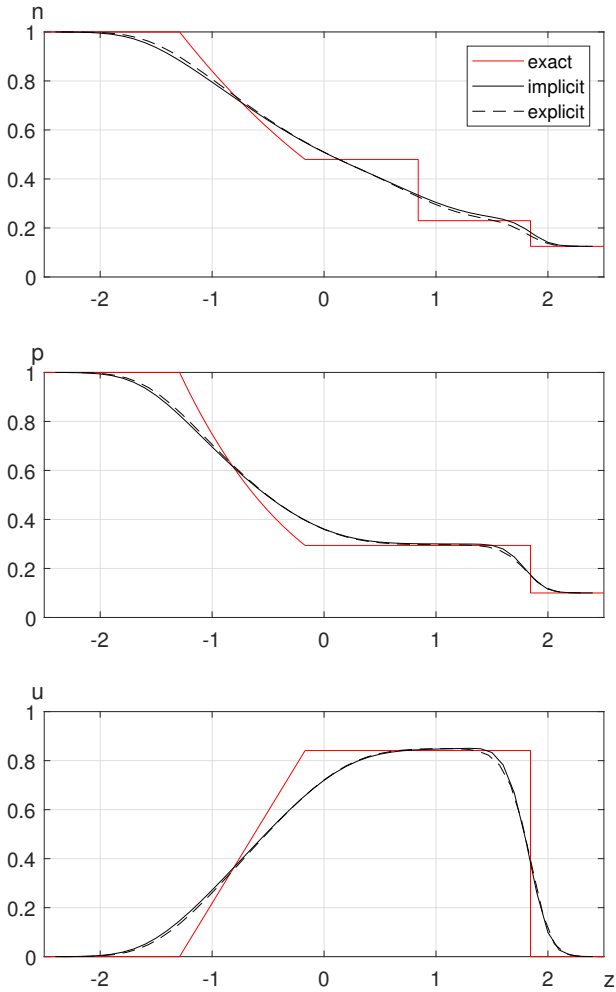
Figure 4.2.: Comparison of implicit mass flux scheme and explicit scheme for Sod's shock tube problem; data at $t = 1$ on coarse grid.

$\bar{T}$	10 kK
$\bar{x}$	10 mm
$\bar{p}$	1 bar
$\bar{m}$	39.948 u

$\bar{Q}$	$1.36 \times 10^{-21}\,\mathrm{m}^2$
$\bar{n}$	$7.34 \times 10^{22}\,\mathrm{m}^{-3}$
$\bar{t}$	$13.1\,\mu\mathrm{s}$

Table 4.2.: Scaling units. Left: reference values for a thermal argon plasma. Right: derived scaling units using ideal gas law.

momentum source is given by the electrostatic force and proportional to species charge. Initial conditions are $n_* = 1$, $p_* = 1$, and $\mathbf{u}_* = \mathbf{0}$ for all species identically. Boundary conditions in axial direction are defined as Neumann conditions, i.e., the species flow freely across the plasma-electrode boundary.

Figure 4.3 shows that species velocities increase linearly in time, and proportional to species charge, i.e., in opposite directions for negatively charged ions, as expected. Neutral atoms are not accelerated. We have checked that number densities are identical to their initial values in space and time. A grid study shows that species velocities are not affected by mesh resolution. However, it shows that charged species temperature is slightly decreasing in time with first-order accuracy in mesh resolution, see figure 4.4. Nevertheless, neutral species temperature is constant in time.

4.3. Collisional sources

After checking the classical components of the Euler solver we now turn to the source terms due to collisions see sections 3.2.5 and 3.2.6.
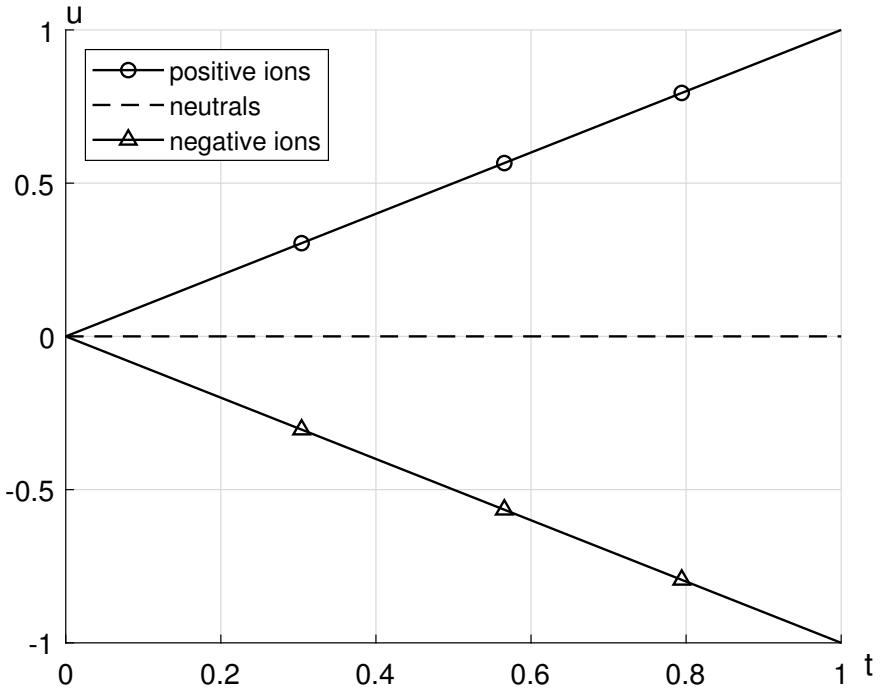
Figure 4.3.: Species velocities in axial direction due to constant and uniform electric field $\mathbf{E} = \hat{\mathbf{z}}$.
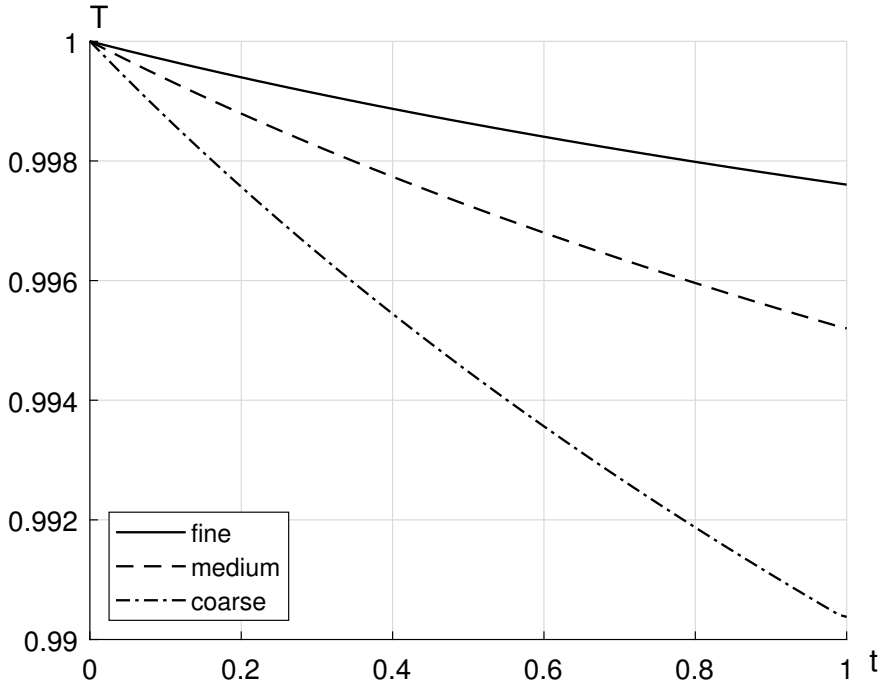
Figure 4.4.: Grid dependency of temperature for charged species. The data converges to $T \to 1$ as grids are refined.

The collision model requires to specify dimensional parameters: we define reference scales for temperature, length, pressure, and species mass that correspond to thermal argon plasmas, see table 4.2. The time scale is then found by the ideal gas law and the definition of scaled Debye length ($\lambda = 2.55 \times 10^{-6}$, see eq. (3.8c)). That is, we find

$$\bar{t} = \frac{\bar{x}}{\lambda c_0} = \frac{q}{\varepsilon_0^{1/2} c_0 k_B} \bar{x}^2 \frac{\bar{p}^{1/2}}{\bar{T}} = 13.1\,\mu\text{s}. \tag{4.2}$$

For easing computational burden we use $\varepsilon_e^2 = 1 \times 10^{-3}$ for the electron mass ratio instead of the correct value $\varepsilon_e^2 \approx \frac{1}{40 \cdot 1836} = 1.36 \times 10^{-5}$. Moreover, we consider a partially ionized quasineutral plasma, i.e., we set the neutral species number density to $n_{\text{Ar}} = 1$ and for charged species $n_{\text{Ar+}} = n_e = 5 \times 10^{-3}$.

Our testcases are defined with uniform species data. Because the collision model is defined locally, it follows that mesh resolution affects the model dynamics only through the timestep size. We perform our testcases only on the coarse grid and mimic mesh resolutions by varying the CFL number. As the stiff collisional source terms are modeled with an implicit scheme, we expect that a small CFL number reveals the true system dynamics whereas a relatively large CFL number of unity allows for much larger timesteps at the cost of some possible inaccuracies in the state variables.

In a first case, we set the initial electron temperature to $T_e = 1.6$ and velocity $u_e = 1$ in axial direction, while the heavy species are both set to $T_{\text{Ar}} = T_{\text{Ar+}} = 1.5$ and at rest $u = 0$. Figure 4.5 shows that the electron species temperature relaxes to that of heavy species on
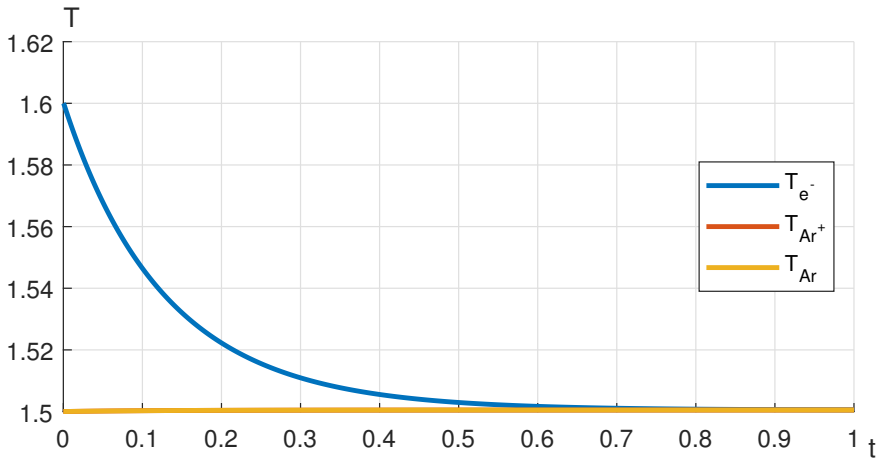
Figure 4.5.: Thermal relaxation of electron species to heavy species on coarse mesh at CFL = 1.

a timescale of order 10^{-1}. The heavy species temperature increases slightly but not noticeable in the graph. We have reduced the CFL number by orders of magnitudes to mimic finer mesh resolutions and resolving the true system dynamics, see figure 4.6. We see that the thermal dynamics are recovered at large CFL numbers and smaller timesteps would only lead to marginally different temperatures. This effect is also observed in the electron velocity as shown in figure 4.7: we see that electrons quickly exchange their momentum with heavy species. The momentum relaxation timescale is on the order of 10^{-4}, in agreement with eq. (3.30). A smaller CFL number ($< 10^{-1}$) would resolve the detailed dynamics, however the implicit scheme allows us to use larger CFL numbers and reduce computational costs with just
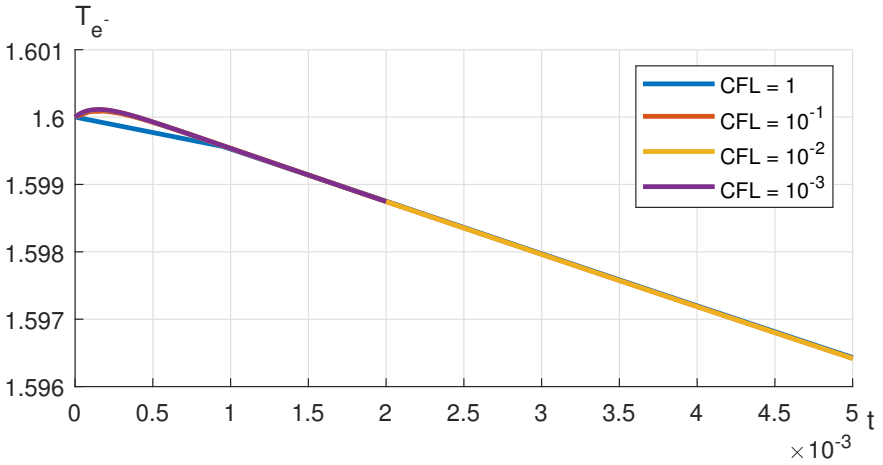
Figure 4.6.: Electron temperature at smaller CFL numbers. Smaller CFL numbers affect the thermal dynamics only on a very short timescale but is recovered by a large CFL number (CFL = 1).
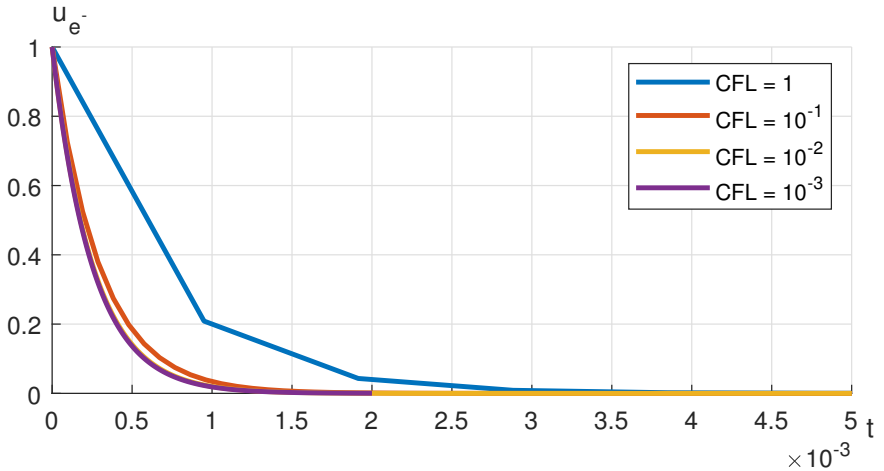
Figure 4.7.: Electron velocity at short times. The dynamics are re-
solved at small CFL number ($< 10^{-1}$).

minor deviations in accuracy.

The second case considers relaxation of heavy species: we set neu-
tral species temperature to $T_{\text{Ar}} = 1.6$ and velocity $u_{\text{Ar}} = 1$ whereas
charged species are at $T = 1.5$ and at rest. Figure 4.8 shows the
thermal relaxation of electrons and ions. Thermal relaxation of elec-
trons is on order of 10^{-1} and similar to the first case (see figure 4.5),
however, ions relax much faster to neutral species. This behavior is
predicted in eq. (3.28), i.e., collisions of particles with similar masses
relax their kinetic energy faster than particles with disparate masses.
Figure 4.9 shows a detailed view on the thermal relaxation of ions:
similarly to above, we see that the detailed dynamics are not resolved
at CFL = 1 but it allows to reduce computational costs without trad-
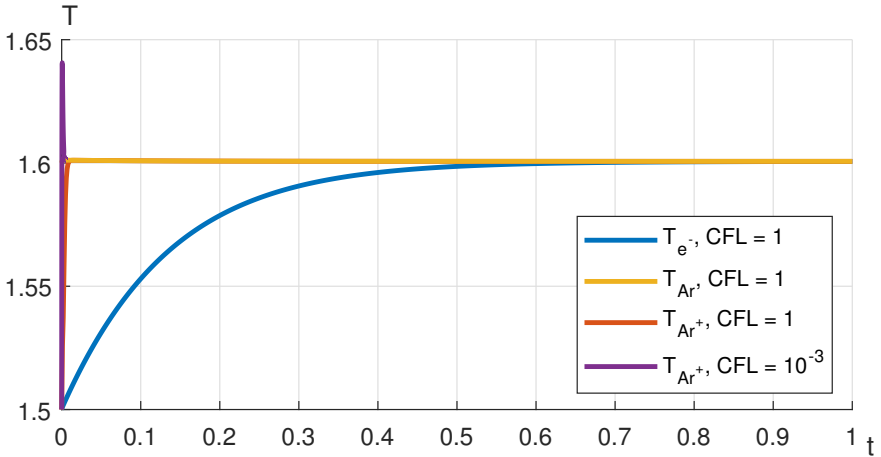
Figure 4.8.: Thermal relaxation of ions (Ar^+) and electrons $(e^-,$ blue) to neutral species (Ar, yellow). Ions relax quickly whereas electron thermal relaxation timescale is on order of 10^{-1}. For small CFL numbers we see that ion temperature overshoots significantly (red and purple). See also figure 4.9 for detailed view.

ing accuracy in the long run. Figure 4.10 shows the momentum relaxation of electrons and ions. We see that both species relax their momentum quickly, with electron momentum relaxation being faster.

4.4. Maxwell solver

Two cases are considered for testing the numerical method for the Maxwell subsystem. Firstly, we consider the whole domain as a dielectric and we neglect the current **J**. Hence, we solve the wave
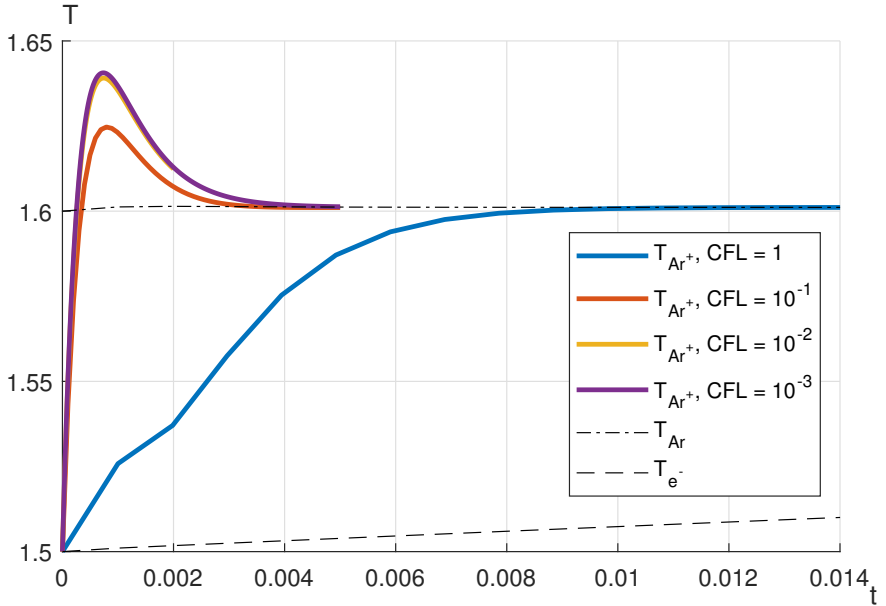
Figure 4.9.: Thermal relaxation of ions (Ar^+) to neutral species (Ar) at short timescale. The detailed dynamics are not resolved for CFL = 1 (blue line). The lines are almost identical for CFL $\leq 10^{-2}$ (yellow and purple). Temperatures for Ar (dash-dotted line) and e^- (dashed line) are given as a reference.
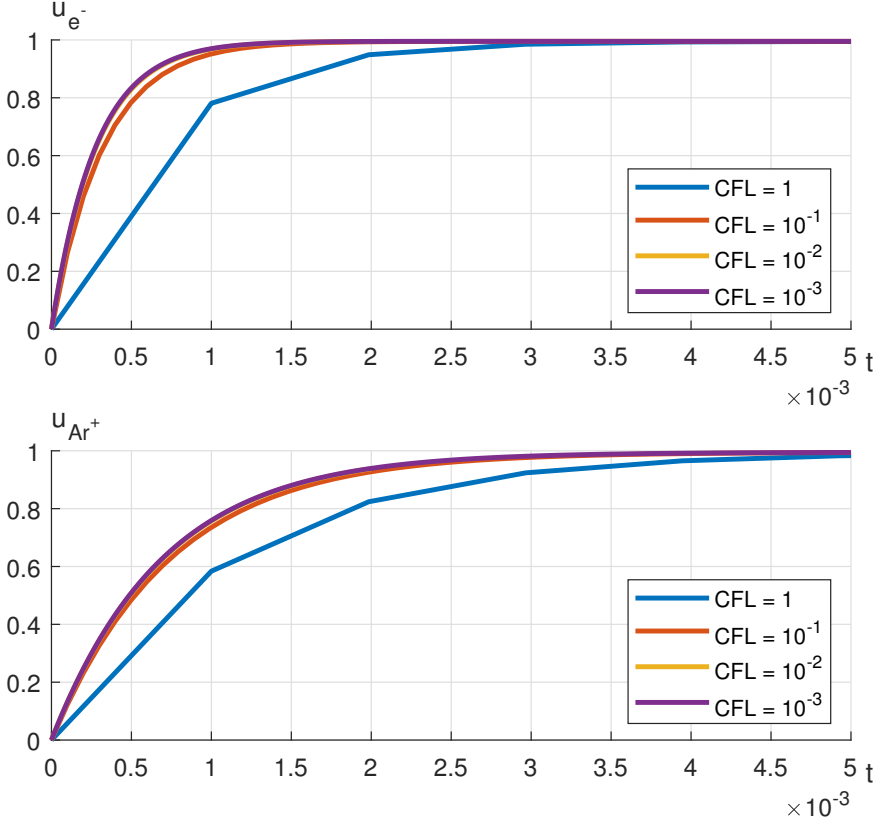
Figure 4.10.: Momentum relaxation of electrons (e^-) and ions (Ar^+) at short timescale.

equation

$$\lambda^2 \partial_t^2(\varepsilon\mathbf{E}) + \nabla \times \nabla \times \mathbf{E} = \mathbf{0} \qquad (4.3)$$

as given by the implicit numerical scheme in eq. (3.99). The boundary conditions are given by a step-like voltage profile

$$\varphi(t) = \frac{1}{2}\left(1 + \tanh\left(\frac{t - t_0}{\tau}\right)\right) \qquad (4.4)$$

with $t_0 = 1$ and $\tau = 0.1$. We use a constant timestep size $\delta_m = 0.1$. We expect that the voltage profile leads to an electromagnetic wave in the domain with an amplitude that eventually vanishes. Ultimately, it should lead to a constant and uniform electric field $\mathbf{E} = 0.2\mathbf{z}$ between the contacts. We perform a parameter study on the AP parameter λ: for $\lambda = 1$ we expect that the voltage jump leads to a large wave amplitude whereas $\lambda \to 0$ dampens the wave amplitude and leads to an electric field that follows the voltage boundary condition closely.

We evaluate the z-component of the electric field E_z at the origin $\mathbf{x} = (0,0,0)$ and the y-component of the magnetic flux B_y at position $\mathbf{x} = (1,0,0)$. The results are shown in figure 4.11 for the electric field and in figure 4.12 for the magnetic flux. We see that the AP parameter leads to wave dampening, indeed, and matches the predicted behavior. The amplitude is fully damped for $\lambda^2 = 10^{-4}$, and the electric field follows exactly the voltage boundary conditions whereas the magnetic flux vanishes. We also show data of the grid study for $\lambda = 1$: we see that finer meshes lead to marginally larger amplitudes

and phase shift in comparison to the coarse mesh. The differences are most pronounced for the magnetic flux. For clarity, we do not show data of the grid study for smaller values in λ because no differences are recognizable in the plots.

The second testcase includes the electric current $\mathbf{J}$. We consider the whole domain as a solid material with constant and uniform electrical conductivity $\sigma = 1$. That is, we solve the equation

$$\lambda^2 \partial_t^2(\varepsilon \mathbf{E}) + \nabla \times \nabla \times \mathbf{E} + \sigma \partial_t(\mathbf{E}) = \mathbf{0} \qquad (4.5)$$

with the same method as discussed above, and we apply identical conditions as in the first testcase. Figures 4.13 and 4.14 show the results for axial electric field and azimuthal magnetic flux as above. We see that including Ohm's law leads to further wave dampening. We also observe that the current leads to a magnetic field $|\mathbf{B}| = 0.1$, approximately, as given by Ohm's law. The magnetic field is smaller than expected because the dual plasma domain has a radius that is a half cell height larger than the primal domain, see also section 3.4.1. We also include the results for medium mesh and $\lambda^2 \geq 0.1$, and we notice the same effect as in the first testcase. The difference in the magnetic flux density is clearly attributed to the radial mesh resolution of the plasma domain.
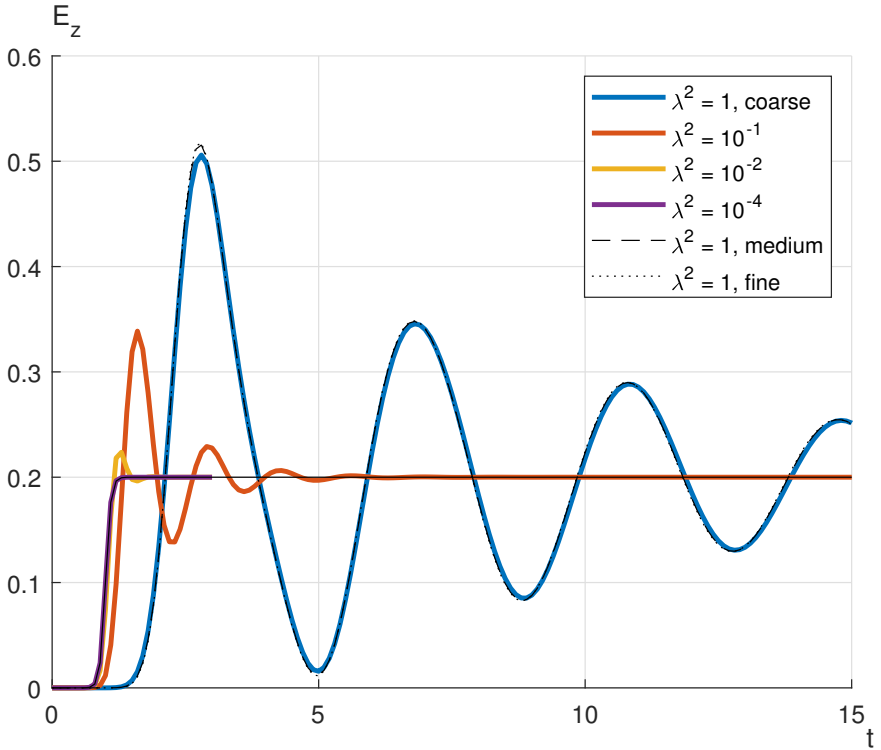
Figure 4.11.: Axial component of electric field for the wave equation evaluated at the origin. Coarse domain Data from mesh study is shown only for $\lambda = 1$; differences are not visible for smaller values in λ and therefore not shown.
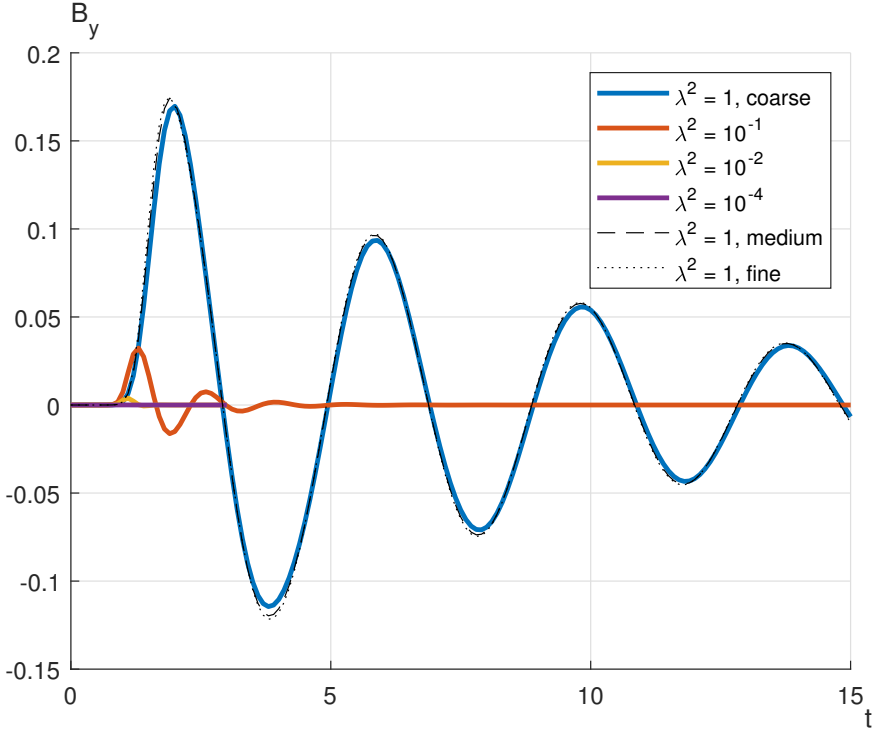
Figure 4.12.: Azimuthal component of magnetic flux density for the wave equation evaluated at $\mathbf{x} = (1,0,0)$. Data from mesh study is shown only for $\lambda = 1$; differences are not visible for smaller values in λ and therefore not shown.
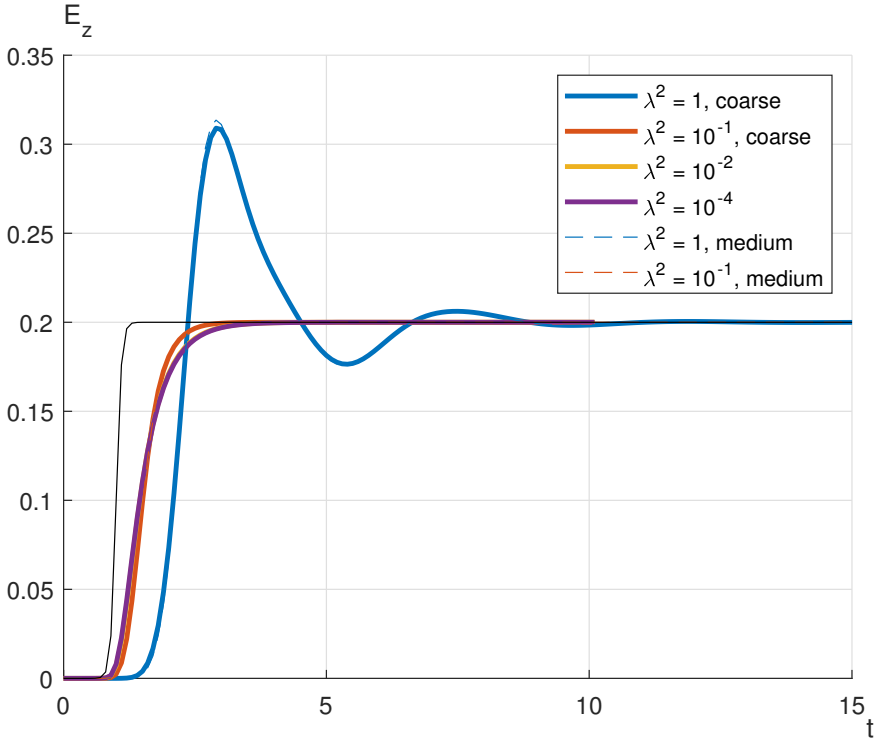
Figure 4.13.: Axial component of electric field for the wave equation including electric current by Ohm's law, evaluated at the origin. Thick lines are computed on the coarse mesh, dashed lines are on the medium mesh. The voltage boundary condition is plotted for reference (thin black line).
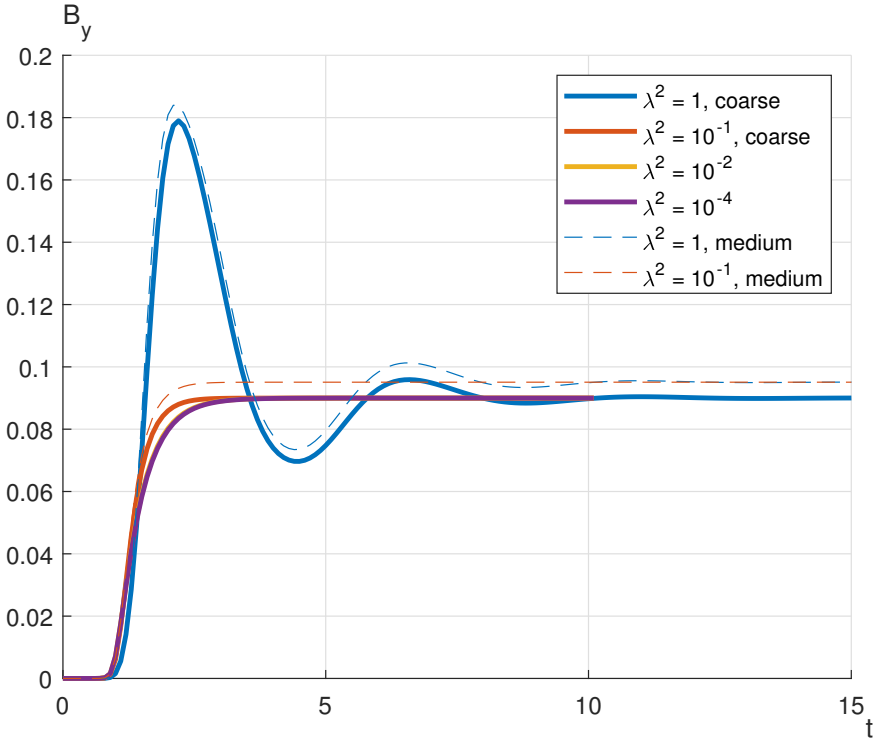
Figure 4.14.: Azimuthal component of magnetic flux density for the wave equation including electric current by Ohm's law, evaluated at the origin, evaluated at $\mathbf{x} = (1, 0, 0)$. Thick lines are computed on the coarse mesh, dashed lines are on the medium mesh.

4.5. Fully coupled Euler-Maxwell system

We consider the fully coupled Euler-Maxwell system. We specify the voltage boundary condition (4.4) with $t_0 = 0.1$ and $\tau = 0.01$, and we use the scaling parameters given in table 4.2. We stress that the number density scale is found from the ideal gas law; the corresponding value for the scaled Debye length (the AP parameter, see eq. (3.8c)) is $\lambda^2 = 6.5 \times 10^{-12}$. The multi-species plasma is initialized uniformly with $T_* = 1.5$ and $u_* = 0$ for all species, and number densities are set to $n_{\mathrm{Ar}} = 1$ and $n_{\mathrm{Ar}^+} = n_{\mathrm{e}^-} = 5 \times 10^{-3}$. The geometric symmetries in the model setup results in data that depend only on the radial coordinate; nevertheless, the system is solved in 3D. In contrast to the previous section, the plasma domain has finite electrical conductivity whereas the outer solid is dielectric.

Firstly, we check the coupling of the numerical model. For this purpose, we replace the scaled Debye length with $\lambda^2 = 1$ in case 1 and $\lambda^2 = 10^{-4}$ in case 2. It is clear that these are not the physically correct values but it allows to study the modeling effect due to this AP parameter.

We have checked the results visually and confirm that the results are only functions of the radial position.

4.5.1. Case 1: $\lambda^2 = 1$

Figure 4.15 shows the total current $\mathbf{J}$ across the xy-plane, which is carried by the electrons $\mathbf{J}_e$ because of their small inertia. One would expect that the electrons are accelerated by the electric field

and reach a terminal speed and constant current. But this is not the case and explained as follows. Because of $\lambda^2 = 1$, the voltage boundary conditions lead to an electromagnetic wave (compare also figure 4.12) that propagates radially into the plasma at finite speed. This gives rise to a phase shift of the electric field with respect to radial coordinate and results in a complex structure of the measured value at a single point, as shown in figure 4.16. When integrating over the cylinder cross section, we see that the electric current – or electron mass flux, equivalently – overshoots and induces an opposing electric field. In total, this effect results in a periodic interaction with the voltage boundary condition and explains the complex structure of the measured current in figure 4.15 and the electric field in figure 4.16. We observe a period $T = 4$.

Figures 4.17 to 4.19 show data of the gas species at the origin. Figure 4.17 shows the velocity of electrons and heavy species. The electron velocity is much larger than that of the heavy species because of its inertia. We also see that the charged species react on the electric field as given by the electrostatic Lorentz force and the species charge. We also see a net drift velocity in negative direction which is due to the relatively fast electrons and their collisions with heavy species. Figure 4.18 shows the species temperature. Although we add electrical energy to the system and not having specified a radiative energy sink, we observe a general trend to slightly lower temperatures. This is not yet fully understood and should be checked by additional testcases. The larger amplitudes in electron temperature is due to their acceleration as given by the electric field. Figure 4.19 shows
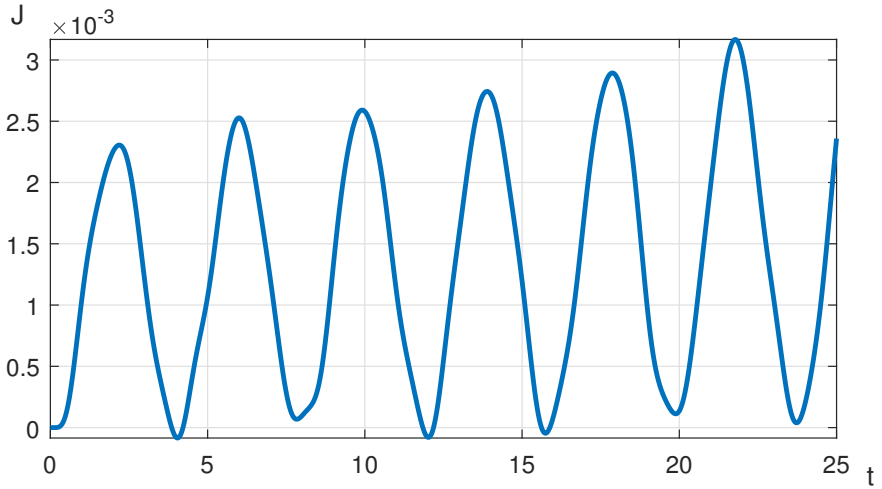
Figure 4.15.: Total current across xy-plane.
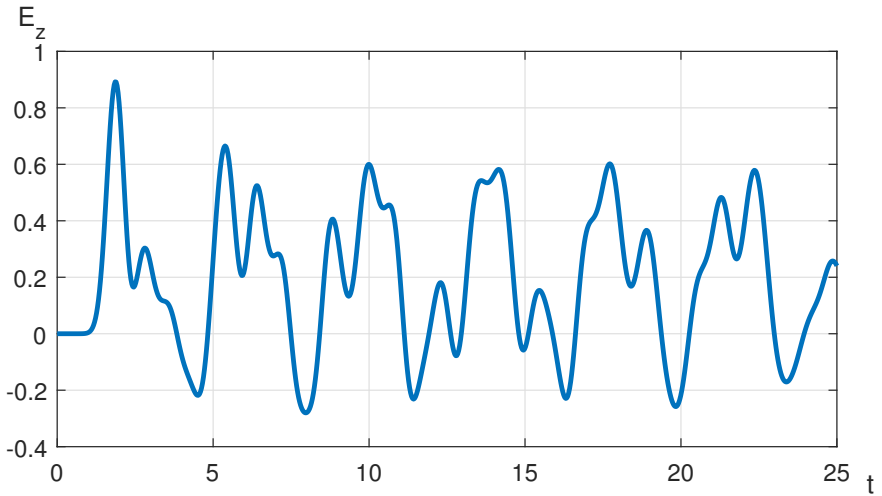
Figure 4.16.: Axial component of electric field at origin.
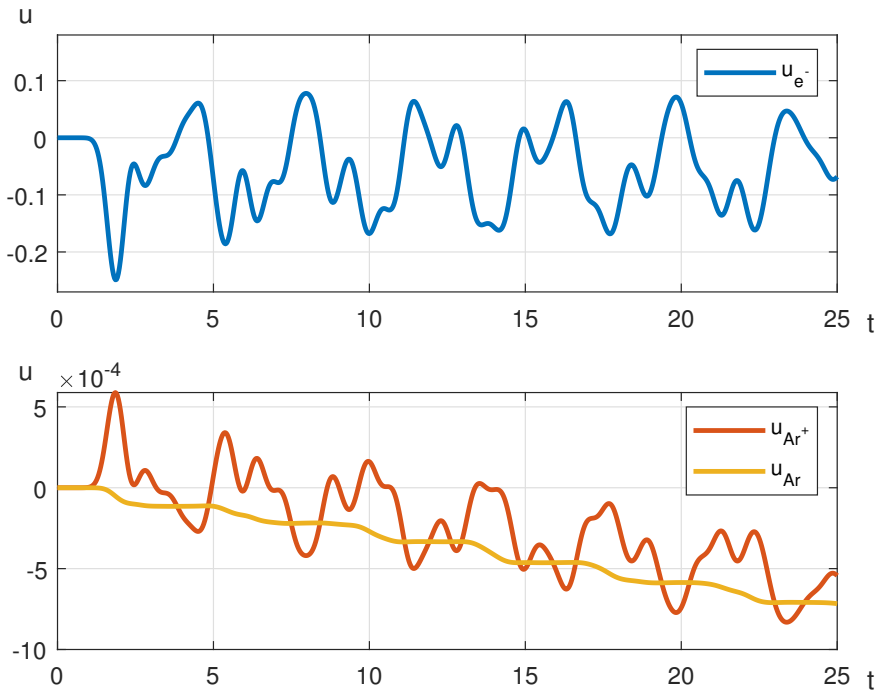
Figure 4.17.: Velocity of electrons, argon ions and neutral atoms at origin.
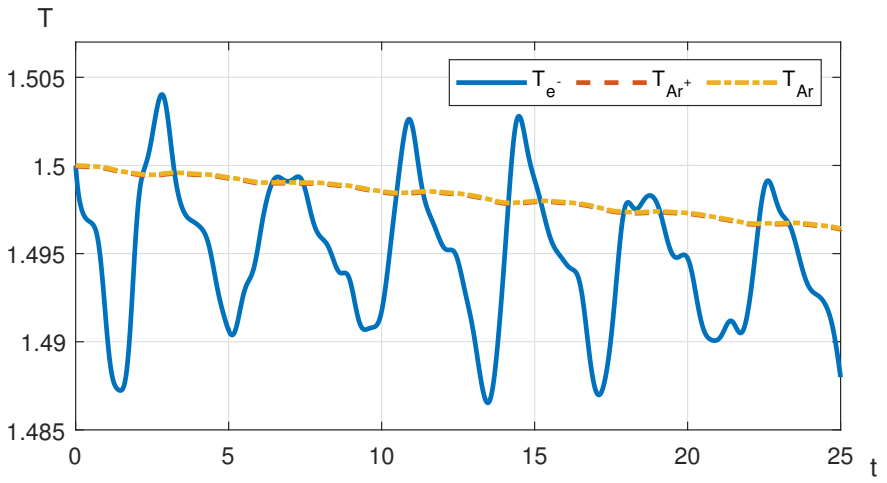
Figure 4.18.: Temperature of electrons, argon ions and neutral atoms at origin.
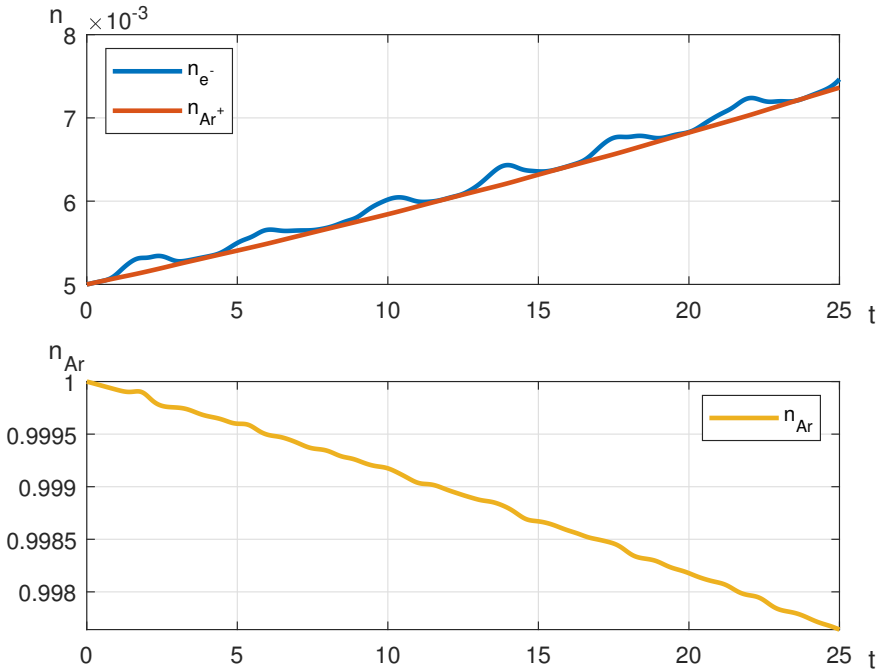
Figure 4.19.: Number densities of electrons, argon ions and neutral atoms at origin.

the number densities. The temperature level is above the ionization equilibrium temperature (see Saha equation (3.46)). We therefore observe ionization, i.e., number densities increasing for charged species and decreasing for neutral species; this is due to the inelastic collision model.

4.5.2. Case 2: $\lambda^2 = 10^{-4}$

Let us consider the same settings as in the first case but with $\lambda^2 = 10^{-4}$. Informed by the results of the testcases in section 4.4 we expect that the oscillations in the electric field are more damped.

Figures 4.20 and 4.21 show the total current across xy-plane and the electric field at the origin. We see that the oscillations are more damped, indeed, and they are at higher frequency with period $T = 0.4$. This is an expected value as compared to above since the AP parameter λ is proportional to the wave frequency. We also notice that the mean value of the total current is increasing. That is, on average the electrons are accelerated in the electric field. This corresponds to our observation in figure 4.21 that the electric field mean value ($E_z = 0.2$) is given by the voltage boundary conditions.

Figures 4.22 to 4.24 show gas species data. In comparison to above (figures 4.17 to 4.19), we see that the data is much smoother with identical trends. Additionally, it becomes clear that the mean electron velocity tends to $u_e = 0.06$ whereas the ions tend to $u_{\mathrm{Ar}^+} = 1.4 \times 10^{-4}$, see figure 4.22.

However, we also recognize in all figures that the situation starts
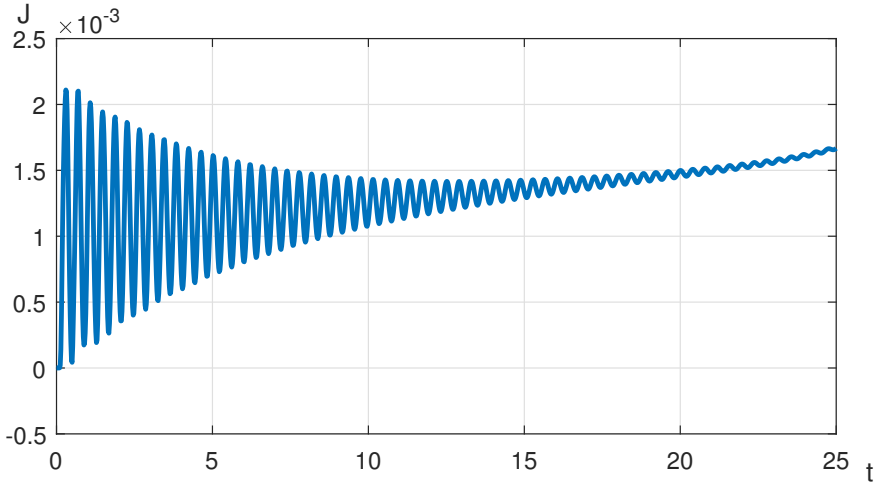
Figure 4.20.: Total current across xy-plane.

to change at time $t = 15$ to 20, approximately. Visualizing the data we observed that the solver begins to drive away from the uniform setup, in particular near the Neumann boundaries at the imaginary electrode surfaces. This effect is even more pronounced for smaller values $\lambda \to 0$. We realized that the numerical design is not yet complete, as described next.

4.5.3. Case 3: $\lambda^2 = 0$

We aimed for checking if the designed model is truly asymptotic preserving and set $\lambda^2 = 0$. We then understood that a small electrical conductivity ($\sigma = 1 \times 10^{-6}$) should be defined in the dielectric domain, otherwise the Maxwell system solver does not converge.
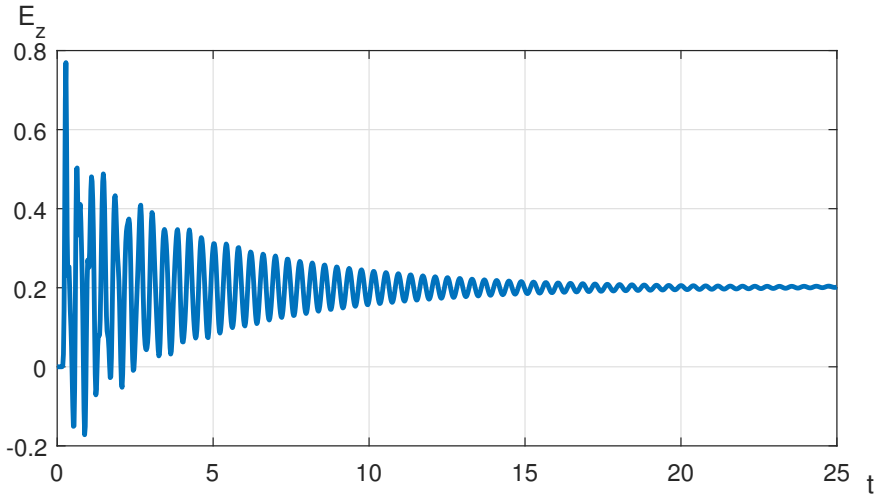
Figure 4.21.: Axial component of electric field at origin.

Restarting the solver proved that it converged initially, but the electric field becomes wrong when the voltage boundary condition drives the system away from its initial configuration.

We became aware that the present model is not asymptotic preserving in 3D because quasineutrality is not respected. To see this, we remember that the limiting case $(\lambda^2 = 0)$ in Maxwell's equations is given by

$$\partial_t(\mu\mathbf{H}) + \nabla \times \mathbf{E} = \mathbf{0}, \tag{4.6a}$$

$$\nabla \times \mathbf{H} = \mathbf{J}. \tag{4.6b}$$

There is a consistency problem with Ohm's law: a linear relation
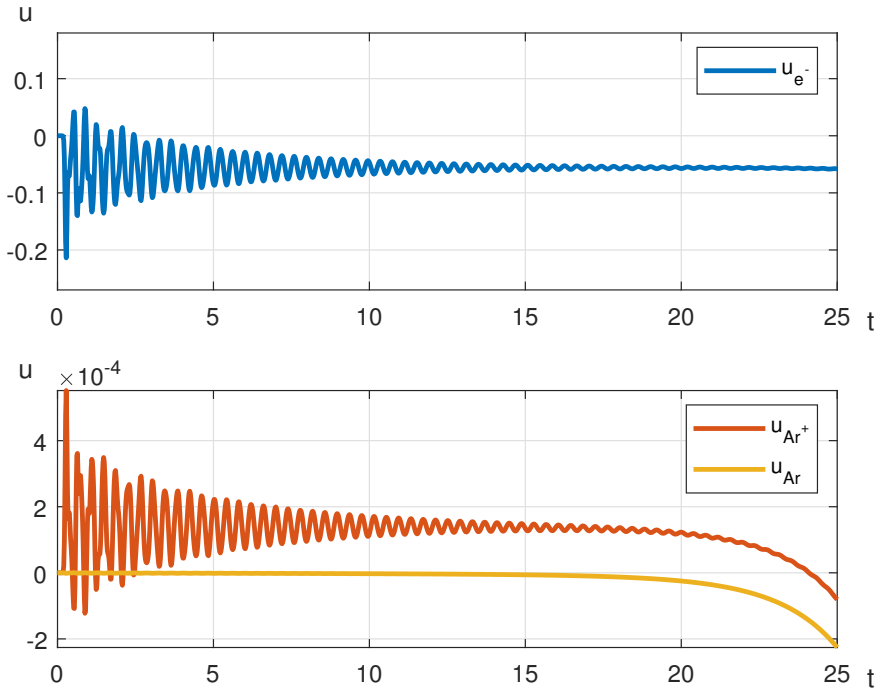
Figure 4.22.: Velocity of electrons, argon ions and neutral atoms at origin.
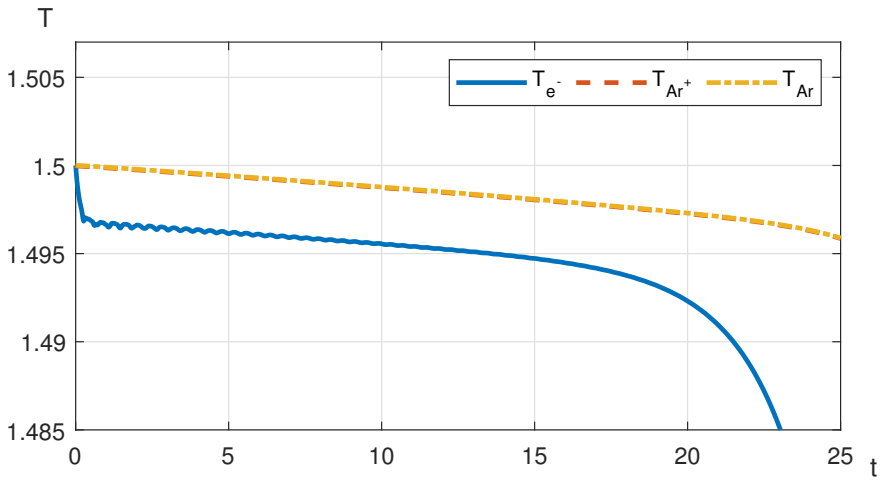
Figure 4.23.: Temperature of electrons, argon ions and neutral atoms at origin.
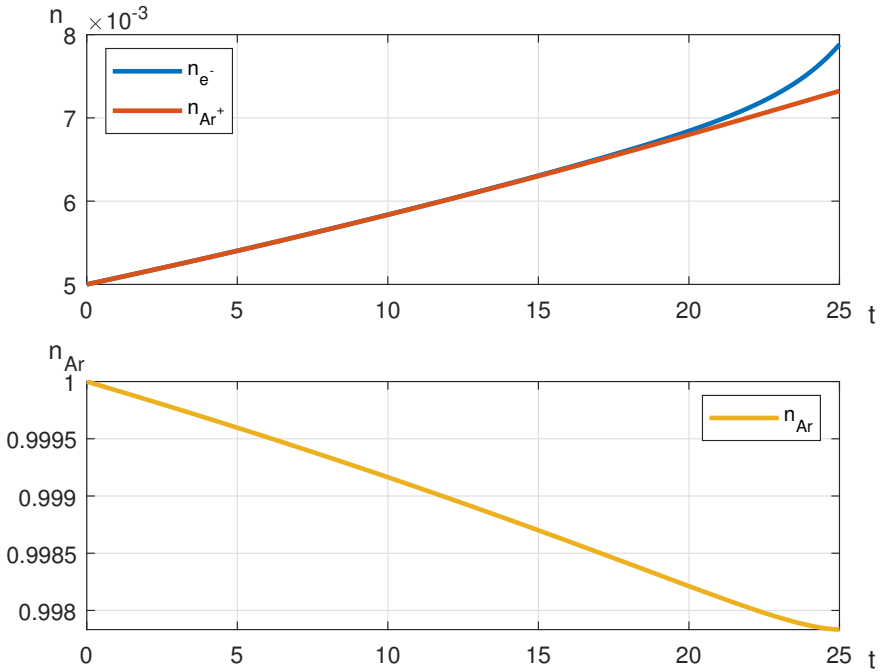
Figure 4.24.: Number densities of electrons, argon ions and neutral atoms at origin.

($\mathbf{J} = \sigma \mathbf{E}$, and eq. (3.89) for its discrete analogy) is not compatible with the requirement that $\nabla \cdot \mathbf{J} = 0$ in the limit $\lambda = 0$. This issue requires further work and is currently investigated.

5. Summary & Outlook

5.1. Summary

We generalized a numerical scheme for plasma simulations to 3D building on the Finite Integration Technique or Cell Method. This permits for more general mesh topologies. The new method allows for non-constant timestepping based on an argument from stiffly accurate methods. Moreover, the presented model includes a friction model that accounts for the species interactions in the collision dominated plasma, using a minimal set of an argon plasma. Lowest-order Raviart-Thomas elements are used to interpolate the magnetic flux density, and we apply a reconstruction method to approximate the electric field in the dual cell center. We also make use of the implicit current or mass flux for coupling the gas dynamic and electromagnetic subsystems. The numerical experiments validated the subsystems, and the new method works for the fully coupled system for finite values in the scaling parameter λ. However, the experiments showed that the new method is not asymptotic preserving if one sets $\lambda = 0$ because of an inconsistency in this limiting case.

5.2. Outlook

Further work is required to make the generalized numerical scheme asymptotic preserving. Future research should also focus on points highlighted in this thesis. The most thrilling aspect is to review and improve the reconstruction of the **E**-field to cell centers based on the recent findings in [128]. This could be key for applying higher order methods in time and space, which are also separate topics on their own. Interpolation of **B**-field with Raviart-Thomas elements in hexahedrons should be straightforward and reduce errors at the plasma domain boundary. The present method should also be extended to non-uniform materials, in particular with respect to magnetic permeability. This would allow for studies including iron bodies, for instance. One should also consider other plasma species and their chemistry, and extend the collision modeling for other types of collisions and processes. In addition, the numerical modeling of implicit momentum sources may be reviewed and improved.

We also mention two aspects that should be considered in future work but have not been in focus of this thesis.

The first aspect is similar to the AP property (see section 3.3) and physical modeling. We discussed in section 3.2.2 that the plasma exhibits separate temperatures for each species which is due to the species mass ratio and the collision frequency. As ions and neutral species collide frequently, they equilibrate quickly and one will subsume them in a single, heavy species gas. Let us now assume that the large mass ratio between electrons and heavy species leads to negli-

gible electron momentum flux. This implies that the plasma forces are dominated by friction and one finds in the limit case

$$\mathbf{u}_e = \mathbf{u}_h + \frac{1}{\gamma_e}(\mathbf{E} + \mathbf{u}_e \times \mathbf{B}) + \frac{1}{n_e \gamma_e}\nabla p_e, \qquad (5.1)$$

that is, the electron velocity is expressed by a friction coefficient γ_e, the heavy species velocity and the Lorentz force. It would be worth to check in detail the relation of this approach and drift-diffusion models. See also [46, 47].

The second aspect is of numerical nature. The Euler equations with gravitation describe a huge class of phenomena including atmospheric weather predictions as well as supernovae explosions. [87] An interesting task is to consider non-trivial steady states, which imply that the pressure gradient balances the gravitational force. This situation should be modeled with well-balanced schemes (see, e.g., [7]), i.e., a finite volume scheme that satisfies a discrete version of the flux-source balance and preserves a discrete steady state of interest, up to machine precision. They are especially known in the context of shallow water equations with non-uniform topography (see, e.g., [66], [37, sec. 6.5]). High order well-balanced schemes have been designed for ideal MHD with gravity [60], and other work focused on implicit-explicit schemes for flow equations with stiff source terms. [159, 100] It would be of interest to combine these aspects for resistive MHD as considered in this thesis.

Part II.

On modeling radiative heat transfer in electric arc simulations

6. Introduction

This parts is concerned with radiative heat transfer modeling, because radiation is the main energy transfer mode in electric arcs and other thermal plasmas.

The main difficulty lies in trading accuracy with computational costs. The ultimate interest in thermal radiation modeling is to solve for the net emission; this is the quantity that enters the energy balance equation as a source term in a plasma model. In principle, net emission is defined through the radiative transfer equation (RTE). The equation itself is computationally demanding, but it is also the absorption coefficient κ – the main material parameter in thermal radiation modeling – of the plasma that increases computational costs and prevents from an exact numerical solution.

The situation becomes even more involved: even if the carrier gas is initially a pure substance, the plasma is always affected by other gas components since nearby surfaces are heated by radiation and evaporate. This includes not only the metallic electrodes that are in direct contact with the electric arc, but also the enclosure of molded case circuit breakers (see also part III). In consequence, the radiative properties should be available not only for the (pure) plasma but

also for its mixtures with other substances like metal vapors (copper, iron, silver, and other metal and alloys) and polymer vapors (e.g., polytetrafluoroethylene or PTFE) and plastics (e.g., acrylic glass). However, we will focus on the modeling techniques in this part and stay with a "pure" plasma for dry air (i.e., an artificial mixture of nitrogen, oxygen, argon, and carbon dioxide).

A comprehensive discussion of radiative heat transfer may be found, e.g., in [112]. An introduction to thermal plasma modeling and its material properties is given, e.g., in [67] and [42]. The effects of metal vapor on radiative transfer – in particular air-copper plasmas – are discussed in, e.g., [89] and [69]. An example of an ablation-dominated arc is given, for instance, in [52].

We firstly summarize fundamental concepts (see chapter 7) and methods aimed towards mean absorption coefficients as they are used in applied numerical simulations (see part III). Chapters 8 to 10 present research results in radiation modeling. Those are based on a simple model of an electric arc – the Elenbaas-Heller equation – solved at constant current, and a spectral analysis of the net emission. Chapter 11 summarizes the results and gives an outlook to further work.

7. Fundamentals

7.1. Basic quantities

The term *radiative heat transfer*, or *thermal radiation*, refers to the process of heat transfer by electromagnetic waves, i.e., those waves that are emitted by a medium due solely to its temperature. [112, p. 1 and 4] These waves are specified by wavelengths λ from $0.1\,\mu\text{m}$ to $100\,\mu\text{m}$, which stretches over the electromagnetic spectrum categories of ultraviolet, visible, and mid-infrared waves. Their frequency ν is given by the relation

$$\nu = \frac{c_0}{\lambda},\tag{7.1}$$

where c_0 is the speed of light in vacuum; we remark that the refractive index is approximately unity for ordinary gases and plasmas (see, e.g., [112, 133, 149]) and therefore neglected in this text. The waves may also be regarded interchangeably as massless energy parcels, each of them carrying an amount of energy $E = h\nu$, where h is the Planck constant

$$h = 6.626\,070\,15 \times 10^{-34}\,\text{J s}.\tag{7.2}$$

Every material at a finite absolute temperature T emits thermal

radiation. The radiative heat flux emitted from a surface is called the *emissive power* (in units of $\mathrm{W\,m^{-2}}$),

$$E(T) = \int_0^\infty E_\nu(T, \nu)\,\mathrm{d}\nu, \qquad (7.3)$$

where E_ν denotes the spectral emissive power at a given frequency ν.

An idealized but key concept is the notion of a *black surface* or *black body*, which refers to an opaque surface that does not reflect any radiation but absorbs it completely. It was shown by Max Planck [130] that the spectral emissive power of a black surface bounded by a transparent medium is given as

$$E_{b\nu}(T, \nu) = \frac{2\pi h}{c_0^2} \frac{\nu^3}{\exp(\xi) - 1}, \quad \xi = \frac{h\nu}{k_B T}, \qquad (7.4)$$

where k_B is Boltzmann's constant, see eq. 3.7; this relation is also known as Planck's law. The dimensionless number ξ is frequently used. For instance, one finds that the maximum spectral emissive power is found at $\xi = 2.8214$, i.e.,

$$\nu_{peak} = \frac{\xi k_B}{h} T = (5.8789 \times 10^{10}\,\mathrm{Hz\,K^{-1}}) \cdot T. \qquad (7.5)$$

The total blackbody emissive power is therefore found by the Stefan-

Boltzmann law

$$E_b(T) = \frac{2\pi h}{c_0^2} \left(\frac{k_B T}{h}\right)^4 \int_0^\infty \frac{\xi^3}{\exp(\xi) - 1} \, d\xi \qquad (7.6\text{a})$$

$$= \sigma T^4, \qquad (7.6\text{b})$$

where σ is the Stefan-Boltzmann constant

$$\sigma = \frac{2\pi^5 k^4}{15 c_0^2 h^3} = 5.670\,374\,419 \times 10^{-8}\,\text{W}\,\text{m}^{-2}\,\text{K}^{-4}. \qquad (7.7)$$

Radiative energy flux varies at any point $\mathbf{r}$ inside a medium with direction. The unit direction vector $\hat{\mathbf{s}}$ is often given in spherical coordinates, i.e., in terms of polar angle $\theta \in [0, \pi]$ and azimuthal angle $\psi \in [0, 2\pi]$, relative to a coordinate system. On a surface, the polar axis is customarily identified with its unit normal vector $\hat{\mathbf{n}}$. The *solid angle* $d\Omega$ of an infinitesimal surface element dA seen from a point is defined as the projection of dA in direction of $\hat{\mathbf{s}}$ onto the unit sphere, i.e., it is identified with a surface element

$$d\Omega = \sin\theta \, d\theta \, d\psi \qquad (7.8)$$

on the unit sphere (in units of sr). The unit sphere has a total surface area equal to 4π.

While emissive power is associated with a surface describing the radiative heat flux leaving it, another quantity is required for describing the radiative energy flow in space and its direction: this is the *radiative intensity* $I(\mathbf{r}, \hat{\mathbf{s}})$ defined as the radiative energy flow

per unit solid angle and unit area normal to the rays in direction of $\hat{\mathbf{s}}$. The spectral radiative intensity $I_\nu(\mathbf{r}, \hat{\mathbf{s}})$ is defined analogously as the radiative intensity at frequency ν, and it is measured in units of $\mathrm{W\,m^{-2}\,sr^{-1}\,Hz^{-1}}$. It can be shown that the radiative intensity leaving a black surface is independent of direction and it holds $E_{b\nu} = \pi I_{b\nu}$, i.e., the spectral blackbody intensity or *Planck function* varies with temperature only,

$$B_\nu(T) = \frac{2h}{c_0^2} \frac{\nu^3}{\exp(\xi) - 1}, \quad \xi = \frac{h\nu}{k_B T}. \tag{7.9}$$

The Planck function is also denoted by $I_{b\nu}(T)$ in the literature. We write for its derivative with respect to temperature

$$B_\nu'(T) := \frac{\mathrm{d}B_\nu}{\mathrm{d}T} = \frac{2h}{c^2} \frac{\nu^3 \exp(\xi)}{(\exp(\xi) - 1)^2} \frac{(-\xi)}{T} \tag{7.10a}$$

$$= (-1)\frac{\xi}{T}\frac{\exp(\xi)}{\exp(\xi) - 1} B_\nu(T). \tag{7.10b}$$

The amount of *incident radiation*, or *irradiation*, is given by the integral over all solid angles, i.e., the spectral irradiation is

$$G_\nu = \int_{4\pi} I_\nu \, \mathrm{d}\Omega, \tag{7.11}$$

and the total irradiation

$$G = \int_0^\infty G_\nu \, \mathrm{d}\nu. \tag{7.12}$$

Likewise, the spectral and total *radiative heat flux* are defined as

$$\mathbf{q}_\nu = \int_{4\pi} I_\nu(\hat{\mathbf{s}})\hat{\mathbf{s}} \, \mathrm{d}\Omega, \tag{7.13}$$

and

$$\mathbf{q} = \int_0^\infty \mathbf{q}_\nu \, \mathrm{d}\nu. \tag{7.14}$$

7.2. Radiative material properties

Let us consider thermal radiation impinging onto a medium of finite thickness (see, e.g., [112, sec. 1.11]). Some part of the irradiation is reflected away at its surface, another part is absorbed inside the layer, and the rest is transmitted through it. This motivates the definition of three radiative properties, namely reflectance (ρ), absorptance (α), and transmittance (τ), being the ratios of the reflected, absorbed, and transmitted part of incoming radiation relative to the total incoming radiation. Consequently, they sum up to 1. A fourth property, the emittance (ε), is given by the ratio of emitted thermal radiation to the maximum possible (i.e., by a black surface at same temperature).

In particular for gases, all properties depend on frequency, temperature, and direction (both, incoming and outgoing). Therefore, they are defined as spectral properties, total properties (i.e., an average over the spectrum), directional properties, and hemispherical properties (i.e., an average over all directions).

A medium is said to be opaque if radiative energy is completely attenuated inside and therefore nothing transmitted ($\tau = 0$). The

medium is transparent if it passes without being attenuated ($\tau = 1$). A black surface does not reflect any radiation and absorbs all incoming radiation, i.e., $\alpha = 1$ and $\rho = \tau = 0$; moreover, we have $\varepsilon = 1$ for a black surface.

Let us consider a gas layer with thickness s. Because radiative energy is not reflected, it is concluded that absorptance is given as $\alpha_\nu = 1 - \tau_\nu$. The radiative energy becomes gradually attenuated when passing through the gas layer. According to Beer's law, the spectral transmittance may be written as

$$\tau_\nu = \exp\left(-d\right), \quad d = \int_0^s \kappa_\nu \, \mathrm{d}s, \tag{7.15}$$

where κ_ν is known as the spectral absorption coefficient measured in units of m^{-1}. The optical depth d of the medium is used to discriminate between optically thin ($d \ll 1$) and optically thick ($d \gg 1$) media. For a homogeneous and isothermal gas layer, the expression above simplifies to

$$\tau_\nu = \exp(-\kappa_\nu s). \tag{7.16}$$

The absorption coefficient is equal to the inverse of the mean free path for a photon until it undergoes absorption. [112, p. 281] It is the basic quantity for radiation modeling in particular for electric arc simulations, and it will be in focus of the following work.

The spectral structure of the absorption coefficient is shown in figure 7.1. The complex structure is due to elementary interactions of photons and gas particles at an atomic level (see, e.g., [34, 23, 112]).

Absorption or emission of a photon goes with a change in the total energy of the particle, i.e., its kinetic, translational (for molecules), and internal energy levels (electronic, rotational, vibrational). Quantum mechanics dictates that the internal energy levels are discrete, so that only photons with distinct energies $E = h\nu$ may interact.

If the gas is relatively cold when compared to its ionization energy, these interactions result in bound-bound transitions (bb), i.e., the molecule is not ionized before and after the transition and electrons remain bounded to the atom or molecule. This results in sharp peaks (known as spectral lines) observable in the spectral structure that are characteristic for the gas. Those lines, however, show a narrow but finite thickness due to line broadening effects and simultaneous changes in the internal energy structure of the particle. If the energy of an absorbed photon exceeds the ionization energy, the transition is termed bound-free (bf) because the electron is released from the atomic structure and it can take an arbitrary amount of kinetic energy; conversely, a free-bound transition results in an emitted photon. Free electrons may interact with photons of arbitrary energies, i.e., free-free transitions (ff). All transitions involving free electrons contribute to the continuous spectrum (see, e.g., [112, sec. 1.12]). Therefore we write (see also, e.g., [11])

$$\kappa_\nu = \kappa_\nu^{bb} + \kappa_\nu^{bf} + \kappa_\nu^{ff}$$
$$= \kappa_\nu^{cont} + \kappa_\nu^{line}. \tag{7.17}$$

The spectral absorption coefficient varies with increasing tempera-
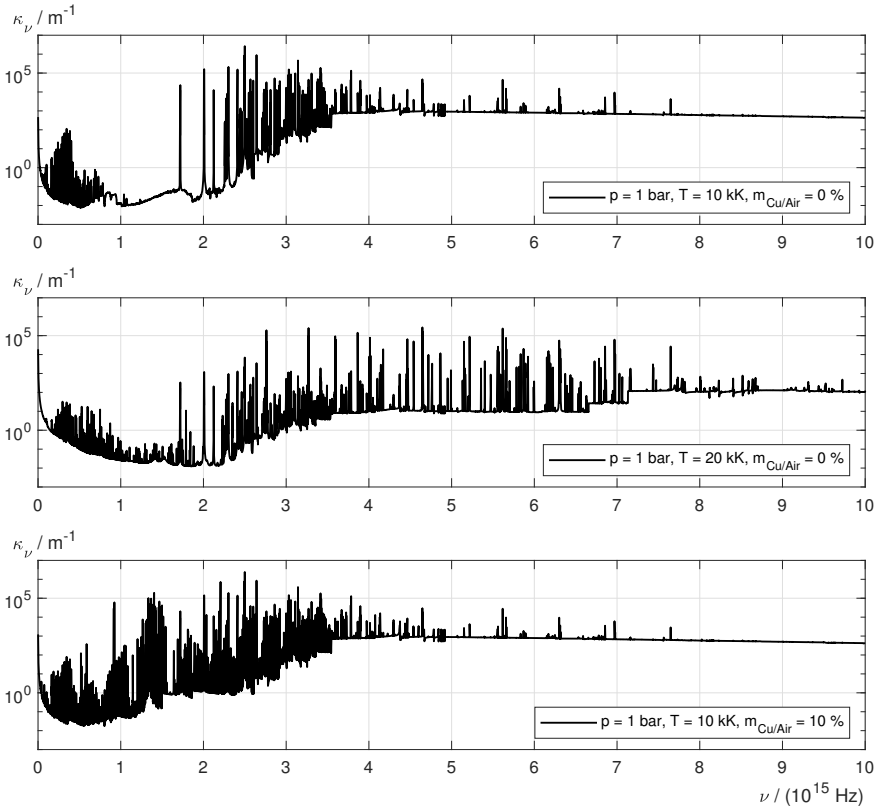
Figure 7.1.: Spectral absorption coefficient of air-copper plasma. [91]

ture: it decreases in the ultraviolet range, remains almost constant for frequencies in the near-visible range, and increases in the infrared range. [34] The addition of copper vapor significantly affects the spectral structure and results in increased net emission of the plasma. [89]

For completeness, we also mention the process of scattering which is typically observed when light passes through a particle cloud (see also, e.g., [112, sec. 1.14]). This process summarizes the effects of diffraction, reflection, and refraction that redirect radiative energy into other directions than the incoming beam. The scattering coefficient σ_s describes the fraction of radiative energy losses along a line of sight, and the scattering phase function $\Phi_s(\hat{\mathbf{s}}_i, \hat{\mathbf{s}})$ stands for the probability that an incoming ray from $\hat{\mathbf{s}}_i$ is scattered towards $\hat{\mathbf{s}}$. In arc simulations, scattering is most often neglected because is not considered as a dominant process; its absence also simplifies the radiative transfer equation substantially.

7.3. Radiative transfer equation

The radiative transfer equation (RTE) is a spectral energy balance on the radiative energy at a point $\mathbf{r}$ in direction of $\hat{\mathbf{s}}$ and within an infinitesimal solid angle $d\Omega$ at frequency ν. For a participating medium, i.e., a medium that emits, absorbs, and scatters radiative energy, it is given as [112, p. 284]

$$\frac{1}{c}\frac{\partial I_\nu}{\partial t} + \hat{\mathbf{s}}\cdot\nabla I_\nu = j_\nu - \kappa_\nu I_\nu - \sigma_{s\nu} I_\nu + \frac{\sigma_{s\nu}}{4\pi}\int_{4\pi} I_\nu(\hat{\mathbf{s}}_i)\Phi_\nu(\hat{\mathbf{s}}_i, \hat{\mathbf{s}})\,d\Omega_i, \quad (7.18)$$

with the terms on the right side being the emitted, absorbed, out-scattered, and in-scattered radiative energy flux. The inherent assumptions to this equation are that the medium is homogeneous and at rest as compared to the speed of light, nonpolarizing and its polarization state neglected, and a constant index of refraction. Nevertheless, this equation is valid at local thermodynamic equilibrium (LTE) as well as nonequilibrium.

The RTE (7.18) is an integro-differential equation for radiative intensity I_ν in seven variables (time, position, direction, and radiation frequency), its solution is a rather complex task and computationally extremely demanding. From an engineering point of view, we note that thermal radiation represents ultimately an additional energy transfer mode. In fact, it is the total net emission (or divergence of radiative heat flux) that enters the thermal energy balance of the plasma and its bounding surfaces, while a detailed solution for the spectral radiative intensity field is not an appropriate strategy.

The following assumptions are aimed at simplifying the RTE towards a tractable model. Firstly, at local thermodynamic equilibrium, the emittance must be equal to absorbance and the radiative intensity is equal to the blackbody intensity [112, eq. 11.22]; therefore the first term is replaced by $j_\nu = \kappa_\nu B_\nu$. Secondly, computational complexity is greatly simplified if scattering is neglected ($\sigma_s = 0$). This simplification is also due to practical reasons, most importantly because detailed data of scattering coefficients are hardly available for the extreme range of pressure and temperature as required for arc simulations, and validating or verifying its effect seems to be impossi-

ble. Finally, the RTE is considered in equilibrium, quasi-steady state because the speed of light is much larger than the relevant length and time scales. As a result, the RTE (7.18) simplifies to

$$\hat{\mathbf{s}} \cdot \nabla I_\nu = \kappa_\nu (B_\nu - I_\nu), \tag{7.19}$$

that is, the radiative intensity along a line of sight is augmented by emission and attenuated by absorption of the gas.

The final step towards an expression for the total radiative heat flux is to account for all directions of solid angles, and all frequencies. This immediately yields the quasi-steady RTE for a non-scattering medium [112, p. 294],

$$\nabla \cdot \mathbf{q} = \int_0^\infty \nabla \cdot \mathbf{q}_\nu \, \mathrm{d}\nu = \int_0^\infty \kappa_\nu (4\pi B_\nu - G_\nu) \, \mathrm{d}\nu, \tag{7.20}$$

which is a balance equation of radiative energy stating that the net loss of radiative energy in a control volume is equal to the difference of emitted energy and absorbed irradiation. [112, p. 287 and 292] This is also why the divergence of radiative heat flux ($\nabla \cdot \mathbf{q}$) is also known as *net emission*. Moreover, it is this term that appears in the thermal energy balance.

7.4. Exact solution of RTE

Exact analytical solutions of the RTE exist only for the simplest situations [112, p. 299], such as for gray media in a one-dimensional

domain. For instance, it can be shown that the net emission at a point $\mathbf{r}_0$, may be written as

$$\nabla \cdot \mathbf{q}_\nu = -\kappa_\nu \int_{4\pi} \int_0^\infty \frac{\mathrm{d}B_\nu}{\mathrm{d}l} \exp\left(-\int_0^l \kappa_\nu(l') \, \mathrm{d}l'\right) \mathrm{d}l \, \mathrm{d}\Omega, \quad (7.21)$$

neglecting contributions from the wall (see, e.g., [119]). Here, l is a parametrization of for the position $\mathbf{r}(l) = \mathbf{r}_0 - l\hat{\mathbf{s}}$ on a straight path in direction of incident radiation. Equation (7.21) shows clearly that the net emission is not a local quantity but rather depends on the temperature distribution within a domain size $1/\kappa_\nu$; this length scale defines the spatial discretization required for an accurate solution of the RTE. [119]

An exact integration may be performed numerically for a wall-stabilized arc defined in an infinitely long cylinder (see [119, Appendix A]). The temperature profile $T(r)$ is given with respect to radius r. Let the directional vector be given in spherical coordinates, i.e.,

$$\hat{\mathbf{s}} = \begin{bmatrix} \cos(\varphi)\sin(\theta) \\ \sin(\varphi)\sin(\theta) \\ \cos(\theta) \end{bmatrix}. \quad (7.22)$$

The simple setup allows for using symmetries so that spherical integration is reduced to $(\varphi, \theta) \in [0, \pi] \times [0, \frac{\pi}{2}]$. The observation point is taken on the x-axis. Any point P in the cross section plane may be
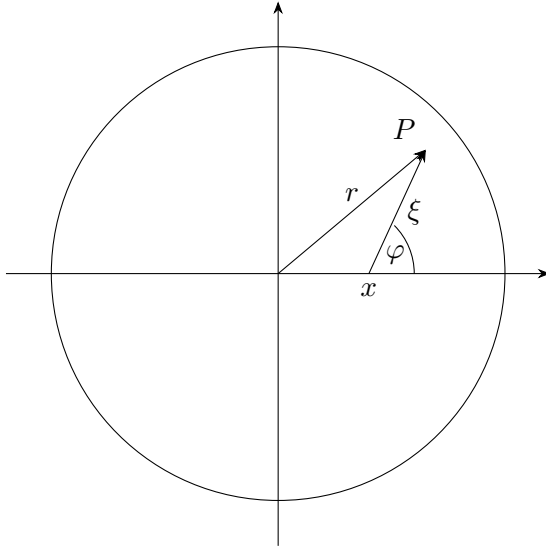
Figure 7.2.: Sketch of geometric definitions for exact solution of net emission in an infinitely long cylinder in its cross section. See also [119] for the method.

described as (see also figure 7.2)

$$P = \begin{bmatrix} x \\ 0 \end{bmatrix} + \xi \begin{bmatrix} \cos(\varphi) \\ \sin(\varphi) \end{bmatrix}, \tag{7.23}$$

where ξ is the distance from observation point $(x, 0)$ to P. The radial distance of P from the cylinder axis is found as

$$r(\xi, \varphi) = \sqrt{x^2 + 2x\xi \cos(\varphi) + \xi^2}, \tag{7.24}$$

from which it immediately follows an expression for the distance ξ to the observation point,

$$\xi = -x\cos(\varphi) \pm \sqrt{r^2 - (x\sin(\varphi))^2}. \tag{7.25}$$

Finally, one notes that ξ is the distance of the emissive source point in 3D projected to the cross section plane, and one finds $\xi = l\sin(\theta)$ with l as the axial cylinder length. Rearranging the integrals one finds the net emission at observation point x as

$$(\nabla \cdot \mathbf{q})(x)$$
$$= -\int_0^\pi \int_0^\infty \kappa_\nu(x) \int_0^\infty \frac{\mathrm{d}B_\nu}{\mathrm{d}\xi} G_\theta \left(\int_0^\xi \kappa_\nu(\xi')\,\mathrm{d}\xi' \right)\,\mathrm{d}\xi\,\mathrm{d}\nu\,\mathrm{d}\varphi \tag{7.26}$$

with

$$G_\theta(\zeta) = 4\int_0^{\pi/2} \sin(\theta)\exp(-\zeta/\sin(\theta))\,\mathrm{d}\theta. \tag{7.27}$$

The factor 4 is due to the symmetries. The function G_θ is computed in advance and stored as a table. The integrals over φ, ν, and ξ are computed with adaptive integration routines. [119]

7.5. RTE complexity reduction

Solving for the radiative heat flux or the net emission requires, in principle and naively, to find the irradiation which in turn is given by the radiative intensity, which is only obtained by solving the RTE. However, the large parameter space does not allow to find an ex-

plicit or exact solution in all but the simplest situations. Despite
that such idealized cases may serve as a useful reference, applied en-
gineering tasks require approximate models that are applicable in a
more general context and that allow for trading computational costs
with accuracy.

The problem complexity is discussed along three categories [112,
p. 299], followed by a list of solution methods.

- Most objects of interest are of three-dimensional shape and have
  geometric details that are relevant for their functionality. Al-
  though symmetry conditions may be defined to help reducing
  computational efforts, it is often only for fundamental studies
  that allow for a two- or one-dimensional model.

  Directionally-averaging methods (see section 7.6) eliminate the
  directional variable; geometric information is retained.

- The absorption coefficient κ and other radiative properties strongly
  depend on radiative frequency, temperature, gas composition,
  and other parameters. Therefore, the RTE should be solved in
  principle for each frequency value at which the spectral data is
  available; however, limitations on computer power often allow
  only for a few – typically less than a dozen – evaluations in the
  frequency domain even for directionally-approximating models.

  This situation is resolved by sampling the spectral domain and
  define intervals or frequency bands with band-averaged quan-
  tities, see section 7.7. Band-averaged *mean absorption coeffi-
  cients* are discussed in section 7.8. The limiting case of a single

spectral interval, i.e., a *gray* medium with globally averaged radiative properties, leads seldom to acceptable results because it is not capable to reflect the effects of the detailed processes in radiative heat transfer.

- The third category is a modeling aspect: the net emission and/or radiative heat flux is often studied with artificial fixed temperature profiles (see, e.g., [89, 137, 71, 109]). Despite its simplicity and being useful for fundamental studies, this situation does not correspond to a system in thermal equilibrium and makes it hard to compare with experimental results.

We therefore suggest to augment such studies with a numerical solution that is found at the system's thermal equilibrium. For instance, the experimental setup of wall-stabilized arcs corresponds to solving the Elenbaas-Heller equation (see eq. (8.1)) iteratively including the radiative thermal losses (see, e.g., [103, 10, 67]). Drawbacks are that additional parameters must be included (e.g., thermal conductivity) and increased computational costs.

7.6. Directionally-approximating methods

We mention the P_1 and DOM methods as they are widely available in software packages and used in electric arcs simulations. We stress that these models simplify on the directional coordinate $\hat{s}$ and they lead to additional transport equations to be solved for. They are

formulated on a spectral level; however, they should only be applied after averaging in the spectral domain and substituting the spectral absorption coefficient κ_ν with band-averaged mean absorption coefficients (see section 7.8).

7.6.1. Spherical Harmonics Method (P-N model)

The spherical harmonics method or P_N model is a popular method that is widely available in numerical simulation packages. The model stems from reducing the problem complexity of the RTE (7.19) in the directional variable $\hat{\mathbf{s}}$ (see, e.g., [112, ch. 16]): the radiative intensity $I_\nu(\mathbf{r}, \hat{\mathbf{s}})$ is expanded into a Fourier series using spherical harmonics, i.e., functions defined on the unit sphere that are orthogonal and satisfy Laplace's equation in spherical coordinates. The series is truncated retaining terms up to N-th order, which yields the name of the method. In first order approximation one finds

$$I_\nu(\mathbf{r}, \hat{\mathbf{s}}) \approx \frac{1}{4\pi} G_\nu(\mathbf{r}) + \frac{3}{4\pi} \hat{\mathbf{s}} \cdot \mathbf{q}_\nu(\mathbf{r}); \qquad (7.28)$$

substituting this expression into the RTE and taking moments of $\hat{\mathbf{s}}$ shows that the radiative heat flux may be written as

$$\mathbf{q}_\nu = \frac{-1}{3\kappa_\nu} \nabla G_\nu, \qquad (7.29)$$

which yields the defining P_1 model equation:

$$\nabla \cdot \left(\frac{-1}{3\kappa_\nu} \nabla G_\nu \right) + \kappa_\nu G_\nu = 4\pi \kappa_\nu B_\nu. \qquad (7.30)$$

Hence, the RTE is transformed into a substantially simpler elliptic partial differential equation of Helmholtz type for the irradiance G_ν. It requires a boundary condition specified everywhere on the enclosure boundary. The Marshak boundary condition defines that the normal component of radiative heat flux is a continuous function at the interface and satisfied in an integral sense. The condition is given by

$$\hat{\mathbf{n}} \cdot \nabla G_\nu + \frac{1}{2} \frac{\varepsilon_w}{2 - \varepsilon_w} 3\kappa_\nu (4\pi B_\nu - G_\nu) = 0, \qquad (7.31)$$

where ε_w is the boundary surface emittance, and $\hat{\mathbf{n}}$ is the wall surface unit normal vector pointing into the radiatively participating medium. This equation is valid for an opaque surface that emits and reflects radiation diffusely. For a blackbody one has $\varepsilon_w = 1$.

The P_1 approximation is widely used in radiation modeling because it allows for non-black surfaces and non-constant radiative properties. Another advantage lies in the fact that energy conservation is inherently ensured. However, it falls short in optically thin media with strongly directionally dependent (i.e., anisotropic) intensity distributions, and/or when surface emission dominates over medium emission. Higher orders of the P_N model are available but seldom used in the arc simulation community. [112]

7.6.2. Discrete Ordinate Method

The discrete ordinate method (DO, or DOM), or S_N approximation, is together with the P_1 approximation the most popular method for calculating radiative heat transfer. [112, ch. 17] Similarly to the P_1

model, the discrete ordinate method is based on a discrete representation of the directional variable $\hat{\mathbf{s}}$ of radiative intensity $I_\nu(\mathbf{r}, \hat{\mathbf{s}})$; here, the solid angle is discretized with a finite number of directions to approximate its integral,

$$\int_{4\pi} I_\nu(\mathbf{r}, \hat{\mathbf{s}}) \, \mathrm{d}\Omega \approx \sum_{i=1}^{n} w_i I_\nu(\mathbf{r}, \hat{\mathbf{s}}_i), \tag{7.32}$$

where w_i are the quadrature weights. The discretization is usually based on finite differences but also finite volumes have been used (see, e.g., [112]). The selection of directions $\hat{\mathbf{s}}_i$ is arbitrary, in principle, but there is a desire to preserve symmetry, i.e., the directions should be invariant after any rotation of 90°, and that the directions and weights should satisfy the zeroth, first, and second moments. The number N refers to the number of different direction cosines for each principal direction, resulting in $n = N(N + 2)$ discretization directions. [112] Increasing the number of direction cosines yields a finer resolution, at the cost of computing power and memory requirements; typically $N = 4$ is used in 3D simulations. [119]

A comparison of the discrete ordinate method, implemented with the finite volume method, and P_1 model shows that the DOM provides better results. [109] Shortcomings of the discrete ordinate method are that it is prone to ray effects and false scattering, which are due to angular and spatial discretization errors, respectively, and that it tends to converge slowly for optically thick media. [112]

7.7. Spectrally-approximating methods

The complex nature of the spectral absorption coefficient asks for approximations that drastically reduce computational costs while retaining the physical effects. We start with the limit cases of optically thin and thick media; they lay the grounds for the Planck and Rosseland mean absorption coefficients (see section 7.8). Both approximations may be applied on the full spectrum – leading to a *gray* medium – as well as separate spectral intervals, or group of intervals (see, e.g., [119]). We also mention the approximation of net emission coefficient. We also list a few other methods that were used in electric arc simulations, or that may enter into the research community in the near future.

7.7.1. Optically thin approximation

Radiative intensity is attenuated only slightly in an optically thin medium ($\tau \ll 1$), so that these media may be judged as non-participating. This category includes vacuum, monatomic and most diatomic gases including air, at low temperature levels well before ionization and dissociation occurs. [112, p. 129] In this situation, radiative heat transfer is computed based on view factors, which is often known as *surface-to-surface* model in software packages. This model category is not appropriate to thermal plasma simulations.

7.7.2. Optically thick approximation

The other limiting case is found for optically thick media ($\tau \gg 1$), i.e., radiative intensity is absorbed and redistributed on a short length suggesting that radiative heat transfer is a diffusive processes. In fact, one can show that the spectral radiative heat flux is given by (see, e.g., [112, p. 483])

$$\mathbf{q}_\nu = -\frac{4\pi}{3\kappa_\nu}\nabla B_\nu. \tag{7.33}$$

Since blackbody radiative intensity depends on spatial position only through temperature, we find for the total radiative heat flux

$$\mathbf{q} = -\frac{4\pi}{3}\nabla T \int_0^\infty \frac{1}{\kappa_\nu}\frac{\partial B_\nu}{\partial T}\,\mathrm{d}\nu. \tag{7.34}$$

With the definition of *Rosseland mean absorption coefficient* (see also section 7.8)

$$\frac{1}{\overline{\kappa}^R} := \frac{\displaystyle\int_0^\infty \frac{1}{\kappa_\nu}\frac{\partial B_\nu}{\partial T}\,\mathrm{d}\nu}{\displaystyle\int_0^\infty \frac{\partial B_\nu}{\partial T}\,\mathrm{d}\nu}, \tag{7.35}$$

and noting that the denominator is equal to

$$\int_0^\infty \frac{\partial B_\nu}{\partial T}\,\mathrm{d}\nu = \frac{4\sigma}{\pi}T^3, \tag{7.36}$$

equation (7.34) may be written in the form of Fourier's law,

$$\mathbf{q} = -\lambda_R \nabla T, \quad \lambda_R = \frac{16}{3}\frac{\sigma}{\overline{\kappa}^R}T^3. \tag{7.37}$$

The factor λ_R is known as *radiative (thermal) conductivity*, and equations (7.34) and (7.37) are known as *Rosseland* or *diffusion approximation*. [141] [112, p. 483]

This method is easily implemented into software tools since the radiative conductivity may be regarded as a transport property of the material. For instance, it has also been used with a blending factor to the thermal conductivity of a plasma. (see, e.g., [118, 146])

The diffusion approximation greatly reduces computational costs, however, it is not valid at boundaries and should only be considered in optically extremely thick situations. [112]

7.7.3. Net emission coefficients

The spectral net emission $\varepsilon_{N,\nu}$ (see eq. (7.20)) of a gas can be represented by

$$\nabla \cdot \mathbf{q}_\nu = 4\pi\varepsilon_{N,\nu} = 4\pi\kappa_\nu(B_\nu - J_\nu), \quad J_\nu = \frac{1}{4\pi}G_\nu, \tag{7.38}$$

where J_ν is the average radiation intensity per unit solid angle that is absorbed. Considering an isothermal sphere of radius R, one finds that J_ν at the center of the sphere is given by [103]

$$J_\nu = B_\nu(1 - \exp(-\kappa_\nu R)). \tag{7.39}$$

The net emission coefficient ε_N is then found to be

$$\varepsilon_N = \int_0^\infty \kappa_\nu B_\nu \exp(-\kappa_\nu R)\,\mathrm{d}\nu, \tag{7.40}$$

and represents the amount of radiative power per unit volume and unit solid angle that escapes from the point of interest after penetrating through a sphere of radius R. That is, specifying $R = 0$ neglects self-absorption and maximizes net emission.

If the radius of the sphere R is appropriately chosen, this method allows for a good approximation of the radiative losses in an arc plasma. The main advantage lies in the fact that it accounts for the spectral nature of the absorption coefficient. Another positive aspect is that the net emission coefficient can be computed and tabulated in advance, so that its computational costs are remarkably low for engineering applications. It is therefore widely used in electric arc simulations [67], but it also serves useful in comparing modeling aspects of radiative properties (see, e.g. [11, 23]). A drawback of using net emission coefficients is that it fails in regions of steep temperature gradients, which are typically found in the arc fringes. Moreover, it is a local model that does not account for radiative heat flux originating from other parts of the computational domain and therefore not conservative. Finally, it does not provide an expression for radiative heat flux which is required, e.g., for modeling radiatively induced wall ablation; radiative heat flux is evaluated in chapter 15, for instance.

7.7.4. Other models

We mention a few other models for radiative heat transfer that have been used in electric arc simulations. For instance, the method of partial characteristics is described in [10, 151]. A semi-empirical model

based on net emission is found in [180]. A comparison [48] to a five-band P_1 model [51] showed that the P_1 was the most accurate with respect to measurements.

In [40], the RTE is discussed from a viewpoint that focuses on moment expansions. They present a closure based on entropy production rates and that is also valid if radiative heat transfer is in a general nonequilibrium state. The Monte Carlo method has also been used to radiative heat transfer for decades (see [112] and references therein).

A novel perspective on radiative heat transfer is given by [58]; they consider radiation as a dynamical system and apply model order reduction techniques.

7.8. Mean absorption coefficients

The P_1 model and discrete ordinate model (DOM), see section 7.6, are widely used in arc simulations because they are generally applicable, provide sufficiently good approximations of radiative heat transfer at reasonable computational costs, and the fundamental principle of energy conservation is respected. [112]

One key problem in modeling radiative heat transfer stems from the fact that the net emission (7.20) should be evaluated – in principle – for each frequency separately because of the large variations in the spectral absorption coefficient κ_ν, and the net emission is obtained by averaging over the spectral net emissions. This approach, however, becomes a computationally prohibitively expensive task since solving

those approximate models amount in additional partial differential equations for each single frequency.

This situation is resolved by pulling the averaging step onto the material data: the spectral absorption coefficient becomes a band-averaged or mean absorption coefficient with respect to a frequency interval. This leaves us with choosing an appropriate averaging method that retains the physical effects.

Let us first consider the definition of frequency bands. In mathematical terms, we are looking for a partition of the frequency domain that results in N_b bands or intervals $D_i := [\nu_i, \nu_{i+1}]$,

$$\nu_{lo} = \nu_0 < \nu_1 < \nu_2 < \ldots < \nu_{N_b-1} < \nu_{N_b} = \nu_{hi}, \qquad (7.41)$$

where the lower and upper limits are given by the spectral dataset. A sufficiently fine or problem-specific partition will yield accurate results. Unfortunately, there is no general method of defining the inner band boundaries ν_i, but physical insights into the fundamental processes provide useful hints. For instance, [137] define seven bands for a SF_6 plasma based on the shape of the absorption coefficient at typical temperature values. [142] defines six bands for an air plasma with the upper there band boundaries corresponding to ionization energy levels of atomic nitrogen (see also [34, p. 365]). In the following, band-integrated quantities are identified by their band index, for instance,

$$B_i = \int_{\nu_i}^{\nu_{i+1}} B_\nu \, d\nu. \qquad (7.42)$$

We turn now to the averaging methods. If the absorption spectrum had a constant value, all the definitions of averaging methods yielded identical mean values; the problem stems from the sharp peaks which are due to line emission (see section 7.2). Their effects on radiative heat transfer should be adequately represented in the averaging process.

Two physical limits have led to often used methods. Although both are valid in their limiting cases, neither of them is correct in general (see, e.g., [132]). Writing the band-integrated equation for net emission,

$$\int_{\nu_i}^{\nu_{i+1}} \nabla \cdot \mathbf{q}_\nu \; \mathrm{d}\nu = 4\pi \int_{\nu_i}^{\nu_{i+1}} \kappa_\nu B_\nu \; \mathrm{d}\nu + \int_{\nu_i}^{\nu_{i+1}} \kappa_\nu G_\nu \; \mathrm{d}\nu, \qquad (7.43)$$

and comparing it with band-integrated quantities for band number i,

$$\nabla \cdot \mathbf{q}_i = 4\pi\bar{\kappa}_i B_i + \bar{\kappa}_i \bar{G}_i, \qquad (7.44)$$

we see that the *Planck mean*,

$$\bar{\kappa}_i^P := \frac{\displaystyle\int_{\nu_i}^{\nu_{i+1}} \kappa_\nu B_\nu \; \mathrm{d}\nu}{\displaystyle\int_{\nu_i}^{\nu_{i+1}} B_\nu \; \mathrm{d}\nu}, \qquad (7.45)$$

yields the correct expression for thermal emission. It can be shown (see, e.g., [132]) that the Planck mean is appropriate for optically thin, emission dominated media. The second method is related to

the limiting case of radiative heat flux in optically thick media (see section 7.7.2). The band-integrated radiative heat flux is

$$\int_{\nu_i}^{\nu_{i+1}} \mathbf{q}_\nu \; d\nu = -\frac{4\pi}{3} \nabla T \int_{\nu_i}^{\nu_{i+1}} \frac{1}{\kappa_\nu} \frac{\partial B_\nu}{\partial T} \; d\nu; \qquad (7.46)$$

and we see that the *Rosseland mean*, defined as

$$\frac{1}{\bar{\kappa}_i^R} := \frac{\displaystyle\int_{\nu_i}^{\nu_{i+1}} \frac{1}{\kappa_\nu} \frac{\partial B_\nu}{\partial T} \; d\nu}{\displaystyle\int_{\nu_i}^{\nu_{i+1}} \frac{\partial B_\nu}{\partial T} \; d\nu}, \qquad (7.47)$$

provides the correct expression for the energy flux. It is clear from their definitions that the Planck mean is dominated by large values of the absorption coefficient and overestimates emission, while the Rosseland mean follows the small values and underestimates emission.

Based on these insights, another averaging method was suggested in [119] which was later referred to as *line limited Planck mean* [90, 160]. The method is motivated by the fact (see also eq. (7.21)) that the spectral emission of the peaks saturates if $1/\kappa_\nu > r_a$, with r_a being the arc radius. Therefore, [119] introduced a line limiting factor that limits the maximum peak height to $1/h$ by the definition of a *renormalized absorption coefficient*

$$\kappa_\nu^{renorm} := \frac{1}{h}(1 - \exp(-\kappa_\nu^{line} h)), \qquad (7.48)$$

and used this quantity to replace the line contributions (see eq. (7.17)).

The main shortcoming of the line limited Planck mean is that the maximum peak height h must be chosen prior to the simulation setup; the original paper suggests a value $h = 2r_a$, while [90] found that $h = 3r_a$ is optimal. Using this ansatz, optimal band boundary values were determined for air plasma [90], SF_6-Cu plasma [70], and C_4F_7N-CO_2 plasma [71], all based on the criterion that the error between the approximate and exact value of net emission should be minimized.

8. Sensitivity analysis of the temperature profile of electric arcs due to band-averaged absorption coefficients

The text of this chapter was submitted to and presented at the 21st International Conference on Gas Discharges and their Applications (GD 2016) in Nagoya, Japan. [65]

8.1. Abstract

A sensitivity analysis of electric arcs in thermal equilibrium is presented, that relates variations in the absorption coefficient to changes in the temperature profile. Even if the absorption data is given in full accuracy, further modelling steps are required to obtain a computationally tractable model; therefore uncertainties are inherently introduced to any radiation model. Our modelling approach allows to compute the temperature profile of wall-stabilized arcs based on the energy balance equation and a given number of frequency bands.

We analyse the net emission with respect to the frequency bands and radial coordinate. The results obtained are of importance in the design of procedures that determine the required number of frequency bands and their boundaries for optimal accuracy.

8.2. Introduction

Radiation represents the most important energy transfer mode in electric arcs. [67] Although the basic relations of radiative heat transfer can be stated in rather simple terms, its computational complexity does not allow for a naive implementation in computer codes in all but the simplest test cases.

Radiative emission and absorption are related to the absorption coefficient κ_ν which is the most basic material parameter. It is a strong function of the frequency (see figure 8.1) and temperature, and also depends on the gas pressure and its chemical composition. An exact calculation of the radiative intensity would require to solve a spatial 3D problem for each given value in the frequency domain, which is very time consuming.

In order to simplify the computations, many radiation models and methodologies were proposed over the years. Those include assumptions with respect to at least two questions: how detailed is the absorption coefficient to be included in the calculations, and which radiation processes are to be modelled?

The simplest radiation model is the net emission coefficient (NEC), which is determined as the net radiation in the center of an isother-
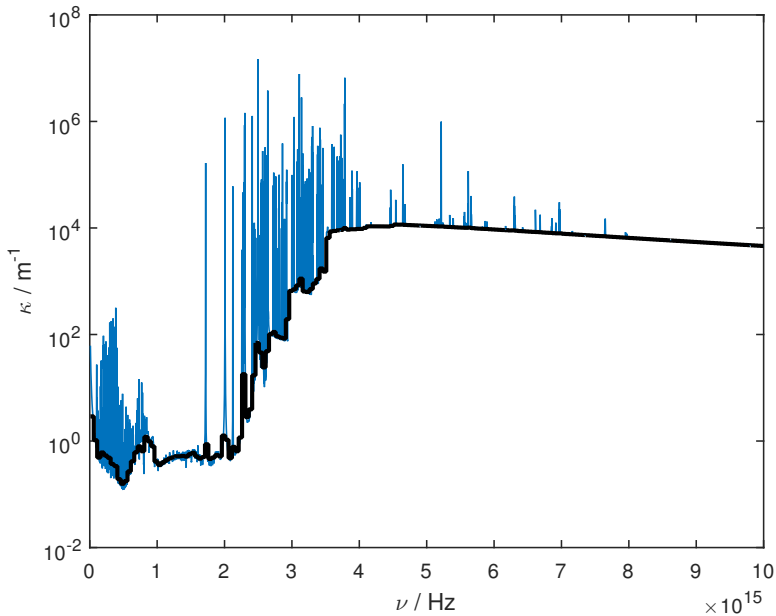
Figure 8.1.: Absorption coefficient of air at $p = 10\,\mathrm{bar}$ (courtesy of P Kloc [91]). The Rosseland average computed with a frequency interval length of $d\nu = 5 \times 10^{13}\,\mathrm{Hz}$ follows on the lower limit, as it almost discards sharp peaks.

mal sphere. [67] The NEC is tabulated as a function of temperature and a predefined plasma radius using the full absorption spectrum. Then, the tabulated values are used to determine the energy sink terms based on the local temperature. The NEC method, however, does not conserve energy. A more complex model, often being chosen by application oriented engineers, is the P1-model since it allows to account for absorption at the plasma edges and energy deposited on walls. [67] The radiative heat fluxes are computed via a diffusion-type equation using the temperature field of the computational domain. In principle the equation must be solved for each frequency separately, yielding to prohibitive computational costs for any practical application. This situation is remedied by an additional modelling step: the gas is considered as a grey body for a small number of frequency intervals (or bands), i.e. an averaged value of absorption coefficient is computed for each band.

Nordborg and Iordanidis [119] compared the net emission (i.e. the divergence of the radiative heat flux) obtained by exact integration and the P1-model with frequency bands defined via the frequency dependency of the absorption coefficient as well as its value. They reported that the main source of errors lie in errors of the raw data of the absorption coefficient as well as the averaging method applied to each frequency band. Randrianandraina, Cressault and Gleizes [137] reported in a similar study, comparing exact integration and the NEC method, that the averaging method should be chosen based on the temperature range. They also noted that radiative transfer calculations can be improved by better knowledge of the underlying physics

that yield to the absorption data. However, both of these studies used a fixed temperature profile as input data. It is more wisely to compute the temperature profile from the energy balance equation, since the radiative sink term in the energy equation is proportional to T^4 and therefore a small change in the temperature profile T is sufficient to equilibrate energy imbalances.

The aim of this paper is to provide a method that quantifies the influence of uncertainties (or modelling errors) in the absorption coefficient onto the temperature profile of electric arcs, which in turn is obtained as a solution to the energy conservation equation at a given total current. Therefore, the stationary wall-stabilized arc is considered since it is the simplest model of an electric arc. [67] The authors are not aware of any publicly available contribution addressing this research topic.

8.3. Numerical Model

A wall-stabilized arc is characterized as a cylindrical plasma column of small aspect ratio encircled by cooling plates to control the temperature at the periphery of the arc. [35] As described in [67], we further assume that the plasma is in local thermodynamic equilibrium (LTE) so that the gas pressure p and electric field E is uniform and that convection is weak enough to neglect its effect on the temperature distribution. In such a situation the temperature T depends only on the radial position r, and the energy conservation equation reduces to a stationary one-dimensional equation in radial coordinate with terms

that stand for the heat conduction, Joule heating and radiative heat losses,

$$\text{div}(-\lambda \, \text{grad}(T)) = P - \text{div}(F); \tag{8.1}$$

here, λ represents the thermal conductivity, $P = \sigma E^2$ is the Joule heating and $\text{div}(F)$ is the energy sink due to radiation, and all material data are functions of temperature.

In general, the net emission is given as

$$\text{div}(F) = \int_0^\infty \text{div}(F_\nu) \, d\nu = \int_0^\infty \kappa_\nu (4\pi B_\nu - G_\nu) \, d\nu, \tag{8.2}$$

and could be calculated in principle to arbitrary accuracy if the spectral absorption coefficient $\kappa_\nu = \kappa(\nu, T)$ is resolved fine enough. The Planck intensity is given as

$$B_\nu(T) = \frac{2h}{c^2} \frac{\nu^3}{\exp(h\nu/k_B T) - 1} \tag{8.3}$$

using standard notation, and G_ν denotes the spectral incident radiation. However, such an approach would incur excessive computational costs since the absorption coefficient is a strong function of frequency (see figure 8.1). On the other hand, the computing time can be limited by splitting the frequency domain into a small number of bands and using a constant value κ_i for the absorption coefficient in each band $i = 1, \ldots, N$ computed in advance, which is calculated by any

suitable averaging method:

$$\text{div}(F) = \sum_{i=1}^{N} \text{div}(F_i), \tag{8.4a}$$

$$\text{div}(F_i) = \kappa_i \int_{\nu_i}^{\nu_{i+1}} (4\pi B_\nu - G_\nu) \, d\nu. \tag{8.4b}$$

Often the Planck, Rosseland, or Natural average is applied (see [137] for a discussion), but also a renormalization technique [119] may be used. Anyways, the averaging induces errors and uncertainties if the absorption coefficient is not constant in the frequency band. A sensitivity analysis allows to quantify the effects on the temperature profile of the arc.

8.3.1. Sensitivity Analysis

A linear expansion of the energy conservation equation (8.1) in temperature and absorption coefficient allows to study the first-order effects of variations in the given data. This section presents the sensitivity analysis for the P1-model.

The linear increments in the heat conduction term lead to

$$\text{div}(-\lambda(T) \, \text{grad}(\delta T) - \lambda'(T)(\delta T) \, \text{grad}(T)) \tag{8.5}$$

and is denoted as $C_{th}(\delta T)$. Since the total current $I = \int_A j dA$ is kept

constant, we obtain for the Joule heating term:

$$P = \sigma E^2 = \sigma \left(\frac{I}{S}\right)^2,\qquad(8.6)$$

where $S = \int_A \sigma dA$ denotes the conductance. Therefore, the incremental Joule heating is given as

$$\delta P = (\delta T)\left(\sigma'(T) - 2\sigma(T)\frac{S'(T)}{S}\right)\frac{1}{S^2}\qquad(8.7)$$

and denoted by $\delta P = M_J(\delta T)$.

In the following we drop the subscript of the spectral variable for simplicity. For each frequency band, the linear increment in the net emission is obtained as

$$\delta F = (\delta\kappa)(4\pi B - G) + \kappa(4\pi B'(T)(\delta T) - \delta G).\qquad(8.8)$$

The P1-model assumes that the radiative flux is given by $F = \frac{-1}{3\kappa}\operatorname{grad}(G)$, so that net emission is obtained after solving the following linear equation for the radiative immission G:

$$\operatorname{div}\left(\frac{-1}{3\kappa}\operatorname{grad}(G)\right) + \kappa G = \kappa 4\pi B.\qquad(8.9)$$

Let $\mathcal{L}$ denote the linear operator on the left-hand side of the equation above. Then the incremental immission δG is related to those in κ and T via

$$\mathcal{L}(\delta G) = M_\kappa(\delta\kappa) + M_{th}(\delta T)\qquad(8.10)$$

with

$$M_\kappa(\delta\kappa) = \text{div}\left(\frac{-1}{3\kappa^2}(\delta\kappa)\,\text{grad}(G)\right) + (\delta\kappa)(4\pi B - G) \qquad (8.11)$$

and

$$M_{th}(\delta T) = \kappa 4\pi B'(\delta T). \qquad (8.12)$$

In total, the N-banded P1-model relates the linear increment in the temperature profile to the variations of the absorption coefficient in the i-th frequency band by

$$Z(\delta T) = \sum_{i=1}^{N} Y_i(\delta\kappa_i) \qquad (8.13)$$

with the linear operators

$$Z := C_{th} - M_J + \sum_{i=1}^{N} \kappa_i 4\pi B_i' - \kappa_i \mathcal{L}_i^{-1} M_{i,th} \qquad (8.14)$$

and

$$Y_i := \kappa_i \mathcal{L}_i^{-1} M_{\kappa_i} - (4\pi B_i - G_i) \qquad (8.15)$$

where the subscript i denotes the quantities with respect to the i-th frequency band.

8.3.2. Simulation conditions

We solve the energy equation for the temperature profile using the finite volume method on a uniform grid of $M = 100$ cells. The outside

wall temperature is fixed at $300\,\mathrm{K}$ at $r_{wall} = 0.1\,\mathrm{m}$; the domain was chosen arbitrary although it may be argued being atypically large. The equation is iterated by a simple relaxation method until the update in T is small.

The material data and absorption spectrum of dry air at $10\,\mathrm{bar}$ was provided by Kloc [91] in the interval $[10^{13}, 10^{16}]\mathrm{Hz}$ and a resolution of $d\nu = 2 \times 10^{10}\,\mathrm{Hz}$. The results are computed using 201 bands and an interval length of $5 \times 10^{13}\,\mathrm{Hz}$. The Rosseland average,

$$\kappa_i(T) = \frac{\int_{\nu_i}^{\nu_{i+1}} B'_\nu \, d\nu}{\int_{\nu_i}^{\nu_{i+1}} \kappa_\nu^{-1} B'_\nu \, d\nu,} \tag{8.16}$$

is applied to each frequency band for simplicity, although any other averaging method could be used; the present choice will be assessed in subsequent work.

8.4. Results

Figure 8.2 shows the temperature profiles for various total currents. We observe that the temperature profile thickens with increasing current. The S-like shape is a consequence of the energy balance and especially due to radiation. The arc center temperature corresponds to a local minimum of the thermal conductivity, and is almost constant with respect to the applied total current.

Figure 8.3 shows the average electric field as a function of the total current applied to the arc. We notice that the arc has negative differential resistivity, and the electric field decreases about 5% as the
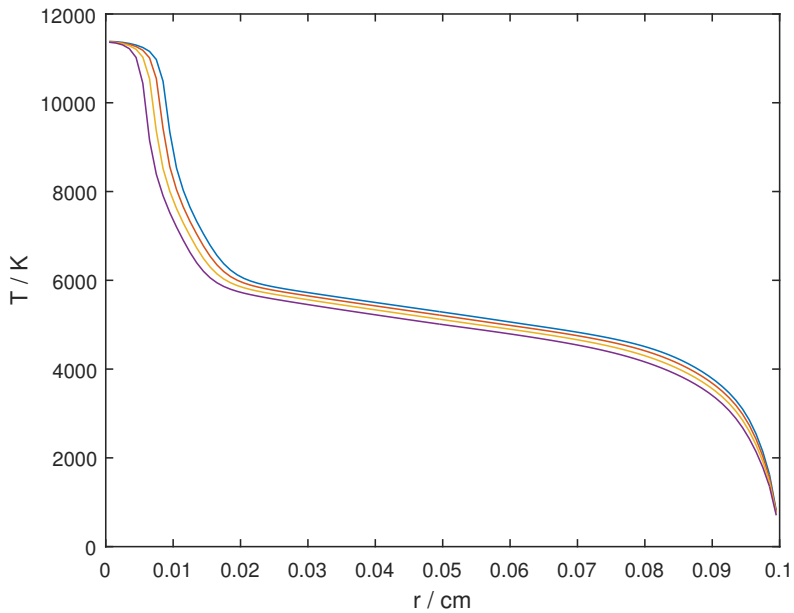
Figure 8.2.: Temperature profiles obtained by the energy conservation equation for total currents $I = 130, 170, 210, 250$A. The widest profile corresponds to the highest current.
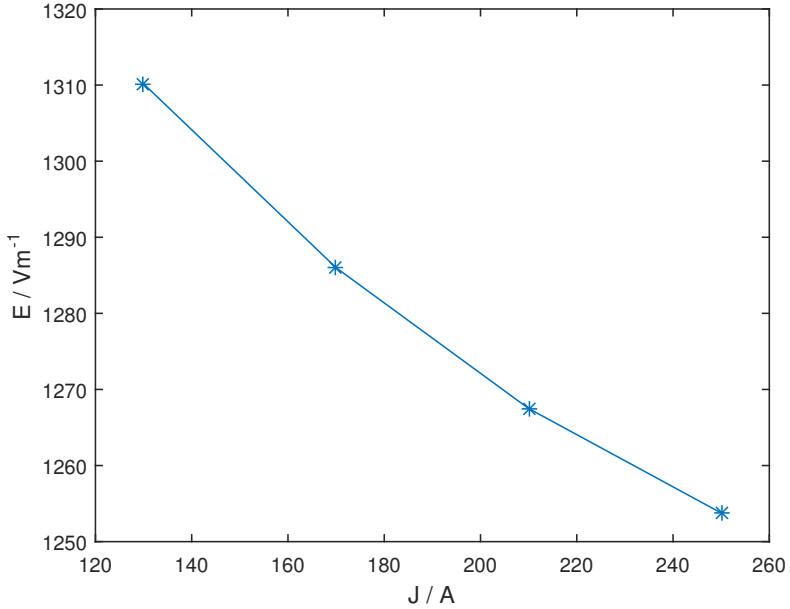
Figure 8.3.: Electrical field as a function of total current.

current is doubled.

Figure 8.4 shows the net emission as a function of the radial coordinate and the radiation frequency. On an overall view we observe that the inner, hot region ($r < 0.01$ m) emits radiative energy and is absorbed in the outer parts of the domain as indicated by the bold line. We identify two regions of interest with respect to the radiation frequency: the full domain emits radiative energy at frequencies below 1×10^{15} Hz and in a more narrow interval close to 2×10^{15} Hz

less intensively. We also note that the radiative emission is maximum in the inner region at frequencies below 1×10^{15} Hz and in an interval around 2.6×10^{15} Hz.

Figure 8.5 shows an example of a transfer matrix as obtained by the sensitivity analysis. It represents the influence of variations in the absorption coefficient of the i-th frequency band $[\nu_i, \nu_{i+1}]$ in grid cell j towards the temperature in grid cell k. We generally observe a diagonal structure of small bandwidth, i.e. the temperature profile is influenced almost only by local changes in $\kappa_i(r_j)$. In the outer region, however, the bandwidth increases and becomes asymmetric: the temperature profile is affected by changes of κ in a wider region. It is stressed that this matrix shows information on changes in the absolute value of κ (i.e. $\kappa + \delta \kappa$) and not relative values (i.e. $\kappa(1 + \delta \kappa)$).

8.5. Conclusions and Outlook

The temperature profile is calculated based on the energy conservation equation, detailed material parameters and absorption coefficient data. This allows to analyse the effective processes and relations of electric arcs in thermal equilibrium rather than starting from an artificial temperature profile. We have shown that an increasing current widens the arc while the central temperature remains almost constant. This is attributed to the equilibration process in the sense that a thicker arc leads to a larger surface area or volume which in turn allows for more radiative energy being transported to its ambient at lower temperature.
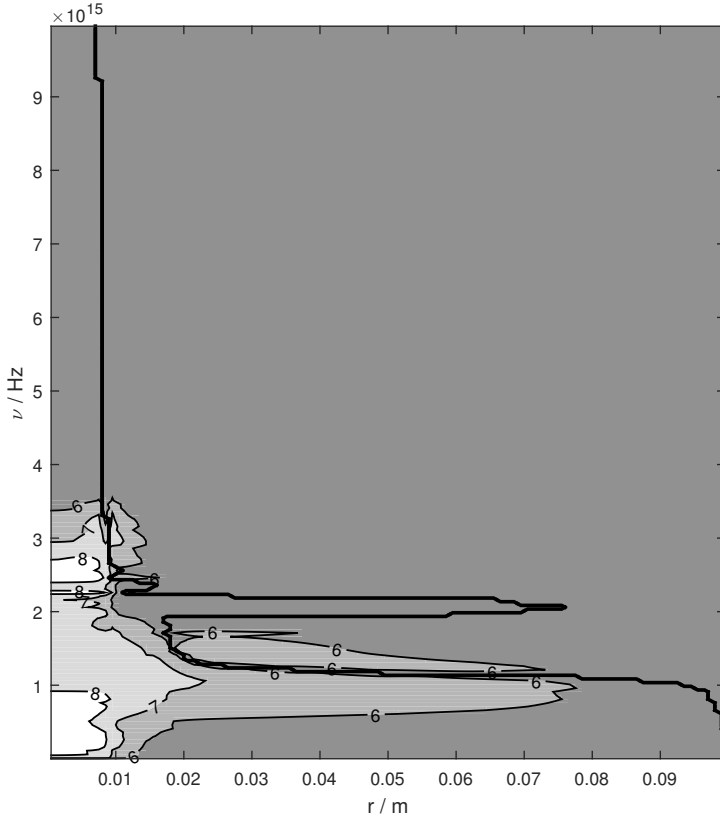
Figure 8.4.: Contour plot of the net emission in log_{10}-scale at a total current $I = 250\,\text{A}$ as a function of radial coordinate and radiation frequency. The bold line separates the regions of positive values on the left-bottom from the negative values on the upper-right part.
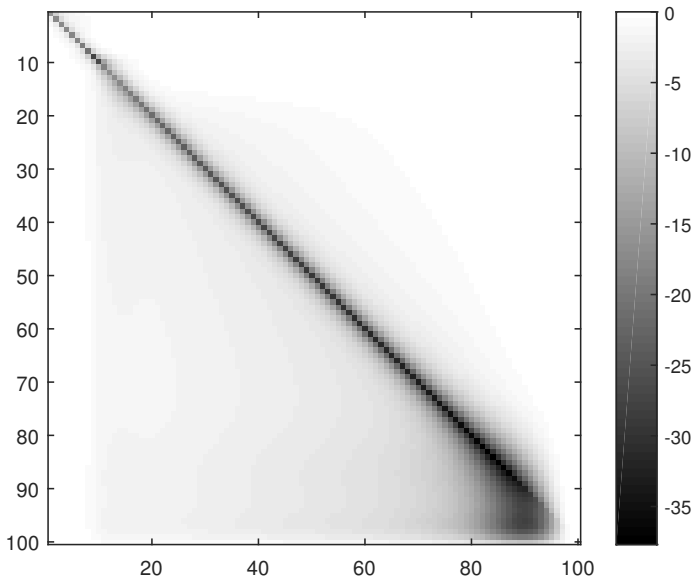
Figure 8.5.: Example of a transfer matrix $W_i = Z^{-1}Y_i$; here band number $i = 10$. The increment in temperature due to changes in the absorption coefficient is given as $\delta T = W_i(\delta\kappa_i)$, with $(\delta\kappa_i)_j = (\delta\kappa_i)(r_j)$.

We identified radiation frequencies that are important to the heat transfer process in air at elevated pressure. It is pointed out that radiation at lower frequencies are only weakly absorbed in the outer region whereas higher frequencies (here 3×10^{15} Hz) are strongly absorbed. Furthermore we also studied in detail the sensitivity of the temperature profile due to variations (or uncertainties) in the band-averaged absorption coefficient data. Despite the minimal modelling approach and neglecting other processes like chemical reactions, for instance, this model yields valuable insights for modelling radiation and choosing appropriate band models in more complex situations. It may also be a valuable source of information for choosing the frequency band boundaries more wisely.

Further work will include a comparison to exact radiation calculations in order to quantify the errors introduced in the band-averaging steps. This will allow to give advice on the appropriate averaging method as well as the choice of band boundaries. We also believe that the sensitivity analysis will be of importance in the design of automated procedures that optimize the computing time of arc simulations by trading the required number of frequency bands with modelling errors.

9. Quantifying uncertainties in mean absorption coefficients for a wall-stabilized electric arc

The text of this chapter was submitted to and presented at the the 22nd Symposium on Physics of Switching Arcs (FSO 2017) in Nove Mesto na Morave, Czech Republic. [63]

9.1. Abstract

The quality of arc simulations depends significantly on radiation modeling. Uncertainties due to physical parameters and modeling errors should be systematically quantified. We solve the energy balance equation for a wall-stabilized arc using the P1 model, i.e. without a prescribed temperature profile. We derive the linearized equation and assess the arc voltage sensitivity. This method allows us to optimize the definition of mean absorption coefficients consistently and at low computational costs.

9.2. Introduction

Electric arcs and their numerical modeling in industrial devices lead to a diverse set of questions raising many separate research topics. One of them is radiation, since electric arcs dissipate enormous amounts of thermal energy leading to elevated temperature levels. Therefore, radiation is almost always an important energy transfer mode in electric arcs.

The basic relations of radiation are given by the radiative transfer equation (RTE)

$$\hat{s} \cdot \nabla I_\nu = \kappa_\nu (B_\nu - I_\nu), \tag{9.1}$$

which is stated here for the simplest case of a non-scattering medium in local thermal equilibrium (LTE). [112] It describes the change of radiative intensity I_ν along direction $\hat{s}$ that is due to emission, described by the Planck function B_ν and given in equation (9.5) below, and absorption of the medium. Solving the RTE is computationally demanding since the radiative intensity is a function of location, direction, and frequency. The absorption coefficient κ_ν and its impact on the computational complexity of the RTE are discussed subsequently.

To meet the limited computer resources available to application engineers, the complexity of the RTE must be reduced to simpler models that account appropriately for the radiative thermal energy transport. The method of net emission coefficients (NEC) [103] is often used and has been developed to acceptable accuracy [137]. Its main advantage lies in the marginal computational costs incurred at

run time of a plasma simulation, since the radiative thermal source term is tabulated in advance.

However, evaluating the radiative heat flux on a nearby surface requires more sophisticated methods. One option is the P1 model, which is a first-order approximation of the RTE in spherical harmonics and frequently used in industrial arc simulations. This model leads to additional differential equations that are of the same structure as the conservation equations for mass, momentum, and energy.

We also have to consider the material data. The most important quantity in radiation modeling is the spectral absorption coefficient κ_ν, which depends on the radiation frequency ν, gas pressure, temperature, and gas composition. The complex structure of the absorption spectrum (see figure 9.1) is due to the atomic structure of the gas (see, e.g., [112]). It does not allow for a naive usage of this data, since an appropriate resolution of the frequency domain would lead to excessive computational costs. Despite the large variations in the value of the absorption coefficient, the frequency domain is split into a small number of intervals or bands and mean absorption coefficients (MAC) are computed for each of them. Since each frequency band acts as a gray body, this approach is termed as the multi-banded gray P1 model.

The main problem of the averaging step is how the absorption lines shall be treated that span over multiple orders of magnitudes. Classically, the Planck and Rosseland average are considered which are weighted averages of κ_ν and κ_ν^{-1}, respectively. The former is dominated by the peak values of the absorption lines while the latter al-
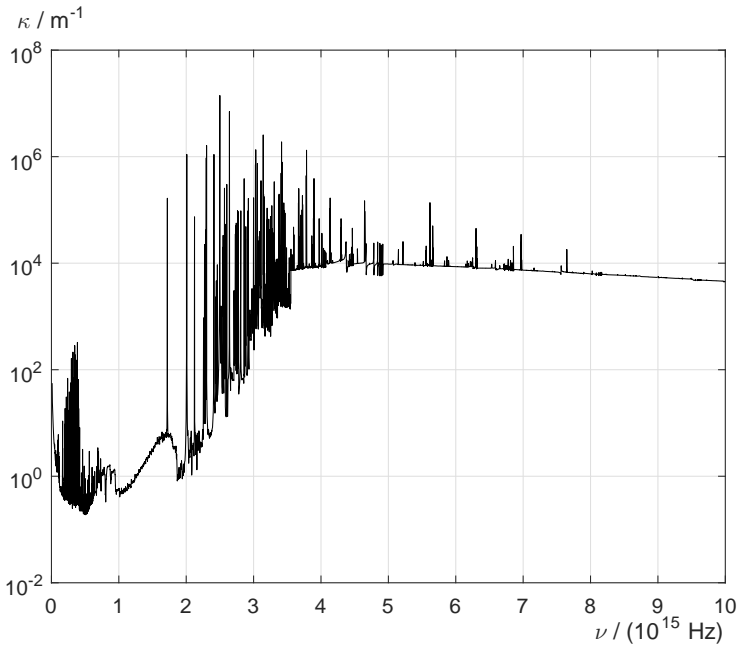
Figure 9.1.: Absorption spectrum of air at $T = 10\,\text{kK}$. [89]

most ignores them. It is clear that the MAC depend on the definition of the frequency band boundaries that are often chosen heuristically.

The raw data itself comes with uncertainties that affect the MAC values and propagate to the final results. Their sensitivities can be quantified by running simulations repeatedly with slightly edited input data, but comes with major computational costs. For small changes in the MAC, however, we will show that the same information can be obtained much quicker by deriving the linearized equations and solving for the first-order effects on the temperature profile and the quantities depending on it. Such modeling errors are often studied using a fixed temperature profile. From a physical point of view it makes more sense to solve the energy conservation equation, since any change in the radiation model results in an updated temperature field and, consequently, other quantities such as arc voltage.

In this paper, we quantify modeling errors in the mean absorption coefficient that are due to the averaging procedure or inherent to the raw data itself. We iteratively solve the energy balance equation for a wall-stabilized arc to ensure energy conservation. Ultimately, we present the linearized equations as a validated and computationally efficient methodology to determine first-order effects on the arc voltage.

9.3. Model

9.3.1. Energy conservation equation

We consider a wall-stabilized arc, i.e. a cylindrical plasma column of radius R, large aspect ratio, and a fixed wall temperature. Moreover, we assume that the plasma is in local thermal equilibrium (LTE) so that the pressure p and electric field E are constant across the plasma column. Further, convective heat transfer is considered weak enough to be negligible. This results in a temperature profile $T(r)$ that only depends on the arc radius r. In this case, the energy conservation equation consists of heat conduction, Ohmic heating, and a radiative heat sink U,

$$\operatorname{div}(-\lambda \operatorname{grad}(T)) = \sigma E^2 + U; \tag{9.2}$$

here, $\lambda(T)$ and $\sigma(T)$ denote the thermal and electrical conductivities. The electric field is given as the ratio of electric current I to the plasma conductivity $S[T]$, which is a functional of the temperature profile:

$$E = \frac{I}{S[T]}, \quad S[T] = \int_0^R \sigma(T(r)) r \, \mathrm{d}r. \tag{9.3}$$

In this model, we consider the current as a constant.

The radiative heat sink U is given by the divergence of the total radiative heat flux. We use the multi-banded gray P1 model to account for radiative heat transfer. Hence, we split the spectral domain

into a finite number of intervals $D_i = [\nu_{i-1}, \nu_i]$. The mean absorption coefficients $\kappa_i = \langle \kappa \rangle_i$ are obtained using the Planck and Rosseland average

$$\langle \kappa \rangle_i^{Pl} = \frac{\int_{D_i} B_\nu \kappa_\nu \mathrm{d}\nu}{\int_{D_i} B_\nu \mathrm{d}\nu}, \quad \langle \kappa \rangle_i^{Ro} = \frac{\int_{D_i} B_\nu' \mathrm{d}\nu}{\int_{D_i} B_\nu' \kappa_\nu^{-1} \mathrm{d}\nu}, \tag{9.4}$$

respectively. Therein, $B_\nu(T)$ denotes the Planck function

$$B_\nu(T) = \frac{2h}{c^2} \frac{\nu^3}{\exp(\frac{h\nu}{k_B T}) - 1}, \tag{9.5}$$

B_ν' is its derivative with respect to temperature, c denotes the speed of light in vacuum, and h, k_B are the Planck and Boltzmann constants, respectively. The P1 model approximation results in an expression relating the radiative heat flux $\vec{F}_\nu$ and the irradiation function G_ν by:

$$\vec{F}_\nu = \frac{-1}{3\kappa_\nu} \operatorname{grad}(G_\nu). \tag{9.6}$$

This also holds for band-averaged quantities, so that G_i is obtained as the solution of the linear problem

$$\mathcal{L}_i(G_i) := \operatorname{div}\left(\frac{-1}{3\kappa_i} \operatorname{grad}(G_i)\right) + \kappa_i(G_i) = \kappa_i 4\pi B_i(T) \tag{9.7}$$

with $B_i(T)$ denoting the band-integrated Planck function. The radiative heat sink is then given by

$$U = (-1) \sum_i \kappa_i (4\pi B_i(T) - G_i), \qquad (9.8)$$

which follows from the RTE (9.1) by integration over the solid angle.

9.3.2. Linearized equation

Equations (9.2) and (9.8) show that any change in the absorption coefficient results in changes to the temperature profile. For small variations, we can derive the linearized energy conservation equation with respect to increments in the MAC ($\delta\kappa_i$) and temperature (δT). This first-order expansion provides a relation which we write as

$$C_{th}(\delta T) - M_I(\delta T) = \delta U, \qquad (9.9)$$

with $\delta U = \delta U(\delta\kappa_i, \delta T)$ summarizing the linear effects in the radiation model. The details are derived in the remainder of this section.

The linearized heat conduction is given by

$$C_{th}(\delta T) = \mathrm{div}\left(-\lambda(T)\,\mathrm{grad}(\delta T)\right) - \mathrm{div}\left(\lambda'(T)\,\mathrm{grad}(T)\delta T\right), \quad (9.10)$$

with $\lambda'(T) = \frac{\mathrm{d}}{\mathrm{d}T}\lambda(T)$. The linearized Ohmic heating at constant current results in

$$M_I(\delta T) = \left(\sigma'(T) - 2\frac{\sigma(T)}{S[T]}\frac{\delta S[T]}{\delta T(r)}\right)\frac{I^2}{S[T]^2}\delta T \qquad (9.11)$$

where $\frac{\delta S[T]}{\delta T(r)}$ represents the functional derivative of the conductivity, $\sigma'(T) = \frac{\mathrm{d}}{\mathrm{d}T}\sigma(T)$, and the radiative heat sink increment is expanded to

$$\delta U = (-1)\sum_i (4\pi B_i(T) - G_i)\delta\kappa_i + \kappa_i(4\pi B_i'(T)\delta T - \delta G_i). \quad (9.12)$$

The linear increment in the irradiation function δG_i is obtained as the solution of

$$\delta G_i = \mathcal{L}_i^{-1}(M_{\kappa,i}\delta\kappa_i + M_{th,i}\delta T) \qquad (9.13)$$

with

$$M_{\kappa,i}(\delta\kappa_i) = \mathrm{div}\left(\frac{-1}{3\kappa_i^2}\,\mathrm{grad}(G_i)\delta\kappa_i\right) + (4\pi B_i(T) - G_i)\delta\kappa_i, \quad (9.14\text{a})$$

$$M_{th,i}(\delta T) = \kappa_i 4\pi B_i'(T)\delta T. \qquad (9.14\text{b})$$

In summary, the terms can be rearranged so that the increment in the temperature profile is given as a linear function of those in the MACs,

$$\delta T = Z^{-1}\sum_i Y_i \delta\kappa_i, \qquad (9.15)$$

with Z and Y being linear operators given by

$$Z := C_{th} - M_I + \sum_i \kappa_i 4\pi B_i'(T) - \kappa_i \mathcal{L}_i^{-1} M_{th,i}, \qquad (9.16a)$$

$$Y_i := \kappa_i \mathcal{L}_i^{-1} M_{th,i} - (4\pi B_i(T) - G_i). \qquad (9.16b)$$

Finally, we find an expression for the linear increment in the electric field with respect to a temperature increment:

$$\delta E = (-1) \frac{I}{S^2[T]} \frac{\delta S[T]}{\delta T(r)} \delta T. \qquad (9.17)$$

9.3.3. Simulation conditions

We use a domain radius of $R = 5\,\mathrm{mm}$ discretized with 200 cells and cell-centered quantities. The wall temperature is fixed at $300\,\mathrm{K}$. The energy conservation equation (9.2) is iteratively solved using a relaxation update with a constant current of $I = 50\,\mathrm{A}$ until the maximal temperature update is smaller than $1\,\mathrm{K}$.

The radiation frequency bands are defined as N uniformly spaced intervals $D_i = [\nu_{i-1}, \nu_i]$, $i = 1, \ldots, N$, with $\nu_0 = 1 \times 10^{10}\,\mathrm{Hz}$ and $\nu_N = 6 \times 10^{15}\,\mathrm{Hz}$. An additional frequency band is defined $D_{N+1} = [\nu_N, 1 \times 10^{16}\,\mathrm{Hz}]$. Material data and spectral absorption coefficients are taken for air at $p = 10\,\mathrm{bar}$. [89]
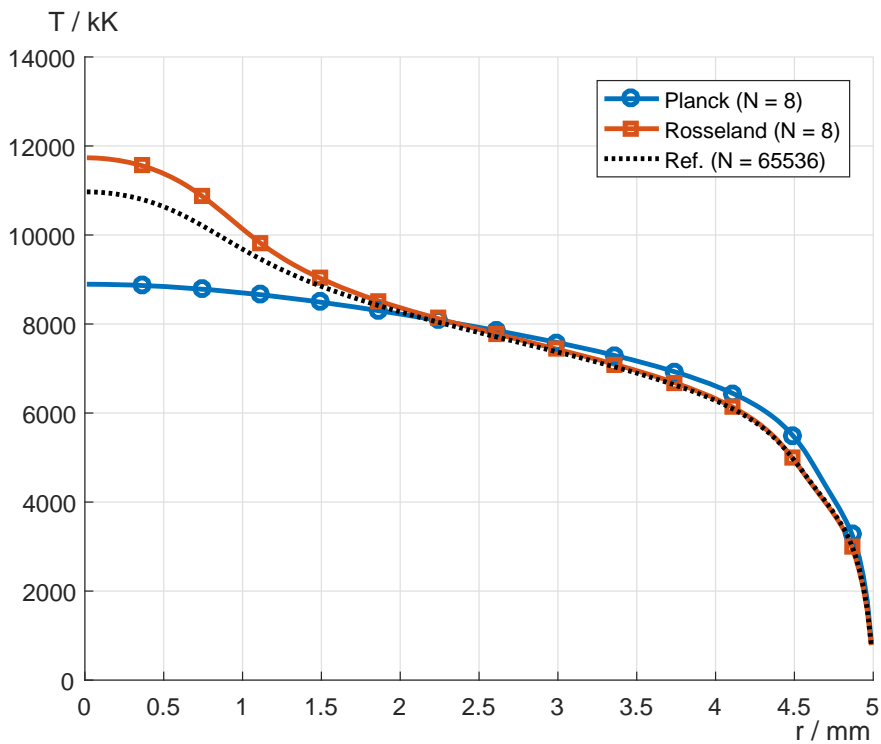
Figure 9.2.: Temperature profiles at 50 A total current.

9.4. Results and Discussion

Figure 9.2 shows temperature profiles of the wall-stabilized arc obtained with Planck and Rosseland average using 8 bands. We also plot the reference solution with $N = 65536$ bands, which shows an arc center temperature of $10\,970\,\mathrm{K}$ and a noticeable core region with a higher temperature gradient than in the outer parts. Near the wall, the temperature drops quickly to the prescribed wall temperature. In comparison to this, the Rosseland average leads to a more pronounced core region with a higher arc center temperature but qualitatively similar temperature profile. In contrast, the Planck average shows a diffusive temperature profile with an arc center temperature much lower than the reference solution, and a sightly increased temperature in the outer parts. These differences disappear gradually with finer spectral resolutions and the temperature profiles converge to the reference solution.

This data is explained by the properties of the averaging methods. Since the Planck average is dominated by the peak values of the absorption lines, it resembles an optically thick plasma, and the radiative heat transfer has the same effect as an increased thermal conductivity. On the other hand, the Rosseland average yields an optically thin material and radiative energy is transported to the walls.

Figure 9.3 shows the electric field in variation of the spectral resolution and for several arc currents. We see that, at low spectral resolutions, the Planck average yields a higher electric field than the Rosseland average. This is due to the lower temperature levels and
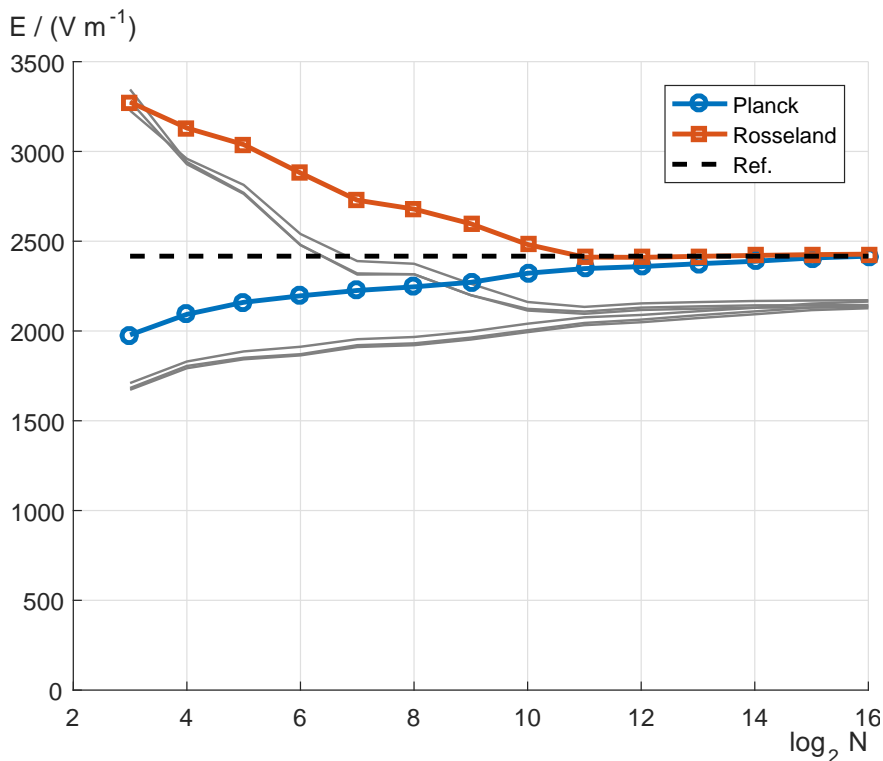
Figure 9.3.: Electric field at 50 A total current as a function of spectral resolution. The reference value is taken for the finest spectral resolution. Gray lines: 100, 150, and 200 A.

lower electrical conductivity. We also note that the curves converge to the reference solution, with the Planck average being rather constant for spectral resolutions $N > 2^{10}$. This figure shows that accurate results are only obtained with a finely resolved absorption spectrum.

We now turn to the question, which parts of the spectrum are most significant. Figures 9.4 and 9.5 show the relative sensitivity of the electric field obtained by the linearized equation for the two averaging methods. We used an uncertainty of 1% in the MAC for each band individually. The same data is also obtained with direct computations for $N \leq 256$, i.e. editing the MAC values and running the simulation until convergence, but at much higher computational costs. The results coincide almost exactly and validate the linearized method. Only minor differences are noted for the solution using $N = 8$ bands and Rosseland average: however, they are at higher radiation frequencies where the sensitivities are orders of magnitudes lower and therefore negligible. This method has also been applied to finely resolved spectral data with drastically reduced computational effort.

The sensitivity of the electric field is limited by 1‰ for the 8-banded solution. The sensitivity curves scale with the interval length; in fact, considering the relative sensitivity of the electric field per interval length, i.e. $\Delta E/(E_{ref}\Delta\nu)$, results in a characteristic curve. We also see that a higher number of spectral bands allows to resolve the sensitivities of the absorption lines. The sensitivity curve of a finer resolved solution is bounded almost everywhere by the coarser ones. The Planck average yields notable lower sensitivities at frequencies above $2.5 \times 10^{15}\,\mathrm{Hz}$ and band resolutions $N \leq 256$.
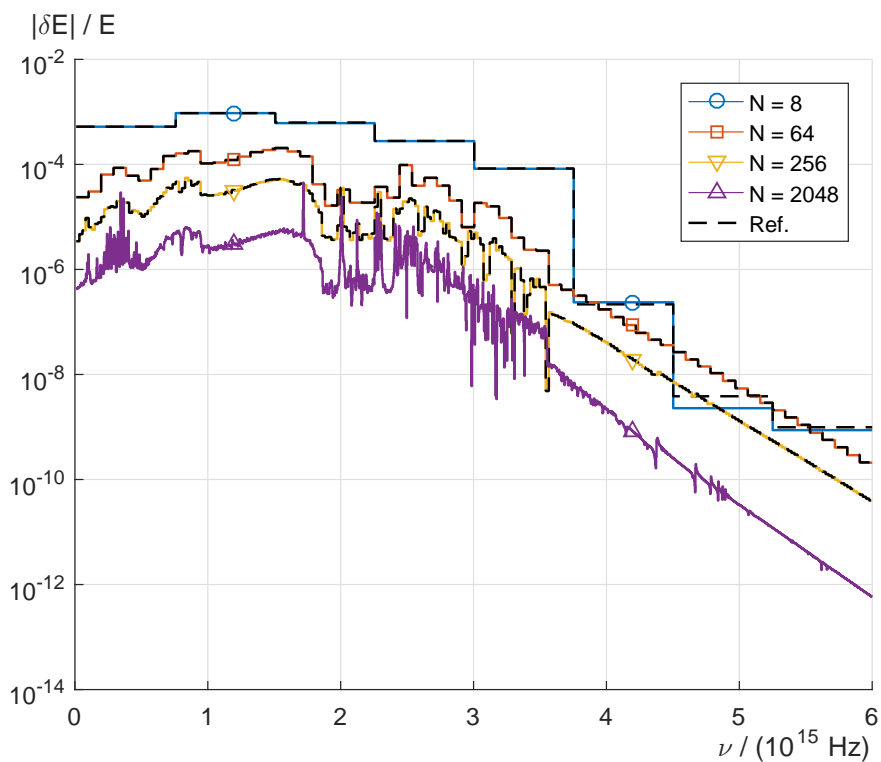
Figure 9.4.: Relative sensitivity of the electric field at 50 A using Rosseland average and uncertainty of 1%.
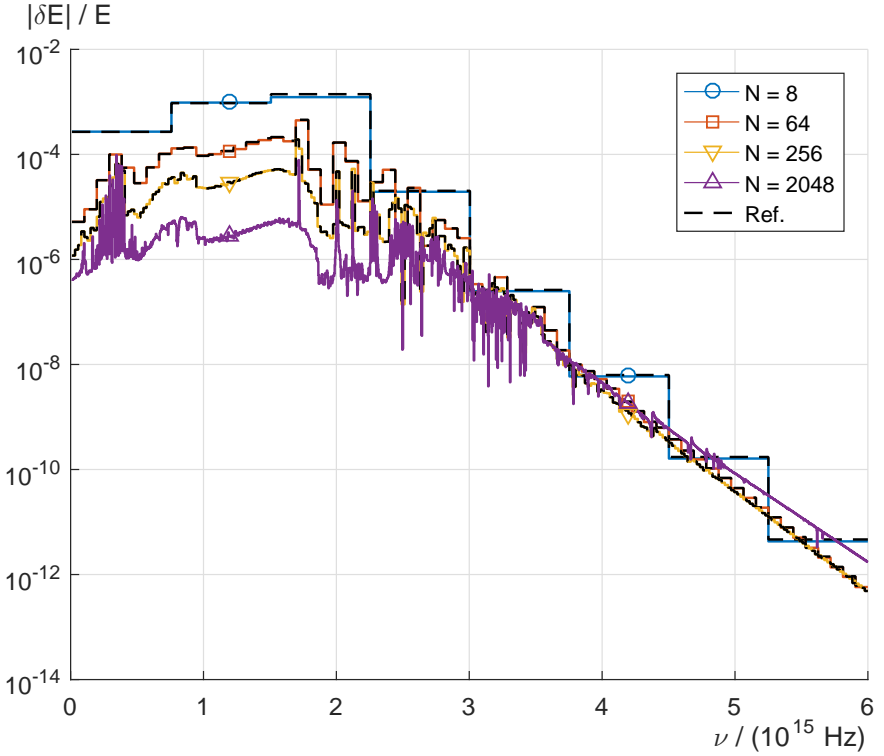
Figure 9.5.: Relative sensitivity of the electric field at $50\,\text{A}$ using Planck average and uncertainty of 1%.

9.5. Conclusions

We presented a simple model to study effects of band-averaged MACs on the temperature profile and the electric field of a wall-stabilized arc. The linearized method provides a systematic methodology to assess the sensitivity of the frequency bands at low computational costs, and helps to define MAC inside each band. Hence, frequency bands of low sensitivity can be identified and may be merged or grouped into coarser ones. For future work, the method is easily extended to non-uniform intervals. Preliminary tests with a renormalization length [119] are promising and are currently being investigated.

Acknowledgments
We gratefully thank P Kloc for providing the material data and absorption coefficients.

10. Systematic investigation on radiation modeling errors of a wall-stabilized arc simulations

The text of this chapter was submitted to and presented at the 22nd International Conference on Gas Discharges and their Applications (GD 2018) in Novi Sad, Republic of Serbia. [63]

10.1. Abstract

Radiation modeling is key for accurate numerical simulations of electric arcs. The spectral domain must be reduced to a few band- averaged quantities because of the limited computing power. We consider a wall-stabilized arc and we systematically refine the spectral domain to find an independent solution of the averaging schemes. It is shown that Planck and Rosseland averages require rather fine spectral resolutions, but accurate temperature profiles can be obtained much faster when the renormalized average is used.

10.2. Introduction

Radiation is the main energy transfer mode of electric arcs to their ambient due to the high temperatures in the arc column. In numerical simulations, radiation enters the energy balance equation as a source term, but solving for the radiative heat transfer in full details is computationally expensive, because the radiative transfer equation (RTE) is a partial differential equation in six dimensions (i.e., the geometric position, directions, and radiation frequency) and therefore only viable for the simplest geometries. For any other geometries we must rely on models that reduce the complexity of radiative heat transfer.

Approximate solutions of the RTE respecting global energy conservation may be obtained with the commonly used P1 approximation or the Discrete Ordinate Method (DOM), reducing the geometric complexity. Simplifying the spectral dimension is more involved since the absorption coefficient is the main material parameter and varies with radiation frequency in narrow peaks and over many orders of magnitude due to line emission; other parameters are temperature, pressure, and plasma composition. Although the RTE can be solved for each frequency separately, the computational resources only allow for a few representative values in the spectral domain in typical engineering tasks. Therefore, the spectral domain is split into a small set of intervals or frequency bands. Applying an averaging scheme to each of them results in band-averaged or mean absorption coefficients (MAC).

The specific choice of band boundaries and averaging schemes is an active research topic, since their specific selection influences the total radiative heat flux entering the energy balance equation. It is known that Planck average overestimates the contributions of peaks in the absorption spectrum whereas Rosseland average underestimates them. For instance, electric arcs in air were considered in [142] using six frequency bands that correspond to the ionization frequencies of nitrogen atoms and the Planck average was applied. Eleven bands and Rosseland average were used by [126]. Electric arcs in SF_6 with 7 bands were investigated in [137], and it was recommended to use Planck average for high temperatures but Natural average for low temperatures. Optimal band boundaries for a SF_6-Cu plasma were found in [70] for up to seven bands.

Another option was introduced by [119] based on physical arguments: the peaks of line emission in the spectral absorption coefficient can be limited by a characteristic absorption length that is on the scale of the plasma radius followed by Planck averaging. This method is called *renormalized average* in the following. It has been applied in [90] to find optimal values for the characteristic absorption length with three bands in air plasma, as well as optimal band boundaries. A linearized P1 model has been presented [65] that allows to quantify uncertainties in MAC and their propagation on the temperature profile and arc voltage.

The aim of this paper is to address systematically modeling errors due to spectral resolution and band-averaging schemes. For that, we

solve the self-consistent energy balance equation of a wall-stabilized arc with radiative heat transfer using the P1 model. The classical Planck and Rosseland averages as well as the renormalized average are considered. The temperature profile and arc voltage is obtained as the spectral resolution is refined, and the net emission of the P1 model is also compared to exact integration. Results are also shown for a common band frequency definition used in industrial contexts.

10.3. Method

10.3.1. Numerical model

We consider a wall-stabilized arc, i.e., a cylindrical plasma column of long aspect ratio encircled by walls fixing the temperature at its periphery, and a given electrical current I. The plasma column is considered in local thermal equilibrium (LTE), so that a uniform pressure and electric field E may be assumed and convection is weak enough to be negligible. [67] Then, the plasma state only depends on its radial position and the self-consistent energy balance equation reads

$$\operatorname{div}(-\lambda \operatorname{grad}(T)) = \sigma E^2 - \operatorname{div}(F), \qquad (10.1)$$

where λ and σ denote the thermal and electrical conductivity, respectively, $T = T(r)$ is the temperature at radial position r, and $\operatorname{div}(F)$ is the total net emission or divergence of total radiative heat flux. The electric field is obtained by Ohm's law. Generally, the spectral

net emission can be written as

$$\text{div}(F_\nu) = \int_0^\infty \kappa_\nu (4\pi B_\nu - G_\nu)\, d\nu, \qquad (10.2)$$

where $\kappa_\nu = \kappa(\nu, T)$ denotes the spectral absorption coefficient, $B_\nu(T)$ is the Planck blackbody intensity and G_ν is the spectral irradiation. The spectral absorption coefficient consists of continuum and line contributions. As proposed in [119], a characteristic absorption length h is applied to the line contributions,

$$\kappa_{\nu,line} = \frac{1}{h}(1 - \exp(-\kappa_{\nu,line}h)), \qquad (10.3)$$

so that their peaks are limited on the order of h^{-1}.

The spectral domain is split into N intervals, $D_i = [\nu_{i-1}, \nu_i]$, $i = 1, \dots, N$. Mean absorption coefficients $\bar\kappa_i$ are obtained by applying the Planck or Rosseland mean on the spectral absorption coefficient in each band:

$$\bar\kappa_i^P = \frac{\int_{D_i} \kappa_\nu B_\nu\, d\nu}{\int_{D_i} B_\nu\, d\nu}, \; \bar\kappa_i^R = \frac{\int_{D_i} \frac{dB_\nu}{dT}\, d\nu}{\int_{D_i} \kappa_\nu^{-1} \frac{dB_\nu}{dT}\, d\nu}. \qquad (10.4)$$

In the following, the index i indicates band-integrated quantities. The net emission is computed by the P1 model, which assumes that the radiative heat flux can be written as $F_i = \frac{-1}{3\bar\kappa_i} \text{grad}(G_i)$; then, the irradiation is obtained from a linear equation,

$$\text{div}\left(\frac{-1}{3\kappa_i} \text{grad}(G_i)\right) + \kappa_i G_i = \kappa_i 4\pi B_i. \qquad (10.5)$$

The simple geometric layout allows for a comparison of the net emission obtained by the P1 model and an exact solution of the RTE. The exact net emission at radial position r is given by

$$\mathrm{div}(F)(r) = (-1) \int_0^\pi \mathrm{d}\varphi \int_0^\infty \mathrm{d}\nu \, \kappa_\nu(r)$$
$$\times \int_0^{\xi_{max}} \mathrm{d}\xi \, \frac{\mathrm{d}B_\nu}{\mathrm{d}\xi} G_\theta \left(\int_0^\xi \mathrm{d}\xi' \kappa_\nu(\xi') \right) \quad (10.6)$$

where ξ parametrizes the line from position r across the arc cross-section to the domain boundary at angle φ, and G_θ is a geometric factor given by

$$G_\theta(x) = 4 \int_0^{\frac{\pi}{2}} \sin(\theta) \exp(-x/\sin(\theta)) \, \mathrm{d}\theta. \quad (10.7)$$

In (10.6), the frequency integral is taken as a discrete sum over each spectral data point, and all other integrals are calculated adaptively. The developed code is written in parallel allowing for fast results obtained for a given list of radial coordinates.

10.3.2. Simulation parameters

We solve equation (10.1) for the temperature profile on a uniform, cell-centered grid with 400 points and a total current $I = 100 \, \mathrm{A}$. The wall temperature is defined as $T_{wall} = 300 \, \mathrm{K}$ at $r_{wall} = 5 \, \mathrm{mm}$. The material data is taken at $p = 10 \, \mathrm{bar}$ absolute pressure, and the absorption coefficient is given in the range of 1×10^{13} to $1 \times 10^{16} \, \mathrm{Hz}$

spaced at 2×10^{10} Hz. [89]

Results are computed for the classical Rosseland and Planck average as well as the renormalized average. The spectral resolution is taken in powers of 2 ($N = 2^M$ with $M = 5, \ldots, 17$). Additionally, we also show results using band frequencies that correspond to ionization energies of nitrogen atoms. The inner boundaries are given at $0.066, 0.35, 1.54, 2.65, 2.94, 3.52 \times 1 \times 10^{15}$Hz. [142]

10.4. Results

Figure 10.1 shows the temperature profiles for the band definition in [142]. The reference solution is given by the finest band discretization and is visually independent of the averaging scheme. We note that the classical averages yield temperature profiles deviating significantly from the reference solution: the arc center temperature is underestimated by the Planck average while the Rosseland average yields overestimated values. In contrast, the renormalized average with $h = 2.3$ mm results in a temperature profile that is very close to the reference.

This behavior becomes more obvious in figure 10.2, which shows the arc center temperature with respect to the spectral discretization. It is seen that the Planck and Rosseland average converge with finer spectral discretization, however, they only get close for more than 1×10^3 bands. The renormalized average leads to arc center temperatures rather independent of the spectral discretization. We see that the characteristic absorption length h acts as a blending factor for
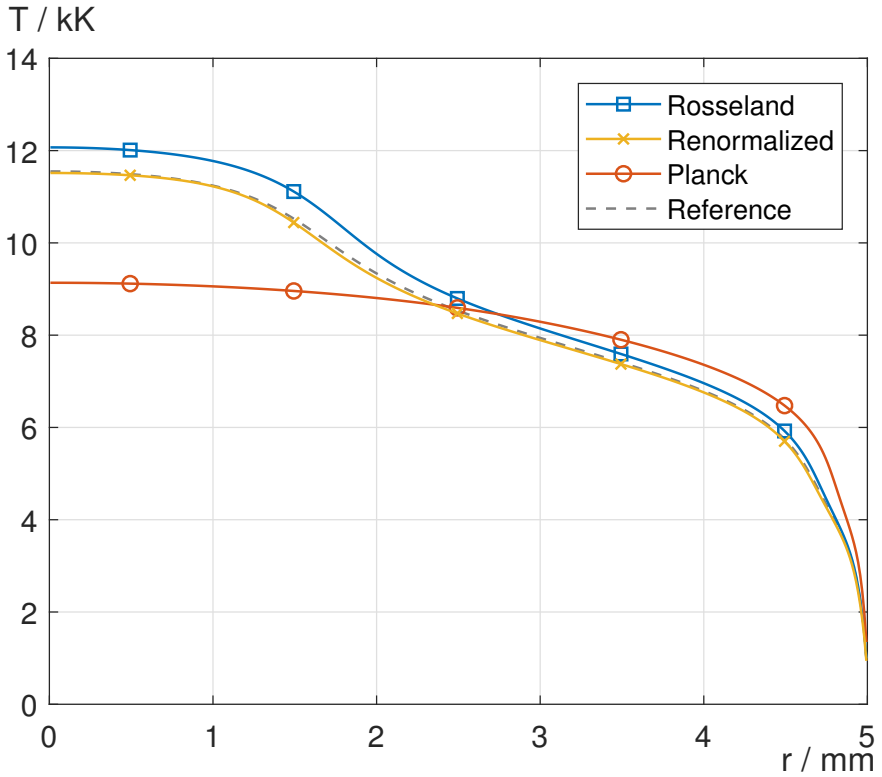
Figure 10.1.: Temperature profiles for low number of spectral bands.

the solutions obtained by the classical averages. Choosing the characteristic length appropriately ($h = 2.3\,\mathrm{mm}$) matches the reference solution rather well for any spectral resolution.

Figure 10.3 shows the electric field E with respect to spectral discretization. Similarly to figure 10.2, we see that the renormalized average is much less sensitive to spectral discretization than the Planck and Rosseland averages. For the Planck average we note a steeply increasing electric field for lower spectral resolution. This is explained by the electric conductivity: although resulting in radially wider temperature profile and higher temperatures in the outer parts, it cannot counterbalance the smaller electrical conductivity in the central region.

Figure 10.4 shows the net emissions of exact integration and the P1 model of the temperature profile obtained with the renormalized average with $h = 2.3\,\mathrm{mm}$ and the band boundaries in [142]. The graphs are qualitatively comparable with large net emission in the arc center, a flatter intermediate section, and an outer section with negative values. Quantitatively, the P1 model results in lower values for any radial position than the exact solution. This is similar to results reported in [119], arguing that limited contributions from the absorption peaks lead to underestimated net emission.

10.5. Conclusions

A self-consistent model for wall-stabilized arcs was presented that allows to study modeling errors due to band-averaging of the spectral
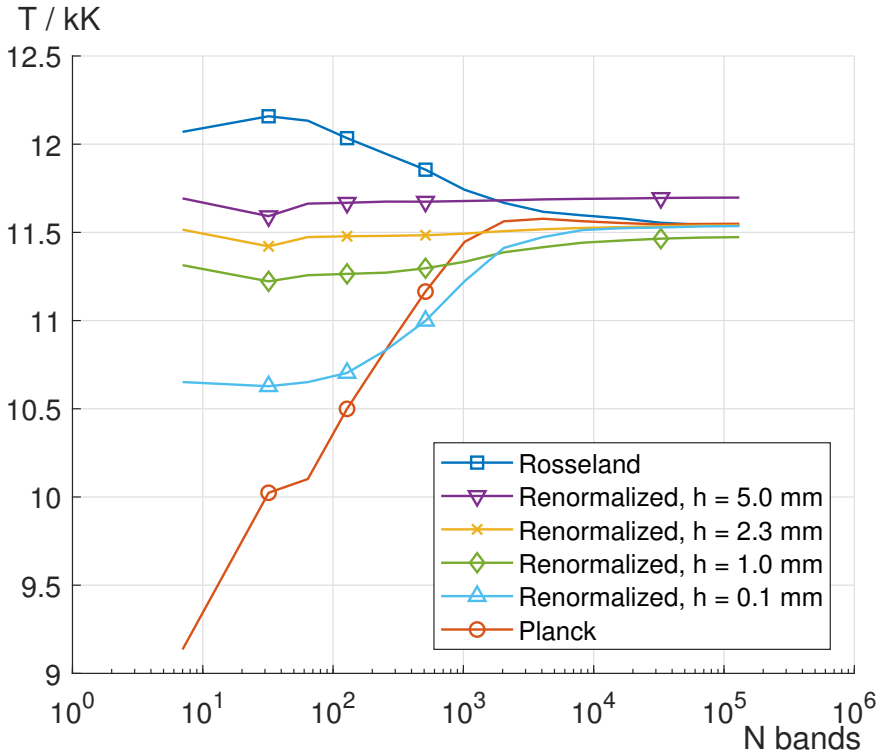
Figure 10.2.: Arc center temperatures as spectral domain is refined.
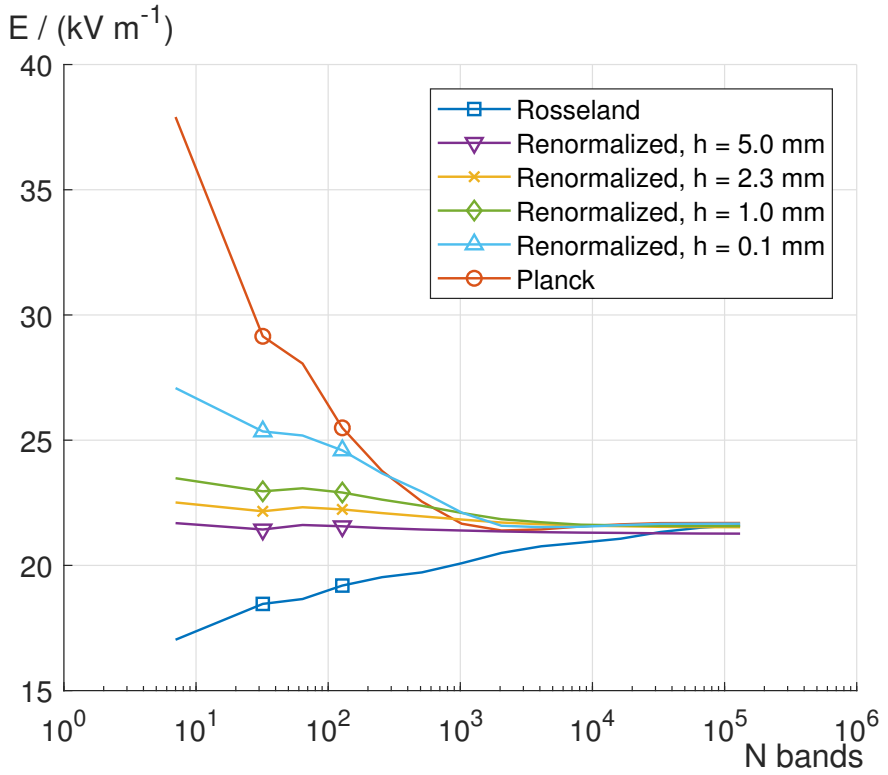
Figure 10.3.: Arc voltage as spectral domain is refined.
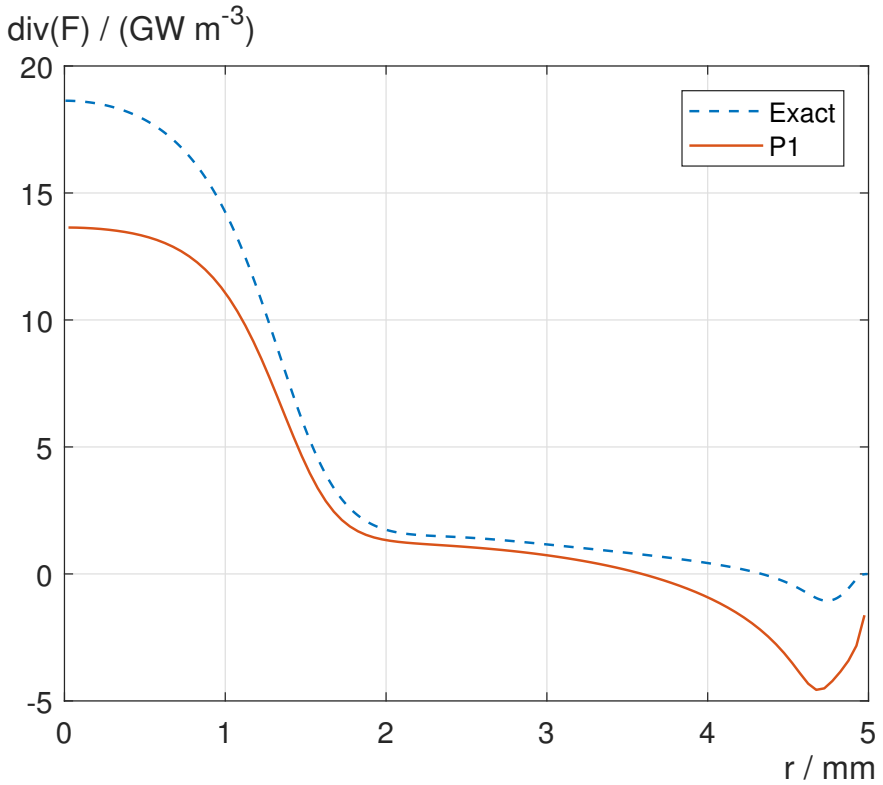
Figure 10.4.: Net emission computed by exact solution and P1 model.

absorption coefficient. It was shown that the Rosseland and Planck average require rather fine band discretization to converge, while the renormalized average is much less sensitive. Moreover, if the characteristic absorption length is chosen appropriately, seven frequency bands are sufficient to obtain very good results for the temperature profile and the arc voltage. The P1 model with renormalized average leads to underestimated net emission in comparison to exact integration. Future work will analyse this data in more detail for separate bands. This model will also serve as a testcase for material data and band boundary definitions.

11. Summary & Outlook

11.1. Summary

We reviewed fundamentals of radiative heat transfer modeling from a perspective of modeling electric arcs. We studied the radiative transfer equation and its modeling assumptions that yield to the quasi-steady RTE for non-scattering media (eq. 7.19). We discussed that an exact solution is computationally feasible only in the simplest situations and how the computational complexity is further reduced. For applied numerical simulations, we require a reasonable definition of frequency bands that yield to mean absorption coefficients.

We then considered the Elenbaas-Heller equation, the simplest model that allows to solve for a self-consistent temperature profile of a wall-stabilized arc. We performed a linear sensitivity analysis that allows to relate uncertainties in the absorption coefficient with their effects on the arc voltage; these results are more of theoretical interest. The more applied results are found in comparison to mean absorption coefficients as computed by the Planck average, the Rosseland average, and the line limited Planck average. We showed that choosing the line limiting length h adequately permits to retrieve the

correct temperature profile with minimal computational efforts.

11.2. Outlook

Further work may continue with analyzing the absorption coefficient data of plasmas that are contaminated with metal vapors. One should also discuss how the linear sensitivity analysis may support further work in absorption coefficient modeling, for instance with the research community that provides the absorption coefficient data. From an applied point of view, it would be interesting to see if the line limited Planck mean leads to generally useful results in arc simulations despite the fact that the line limiting length must be chosen in advance.

Part III.

Applied numerical simulations of electric arcs in circuit breakers

12. Introduction

Circuit breakers are safety elements in electrical power grids. They
are designed to interrupt fault currents (e.g., due to an accident
or malfunction of other network elements) and therefore protecting
the power system and its environment. Their design is determined
by voltage level at which they are installed in the power grid; see,
e.g., [120]. The operation principle is summarized as follows: Ini-
tially, the contacts are closed and current is flowing. When the open-
ing mechanism is triggered, the contacts separate and form inevitably
an electric arc; see, e.g., [169, ch. 2] for details on low voltage circuit
breakers, and [150] on high voltage circuit breakers, respectively. This
arc has to be controlled and extinguished quickly, i.e., in a few mil-
liseconds "in order to not cause damage to the power system, or to
destroy the breaker from the large power that is produced during arc-
ing." [120] Performing experimental investigations are tremendously
limited by the extreme conditions during the arcing process (see also,
e.g., [147]). In consequence, numerical simulations are the only source
for spatially resolved insights towards further product development
(see, e.g., [120] but also [118, 142, 146, 114]).

Applied numerical simulations in context of industrial product de-

velopment always have to trade off model complexity against short time to delivery. This issue is even more pronounced in electric arc simulations since dedicated solvers for gas flow and electromagnetism must be coupled with other modeling aspects such as radiation, wall ablation, electrode erosion, external circuit model, and mechanics; see, e.g., [142, 143]. However, it is hard to find software suites that allow for a robust multiphysics coupling in this field of research. We used a simulation framework [154] that allows for coupling of all submodels within a single graphical user interface. User-specific programming was limited to control remeshing events and data exchange among the solvers.

The following chapters present numerical simulations of electric arcs in circuit breakers. Chapter 13 focuses on the contact arm motion in a low voltage circuit breaker due to the mechanics, fluid pressure, and electromagnetic force. Chapters 14 and 15 consider an axially blown electric arc. The former focuses on an energy balance and gives insights that are difficult or impossible to measure; the latter considers radiative heat flux from the arc to the nozzle wall in details. These two contributions started from informal discussions of experimental work [28] by Dr Lorenz Bort and Prof Dr Christian Franck at the High Voltage Laboratory research group of ETH Zurich. The contents of the three chapters were presented at conferences. [61, 64, 62]

The numerical simulations would not have been possible without the data provided by Dr Petr Kloc (Brno Technical University) for absorption coefficients and Dr Anthony Murphy (CSIRO) for the

13. Self-consistent modeling of electrode motion in a model circuit breaker

The text of this chapter has been submitted to and presented at the 23rd Symposium on Physics of Switching Arcs (FSO 2019) in Nove Mesto na Morave, Czech Republic. [61]

13.1. Abstract

Numerical simulations of low-voltage circuit breakers require a coupled solution of gas flow, electromagnetism, electrical circuit, and other aspects. Including electrode motion is challenging because the computational grid is deformed and data is to be exchanged among dedicated solvers. A central issue is to keep them synchronized. This is addressed with a single framework that allows for a continuously morphing grid and accounting for the cumulative effects of mechanics, Lorentz force, and gas pressure. It is shown that gas pressure has negligible effect.

13.2. Introduction

Low-voltage circuit breakers are designed to carry electrical current in normal operation as well as safely interrupt short-circuit currents in case of failures. In case of a fault, the contacts are opened by means of mechanical actuators and/or electromagnetic forces available due to fault current. This contact opening inevitably leads to an electric arc. Depending on geometrical and other factors, the arc is ultimately driven into a deion chamber with splitter plates, in which it is elongated and cooled until extinction.

Contact opening can be a major design aspect in the current interruption process and numerical simulations should allow for including this effect appropriately and efficiently. In [176], the computational domain was deformed and remeshed to accommodate for the motion of the opening contact; however, the motion as well as current were not computed but followed input values obtained from experiment. Later, it was shown in [144, 143] that numerical simulations should include contact motion appropriately, especially if large contact gaps and contact motion are studied right in front of splitter plates. The adopted workflow consisted of creating a sequence of meshes that correspond to various contact positions. Contact position was calculated by a separate ordinary differential equation. While the meshes remained constant without any deformation, they are swapped frequently to follow contact position. However, the numerical framework involved three codes that must be kept synchronized and being a challenging task. [143] The same approach has been recently adopted in

[152].

This contribution presents a self-consistent and seamless implementation of contact motion for a three dimensional model geometry of a low-voltage circuit breaker. The moving contact is assumed to be subject to a mechanical actuator represented as a torsional spring for simplicity, the Lorentz force that becomes important at larger current values, and we account for plasma pressure that acts on the moving contact surface. Additionally, we include an electrical circuit that defines electrical boundary conditions for the circuit breaker. In contrast to [176, 144, 143, 152], our software framework allows for a continuous deformation and event-based remeshing. Data interpolation and exchange among dedicated solvers is inherently supported in a single user interface, that results in a uniform setup process. An earlier version of the same software framework was used in [57, 148] with an advanced plasma model; however, details on specifications of rigid body motion and electrical boundary conditions are not given.

13.3. Numerical Simulation Model

A model circuit breaker (see figure 15.1) is considered that consists of a fixed electrode, a rotationally opening bridge, and five U-shaped splitter plates enclosed in an insulating box with venting openings. The virtual geometry is designed to be of comparable size to a real device; for reference, the enclosure size is $47\,\text{mm} \times 36\,\text{mm} \times 24\,\text{mm}$. The ambient gas is dry air at atmospheric pressure and gas flow is considered in a box of size $69\,\text{mm} \times 49\,\text{mm} \times 36\,\text{mm}$ with pressure

outlets in all directions and solid bodies located centrally. The moving electrode is $2.5\,\mathrm{mm}$ thick and the fixed electrode cross-section is $2\,\mathrm{mm} \times 5\,\mathrm{mm}$. Splitter plates are $1.5\,\mathrm{mm}$ thick and separated in y-direction by the same distance. A symmetry plane is applied at $z = 0$. The model circuit breaker is thought to be installed serially in an electrical circuit (see figure 13.2) that consists of a voltage source ($V_{rms} = 230\,\mathrm{V}, 50\,\mathrm{Hz}$), a resistor $R = 2\,\mathrm{m}\Omega$, and an inductor $L = 25\,\mathrm{\mu H}$.

We solve the magnetohydrodynamic equations for a thermal plasma in local thermodynamic equilibrium (LTE), i.e., we consider the Navier-Stokes equations

$$\partial_t(\rho) + \nabla \cdot (\rho\mathbf{u}) = 0, \tag{13.1a}$$

$$\partial_t(\rho\mathbf{u}) + \nabla \cdot (\rho\mathbf{u} \otimes \mathbf{u}) = -\nabla p + \mathbf{f}_L, \tag{13.1b}$$

$$\partial_t(\rho e_{tot}) + \nabla \cdot ((\rho e_{tot} + p)\mathbf{u}) = S_{ohm} + \nabla \cdot (\lambda\nabla T) - \nabla \cdot \mathbf{q}_{rad}, \tag{13.1c}$$

together with Maxwell's equations in low-frequency limit in A-φ formulation, i.e.,

$$\nabla \times \mu^{-1}\nabla \times \mathbf{A} = \mathbf{J}, \tag{13.1d}$$

$$\nabla \cdot \mathbf{J} = 0. \tag{13.1e}$$

In these equations, ρ stands for gas density, $\mathbf{u}$ gas velocity, p gas pressure, e_{tot} total energy, T gas temperature, $\mathbf{q}_{rad}$ radiative heat flux, $\mathbf{J}$ electric current density, $\mathbf{B}$ magnetic flux density, μ magnetic permeability, σ electrical conductivity, and $\mathbf{A}$ magnetic vector potential. Moreover, we have by definition $\mathbf{B} = \nabla \times \mathbf{A}$ and $\mathbf{E} = -\nabla\varphi$,
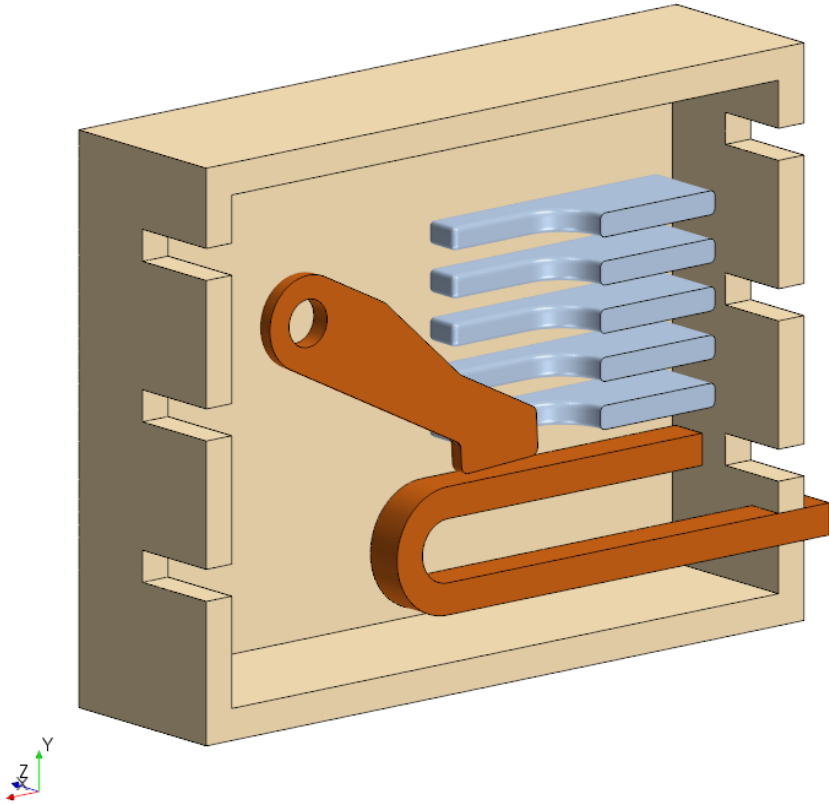
Figure 13.1.: Model geometry of a low-voltage circuit breaker, cut at symmetry plane $z = 0$.
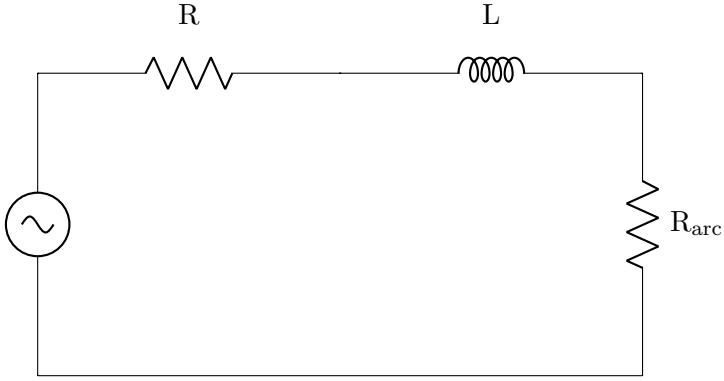
Figure 13.2.: Electrical circuit.

and Ohm's law $\mathbf{J} = \sigma\mathbf{E}$, where $\mathbf{E}$ denotes electric field and φ is the electric potential. The gas flow is considered as laminar. The system of equations is coupled via the source terms for Lorentz force density $\mathbf{f}_L = \mathbf{J} \times \mathbf{B}$ and Ohmic heating source density $S_{ohm} = \mathbf{J} \cdot \mathbf{E}$. Radiative heat flux $\mathbf{q}_{rad}$ is calculated using the Discrete Ordinate method (see, e.g., [112]) with six frequency bands defined by the ionization energies of nitrogen [142]. Band-averaged absorption coefficients were computed by Planck averaging from spectral data provided by [89]. Thermodynamic and transport properties of dry air plasma are taken from [75]. Material data for electrodes and splitter plates are those of copper and iron, respectively, with relative permeability $\mu_{Fe,rel} = 1 \times 10^4$.

We account for voltage drop in arc roots on the anode and cathode

following [142],

$$U_{a/c}(J) = \frac{a\tilde{J} + b\tilde{J}^d}{c + \tilde{J}^d}, \quad \tilde{J} = eJ, \tag{13.2}$$

with $a = 5 \times 10^8$, $c = 9 \times 10^{14}$, $d = 2$, $e = 5$, and $b = 5$ on the anode and $b = 10$ on the cathode. Comparing to [142], we use modified values for coefficients a, c, and e, so that maximum voltage drop on anode and cathode are reduced to $11.2\,\mathrm{V}$ and $14.7\,\mathrm{V}$, respectively. Hence, the arc is able to run faster into the deion chamber since new arc spots are formed more easily on the splitter plates. The corresponding heat source is included at the plasma-solid interface. This difference in voltage drop modeling is assumed to be of minor importance towards the aim of this study, since we also neglect evaporation and erosion of any solid bodies.

The bridge is assumed to move as a rigid body with rotation axis parallel to z-axis. Total torque is computed by the contributions of a torsional spring, gas pressure of the plasma acting on the electrode surface, and Lorentz force density inside the electrode body:

$$\tau_{tot} = \tau_S + \tau_P + \tau_L, \tag{13.3a}$$

$$\tau_S = -k(\alpha - \alpha_r)\hat{\mathbf{z}}, \tag{13.3b}$$

$$\tau_P = \int_A \mathbf{r} \times (-p\mathbf{n})\,\mathrm{d}A, \tag{13.3c}$$

$$\tau_L = \int_V \mathbf{r} \times \mathbf{f}_L\,\mathrm{d}V. \tag{13.3d}$$

The torsional spring constant $k = 0.2\,\mathrm{N\,m\,rad^{-1}}$ and relaxation angle $\alpha_r = 30\,\mathrm{deg}$ are defined such that the bridge would open to $\alpha_{max} = 45\,\mathrm{deg}$ in $2.5\,\mathrm{ms}$, at which it would be gradually slowed down before hitting the enclosure wall. The natural angular frequency of the torsional spring is $\omega_n = \sqrt{k/I}$ where $I = 2.75 \times 10^{-7}\,\mathrm{kg\,m^2}$ denotes moment of inertia of the moving electrode. If torsional spring was the only acting force, the rotation angle of the moving electrode with respect to z-axis is given by

$$\alpha_S(t) = \alpha_r(1 - \cos(\omega_n t)). \tag{13.4}$$

Initial position of the electrode bridge is defined with a gap of $2\,\mathrm{mm}$ to the fixed electrode. Arc ignition is modeled by a cylinder of radius $1\,\mathrm{mm}$ located centrally between the contacts with electrical conductivity set to $\sigma = 1 \times 10^4\,\mathrm{S\,m^{-1}}$ for $20\,\mathrm{\mu s}$. For simplicity, voltage source is assumed to be at peak voltage.

The outlined model is implemented in the numerical framework of Simcenter STAR-CCM+ (v2019.1). The equations for gas flow, electric potential, and radiative heat transfer are solved with finite volume method, and the magnetic vector potential is formulated in finite elements because of the discontinuous magnetic permeability. Therefore, the computational domain is discretized with two meshes, a polyhedral grid for the FV solvers and a tetrahedral grid for the FE solver, with maximum cell sizes $0.5\,\mathrm{mm}$ and $2\,\mathrm{mm}$, respectively. The meshes are refined at solid-fluid interfaces including prism layers. Timestep size is $1\,\mathrm{\mu s}$. After each timestep, electric current density

J is mapped to the tetrahedral grid, the magnetic vector potential is solved for, and magnetic flux density **B** is mapped back to the polyhedral grid. The domain can be remeshed whenever a specific criterion is met. Here, it is triggered if the upper electrode has moved 0.5 deg since the last remeshing event, or if the simulation had to be restarted. The rigid body dynamics and electrical circuit are also implemented in the user interface.

13.4. Results

Results are presented for time until $t = 400\,\mu$s. Figure 13.3 shows arc voltage and current, as well as current through the lowest two splitter plates. We see that arc current rises almost linearly as defined by the electrical circuit. After ignition, arc voltage is at 26 V comparing well to the sum of voltage drop on anode and cathode, and increases gradually until $t = 200\,\mu$s. This is explained by plasma cloud expanding from the ignition region into a volume bounded by the moving electrode tip, the fixed electrode and the lower two splitter plates. We note that a fraction of the current flows through the first splitter plate, and after $t = 200\,\mu$s, we see that electrical current starts to flow through the second splitter plate. At the same time value, we also note that arc voltage increases more substantially. This is related to the plasma gas expanding upwards and arc root formation at second splitter plate. Since the focus of this work is on electrode motion modeling, we limit the discussion of plasma flow to this level as it becomes more complex.

Figure 13.4 shows total torque on the moving electrode and its contributing terms due to torsional spring, Lorentz force, and plasma pressure. We see that torsional spring and Lorentz force are dominant, while plasma pressure yields a small contribution at arc ignition and quickly becomes negligible. Torsional spring yields an almost constant torque because of mass inertia and therefore relatively slow angular motion in the time interval considered. As current increases, Lorentz force becomes gradually more important and its torque exceeds that of torsional spring after $t = 300\,\mu\text{s}$.

To support the understanding of the data discussed above, the spatial distribution of plasma pressure and Lorentz force density at $t = 100\,\mu\text{s}$ are shown in figures 13.5 and 13.6, respectively. We see that the pressure wave due to arc ignition has already expanded from electrode tip towards splitter plates. Hence, torque due to plasma pressure is small. However, Lorentz force density increases gradually as total current increases and the self-induced magnetic field due to electric flux. Hence, their contribution to total torque becomes more important.

Figure 13.7 shows rotation angles due to total torque as obtained by the simulation and that of the analytical model in equation (13.4). We clearly see that torque due to Lorentz force results in faster electrode motion. This effect becomes more pronounced with increasing time values.
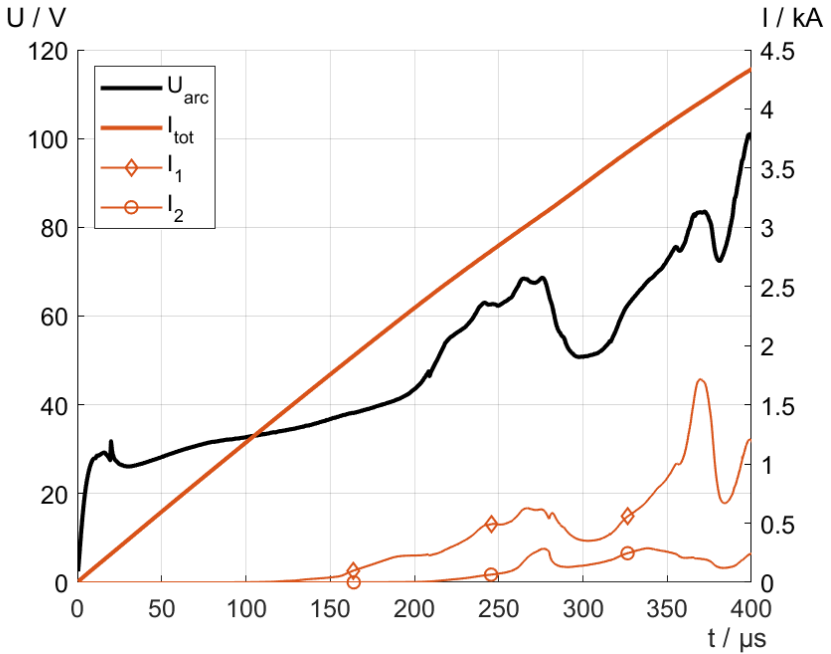
Figure 13.3.: Arc voltage and current in circuit breaker. The lines I_1 and I_2 show electrical current through the lowest splitter plates.
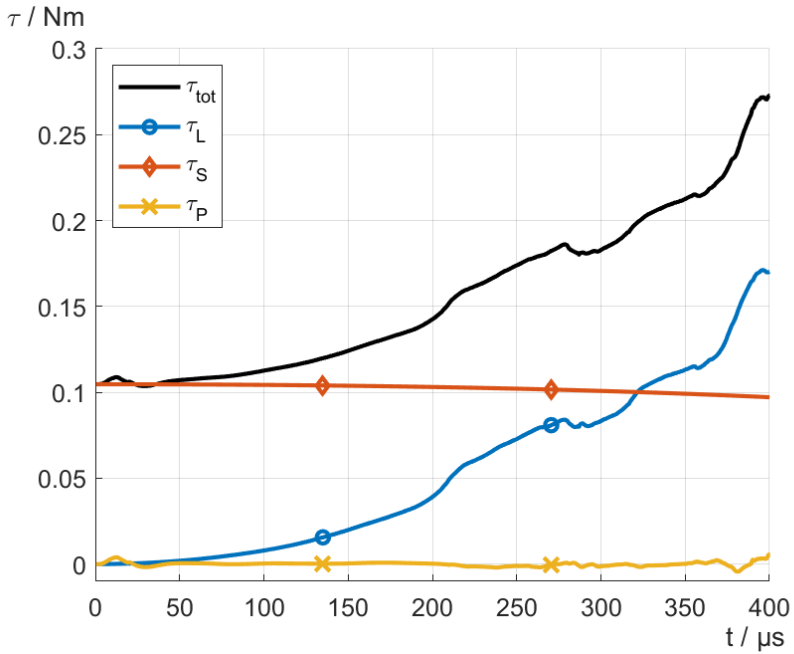
Figure 13.4.: Total torque on the moving electrode, with contributions from Lorentz force density, torsional spring, and plasma pressure.
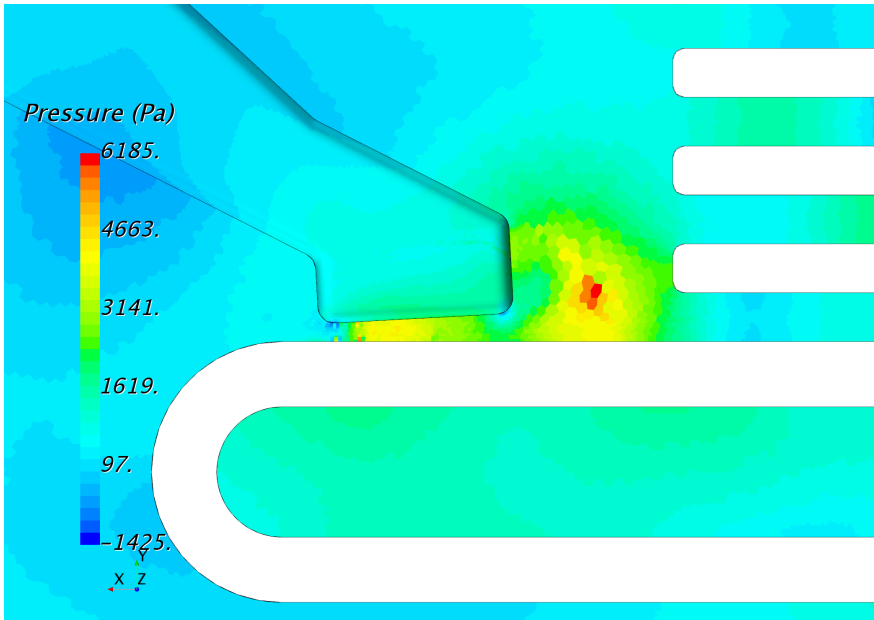
Figure 13.5.: Plasma pressure at $t = 100\,\mu\text{s}$.
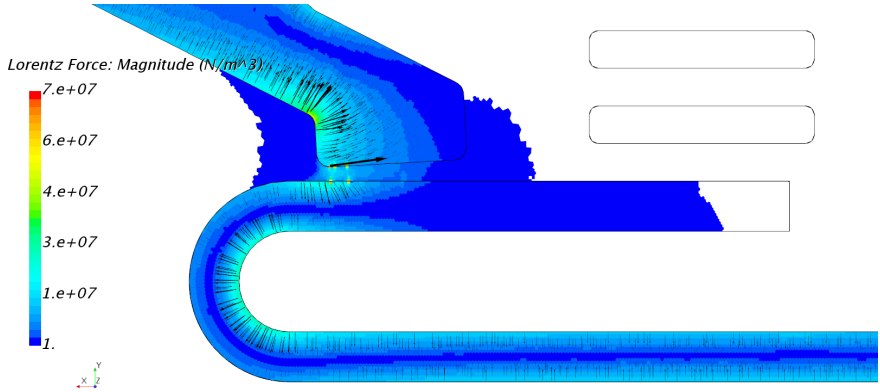
Figure 13.6.: Lorentz force density at $t = 100\,\mu s$.
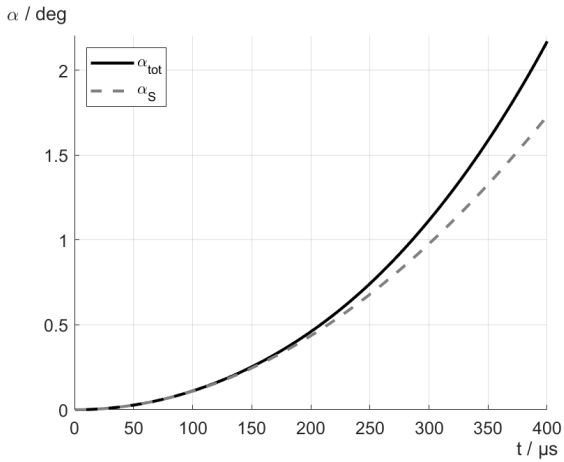
Figure 13.7.: Rotation angle due to total torque and compared to that due to torsional spring only.

13.5. Discussion and Conclusions

This contribution presents a self-consistent model for electrode motion in a virtual low-voltage circuit breaker. The results show that torque is mainly due to torsional spring and Lorentz force. Plasma pressure has negligible influence on rigid body dynamics because of its small torque value and its short interaction time. This does not mean that accurate plasma modeling is of minor importance; it is of uttermost importance because plasma gas flow and electromagnetic fields are directly affected. The mechanical actuator should be modeled appropriately because it affects rigid body dynamics and its interactions with arc plasma. Therefore, a self-consistent arc model should be used that allows to compute electrical current and voltage defined by the circuit elements, as well as to compute rigid body motion including the effects of mechanics and Lorentz force.

In contrast to previous work, the presented model is implemented with a continuously deforming mesh that is remeshed whenever needed. The user interface allows to define rigid body motions directly inside the framework without particular programming. It also inherently allows for data exchange among the solvers. As a consequence, the workflow for preparing simulations with complex body motions and interactions of the plasma with electrical circuit may be eased.

Future work will extend this study to longer simulation time, additional plasma physics including copper vapor due to electrode erosion and wall ablation, non-linearity of *B-H* curve of iron and further modeling techniques to ease user interaction with the software. Ex-

periments would serve ideally to complement this study.

Acknowledgment

14. Energy Budget of electric arcs in a gas-blast circuit breaker

The text of this chapter has been submitted to and presented at Nafems World Congress (NWC 2019) in Quebec, Canada. [64]

14.1. Abstract

Mechanical circuit breakers for high voltage direct current networks have been an important and challenging research topic for experimental studies. The main element of such breakers is an axially-blown electric arc in a convergent-divergent nozzle. Previous work focused on experimental setup and data analysis involving quantities that are difficult or impossible to measure.

This paper provides numerical results that were not accessible in experimental studies. The numerical simulations have been conducted on the original experimental setup using a magnetohydrodynamic framework. We present an analysis of the energy transfer modes of the axially-blown arc under consideration, discriminating between radiative heat transfer and convection. We see that the

largest amount of electrical energy is dissipated to the gas flow and removed from the nozzle geometry convectively, and a notable energy fraction is due to radiative heat flux onto the nozzle wall. With respect to the electric arc, we see that radiative energy transfer is dominant.

Moreover, we show that the electric field along the nozzle axis is larger in the convergent section than in the divergent section because convective cooling leads to a constricted arc shape, and the electric field is locally enhanced at the throat. Comparing electric field values predicted by experiments using a differential method and our numerical simulation results, we show discrepancies between the two methods and provide data for further evaluation of the experimental method.

Although neglecting effects of wall ablation and electrode erosion, the presented results allow for a more complete view on the previous experimental research work, especially on the gas flow field and shock fronts. They also pave the way for further numerical analysis and comparison to experimental data of the geometric layout, and contribute to future developments aimed to more powerful circuit breaker designs.

14.2. Introduction

Circuit breakers are a key element in electrical circuits and designed to protect electrical infrastructure by safely interrupting electrical current flow. Recent research focused on mechanical circuit break-

ers for high voltage direct current network topologies, which consist, among other parts, of an axially-blown gas circuit breaker made of two electrodes in a cylindrical nozzle. [171, 29, 27, 30] In the interruption process, the contacts are triggered to open in axial direction. This inevitably leads to an electric arc between the electrodes. Simultaneously, a gas flow is initiated through the nozzle so that the arc is cooled and ultimately extinguished.

The detailed energy balance of the arc is difficult to establish from experiments. Hence, various authors have pointed to the need for numerical simulations. For instance, [171] characterized parameters of electric arcs in a cylindrical nozzle and pointed out that plasma simulations could help understanding energy transfer and cooling mechanisms. In [29], a convergent-divergent nozzle was considered with electrodes located in varied positions; they concluded that the electric field is largest in the nozzle throat and mentioned CFD simulations to be useful. [27] used a slightly adapted nozzle geometry and noticed that wall ablation is much larger in the upstream section than downstream; they also speculated on energy distribution in axial direction and dissipation modes. Recently, [30] estimated the electric field of arc segments using a differential method under the assumption that those segments are independent. They concluded that this hypothesis holds for many arc segments indeed; however, some segments showed a dependence and the authors guessed that it is a consequence of flow discontinuities near the nozzle exit and at the downstream electrode tip.

The present study shall provide results using numerical simulations

that have been sought for by the publications mentioned above, in order to provide a more complete view of axially-blown arcs. In this work, we separately measure the contributions from convection and radiation as heat transfer modes. Additionally, the results will allow us to take a glimpse on which arc sections contribute most to arc voltage. In combination with insights on the gas flow field, the findings shall support further design steps towards circuit breakers with higher and faster interruption capabilities.

The geometric setup is identical to that in [27, 30]. The study is conducted with a numerical magnetohydrodynamic framework considering a thermal air plasma in local thermal equilibrium. In a first step and considering a single current value for comparison with the experimental data, we neglect electrode erosion and nozzle wall ablation processes. The results are compared to arc voltage and estimated electric field values as obtained from the previous experimental works, and they are brought in context to the mentioned hypotheses.

This publication is organized as follows. In Section 14.3, we outline the numerical model and its boundary conditions for gas flow and electrical current. Sections 14.4 to 14.6 show our numerical results on the arc voltage and electric field, gas flow, and the energy budget, that are discussed in Section 14.7. A summary with outlook on further work is given in Section 14.8.

14.3. Numerical model

The following section describes the computational domain, the mathematical framework, the material model and input data, solver settings, boundary conditions and mesh discretization.

We consider a convergent-divergent nozzle with two cylindrical electrodes, one each located in the upstream and downstream section (see also figure 14.1). The nozzle geometry is identical to [27, 30], i.e., the throat is located at $x = 70 \, \text{mm}$ with a minimum diameter of $20 \, \text{mm}$ and a total nozzle length of $140 \, \text{mm}$. The half angles are $15°$ and $10°$ in the convergent and divergent section. A radius of $20 \, \text{mm}$ is used at the throat for a smooth transition. The electrodes are $5 \, \text{mm}$ in diameter and their tips located at $x_A = 40 \, \text{mm}$ and $x_B = 120 \, \text{mm}$. The upstream section is cylindrical with a diameter $50 \, \text{mm}$ and the gas inlet is located at $x = -80 \, \text{mm}$. At the downstream nozzle end, the gas flow exits to ambient conditions into a computational domain large enough to neglect influence of the pressure outflow conditions. As a minor change to the original setup, we use rounded electrode tips for a more streamlined geometry.

The experiments were conducted in quasi-steady conditions, i.e., the flow conditions vary much slower than the system relaxation timescale. Therefore, we can look for a stationary solution given in the gas domain by the compressible Navier-Stokes equations,
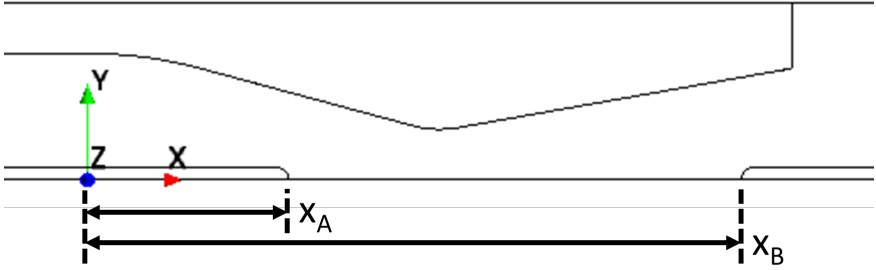
Figure 14.1.: Geometry sketch with nozzle, axially centered electrodes, inlet and outlet.

$$
\nabla \cdot \begin{bmatrix} \rho \mathbf{u} \\ \rho \mathbf{u} \otimes \mathbf{u} \\ \rho H \mathbf{u} \end{bmatrix} = \begin{bmatrix} 0 \\ -\nabla p + \nabla \cdot (\tau + \tau_t) \\ \nabla \cdot (\lambda \nabla T) + \nabla \cdot (\tau \cdot \mathbf{u}) + \mathbf{j} \cdot \mathbf{E} + S_e \end{bmatrix} , \quad (14.1)
$$

where ρ is the gas density, $\mathbf{u}$ gas velocity, p gas pressure, T gas temperature, H total enthalpy, λ thermal conductivity, and τ viscous stress tensor. Turbulence is accounted for with the $k - \omega$ model leading to the Reynolds stress tensor τ_t. Usually, Lorentz force were also included but are neglected, because numerical tests showed marginal effects in the situation at hand. The energy conservation equation includes Ohmic heating $\mathbf{j} \cdot \mathbf{E}$, and the S_e stands for the volumetric energy source term due to radiation as introduced below (see eq. (14.3)).

The electrodynamic potential φ is solved for all domains and in the

low-frequency limit obeying the generalized Ohm's law,

$$\nabla \cdot (-\sigma \nabla \varphi) = \nabla \cdot \mathbf{j}_{ex}, \qquad (14.2)$$

with σ denoting electrical conductivity, and $\mathbf{j}_{ex}$ stands for external source of electric current density.

Radiation modeling is a separate, challenging research topic because it affects the main energy transfer mode in electric arc simulations. Numerical solutions require data reduction of the spectral absorption coefficient κ_ν, which varies in narrow peaks over many orders of magnitude in radiation frequency, and depends also on temperature, pressure, and plasma composition. A computationally tractable model is obtained with splitting the frequency domain into a low number of intervals and applying an averaging method to each of them. In this study, we define six frequency intervals with boundaries according to ionization energies of nitrogen (see [142]) and we apply Planck averaging on spectral data provided by [91]. However, recent work showed that accurate solutions can be obtained with even less frequency intervals in combination with a renormalization length that limits the contributions from peaks in the spectral absorption coefficient data. [119, 90, 63] The radiative transfer equation is spatially discretized by the discrete ordinate method with S4 quadrature.

It is the divergence of radiative heat flux that represents a source term in the plasma energy balance equation,

$$S_e = -\nabla \cdot \mathbf{q}_r = -\int_0^\infty \kappa_\nu \left(4\pi I_{b\nu} \int_{4\pi} I_\nu \mathrm{d}\Omega \right) \mathrm{d}\nu \qquad (14.3)$$

where $I_{b\nu}$ denotes the spectral black body intensity at frequency ν, I_ν is the spectral radiative intensity, and κ_ν is the absorption coefficient of the plasma. The radiation intensity field is computed only in the plasma domain. Therefore, the plasma-solid boundary is defined as adiabatic, and incident radiation is converted to heat in the plasma domain.

The simulations are performed with the numerical framework STAR-CCM+ v13.06 [153] using numerical solvers based on the finite volume method. The plasma material and transport data are functions of temperature and pressure which are based on curve fits [75] ("equilibrium air model"). Electrical conductivity is taken from [44], with a minimum value $\sigma_{\min} = 1 \times 10^{-3}\,\mathrm{S\,m^{-1}}$ for numerical stability. The nozzle is considered as an electrically insulating body, with a finite electrical conductivity equal to $\sigma_{\min}$. Electrodes are made of copper with electrical conductivity given as $\sigma = 5.96 \times 10^7\,\mathrm{S\,m^{-1}}$. In order to improve solver convergence to a stationary solution, we activate the "Continuity Convergence Accelerator", and we select "W cycle" for the algebraic multigrid (AMG) solver for the electric potential solver. All other settings are at their default values.

For simplicity, we do not include wall ablation in this first study although experimental work clearly shows that wall ablation is relevant at large currents, see [27]. Moreover, we also neglect electrode erosion. If those effects were included, the plasma material data would also be functions of gas concentrations (here: copper vapor, PMMA vapor). It may be expected that the major effect of those vapors would be on electrical conductivity and absorption coefficient, and

to a smaller degree on the thermodynamic plasma parameters. One would also have to specify ablation and erosion rates, being further parameters that introduced further modeling uncertainties. The inlet pressure is set to $p_{\mathrm{abs}} = 8.2\,\mathrm{bar}$ absolute. The outlet boundary condition is specified to ambient conditions, i.e., a relative pressure $p_{\mathrm{rel}} = 0\,\mathrm{Pa}$. The upstream electrode contact is stressed with a total current $I = 1\,\mathrm{kA}$, and the downstream electrode is at zero potential.

The computational domain is axially symmetric and is discretized using polyhedral cells with $1\,\mathrm{mm}$ base size (see figure 14.2). The nozzle section is refined by 50% using a double-cone, and the arc region by 25% in a cylinder with $6\,\mathrm{mm}$ radius. Prism layers are added on both sides of solid-fluid interfaces with a first layer height of $0.1\,\mathrm{mm}$, total height of $0.4\,\mathrm{mm}$, and four layers. This results in 57.5k cells, and a mesh study confirms that the results are almost independent of grid refinement, with largest variations in boundary radiative heat flux of a few percent.

14.4. Arc voltage and electric field

Figure 14.3 shows the arc voltage as a function of arc current. The arc voltage is the only directly available quantity for comparison to experiments (see figure 4 in [27]). We see that the voltage decreases with increasing current, i.e., a negative differential resistance, that is more pronounced for lower current values. We notice good agreement especially for intermediate current values (between $I = 0.3\,\mathrm{kA}$ and $0.8\,\mathrm{kA}$). For larger currents, the experimental data show a positive
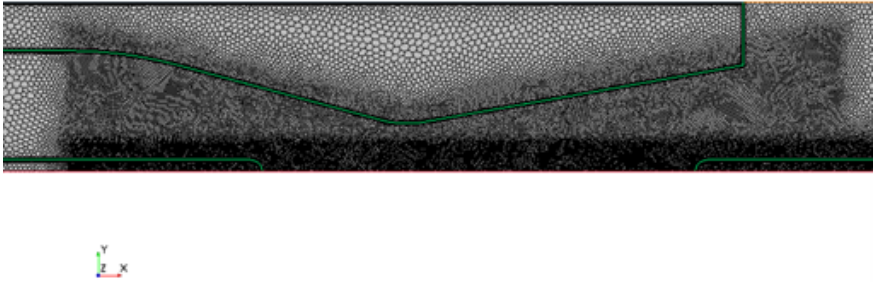
Figure 14.2.: Polyhedral mesh with refinement in nozzle section and
arc region.

differential resistance, a trend that the numerical results are not capable to follow. Similarly, the slope of the experimental curve is also steeper at lower current values than those of this study.

Figure 14.3 shows the electric field in the arc along the symmetry axis. We see that the electric field is largest at the upstream electrode tip with a steep slope in axial direction. The electric field is larger at the nozzle throat with a local maximum slightly before the throat. In the downstream section, the electric field decreases to lower values with a minimum just before the downstream electrode tip. The same figure also shows estimated electric field values for arc segments of 20 mm length using an indirect, differential method. [30] The data was obtained from their publication showing the arc voltage for each segment and dividing those values by the segment length. Comparing with the numerical data of this study, we see that their estimated values agree well for the first and third arc segment, but the electric
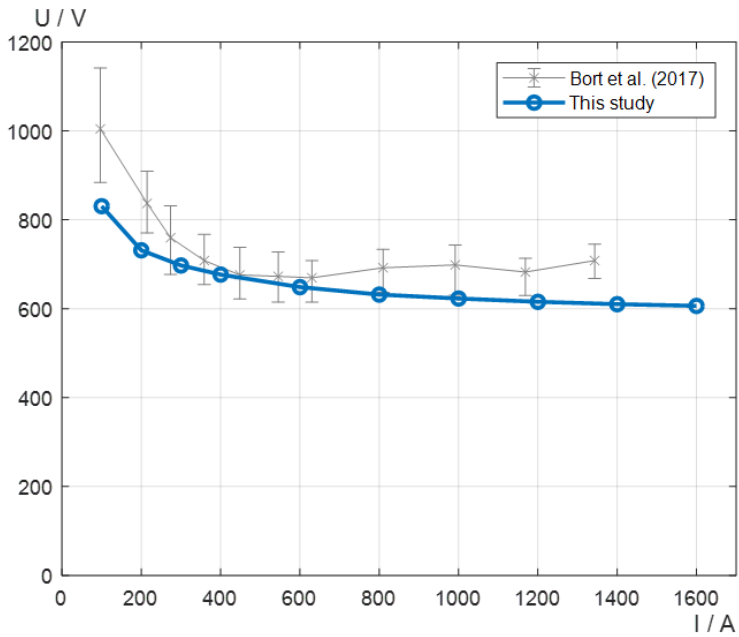
Figure 14.3.: Arc voltage as a function of arc current.
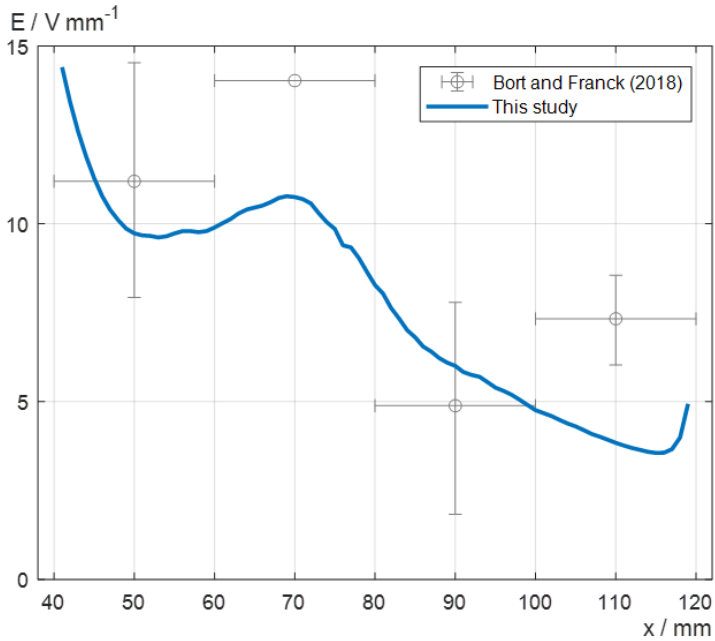
Figure 14.4.: Electric field on symmetry axis between electrode tips.

field is overestimated in the throat and for the last segment.

14.5. Flow Field

Figures 14.5 to 14.7 show the velocity, temperature, and Mach number of the gas flow, and figure 14.8 shows the electrical current density in the plasma.

We see that the gas flow is continuously accelerated as expected

in a convergent-divergent nozzle at supersonic conditions. The gas velocity is largest in the divergent section where the electric arc is located. The downstream electrode tip gives rise to a bow shock. At the nozzle wall, we see at a lateral position of the electrode tip that the flow detaches from the conically shaped wall and forms an oblique shock front. The interaction of these shock fronts is clearly visible in the Mach number. The temperature field shows that the hottest region of the arc is located at the upstream electrode tip, and temperature reduces in downstream direction. We also note a hot gas layer close to solid body surfaces: this is due to incident radiation on the domain boundary and, as a numerical artifact, the finite electrical conductivity.

The shape of the arc can be understood as follows. As shown by the electrical current density and the temperature field, the arc radius at the upstream tip is smaller than the electrode radius and widens to an almost constant cross-section up to the nozzle throat. The convergent section leads to a gas flow directed towards symmetry axis. Therefore, the gas flow is directed towards the arc surface with a cooling effect and mixing. Consequently, the electrically conductive arc section is constricted, and the arc core temperature and electrical field are increased. In the divergent section, we notice a conically widening of the arc cross-section. In that region, the gas flow is parallel to the arc surface and enthalpy flux is not a major energy transfer mode.

Figure 14.5.: Gas velocity contour plot.

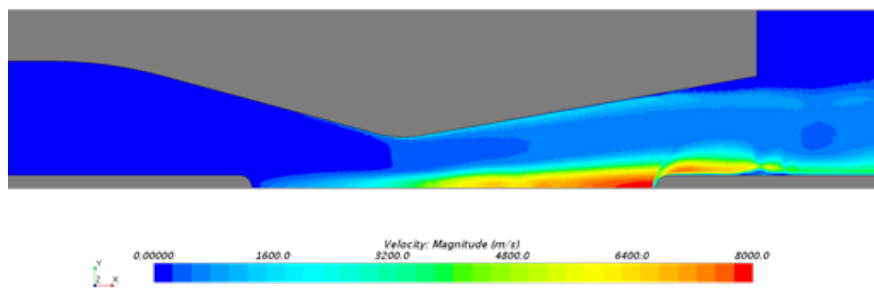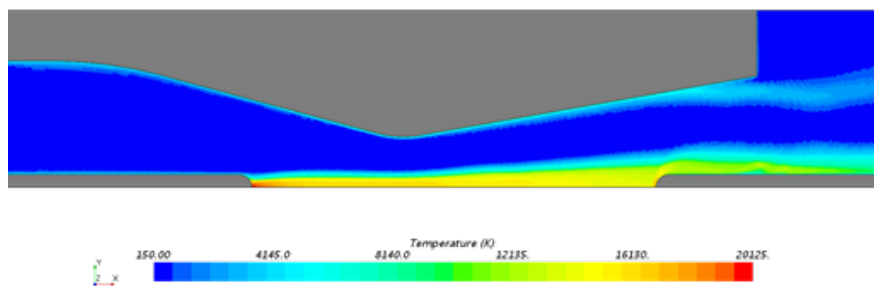Figure 14.6.: Plasma temperature contour plot.
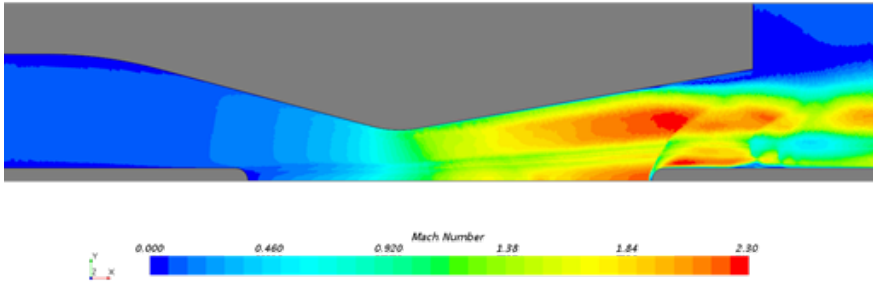
Figure 14.7.: Mach number contour plot.
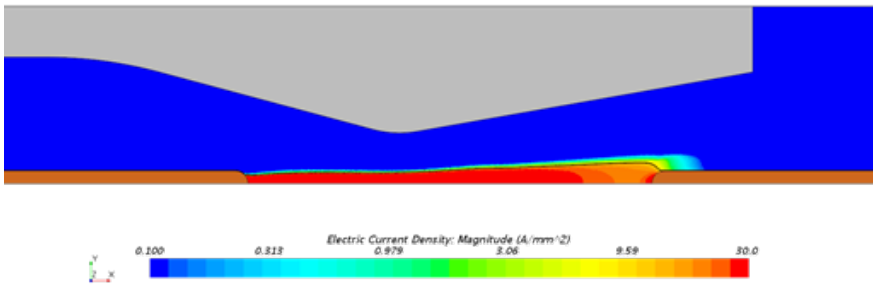
Figure 14.8.: Electrical current density contour plot, with contour line at $10\,\mathrm{A\,mm^{-2}}$ that defines arc core region.

14.6. Energy Budget

In contrast to experimental work, the numerical data allows us to evaluate the energy budget of the axially-blown electric arc. We recapitulate the relevant terms in the energy conservation equation. The electrical energy is released as Ohmic heat $\mathbf{j} \cdot \mathbf{E}$ into the plasma, which can be removed from the arc core in two ways: either the energy can be removed convectively by the gas flow as enthalpy flux $\rho H \mathbf{u}$, or by radiative heat transfer. The emitted radiative energy can be reabsorbed in the surrounding gas ($S_e = -\nabla \cdot \mathbf{q}_{rad}$), or the remainder of radiative heat flux $\mathbf{q}_{rad}$ is absorbed at the nozzle wall.

We calculate this energy budget for two control volumes (see also table 14.1), with quantities for a circular sector of $1\,\mathrm{rad}$ in circumferential direction. We consider, firstly, the gas domain in the nozzle section between $x = 0\,\mathrm{mm}$ and $x = 140\,\mathrm{mm}$, and secondly, the gas domain in the arc core region defined by the electrical current density contour at $j = 10\,\mathrm{A\,mm^{-2}}$. The quantities are numerically evaluated as surface or volume integrals. We do not consider radiative heat flux on the electrode surface, because their surface content is relatively small, and their values are negligible indeed.

The electrically released power is given by the product of total current and arc voltage and is equal to $99.1\,\mathrm{kW\,rad^{-1}}$. Hence, we see that both control volumes contain almost all Ohmic heat, with only a small fraction outside of the arc core. The Ohmic heat with respect to the control volume is taken as a reference for the other energy transfer modes in either evaluation domain.

Energy transfer mode	Nozzle Section (kW rad^{-1})		Arc Core (kW rad^{-1})	
Ohmic Heat	97.9	100%	94.5	100%
Net Enthalpy Flux	78.2	80%	30.8	33%
Boundary Radiation Heat Flux	14.2	15%		
Radiative Heat Source	-32.2 (?)	-33%	-58.2	-62%

Table 14.1.: Energy balance of axially blown electric arc.

For the nozzle section, we see that 80% of the Ohmic heat is re-moved by convection, and 15% is radiated to the nozzle wall. Evaluating the net enthalpy flux across the arc surface, we find that 33% of the energy is convectively removed from the arc core. These quantities are readily available in the simulation framework of STAR-CCM+.

It is more difficult to assess the volumetric radiative heat source. The radiative heat source S_e is evaluated as volume integral. The numbers suggest that 33% of the Ohmic energy leave the nozzle by radiation. However, this does not agree with the boundary radiative heat flux, evaluated as surface integral of radiative heat flux $\mathbf{q}_{rad}$, which should be identical by Gauss theorem up to the neglected contributions from electrode walls.

A possible explanation for the discrepancy in the energy balance lies in the spatial profile of radiative heat source, which shows a steep gradient from negative to positive values across the arc surface. Hence, we suppose that a locally finer mesh resolution would be required for a sound evaluation. Nevertheless, we evaluated with

respect to the arc core control volume that 62% of the Ohmic energy is radiated away. Here, the energy balance seems to be acceptable. This seems to be trustable since the arc core control volume resides inside of the gradient in radiative heat source.

14.7. Discussion & Conclusions

Our numerical simulations reveal interesting features that complement experimental studies.

Figure 14.3 shows the arc voltage as evaluated in this numerical model and experimentally. [27] noted that the positive differential resistance coincides with the onset of wall ablation. This effect is not included in the numerical model and is a plausible explanation for the opposite trends between experiment and simulation, however, this does not explain the differences at lower current values. It remains an open question if this discrepancy is due to erosion (i.e., copper vapor) being neglected, or the slight geometric variation of rounded electrode tips. Nevertheless, the comparison suggests that the numerical model is acceptable and can serve as a basis for further investigations.

In Figure 14.4, we show the electric field at the symmetry axis. The curve shape is explained by the structure of the nozzle and the resulting gas flow (see also Figures 14.5 to 14.8). In the upstream, convergent section, cold gas is blown towards the arc center leading to constriction and effective cooling at its surface. This results in larger electric field value than downstream, as given by Ohm's law, and is especially pronounced near the upstream electrode tip. In the

downstream, divergent section, the plasma cross-section increases, and gas mixing is not effective.

In [30], the arc voltage was evaluated per segments of 20 mm length with several combinations of electrode tip positions. This measurement method resulted in variations of the segment voltage and was explained by normal shocks at the nozzle exit and a bow shock at the downstream electrode tip. Our numerical results (see Figures 14.5 to 14.7) show that a bow shock exists indeed, but there is an *oblique* shock near the nozzle exit.

With respect to the electric field, our study reveals differences to the experimentally estimated values. At the nozzle throat, the experimental method yielded values that are almost independent of the downstream electrode position suggesting small measurement errors; however, our results show that their electric field is overestimated at the throat and the variations in other arc segments are relatively large. The differential method could be assessed in more details with electrode positions varied more finely in experiment, and an equal set of additional simulations.

It was guessed in [29] that the electric field is largest at the throat, and smaller in the convergent and divergent nozzle section. In [30], they concluded that the electric field is larger in the converging section. The numerical results prove this hypothesis and allow for a more detailed description: we found that the electric field is locally increased at the nozzle throat. Moreover, the electric field shows a generally negative slope for with respect to the full nozzle length. This is due to gas mixing at the arc surface that is more effective in

the convergent section and the divergent nozzle shape in the downstream part. Unfortunately, the upstream electrode tip is located rather close to the throat so that a proper characterization of the convergent section is not possible. This drawback in the study setup should be eliminated in further simulations with differently selected electrode positions, e.g., the cathode tip located more upstream.

In Table 14.1 we present an energy balance of the axially-blown electric arc. Our results show that 15% of the electric power is radiated to the nozzle wall. We also see a cold gas layer that separates the electric arc from the nozzle wall. Hence, we can conclude that, in experiments, the heat consumed for wall ablation is not due to heat flux of thermal conduction, but by radiative heat flux. Therefore, our data provides one of the results sought by [171], and it can serve as a basis for further analysis for extending his work. However, our numerical model should be examined in more detail to understand the hot gas layer at the solid surfaces, which we think is due to radiative heat flux and a numerical artifact of finite electrical conductivity. Doing so, we would be able to include radiative wall ablation as an additional physical effect that can be compared to experimental measurements.

Finally, we want to mention that such plasma simulations are ideally suited to study complex tasks such as optimization of nozzle geometries and electrode positions. The present model can be extended to include other interactions that are important during current interruption. For example, the considered type of high voltage direct current circuit breakers consists of an LC-oscillator that is interacting

with the axially-blown arc; hence, such an external electrical circuit can be added in further studies.

14.8. Summary & Outlook

This study presents numerical simulations of an axially-blown arc in a convergent-divergent nozzle in a magnetohydrodynamic framework, that has recently been studied in experiments. Being the first simulations of the specific geometry at hand, the results complement experimental findings with long-sought insights to quantities that cannot be measured directly.

A comparison of arc voltages showed acceptable agreement of the numerical model to the real device, especially at intermediate current values. At larger and lower current values, the results indicate that more physical effects such as wall ablation and erosion should be included in further studies. A comparison of electric field to indirectly estimated values showed that further work is needed to assess the differential method used in experiments. Evaluating the energy budget of the electric arc, our results show that 80% of the electrical power leaves the nozzle geometry convectively, and 15% is radiated to the nozzle wall; with respect to the arc core region, 33% of the energy is transported away by the gas flow and 62% leaves the inner zone by radiative heat flux.

Further work should include wall ablation and electrode erosion, along with more advanced plasma data that includes copper vapor, because those affect the energy budget via radiation and thermody-

namics. The model can also be extended to include thermal conduction into the solid domains, and it can also be coupled with an external electrical circuit to account for effects of other parts in a HVDC circuit breaker. Parameter studies on the electrode position, blow pressure, current levels, and geometric optimization can contribute and complement recent experimental studies.

15. Axially blown arc with PMMA wall ablation and electrode erosion

The text of this chapter has been submitted to the 30th International Conference on Electrical Contacts (ICEC 2021) in Rorschach, Switzerland. The paper is accepted but the conference has been postponed by one year due to the Sars-CoV-2 pandemic. [62]

15.1. Abstract

An axially-blown arc in a PMMA nozzle is analyzed with numerical simulations. Previous experiments showed that wall ablation is observed for current values larger than a threshold and absent otherwise, and it has recently been found that PMMA is optically thick in the ultraviolet (UV) frequency range. An appropriate definition of radiation bands for the UV range has recently been published that allows for evaluating irradiance on the nozzle surface. In this contribution, it is shown that copper vapor affects the spatial temperature profile

of the arc column and increases wall irradiance towards the upstream nozzle section. A caloric estimate for radiation-induced wall ablation is presented, which sheds some light on the experimental findings.

15.2. Introduction

An axially-blown electric arc is considered in a convergent-divergent nozzle made of PMMA (polymethyl methacrylate). The experimental setup was developed as the main functional element for a cost-efficient design of a high voltage direct current (HVDC) circuit breaker. [171] Subsequent work analyzed the electric field in the nozzle. [29, 30] In [27] it was found that the amount of ablated wall material was related to the differential resistance, and mass loss of the PMMA nozzle was measured only for currents larger than 350 A. However, the effect could not be explained by the measurements due to many unknown factors.

The experimental setup was investigated by numerical simulations in a magneto-hydrodynamic (MHD) framework focusing on the gas flow conditions and the energy budget. [64] The numerical results agreed reasonably with previous measurements although the solid bodies were modeled as adiabatic, and wall ablation as well as electrode erosion were neglected. It was found that the arc column is surrounded by a cold gas layer, so that the experimentally observed wall ablation must be due to radiative heat transfer from the plasma to the nozzle surface.

Recent work focused on radiative properties of polymers that are

required for arc simulations. [17] It was found that PMMA is transparent in the visible range but opaque in the ultraviolet (UV) range, that is, for wavelengths shorter than 420 nm. Moreover, band-averaged absorption coefficients have been reported that are a key input for numerical simulations of electric arcs.

This study is aimed at refining the numerical model [64] towards the experimentally measured results [27]. For that, copper vapor due to electrode erosion shall be included and tested for its effect on observable quantities by a parametric study. Moreover, the process of wall irradiation and its ablation shall be investigated, based on the recent findings of radiative properties of PMMA.

The paper is structured as follows. Section 15.3 describes the model and the effects included in this numerical analysis. It also presents an estimate for a minimum irradiance required such that wall ablation is observable. The results are presented in section 15.4, by comparing arc voltage to measured values and the effects of copper erosion on the temperature distribution along the arc axis. We also show the irradiation on the nozzle wall for the UV range. Conclusions are summarized in section 15.5.

15.3. Numerical Model

15.3.1. Geometry

The geometric setup is taken from [27] and described in the following using the nozzle throat and its axis as a reference (see figure 15.1).
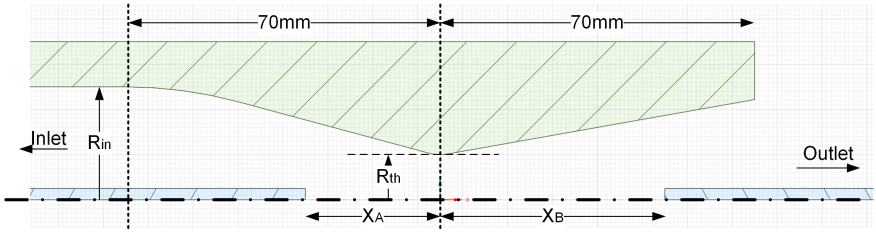
Figure 15.1.: Axisymmetric view of the PMMA nozzle and electrodes.

The inlet section has a radius of $R_{in} = 25\,mm$. The nozzle has conical sections of $70\,mm$ length with half-angles $15°$ upstream and $10°$ downstream, respectively. The throat radius is $R_{th} = 10\,mm$ and connects the two sections with a rounded edge of radius $10\,mm$. Copper rods are used as electrodes with $5\,mm$ diameter and inserted into the nozzle axially at positions $x_A = -30\,mm$ and $x_B = 50\,mm$. The inlet is located at $x = -230\,mm$ and the outlet at $x = 300\,mm$. The geometry allows to perform this study with axial symmetry.

The computational domain has a radius of $100\,mm$ and it is discretized with polyhedral cells. The grid is refined between the electrode tips to a size of $0.25\,mm$. The downstream section is refined well beyond the nozzle exit with cell diameters of $0.5\,mm$ to resolve the shock fronts appropriately. Prism layers are specified on all body interfaces to ensure a perpendicular mesh, since this helps to ensure convergence of the electric potential solver; their height is specified to be $0.1\,mm$.

15.3.2. Model equations and framework

The aim of this study is to evaluate thermal irradiation on the nozzle surface that is exposed to the electric arc. Therefore, we are looking for a numerical and coupled solution in steady state of the Navier-Stokes equations for gas flow, Maxwell's equations for electromagnetism, and the radiative transfer equation accounting for radiative heat transfer. The model is implemented in the numerical framework of Simcenter STAR-CCM+ (version 2019.3.1) [154].

Because the arc is located at the symmetry axis, the magnetic field has a negligible effect and is discarded; as a consequence, the electromagnetic equations reduce to the Gauss law for electric field. The upstream electrode (cathode) is stressed with a current value I, while the downstream electrode (anode) is fixed to zero potential. The electrical conductivity of the plasma is characterized by temperature, pressure, and copper mass fraction, and provided to the software in tabulated format.

The inlet pressure $p = 8.4$ bar is specified in absolute scale and the outlet pressure is set to ambient conditions. This results in supersonic flow conditions downstream of the nozzle throat, and shock fronts will form at the anode tip and nozzle exit. Turbulent flow conditions are accounted for by the standard k-ε model. Ohmic heating is included as energy source term. The thermodynamic and transport properties of air-copper plasma were provided by Murphy. [116, 117]

The radiative transfer equation is solved numerically by the Discrete Ordinate Method. The frequency domain is discretized into

Band	$\lambda_l/\mu m$	$\lambda_u/\mu m$	Radiation category
1	30000.0	4542.3	
2	4542.3	856.5	IR
3	856.5	700.0	
4	700.0	420.0	Visible
5	420.0	290.0	
6	290.0	194.7	
7	194.7	113.1	UV
8	113.1	102.0	
9	102.0	85.2	
10	85.2	30.0	

Table 15.1.: Definition of radiation band boundaries.

bands (see table 15.1) according to the ionization energy levels of atomic nitrogen (see [142]) and the UV frequency band definitions in [17]. Mean absorption coefficients are computed from spectral data provided by Kloc [91] with Planck-averaging in each band, and supplied to the software in tabulated format and as functions of temperature, pressure, and copper mass fractions (see figure 15.2).

A detailed model would account for heat conduction from the plasma to the solid bodies, their erosion, and also include an arc root model for the detailed physics at the plasma-electrode interface (see, e.g., [142]). However, as we are looking for a steady state solution, the thermal inertia is discarded which would lead ultimately to solid bodies at evaporation temperature. This situation is resolved and simplified: the electrodes are excluded from the energy balance and adiabatic boundary conditions applied. Nevertheless, we account
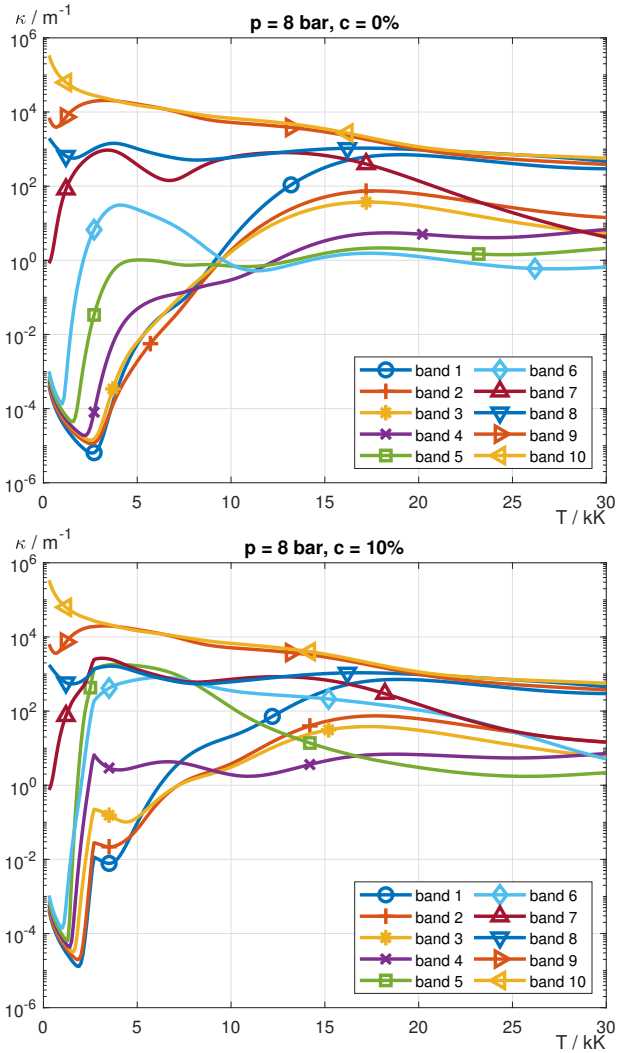
Figure 15.2.: Mean absorption coefficients at 8 bar and for copper mass fraction 0% (above) and 10% (below).

for electrode erosion with a mass species source term $\Phi = gj$ that is proportional to current density j and a constant erosion rate g (units: $\mu g \, C^{-1}$). As in [142], the erosion rate discriminates between anode and cathode by a factor of two: $g_a = 0.5 g_c$. A drawback of this approach is that the electrode surface temperature will be significantly higher than copper evaporation temperature.

Similar modeling issues are observed for the nozzle domain. The solid domain must be included in the energy balance because we aim to evaluate the irradiation on the nozzle surface. With this aim, we set the absorption coefficient as well as the nozzle surface emissivity to zero so that the body is optically transparent and therefore heating effects are suppressed; as a consequence, we do not model any evaporation of PMMA. This aspect is justified by the recent results that those polymer vapors have negligible effects on the total radiative energy balance when exposed to high current arcs. [17] Moreover, if ablation was included, the ablated vapors would be transported along the nozzle surface and likely not be mixed into the arc column. Therefore, it would only affect the gas flow conditions which could be mimicked by a source term for air species.

The simulations run for 1500 iterations. It takes about 1000 to 1200 iterations until the initial conditions disappeared and the quantities of interest converged. Despite of the nonlinear coupling among the gas flow, electromagnetism and thermal radiation, the residuals systematically reduced by three orders of magnitudes.

15.3.3. Estimate on radiation-induced wall ablation

This section presents a caloric relation on the irradiance E_w required to heat the nozzle wall and trigger its ablation in a time interval $[0, t]$.

Let us consider a cylindrical tube with inner wall radius r_w and axial length l irradiated uniformly. We also assume that the absorption coefficient κ and mass density ρ of the tube material are given.

Let us consider the radiative intensity $I(s)$ into the tube wall along a straight line perpendicular to its surface, with $s = 0$ at the inner tube wall. Moreover, let us assume that the tube wall is cold such that its emission is negligible. From the radiative transfer equation, we find that the radiative intensity decays exponentially on the scale of its optical depth τ,

$$I(s) = I(0)e^{-\tau}, \quad \tau = \int_0^s \kappa(x) \, \mathrm{d}x. \tag{15.1}$$

We may assume that the absorption coefficient is constant along this path, which yields $\tau = \kappa s$. We choose s such that the radiative intensity has decayed by two orders of magnitude, i.e., $\tau = -\ln(10^{-2}) = 4.6$. Using this value for optical depth, we define the heated tube volume as

$$V = \pi l((r_w + s)^2 - r_w^2) = 2\pi l \left(r_w + \frac{1}{2}s \right) s \approx A_w s, \tag{15.2}$$

assuming that the material layer thickness s is small compared to the wall radius, and denoting the irradiated wall area by $A_w = 2\pi l r_w$. This volume has mass $m = \rho A_w s$, and the absorbed energy until time

t is equal to

$$Q = E_w A_w t. \tag{15.3}$$

On the other hand, the required heat to increase the temperature of a mass m from ambient temperature T_0 to vaporization temperature T_v and its latent heat of evaporation L_v is equal to

$$Q = m \left(\Delta h + L_v \right), \tag{15.4}$$

where $\Delta h = h(T_v) - h(T_0)$ denotes the difference in specific enthalpy of the solid material. Therefore, the minimum value for wall irradiation E_w required to induce wall ablation in time t is given by:

$$E_w = \frac{Q}{A_w t} = \frac{\rho s}{t} \left(h(T_v) - h(T_0) + L_v \right). \tag{15.5}$$

To be specific and relate to the measurements in [27], in which the nozzle was exposed for $t = 10\,\text{ms}$ to high current arc, we note that the mass density of PMMA is $\rho = 1.18\,\text{g\,cm}^{-3}$ and its melting temperature $T_v = 160\,°\text{C}$. We find data for the enthalpy difference $\Delta h = 211\,\text{kJ\,kg}^{-1}$ [2] and the latent heat of evaporation $L_v = 330\,\text{kJ\,kg}^{-1}$ [102], and use an absorption coefficient $\kappa = 1 \times 10^4\,\text{m}^{-1}$ from the UV range [17]. With this data, we calculate that the irradiation affects a material layer of thickness $s = 0.46\,\text{mm}$, and a minimum irradiance for radiatively induced ablation

$$E_w = 3 \times 10^7\,\text{W\,m}^{-2}. \tag{15.6}$$

15.4. Results & Conclusions

Figure 15.3 provides an overview of the gas flow field. It shows the temperature field for current $I = 1400\,\text{A}$ and erosion rate $g_c = 40\,\mu\text{g}\,\text{C}^{-1}$. We see that the arc temperature in the convergent section is larger than downstream of the throat. We observe flow expansion in the divergent section, and the shock fronts at the anode tip and after the nozzle exit. The increased temperature at the cathode and upstream of the nozzle is due to radiative heat transfer from the arcing zone and that we solved for the steady state. A more detailed analysis of the temperature in the arc column follows in figure 15.5.

Figure 15.4 shows the arc voltage as a function of current and erosion rate. We see that the arc voltage reduces with arc current and agrees rather well with the results reported in [27] for low to intermediate currents. This is an improvement to previous numerical results [64] which used rounded electrode tips and the $k-\omega$ turbulence model, in particular for the lowest current values. We also note that including electrode erosion leads to slightly larger arc voltage, and its effect being more pronounced as current increases.

Figure 15.5 shows the arc center temperature profile in axial direction. At low currents ($I \leq 300\,\text{A}$), we see that copper vapor reduces the arc center temperature only in a region close to the upstream electrode tip, whereas for larger currents the temperature profile is reduced for longer distances downstream.

The temperature profiles reveal further details that are independent of arc current and characteristic to the gas flow field in the noz-
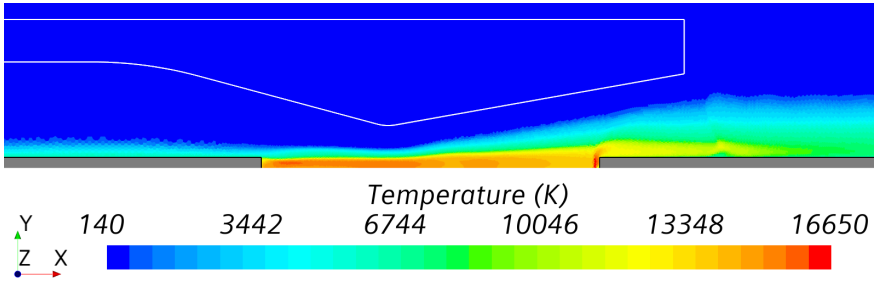
Figure 15.3.: Temperature field for $I = 1400\,\text{A}$ and $g_c = 40\,\mu\text{g}\,\text{C}^{-1}$.
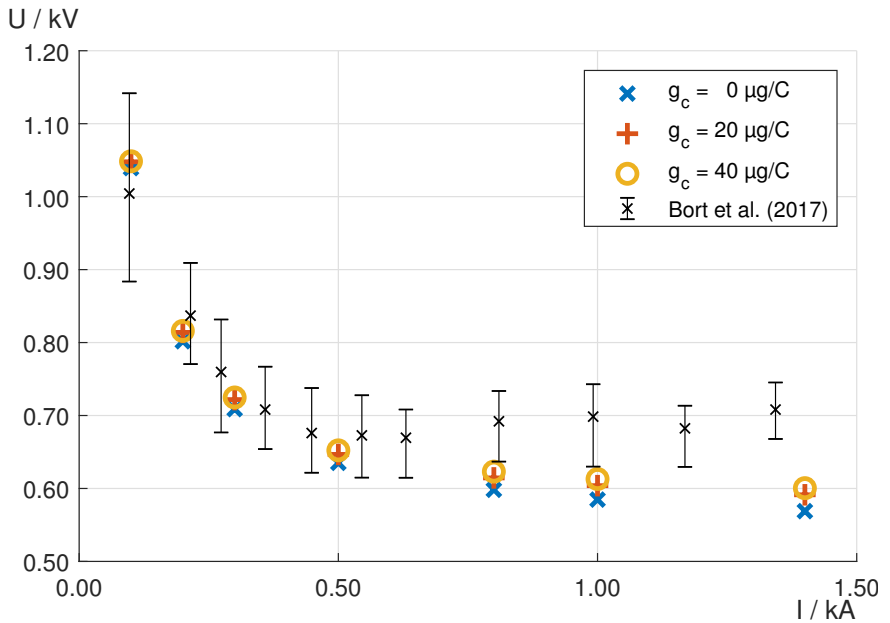
Figure 15.4.: Arc voltage as a function of current and erosion rate.
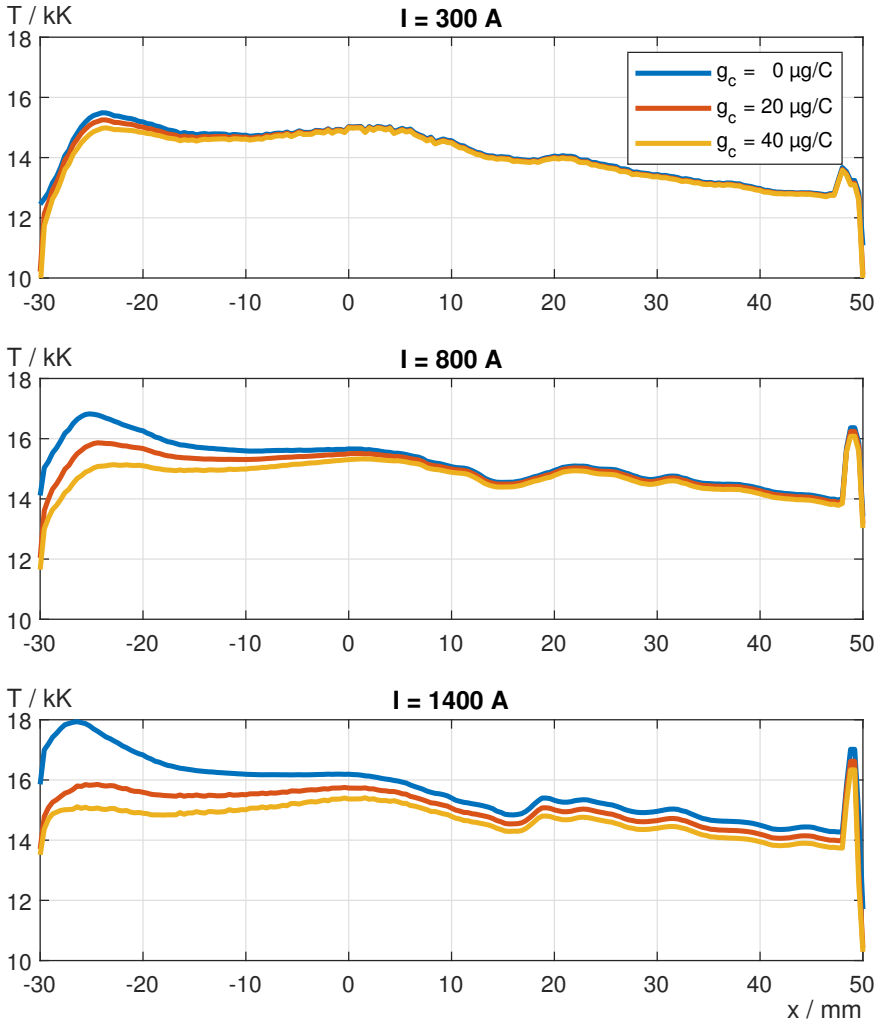
Figure 15.5.: Arc center temperature at axial positions.

zle. A few millimeters after the cathode tip ($x = -25\,\mathrm{mm}$), we note a temperature maximum; this is due to the gas flow being directed towards the nozzle axis enhancing effectively convective heat transfer from the arc column and leading to a constricted arc column. At $x = 15\,\mathrm{mm}$, we note a dip in the temperature profile which is a result of the expanding flow downstream of the throat. At the anode tip, we see a sharp increase in temperature because of a bow shock that is formed by the supersonic flow. Finally, we see that the temperature profiles are rather uniform in the convergent upstream section, whereas a negative slope is observed in the downstream divergent section.

This last observation may be of interest for further developments in the design of the geometric setup. It is interesting to note that these findings on the temperature profile correspond to results on the electric field, both numerically [64] and experimentally [30].

Figure 15.6 shows the boundary irradiance, i.e., the radiant flux received per unit area on the nozzle wall, summed for all radiation bands with wavelengths in the UV range (i.e., for band numbers 5 to 10). We note that irradiance increases with electrode erosion rate. For low currents, we see that irradiance is larger in the upstream section than it is downstream. For larger currents ($I \geq 500\,\mathrm{A}$) we discriminate on the erosion rate: if electrode erosion is neglected ($g_c = 0$), we see that irradiance is larger downstream compared to the same distance upstream of the nozzle. On the other hand, if electrode erosion is included ($g_c > 0$) irradiance remains larger in the upstream section for positions $|x| \leq 25\,\mathrm{mm}$.
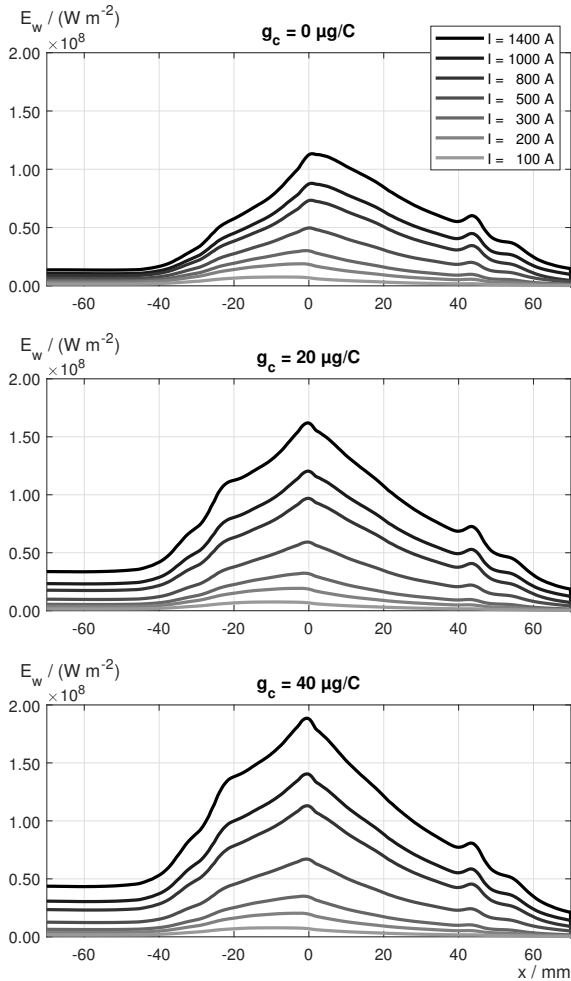
Figure 15.6.: Sum of band-integrated boundary irradiance in UV ranges. The vertical sequence of curves are the same as in the legend.

From these findings on arc voltage, arc center temperature, and boundary irradiation, we conclude that copper vapor enhances radiative heat transfer from the plasma column to its ambient and, as a consequence, reduces the plasma temperature in the upstream section (see also figure 15.5). Although copper-contaminated plasma is more conductive than pure air at otherwise identical temperatures and pressures, the total effect of reduced arc temperature dominates and leads to larger arc voltage (see figure 15.4).

In section 15.3.3 we developed an expression for radiation-induced wall ablation (see eq. (15.6)). A closer look at figure 15.6 reveals that the criterion $E_w \leq 3 \times 10^7 \, \text{W m}^{-2}$ is fulfilled for current $I \leq 300 \, \text{A}$ independently of the erosion rate, and coincides with the observations in [27]. It is therefore concluded that those observations are due to fact that PMMA is opaque in the UV range (as found in [17]). However, the hypothesis on the criterion for radiation-induced wall ablation should be tested with further experiments.

Figure 15.7 shows the wall irradiance for all bands in the two cases of $I = 100 \, \text{A}$ and $I = 1400 \, \text{A}$. The thick line shows the sum of irradiance of all bands in the UV range, and it is the same as in figure 15.6. We highlighted the bands that contribute most for the two cases. For low current it is band 7 and 2 that contribute most along the full arc column. This picture changes for larger current: we observe that band 7 has the largest contribution only in the downstream section, whereas band 6 has the largest contribution upstream. We also read from the figure that the UV bands cover about 2/3 of the total wall irradiance in both cases. It is concluded that the band definition in
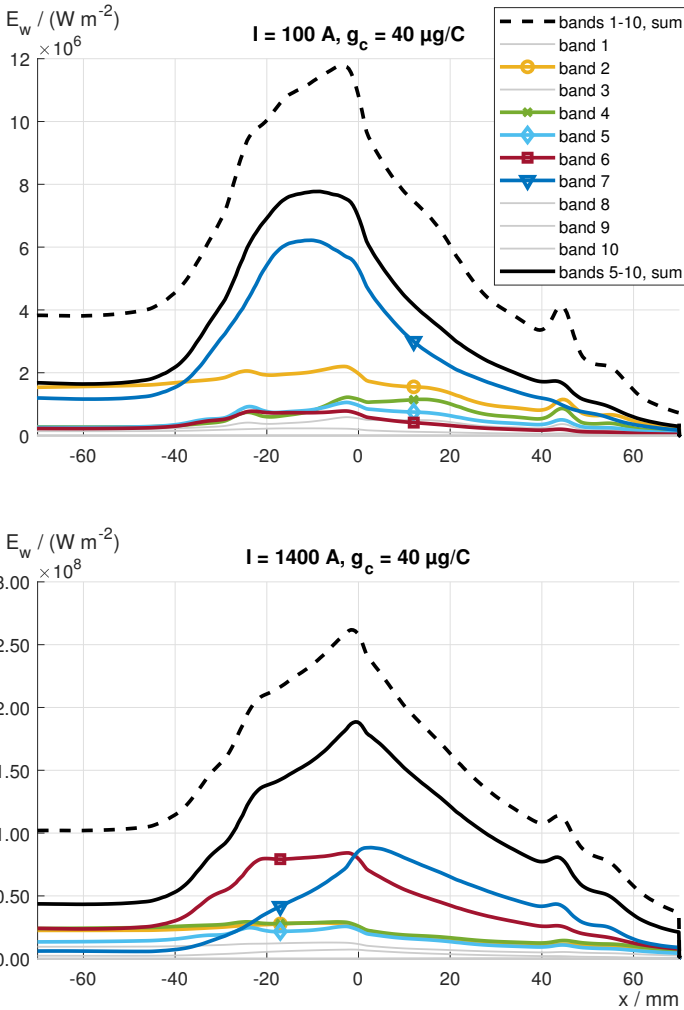
Figure 15.7.: Band-integrated boundary irradiance, total irradiance (dashed line), and irradiance of UV-bands (thick line).

E_w^{tot} / MW
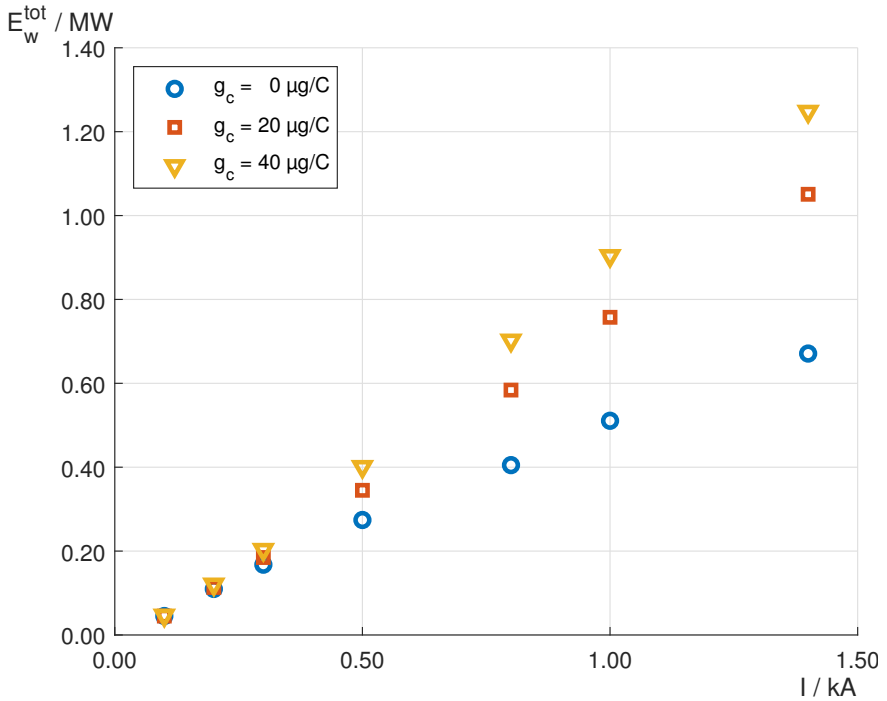
Figure 15.8.: Total radiant flux on nozzle wall in UV range.

table 15.1 will be useful for further studies on PMMA ablation, and it would be useful if measurements of optical properties of PMMA are extended to shorter wavelengths.

Figure 15.8 shows the radiant flux, i.e., the surface integrated value of boundary irradiance, onto the nozzle wall for frequencies in the UV regime. We clearly see that the radiant flux increases with current. Moreover, we see that the total irradiance is enhanced by the erosion

rate for currents larger than 300 A. This may be another indication for the observations in [27] that ablation occurs only for currents above a certain threshold.

15.5. Summary

Numerical results have been presented on an axially-blown arc in a PMMA nozzle. The computational model was refined by including copper erosion and defining the radiation bands to allow for analysis of wall irradiation in the UV range, because PMMA is optically thick for those wavelengths. An estimate for radiation-induced wall ablation has been developed and tested with previous results of measurements and the actual data obtained from these simulations. Additionally, a detailed analysis of the temperature profile in the arc column and the band-averaged wall irradiance has been provided. It has been found that copper erosion leads to higher arc voltage and lower arc center temperature particularly in the upstream section because it enhances radiative transfer to its ambient. It has also been found that copper erosion affects the spatial distribution of irradiance as evaluated on the nozzle wall, in particular that the upstream section is more intensely irradiated if copper vapor is present. Finally, it has been found that irradiance in the UV range covers about 2/3 of the total wall irradiance.

Further work may refine the computational model in various aspects. For instance, heat conduction to the solid bodies and their evaporation would lead to a more complete and consistent model and

might help for more accurate arc voltage at large currents.

The estimate for radiation-induced wall ablation shall be tested with other testcases. For instance, the experiments by [27] should be repeated with a shorter or longer time for high arc current, since this will affect the wall irradiance E_w required to observe ablation as shown by eq. (15.5). The numerical simulations may also be repeated for other inlet pressures and compared to further results in [27].

16. Summary & Outlook

16.1. Summary

This part showed results on applied numerical simulations of electric arcs in circuit breakers. The first contribution demonstrated that the software framework allows for computing the rigid body motion in a self-consistent manner and continuous mesh morphing. It examined the contributions to total torque of the contact arm. It was found that the torsional spring being leads to the largest contribution before electromagnetic force starts to dominate.

The second and third contribution investigated an axially-blown electric arc in a PMMA nozzle. The numerical simulation results complement experimental findings by an analysis of the energy budget from the arc to the nozzle wall. Moreover, the simulations allowed to evaluate the electric field in the arc as well as the flow field. These results were supplemented with the latter study including electrode erosion and evaluating radiative heat transfer to the PMMA nozzle wall. A caloric estimate is provided for the minimum irradiance required for initiating ablation. The numerical results of radiant heat flux to the nozzle wall may explain the experimental observations

that wall ablation is found only for sufficiently large current.

16.2. Outlook

The simulation framework will be applied to other types and geometries of circuit breakers. We will continue with further modeling aspects such as non-linear material data in the magnetic problem and ablation of the wall material.

The numerical model of the PMMA nozzle will be improved for better fitting to results from experiments. This includes further studies on the erosion rate, their melting, and irradiation of the nozzle walls. The numerical results will also continue with other flow conditions, electric current values, and electrode positions for comparison with measurements. The simulations may also be useful in the optimization process of the nozzle design.

17. Summary

In part I we generalized an existing numerical scheme for plasma simulations to 3D and non-constant timestep size. We included a collision model to account for frictional effects among the plasma species. A key issue was to interpolate data consistently between the primal and dual mesh discretization. Numerical experiments validated the subsystems, and the fully coupled Euler-Maxwell system was also tested. The main feature of the numerical scheme is to be asymptotic preserving, with the scaled Debye length λ as a parameter that allows for continuous blending between the full Maxwell model and the eddy current model. However, the testcase for $\lambda = 0$ showed that the extended model is not asymptotic preserving because it is not compatible with Ohm's law.

Part II concerned aspects of modeling radiative heat transfer in electric arc simulations. We revisited the fundamentals and modeling decisions that yield to computationally accessible models for applied simulations. We provided a sensitivity analysis on absorption coefficients and their influence on arc voltage and temperature in the simplest setting of a wall-stabilized arc model. We also considered the averaging methods for mean absorption coefficients and

found, that the line limited Planck mean permits to find the correct temperature profile at minimal computational costs. Its deficiency for applied simulations lies in the requirement that the renormalization length must be chosen a priori. However, this disadvantage should be viewed with the fact that the Planck and Rosseland mean are limiting cases themselves and a truly exact solution is not feasible.

Part III showed results of applied numerical simulations of electric arcs. The first case considered a low voltage circuit breaker. We showed that the simulation framework permits to compute the contact arm motion in a self-consistent manner and to evaluate the contributions of mechanics, plasma pressure, and electromagnetic force to total torque. The framework also allows for a continuous mesh morphing. The latter cases focused on a high voltage direct current circuit breaker nozzle. The same numerical framework has enabled us to evaluate the electric field and gas flow complementing measurement results. We also modeled radiative heat flux onto the nozzle wall and provided an argument for the observation that wall ablation is only measureable for sufficiently large currents.

In total, this thesis showed that performing numerical simulations of electric arcs is an involved task. It streches from the general modeling and coupling of an electrically conductive gas to specific submodels for radiation, contact motion, and many other aspects. They cannot be viewed separately but must be combined to a truly multiphysical framework.

Bibliography

[1] Intel C++ Compiler. URL `https://software.intel.com/content/www/us/en/develop/tools/compilers/c-compilers.html`.

[2] Poly(methyl methacrylate) (PMMA) Heat Capacity, Enthalpy, Entropy, Gibbs Energy: Datasheet from "The Advanced THermal Analysis System (ATHAS) Databank – Polymer Thermodynamics" Release 2014 in Springer-Materials. URL `https://materials.springer.com/polymerthermodynamics/docs/athas_0010`.

[3] N. A. Almeida, M. S. Benilov, and G. V. Naidis. Unified modelling of near-cathode plasma layers in high-pressure arc discharges. *Journal of Physics D: Applied Physics*, 41(24):245201, 2008. doi: 10.1088/0022-3727/41/24/245201.

[4] R. M. S. Almeida, M. S. Benilov, and G. V. Naidis. Simulation of the layer of non-equilibrium ionization in a high-pressure argon plasma with multiply-charged ions. *Journal of Physics D: Applied Physics*, 33(8):960–967, 2000. doi: 10.1088/0022-3727/33/8/312.

[5] Ana Alonso Rodríguez and Alberto Valli. *Eddy current approximation of Maxwell equations: Theory, algorithms and applications*, volume 4 of *MS&A*. Springer, Milan, 2010. ISBN 978-88-470-1506-7.

[6] Piergiorgio Alotto, Fabio Freschi, Maurizio Repetto, and Carlo Rosso. *The Cell Method for Electrical Engineering and Multiphysics Problems*, volume 230. Springer Berlin Heidelberg, Berlin, Heidelberg, 2013. doi: 10.1007/978-3-642-36101-2.

[7] Debora Amadori and Laurent Gosse. *Error Estimates for Well-Balanced Schemes on Simple Balance Laws*. Springer International Publishing, Cham, 2015. doi: 10.1007/978-3-319-24785-4.

[8] Julien Annaloro, Vincent Morel, Arnaud Bultel, and Pierre Omaly. Global rate coefficients for ionization and recombination of carbon, nitrogen, oxygen, and argon. *Physics of Plasmas*, 19(7):073515, 2012. doi: 10.1063/1.4737147.

[9] Neil W. Ashcroft and N. David Mermin. *Solid state physics*. Holt, Rinehart and Winston, New York, 1976. ISBN 0-03-049346-3.

[10] V. Aubrecht and J. J. Lowke. Calculations of radiation transfer in SF 6 plasmas using the method of partial characteristics. *IEEE Transactions on Plasma Science*, 27(10):2066–2073, 1994. doi: 10.1088/0022-3727/27/10/013.

[11] Vladimir Aubrecht and Milada Bartlova. Net Emission Coefficients of Radiation in Air and SF6 Thermal Plasmas. *Plasma Chemistry and Plasma Processing*, 29(2):131–147, 2009. doi: 10.1007/s11090-008-9163-x.

[12] Lisa Avila and Utkarsh Ayachit, editors. *The ParaView guide: Updated for ParaView version 4.3.* Kitware, Los Alamos, full color version edition, 2015. ISBN 978-1930934306.

[13] M. Baeva, M. S. Benilov, N. A. Almeida, and D. Uhrlandt. Novel non-equilibrium modelling of a DC electric arc in argon. *Journal of Physics D: Applied Physics*, 49(24):245205, 2016. doi: 10.1088/0022-3727/49/24/245205.

[14] Margarita Baeva. A Survey of Chemical Nonequilibrium in Argon Arc Plasma. *Plasma Chemistry and Plasma Processing*, 37(3):513–530, 2017. doi: 10.1007/s11090-016-9778-2.

[15] J.A.S. Barata. Integral and differential elastic collision cross-sections for low-energy Ar+ ions with neutral Ar atoms. *Nuclear Instruments and Methods in Physics Research Section A: Accelerators, Spectrometers, Detectors and Associated Equipment*, 580(1):14–17, 2007. doi: 10.1016/j.nima.2007.05.012.

[16] Yann Bartosiewicz, Pierre Proulx, and Yves Mercadier. A self-consistent two-temperature model for the computation of supersonic argon plasma jets. *Plasma Chemistry and Plasma Processing*, 35(17):2139–2148, 2002. doi: 10.1088/0022-3727/35/17/310.

[17] Marley Becerra and Jonas Pettersson. Optical radiative properties of ablating polymers exposed to high-power arc plasmas. *Journal of Physics D: Applied Physics*, 51(12):125202, 2018. doi: 10.1088/1361-6463/aaaeda.

[18] M. S. Benilov. A kinetic derivation of multifluid equations for multispecies nonequilibrium mixtures of reacting gases. *Physics of Plasmas*, 4(3):521–528, 1997. doi: 10.1063/1.872151.

[19] M. S. Benilov. Analysis of thermal non-equilibrium in the near-cathode region of atmospheric-pressure arcs. *Journal of Physics D: Applied Physics*, 30(24):3353–3359, 1997. doi: 10.1088/0022-3727/30/24/014.

[20] M. S. Benilov. Understanding and modelling plasma–electrode interaction in high-pressure arc discharges: a review. *Journal of Physics D: Applied Physics*, 41(14):144001, 2008. doi: 10. 1088/0022-3727/41/14/144001.

[21] M. S. Benilov and G. V. Naidis. Ionization layer at the edge of a fully ionized plasma. *Physical review. E, Statistical physics, plasmas, fluids, and related interdisciplinary topics*, 57 (2):2230–2241, 1998. doi: 10.1103/PhysRevE.57.2230.

[22] M. S. Benilov, N. A. Almeida, M. Baeva, M. D. Cunha, L. G. Benilova, and D. Uhrlandt. Account of near-cathode sheath in numerical models of high-pressure arc discharges. *Journal of Physics D: Applied Physics*, 49(21):215201, 2016. doi: 10.1088/ 0022-3727/49/21/215201.

[23] T. Billoux, Y. Cressault, Ph Teulet, and A. Gleizes. Calculation of the net emission coefficient of an air thermal plasma at very high pressure. *Journal of Physics: Conference Series*, 406: 012010, 2012. doi: 10.1088/1742-6596/406/1/012010.

[24] Udo Blell. *Zur numerischen Berechnung elektrostatischer und zeitharmonischer Felder im nichtorthogonalen dreidimensionalen Gitter*. Dissertation, Technische Hochschule Darmstadt, Darmstadt, 1994.

[25] Sergey Bochkanov. ALGLIB, 2019. URL `www.alglib.net`.

[26] Daniele Boffi, Franco Brezzi, and Michel Fortin. *Mixed Finite Element Methods and Applications*, volume 44. Springer Berlin Heidelberg, Berlin, Heidelberg, 2013. doi: 10.1007/978-3-642-36519-5.

[27] L. S. J. Bort, V. Freiermuth, and C. M. Franck. Influence of ablation on differential arc resistance. *Plasma Physics and Technology*, 4(2):145–148, 2017. doi: 10.14311/ppt.2017.2.145.

[28] Lorenz Bort. *Characterizing Axially Blown Arcs for Passive Oscillation DC Switches*. Doctoral Thesis, ETH Zurich, 2019.

[29] Lorenz S. J. Bort and Christian M. Franck. Effects of nozzle and contact geometry on arc voltage in gas circuit-breakers. In IEEE, editor, *2016 IEEE International Conference on High Voltage Engineering and Application (ICHVE)*, pages 1–4,

2016. ISBN 978-1-5090-0496-6. doi: 10.1109/ICHVE.2016. 7800700.

[30] Lorenz S. J. Bort and Christian M. Franck. Determination of Axial Electric Field Distribution in Blown Arcs With Differential Method. *IEEE Transactions on Plasma Science*, 47(1): 714–720, 2019. doi: 10.1109/TPS.2018.2880950.

[31] A. Bossavit and L. Kettunen. Yee-like schemes on staggered cellular grids: a synthesis between FIT and FEM approaches. *IEEE Transactions on Magnetics*, 36(4):861–867, 2000. doi: 10.1109/20.877580.

[32] Alain Bossavit. Whitney forms: a class of finite elements for three-dimensional computations in electromagnetism. *IEE Proceedings A Physical Science, Measurement and Instrumentation, Management and Education, Reviews*, 135(8):493, 1988. doi: 10.1049/ip-a-1.1988.0077.

[33] Alain Bossavit. Discretization of Electromagnetic Problems: The "Generalized Finite Differences" Approach. In Philippe G. Ciarlet, W.H.A. SCHILDERS, and E.J.W. TER MATEN, editors, *Numerical Methods in Electromagnetics*, volume 13 of *Handbook of Numerical Analysis*, pages 105–197. Elsevier professional, s.l., 2005. ISBN 9780444513755. doi: 10.1016/ S1570-8659(04)13002-0.

[34] Maher I. Boulos, Pierre Fauchais, and Emil Pfender. *Thermal*

Plasmas. Springer US, Boston, MA, 1994. ISBN 978-1-4899-1339-5. doi: 10.1007/978-1-4899-1337-1.

[35] S. Brugeat, H. Coitout, and M. J. Parizet. Description and optimization of a wall-stabilized arc chamber. *Review of Scientific Instruments*, 71(10):3702, 2000. doi: 10.1063/1.1286307.

[36] Daniele Casati, Jasmin Smajic, and Ralf Hiptmair. H-Phi Field Formulation With Lumped Sources and Unbounded Domains. *IEEE Transactions on Magnetics*, 56(1):1–4, 2020. doi: 10.1109/TMAG.2019.2949625.

[37] M. J. Castro, T. Morales de Luna, and C. Parés. Well-Balanced Schemes and Path-Conservative Numerical Methods. In Rémi Abgrall, Chi-Wang Shu, and Qiang Du, editors, *Handbook of numerical methods for hyperbolic problems*, volume 18 of *Handbook of Numerical Analysis*, pages 131–175. North-Holland an imprint of Elsevier, Amsterdam, The Netherlands and Kidlington, Oxford, United Kingdom, 2017. ISBN 9780444639103. doi: 10.1016/bs.hna.2016.10.002.

[38] Francis F. Chen. *Introduction to Plasma Physics and Controlled Fusion.* Springer US, Boston, MA, 1984. doi: 10.1007/978-1-4757-5595-4.

[39] W. L. T. Chen, J. Heberlein, and E. Pfender. Critical analysis of viscosity data of thermal argon plasmas at atmospheric pressure. *Plasma Chemistry and Plasma Processing*, 16(4):635–650, 1996. doi: 10.1007/BF01447012.

[40] Thomas Christen, Frank Kassubek, and Rudolf Gati. Radiative Heat Transfer and Effective Transport Coefficients. In Aziz Belmiloudi, editor, *Heat Transfer - Mathematical Modelling, Numerical Methods and Information Technology*. InTech, 2011. ISBN 978-953-307-550-1. doi: 10.5772/13853.

[41] Thomas C. Corke, C. Lon Enloe, and Stephen P. Wilkinson. Dielectric Barrier Discharge Plasma Actuators for Flow Control. *Annual Review of Fluid Mechanics*, 42(1):505–529, 2010. doi: 10.1146/annurev-fluid-121108-145550.

[42] Y. Cressault. Basic knowledge on radiative and transport properties to begin in thermal plasmas modelling. *AIP Advances*, 5 (5):057112, 2015. doi: 10.1063/1.4920939.

[43] Y. Cressault and A. Gleizes. Thermal plasma properties for Ar–Al, Ar–Fe and Ar–Cu mixtures used in welding plasmas processes: I. Net emission coefficients at atmospheric pressure. *Journal of Physics D: Applied Physics*, 46(41):415206, 2013. doi: 10.1088/0022-3727/46/41/415206.

[44] A. D'Angola, G. Colonna, C. Gorse, and M. Capitelli. Thermodynamic and transport properties in equilibrium air plasmas in a wide pressure and temperature range. *The European Physical Journal D*, 46(1):129–150, 2008. doi: 10.1140/epjd/e2007-00305-4.

[45] P. Degond, F. Deluzet, and D. Savelief. Numerical approximation of the Euler–Maxwell model in the quasineutral limit.

Journal of Computational Physics, 231(4):1917–1946, 2012. doi: 10.1016/j.jcp.2011.11.011.

[46] Pierre Degond and Fabrice Deluzet. Asymptotic-Preserving methods and multiscale models for plasma physics. *Journal of Computational Physics*, 336:429–457, 2017. doi: 10.1016/j.jcp.2017.02.009.

[47] Fabrice Deluzet, Maurizio Ottaviani, and Stefan Possanner. A Drift-Asymptotic scheme for a fluid description of plasmas in strong magnetic fields. *Computer Physics Communications*, 219:164–177, 2017. doi: 10.1016/j.cpc.2017.05.018.

[48] C. M. Dixon, J. D. Yan, and M. T. C. Fang. A comparison of three radiation models for the calculation of nozzle arcs. *Journal of Physics D: Applied Physics*, 37(23):3309–3318, 2004. doi: 10.1088/0022-3727/37/23/013.

[49] P. Drude. Zur Elektronentheorie der Metalle. *Annalen der Physik*, 306(3):566–613, 1900. doi: 10.1002/andp.19003060312.

[50] P. Drude. Zur Ionentheorie der Metalle. *Physikalische Zeitschrift*, 1(14):161–165, 1900.

[51] S. D. Eby, J. Y. Trépanier, and X. D. Zhang. Modelling radiative transfer in circuit-breaker arcs with the P-1 approximation. *Journal of Physics D: Applied Physics*, 31(13):1578–1588, 1998. doi: 10.1088/0022-3727/31/13/012.

[52] D. Eichhoff, A. Kurz, R. Kozakov, G. Gött, D. Uhrlandt, and A. Schnettler. Study of an ablation-dominated arc in a model circuit breaker. *Journal of Physics D: Applied Physics*, 45(30): 305204, 2012. doi: 10.1088/0022-3727/45/30/305204.

[53] O. Eichwald, O. Ducasse, N. Merbahi, M. Yousfi, and D. Dubois. Effect of order fluid models on flue gas streamer dynamics. *Journal of Physics D: Applied Physics*, 39(1):99–107, 2006. doi: 10.1088/0022-3727/39/1/015.

[54] W. Elenbaas. Die Quecksilber-Hochdruckentladung. *Physica*, 1 (7-12):673–688, 1934. doi: 10.1016/S0031-8914(34)80258-3.

[55] W. Elenbaas. Ähnlichkeitsgesetze der Hochdruckentladung. *Physica*, 2(1-12):169–182, 1935. doi: 10.1016/S0031-8914(35) 90079-9.

[56] W. Elenbaas. *Fluorescent Lamps*. Macmillan Education UK, London, 1971. ISBN 978-1-349-00363-1. doi: 10.1007/ 978-1-349-00361-7.

[57] Yoshiaki Enami and Masayoshi Sakata. Simulation of arc in molded-case circuit breaker with metal vapor and moving electrode. In *2nd International Conference on Electric Power Equipment - Switching Technology (ICEPE-ST)*, pages 1–4. IEEE, 20.10.2013 - 23.10.2013. ISBN 978-1-4799-3817-9. doi: 10.1109/ICEPE-ST.2013.6804390.

[58] Lorenzo Fagiano and Rudolf Gati. On the order reduction of the radiative heat transfer model for the simulation of plasma arcs in switchgear devices. *Journal of Quantitative Spectroscopy and Radiative Transfer*, 169:58–78, 2016. doi: 10.1016/j.jqsrt. 2015.10.002.

[59] Jeffrey P. Freidberg. *Ideal MHD*. Cambridge University Press, Cambridge, 2014. ISBN 9780511795046. doi: 10.1017/ CBO9780511795046.

[60] F. G. Fuchs, A. D. McMurry, S. Mishra, N. H. Risebro, and K. Waagan. High order well-balanced finite volume schemes for simulating wave propagation in stratified magnetic atmospheres. *Journal of Computational Physics*, 229(11):4033–4058, 2010. doi: 10.1016/j.jcp.2010.01.038.

[61] Roman Fuchs. Self-consistent modeling of electrode motion in a model circuit breaker. *Plasma Physics and Technology Journal*, 6(1):99–102, 2019. doi: 10.14311/ppt.2019.1.99.

[62] Roman Fuchs. Numerical arc simulations of radiatively-induced PMMA nozzle wall ablation. In *30th International Conference on Electrical Contacts*, 2021.

[63] Roman Fuchs and Henrik Nordborg. Systematic Investigation on Radiation Modeling Errors of a Wall-Stabilized Arc Simulations. In *Proceedings of the 22nd International Conference on Gas Discharges and Their Applications*, 2018.

[64] Roman Fuchs and Henrik Nordborg. Energy budget of electrical arcs in a gas-blast circuit breaker. In *Nafems World Congress 2019*, 2019.

[65] Roman Fuchs, M. Mürmann, and H. Nordborg. Sensitivity analysis of the temperature profile of electrical arcs due to band-averaged absorption coefficients. In *Proceedings of the 21st International Conference on Gas Discharges and their Applications*, pages 49–52, 2016.

[66] José M. Gallardo, Carlos Parés, and Manuel Castro. On a well-balanced high-order finite volume scheme for shallow water equations with topography and dry areas. *Journal of Computational Physics*, 227(1):574–601, 2007. doi: 10.1016/j.jcp. 2007.08.007.

[67] A. Gleizes, J. J. Gonzalez, and P. Freton. Thermal plasma modelling. *Journal of Physics D: Applied Physics*, 38(9):R153–R183, 2005. doi: 10.1088/0022-3727/38/9/R01.

[68] Alain Gleizes. Perspectives on Thermal Plasma Modelling. *Plasma Chemistry and Plasma Processing*, 35(3):455–469, 2015. doi: 10.1007/s11090-014-9589-2.

[69] Alain Gleizes and Yann Cressault. Effect of Metal Vapours on the Radiation Properties of Thermal Plasmas. *Plasma Chemistry and Plasma Processing*, 37(3):581–600, 2017. doi: 10.1007/s11090-016-9761-y.

[70] M. Gnybida, Ch. Rümpler, and V. R. T. Narayanan. OPTI-MAL BAND SELECTION FOR THE CALCULATION OF PLANCK MEAN ABSORPTION COEFFICIENTS. *Plasma Physics and Technology Journal*, 4(1):70–73, 2017. doi: 10.14311/ppt.2017.1.70.

[71] M. Gnybida, Ch. Rümpler, and V. R. T. Narayanan. RADIA-TIVE PROPERTIES AND NUMERICAL MODELING OF C4F7N-CO2 THERMAL PLASMA. *Plasma Physics and Technology Journal*, 6(2):144–147, 2019. doi: 10.14311/ppt.2019.2.144.

[72] David J. Griffiths. *Introduction to electrodynamics*. Pearson Education, Harlow, 4th ed., pearson new international ed. edition, 2014. ISBN 9781292034652.

[73] Paul W. Gross and P. Robert Kotiuga. *Electromagnetic theory and computation: A topological approach*, volume 48 of *Mathematical Sciences Research Institute publications*. Cambridge University Press, Cambridge, U.K. and New York, 2004. ISBN 9780511211522.

[74] Gaël Guennebaud and Benoît Jacob. Eigen, 2010. URL `http://eigen.tuxfamily.org`.

[75] Roop N. Gupta, Kam-Pui Lee, Richard A. Thompson, and Jerrold M. Yos. Calculations and curve fits of thermodynamic and transport properties for equilibrium air to 30000 K.

[76] Ernst Hairer and Gerhard Wanner. *Solving Ordinary Differential Equations II: Stiff and Differential-Algebraic Problems*, volume 14 of *Springer series in computational mathematics*. Springer-Verlag Berlin Heidelberg, Berlin, Heidelberg, 2., rev. ed. edition, 2010. ISBN 978-3-642-05221-7. doi: 10.1007/978-3-642-05221-7.

[77] Makato Hayashi. Bibliography of electron and photon cross sections with atoms and molecules published in the 20th century. Argon. URL https://www.osti.gov/etdeweb/biblio/20380995.

[78] G. Heller. Dynamical Similarity Laws of the Mercury High Pressure Discharge. *Physics*, 6(12):389–394, 1935. doi: 10.1063/1.1745282.

[79] Michael Hiltzik. Farewell to the big-screen plasma TV, 2014. URL https://www.latimes.com/business/hiltzik/la-fi-mh-bigscreen-plasma-tv-20140707-column.html.

[80] R. Hiptmair. Discrete Hodge-Operators: An Algebraic Perspective. *Progress In Electromagnetics Research*, 32:247–269, 2001. doi: 10.2528/PIER00080110.

[81] Ralf Hiptmair. From E to Edge Elements. *The Academician*, 3(1):23–31, 2003.

[82] Ralf Hiptmair. Private communication, 2019.

[83] John David Jackson. *Classical Electrodynamics.* Wiley, 3rd edition, 1999. ISBN 978-0-471-30932-1.

[84] Shi Jin. Efficient Asymptotic-Preserving (AP) Schemes For Some Multiscale Kinetic Equations. *SIAM Journal on Scientific Computing*, 21(2):441–454, 1999. doi: 10.1137/S1064827598334599.

[85] Shi Jin. Asymptotic preserving (AP) schemes for multiscale kinetic and hyperbolic equations: a review. *Rivisita di Matematica della Università di Parma*, 3(2):177–216, 2012.

[86] Ansgar Jüngel and Yue-Jun Peng. A hierarchy of hydrodynamic models for plasmas. Zero-electron-mass limits in the drift-diffusion equations. *Annales de l'insitut Henry Poincaré, section C*, 17(1):83–118, 2000. URL http://www.numdam.org/item/?id=AIHPC_2000__17_1_83_0.

[87] R. Käppeli and S. Mishra. Well-balanced schemes for the Euler equations with gravitation. *Journal of Computational Physics*, 259:199–219, 2014. doi: 10.1016/j.jcp.2013.11.028.

[88] Michael Keidar. *Plasma Cancer Therapy*, volume 115 of *Springer series on atomic, optical, and plasma physics.* Springer International Publishing, Cham, 2020. ISBN 978-3-030-49966-2. doi: 10.1007/978-3-030-49966-2.

[89] P. Kloc, V. Aubrecht, M. Bartlova, and O. Coufal. Radiation transfer in air and air-Cu plasmas for two temperature profiles.

Journal of Physics D: Applied Physics, 48(5):055208, 2015. doi: 10.1088/0022-3727/48/5/055208.

[90] P. Kloc, V. Aubrecht, and M. Bartlova. Numerically optimized band boundaries of Planck mean absorption coefficients in air plasma. *Journal of Physics D: Applied Physics*, 50(30):305201, 2017. doi: 10.1088/1361-6463/aa7627.

[91] Peter Kloc, Vladimír Aubrecht, and Milada Bartlová. Effective plasma radius for Planck mean absorption coefficient: 129425. In *Proceedings of the 21st International Conference on Gas Discharges and their Applications*, pages 89–92, 2016.

[92] Atsushi Komuro and Akira Ando. Simulation of spatiotemporal variation of OH radical density in atmospheric-pressure streamer discharge. *Plasma Sources Science and Technology*, 26(6):065003, 2017. doi: 10.1088/1361-6595/aa638d.

[93] Atsushi Komuro and Ryo Ono. Two-dimensional simulation of fast gas heating in an atmospheric pressure streamer discharge and humidity effects. *Journal of Physics D: Applied Physics*, 47(15):155202, 2014. doi: 10.1088/0022-3727/47/15/155202.

[94] Atsushi Komuro, Ryo Ono, and Tetsuji Oda. Kinetic model of vibrational relaxation in a humid-air pulsed corona discharge. *Plasma Sources Science and Technology*, 19(5):055004, 2010. doi: 10.1088/0963-0252/19/5/055004.

[95] P. Robert Kotiuga. *Hodge Decomposition and Computational Electromagnetics*. PhD thesis, McGill University, Montréal, 1984.

[96] A. A. Kulikovsky. A More Accurate Scharfetter-Gummel Algorithm of Electron Transport for Semiconductor and Gas Discharge Simulation. *Journal of Computational Physics*, 119(1): 149–155, 1995. doi: 10.1006/jcph.1995.1123.

[97] Hai P. Le and Jean-Luc Cambier. Modeling of inelastic collisions in a multifluid plasma: Excitation and deexcitation. *Physics of Plasmas*, 22(9):093512, 2015. doi: 10.1063/1. 4931170.

[98] Hai P. Le and Jean-Luc Cambier. Modeling of inelastic collisions in a multifluid plasma: Ionization and recombination. *Physics of Plasmas*, 23(6):063505, 2016. doi: 10.1063/1. 4953050.

[99] Randall J. LeVeque. *Finite Volume Methods for Hyperbolic Problems*. Cambridge University Press, 2012. ISBN 9780521810876. doi: 10.1017/CBO9780511791253.

[100] Randall J. LeVeque and H.C Yee. A study of numerical methods for hyperbolic conservation laws with stiff source terms. *Journal of Computational Physics*, 86(1):187–210, 1990. doi: 10.1016/ 0021-9991(90)90097-K.

[101] Ju Li, Cunhua Ma, Shengjie Zhu, Feng Yu, Bin Dai, and Dezheng Yang. A Review of Recent Advances of Dielectric Barrier Discharge Plasma in Catalysis. *Nanomaterials (Basel, Switzerland)*, 9(10), 2019. doi: 10.3390/nano9101428.

[102] P. J. Lindstrom and W. G. Mallard. NIST Chemistry WebBook: NIST Standard Reference Database Number 69, 30.01.2020. URL `https://webbook.nist.gov/cgi/inchi/ InChI%3D1S/C5H8O2/c1-4(2)5(6)7-3/h1H2%2C2-3H3`.

[103] J. J. Lowke. Predictions of arc temperature profiles using approximate emission coefficients for radiation losses. *Journal of Quantitative Spectroscopy and Radiative Transfer*, 14(2):111–122, 1974. doi: 10.1016/0022-4073(74)90004-1.

[104] John J. Lowke and D. Kenneth Davies. Properties of electric discharges sustained by a uniform source of ionization. *Journal of Applied Physics*, 48(12):4991–5000, 1977. doi: 10.1063/1. 323606.

[105] Wenjing Lu, Yawar Abbas, Muhammad Farooq Mustafa, Chao Pan, and Hongtao Wang. A review on application of dielectric barrier discharge plasma technology on the abatement of volatile organic compounds. *Frontiers of Environmental Science & Engineering*, 13(2):330, 2019. doi: 10.1007/ s11783-019-1108-5.

[106] A. Luque and U. Ebert. Density models for streamer discharges: Beyond cylindrical symmetry and homogeneous media. *Journal*

of Computational Physics, 231(3):904–918, 2012. doi: 10.1016/
j.jcp.2011.04.019.

[107] LXCat. Plasma Data Exchange Project. URL `www.lxcat.net`.

[108] A. R. Mansour and K. Hara. Multispecies plasma fluid simu-
lation for carbon arc discharge. *Journal of Physics D: Applied
Physics*, 52(10):105204, 2019. doi: 10.1088/1361-6463/aaf945.

[109] Matthieu Melot, Jean-Yves Trépanier, Ricardo Camarero, and
Eddy Petro. Comparison of Two Models for Radiative Heat
Transfer in High Temperature Thermal Plasmas. *Modelling
and Simulation in Engineering*, 2011(2):1–7, 2011. doi: 10.
1155/2011/285108.

[110] J. Mentel and J. Heberlein. The anode region of low current
arcs in high intensity discharge lamps. *Journal of Physics D:
Applied Physics*, 43(2):023002, 2010. doi: 10.1088/0022-3727/
43/2/023002.

[111] Morton Mitchner and Charles H. Kruger. *Partially ionized
gases*. A Wiley-Interscience publication. Wiley, New York NY,
1973. ISBN 0-471-61172-7.

[112] Michael F. Modest. *Radiative heat transfer*. Academic Press,
New York, 3. edition, 2013. ISBN 9780123869906.

[113] Michel Moisan, Jacques Pelletier, and Graeme Lister. *Physics
of collisional plasmas: Introduction to high-frequency dis-*

charges. Grenoble sciences. Springer, Dordrecht, 2012. ISBN 9789400745582.

[114] Mario Mürmann, Alexander Chusov, and Roman Fuchs. Simulation-based Development of a Line Lightning Protection Device. In *30th International Conference on Electrical Contacts*, 2021.

[115] A. B. Murphy. Diffusion in equilibrium mixtures of ionized gases. *Physical review. E, Statistical physics, plasmas, fluids, and related interdisciplinary topics*, 48(5):3594–3603, 1993. doi: 10.1103/PhysRevE.48.3594.

[116] A. B. Murphy. Transport coefficients of air, argon-air, nitrogen-air, and oxygen-air plasmas. *Plasma Chemistry and Plasma Processing*, 15(2):279–307, 1995. doi: 10.1007/BF01459700.

[117] A. B. Murphy. A comparison of treatments of diffusion in thermal plasmas. *Journal of Physics D: Applied Physics*, 29(7): 1922–1932, 1996. doi: 10.1088/0022-3727/29/7/029.

[118] Alexandra Miriam Mutzke. *Lichtbogen-Simulation unter besonderer Berücksichtigung der Fußpunkte*. Dissertation, TU Braunschweig, Braunschweig, 2009.

[119] H. Nordborg and A. A. Iordanidis. Self-consistent radiation based modelling of electric arcs: I. Efficient radiation approximations. *Journal of Physics D: Applied Physics*, 41(13):135205, 2008. doi: 10.1088/0022-3727/41/13/135205.

[120] J. Ostrowski, R. Bianchetti, I. Erceg Baros, B. Galletti, R. Gati, D. Pusch, M. Schwinne, and B. Wüthrich. Computational magnetohydrodynamics in the simulation of gas circuit breakers. *International Journal of Computational Science and Engineering*, 9(5/6):433, 2014. doi: 10.1504/IJCSE.2014.064528.

[121] Cecilia Pagliantini. *Computational Magnetohydrodynamics with Discrete Differential Forms*. PhD thesis, ETH Zurich, 2016.

[122] Friedrich Paschen. Ueber die zum Funkenübergang in Luft, Wasserstoff und Kohlensäure bei verschiedenen Drucken erforderliche Potentialdifferenz. *Annalen der Physik*, 273(5):69–96, 1889. doi: 10.1002/andp.18892730505.

[123] Pedro S. Peixoto and Saulo R.M. Barros. On vector field reconstructions for semi-Lagrangian transport methods on geodesic staggered grids. *Journal of Computational Physics*, 273:185–211, 2014. doi: 10.1016/j.jcp.2014.04.043.

[124] Blair Perot. Conservation Properties of Unstructured Staggered Mesh Schemes. *Journal of Computational Physics*, 159(1):58–89, 2000. doi: 10.1006/jcph.2000.6424.

[125] Per-Olof Persson and Gilbert Strang. A Simple Mesh Generator in MATLAB. *SIAM Review*, 46(2):329–345, 2004. doi: 10.1137/S0036144503429121.

[126] B. Peyrou, L. Chemartin, Ph Lalande, B. G. Chéron, Ph Rivière, M-Y Perrin, and A. Soufiani. Radiative proper-

ties and radiative transfer in high pressure thermal air plasmas. *Journal of Physics D: Applied Physics*, 45(45):455203, 2012. doi: 10.1088/0022-3727/45/45/455203.

[127] A. V. Phelps. The application of scattering cross sections to ion flux models in discharge sheaths. *Journal of Applied Physics*, 76(2):747–753, 1994. doi: 10.1063/1.357820.

[128] Silvano Pitassi, Riccardo Ghiloni, Francesco Trevisan, and Ruben Specogna. The role of the dual grid in low-order compatible numerical schemes on general meshes. *Journal of Computational Physics*, 2020, (to appear).

[129] Leanne C. Pitchford, Luis L. Alves, Klaus Bartschat, Stephen F. Biagi, Marie-Claude Bordage, Igor Bray, Chris E. Brion, Michael J. Brunger, Laurence Campbell, Alise Chachereau, Bhaskar Chaudhury, Loucas G. Christophorou, Emile Carbone, Nikolay A. Dyatko, Christian M. Franck, Dmitry V. Fursa, Reetesh K. Gangwar, Vasco Guerra, Pascal Haefliger, Gerjan J. M. Hagelaar, Andreas Hoesl, Yukikazu Itikawa, Igor V. Kochetov, Robert P. McEachran, W. Lowell Morgan, Anatoly P. Napartovich, Vincent Puech, Mohamed Rabie, Lalita Sharma, Rajesh Srivastava, Allan D. Stauffer, Jonathan Tennyson, Jaime de Urquijo, Jan van Dijk, Larry A. Viehland, Mark C. Zammit, Oleg Zatsarinny, and Sergey Pancheshnyi. LXCat: an Open-Access, Web-Based Platform for Data Needed for Modeling Low Temperature Plasmas.

Plasma Processes and Polymers, 14(1-2):1600098, 2017. doi: 10.1002/ppap.201600098.

[130] Max Planck. Ueber das Gesetz der Energieverteilung im Normalspectrum. *Annalen der Physik*, 309(3):553–563, 1901. doi: 10.1002/andp.19013090310.

[131] J. Poggie. Multi-fluid modelling of pulsed discharges for flow control applications. *International Journal of Computational Fluid Dynamics*, 29(2):180–191, 2015. doi: 10.1080/10618562. 2015.1021694.

[132] Gerald C. Pomraning. *The equations of radiation hydrodynamics*, volume 54 of *International series of monographs in natural philosophy*. Pergamon Press, Oxford, 1st edition, 1973. ISBN 0-08-016893-0.

[133] L. Prevosto, G. Artana, B. Mancinelli, and H. Kelly. Schlieren technique applied to the arc temperature measurement in a high energy density cutting torch. *Journal of Applied Physics*, 107(2):023304, 2010. doi: 10.1063/1.3291099.

[134] A. Prothero and A. Robinson. On the stability and accuracy of one-step methods for solving stiff systems of ordinary differential equations. *Mathematics of Computation*, 28(125):145, 1974. doi: 10.1090/S0025-5718-1974-0331793-2.

[135] Yuri Raizer. *Gas discharge physics*. Springer, Berlin and New York, 1991. ISBN 978-3-642-64760-4.

[136] G. G. Raju. Electron-atom collision cross sections in argon: an analysis and comments. *IEEE Transactions on Dielectrics and Electrical Insulation*, 11(4):649–673, 2004. doi: 10.1109/TDEI. 2004.1324355.

[137] H. Z. Randrianandraina, Y. Cressault, and A. Gleizes. Improvements of radiative transfer calculation for SF 6 thermal plasmas. *Journal of Physics D: Applied Physics*, 44(19):194012, 2011. doi: 10.1088/0022-3727/44/19/194012.

[138] Donald Rapp and Paula Englander-Golden. Total Cross Sections for Ionization and Attachment in Gases by Electron Impact. I. Positive Ionization. *The Journal of Chemical Physics*, 43(5):1464–1479, 1965. doi: 10.1063/1.1696957.

[139] V. Rat, P. André, J. Aubreton, M. F. Elchinger, P. Fauchais, and D. Vacher. Transport coefficients including diffusion in a two-temperature argon plasma. *Journal of Physics D: Applied Physics*, 35(10):981–991, 2002. doi: 10.1088/0022-3727/35/10/ 306.

[140] P. A. Raviart and J. M. Thomas. A mixed finite element method for 2-nd order elliptic problems. In Ilio Galligani and Enrico Magenes, editors, *Mathematical Aspects of Finite Element Methods*, volume 606 of *Lecture Notes in Mathematics*, pages 292–315, Berlin and Heidelberg, 1977. Springer. ISBN 978-3-540-37158-8. doi: 10.1007/BFb0064470.

[141] Svein Rosseland. *Theoretical astrophysics: Atomic theory and the analysis of stellar atmospheres and envelopes.* The International series of monographs on physics. Clarendon Press, Oxford, 1936.

[142] Christian Rümpler. *Lichtbogensimulation für Niederspannungsschaltgeräte.* Dissertation, TU Ilmenau, Ilmenau, 2009.

[143] Christian Rümpler and V.R.T. Naranyanan. Arc Modeling Challenges. *Plasma Physics and Technology*, 2(3):261–270, 2015.

[144] Christian Rümpler, Albert Zacharias, and Hartwig Stammberger. Low–voltage circuit breaker arc simulation including contact arm motion. In Frank Berger, editor, *The 27th International Conference on Electrical Contacts*, pages 290–294, 2014. ISBN 978-3-8007-3624-9.

[145] V. V. Rusanov. The calculation of the interaction of nonstationary shock waves and obstacles. *USSR Computational Mathematics and Mathematical Physics*, 1(2):304–320, 1962. doi: 10.1016/0041-5553(62)90062-9.

[146] Julia Rüther. *Weiterentwicklung und Vereinfachung eines Simulationsmodells für Schaltlichtbögen in Löschblechkammern.* Dissertation, TU Braunschweig, Braunschweig, 2014.

[147] Thomas Rüther. *Experimentelle Untersuchung der Lichtboge-*

naufteilung an Löschblechen. Cuvillier Verlag, Göttingen, 1st edition, 2008. ISBN 9783867275132.

[148] Masayoshi Sakata and Yoshiaki Enami. Arc Simulation Technology. *Fuji Electric Review*, 60(3):195–200, 2014.

[149] Fatemeh Salimi Meidanshahi, Khosro Madanipour, and Babak Shokri. Measurement of temperature and electrons density distribution of atmospheric arc plasma by moiré deflectometry technique. *Optics and Lasers in Engineering*, 51(4):382–387, 2013. doi: 10.1016/j.optlaseng.2012.11.018.

[150] Martin Seeger. Perspectives on Research on High Voltage Gas Circuit Breakers. *Plasma Chemistry and Plasma Processing*, 35(3):527–541, 2015. doi: 10.1007/s11090-014-9595-4.

[151] V. G. Sevast'yanenko. Radiation transfer in a real spectrum. Integration over frequency. *Journal of Engineering Physics*, 36 (2):138–148, 1979. doi: 10.1007/BF00865111.

[152] Dongkyu Shin, John W. McBride, and Igor O. Golosnoy. Arc Modeling to Predict Arc Extinction in Low-Voltage Switching Devices. In *2018 IEEE Holm Conference on Electrical Contacts*, pages 222–228. IEEE, 14.10.2018 - 18.10.2018. ISBN 978-1-5386-6315-8. doi: 10.1109/HOLM.2018.8611712.

[153] Siemens PLM software. STAR-CCM+, 2018.

[154] Siemens PLM software. STAR-CCM+, 2019.

[155] J. Smajic, T. Franz, M. K. Bucher, A. Limone, A. Shoory, S. Skibin, and J. Tepper. Computational and Experimental Investigation of Distribution Transformers Under Differential and Common Mode Transient Conditions. *IEEE Transactions on Magnetics*, 53(6):1–4, 2017. doi: 10.1109/TMAG.2017.2673763.

[156] Jasmin Smajic, Jillian Hughes, Thorsten Steinmetz, David Pusch, Wolfgang Monig, and Martin Carlen. Numerical Computation of Ohmic and Eddy-Current Winding Losses of Converter Transformers Including Higher Harmonics of Load Current. *IEEE Transactions on Magnetics*, 48(2):827–830, 2012. doi: 10.1109/TMAG.2011.2171926.

[157] Gary A. Sod. A survey of several finite difference methods for systems of nonlinear hyperbolic conservation laws. *Journal of Computational Physics*, 27(1):1–31, 1978. doi: 10.1016/0021-9991(78)90023-2.

[158] A. Sommerfeld. Zur Elektronentheorie der Metalle auf Grund der Fermischen Statistik. *Z. Physik (Zeitschrift für Physik)*, 47 (1-2):1–32, 1928. doi: 10.1007/BF01391052.

[159] Magnus Svärd and Siddhartha Mishra. Implicit–explicit schemes for flow equations with stiff source terms. *Journal of Computational and Applied Mathematics*, 235(6):1564–1577, 2011. doi: 10.1016/j.cam.2010.08.015.

[160] Yasunori Tanaka, Takayasu Fujino, and Toru Iwao. Review of Thermal Plasma Simulation Technique. *IEEJ Transactions on*

Electrical and Electronic Engineering, 14(11):1582–1594, 2019. doi: 10.1002/tee.23040.

[161] The HDF Group. Hierarchical Data Format, version 5, 1997-2018. URL `https://www.hdfgroup.org/HDF5/`.

[162] E. Tonti. Finite Formulation of the Electromagnetic Field. *Progress In Electromagnetics Research*, 32:1–44, 2001. doi: 10.2528/PIER00080101.

[163] Juan Pablo Trelles. Advances and challenges in computational fluid dynamics of atmospheric pressure plasmas. *Plasma Sources Science and Technology*, 27(9):093001, 2018. doi: 10.1088/1361-6595/aac9fa.

[164] Juan Pablo Trelles and S. Mahnaz Modirkhazeni. Variational multiscale method for nonequilibrium plasma flows. *Computer Methods in Applied Mechanics and Engineering*, 282:87–131, 2014. doi: 10.1016/j.cma.2014.09.001.

[165] U. van Rienen. *Numerical Methods in Computational Electrodynamics: Linear Systems in Practical Applications*. Lecture Notes in Computational Science and Engineering. Springer Berlin Heidelberg, 2001. ISBN 9783642568022.

[166] Ursula van Rienen, Jürgen Flehr, Ute Schreiber, and Victor Motrescu. Modeling and Simulation of Electro-Quasistatic Fields. In Kurt Antreich, Roland Bulirsch, Albert Gilg, and

Peter Rentrop, editors, *Modeling, Simulation, and Optimization of Integrated Circuits*, volume 79, pages 17–31. Birkhäuser Basel, Basel, 2003. ISBN 978-3-0348-9426-5. doi: 10.1007/978-3-0348-8065-7.

[167] F. Verhulst. *Methods and applications of singular perturbations: Boundary layers and multiple timescale dynamics*, volume 50 of *Texts in applied mathematics*. Springer, New York, 2005.

[168] Dragan Vidovic. Polynomial reconstruction of staggered unstructured vector fields. *Theoretical and Applied Mechanics*, 36 (2):85–99, 2009. doi: 10.2298/TAM0902085V.

[169] Eduard Vinaricky. *Elektrische Kontakte, Werkstoffe und Anwendungen*. Springer Berlin Heidelberg, Berlin, Heidelberg, 2016. doi: 10.1007/978-3-642-45427-1.

[170] Eveline Visee. *Second order velocity reconstruction on unstructured grids*. Master thesis, Utrecht University, Utrecht, 2016.

[171] Michael M. Walter. *Switching arcs in passive resonance HVDC circuit breakers*. PhD thesis, ETH Zurich, 2013.

[172] B. Wang, G. Zhao, and O. B. Fringer. Reconstruction of vector fields for semi-Lagrangian advection on unstructured, staggered grids. *Ocean Modelling*, 40(1):52–71, 2011. doi: 10.1016/j.ocemod.2011.06.003.

[173] Martin H. Weik. magnetic reluctance. In *Computer Science and*

Communications Dictionary, page 960. Springer US, Boston, MA, 2001. ISBN 978-1-4020-0613-5.

[174] T. Weiland. Eine Methode zur Lösung der Maxwellschen Gleichungen für sechskomponentige Felder auf diskreter Basis. *AEÜ - International Journal of Electronics and Communications*, 31:116–120, 1977.

[175] Hermann Weingärtner. *Chemische Thermodynamik: Einführung für Chemiker und Chemieingenieure.* Teubner Studienbücher Chemie. Vieweg+Teubner Verlag, Wiesbaden, 2003. ISBN 9783322912213. doi: 10.1007/978-3-322-91221-3.

[176] Yi Wu, Mingzhe Rong, Zhiqiang Sun, Xiaohua Wang, Fei Yang, and Xingwen Li. Numerical analysis of arc plasma behaviour during contact opening process in low-voltage switching device. *Journal of Physics D: Applied Physics*, 40(3):795–802, 2007. doi: 10.1088/0022-3727/40/3/016.

[177] XDMF. eXtensible Data Model and Format. URL `http://www.xdmf.org`.

[178] Ángel Yanguas-Gil, José Cotrino, and Luís L. Alves. An update of argon inelastic cross sections for plasma discharges. *Journal of Physics D: Applied Physics*, 38(10):1588–1598, 2005. doi: 10.1088/0022-3727/38/10/014.

[179] Kane Yee. Numerical solution of initial boundary value problems involving maxwell's equations in isotropic media. *IEEE*

Transactions on Antennas and Propagation, 14(3):302–307, 1966. doi: 10.1109/TAP.1966.1138693.

[180] J. F. Zhang, M. T. C. Fang, and D. B. Newland. Theoretical investigation of a 2 kA DC nitrogen arc in a supersonic nozzle. *Journal of Physics D: Applied Physics*, 20(3):368–379, 1987. doi: 10.1088/0022-3727/20/3/020.

[181] Vladimir M. Zhdanov. *Transport processes in multicomponent plasma.* Taylor & Francis, London, 2002. ISBN 0-415-27920-8.

[182] M. B. Zheleznyak, A. K. Mnatsakanian, and S. V. Sizykh. Photoionization of mixtures of nitrogen and oxygen by gas discharge radiation. *Teplofiz. Vys. Temp*, 20:423–428, 1982.

Curriculum Vitae

Roman Fuchs was born on February 27, 1987, in Lucerne, and he grew up in Sattel SZ. He went to Gymnasium at Stiftsschule Einsiedeln and graduated in 2005 with baccalaureate (Gymnasiale Maturität) in Latin, Italian and biology. After that he got trained in the Swiss Armed Forces Engineer corps as pontonier (boat driver) and served in the disaster relief standby unit task force.

In 2006, Roman Fuchs started studying mathematics at University of Bern where he got fascinated by numerical analysis as well as the capabilities and complexities of computing. He also took courses in computer science and management of information systems. After graduating as a Bachelor of Science in Mathematics in 2009, he continued his studies in the master curriculum of Computational Science and Engineering at ETH Zurich. The focus program in fluid dynamics drew his interest to turbulence modeling and high performance computing, and opened up an engineering perspective on solving real-life problems with scientific methods. He took the chances for an exchange semester to National University of Singapore and writing his master thesis within the CFDLAB at University of California, Santa Barbara, and graduated with a Master of Science in 2012.

Roman Fuchs then started as a project engineer in Prof. Dr. Henrik Nordborg's research group at the Institute for Energy Technology of OST Eastern Switzerland University of Applied Sciences (formerly HSR). Being a specialist for numerical simulations and in particular computational fluid dynamics, he quickly embarked on engineering topics relevant to industrial partners like gas meter modeling, simulations of vertical axis wind turbines, and renewable energy aspects. He has been teaching assistant for CFD, programming, and mathematical basics courses.

By 2014, electric arc simulations became a new research topic for the group. Roman Fuchs took the chance and started his PhD project as an external doctoral student with Prof. Dr. Ralf Hiptmair and Prof. Dr. Siddharta Mishra at Seminar of Applied Mathematics at ETH Zurich. He is fascinated by the large variety of aspects to be covered for mastering plasma simulations successfully; these range from chemistry, physics, and data modeling to computational aspects and visualization techniques. Roman Fuchs presented regularly his research results at scientific and industrial conferences.